

**Molecular Dynamics Studies of Ionic and
Molecular Liquids in Aqueous and Non-aqueous
Multi-component Systems**

By

Sourav Palchowdhury

CHEM11201204006

**National Institute of Science Education and Research
Bhubaneswar, Odisha – 752050**

*A thesis submitted to the
Board of Studies in Chemical Sciences
In partial fulfillment of requirements
for the Degree of*

DOCTOR OF PHILOSOPHY

Of

HOMI BHABHA NATIONAL INSTITUTE

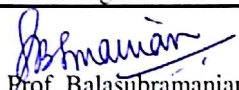
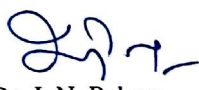


September, 2017

Homi Bhabha National Institute¹

Recommendations of the Viva Voce Committee

As members of the Viva Voce Committee, we certify that we have read the dissertation prepared by Mr. Sourav Palchowdhury entitled "Molecular Dynamics Studies of Molecular and Ionic Liquids in Aqueous and Non-aqueous Multi-component Systems" and recommend that it may be accepted as fulfilling the thesis requirement for the award of Degree of Doctor of Philosophy.

Chairman	 Prof. A. Srinivasan	Date: 05.09.2017
Guide/convenor	 Dr. Bhargava B. L.	Date: 05.09.2017
External examiner	 Prof. Balasubramanian Sundaram	Date: 05.09.2017
Member 1-	 Dr. U. Lourderaj	Date: 5/9/17
Member 2-	 Dr. J. N. Behera	Date: 5/9/17
Member 3-	 Dr. Rudresh Acharya	Date: 5/9/17

Final approval and acceptance of this thesis is contingent upon the candidate's submission of the final copies of the thesis to HBNI.

I hereby certify that I have read this thesis prepared under my direction and recommend that it may be accepted as fulfilling the thesis requirement.

Date: 05.09.2017

Place: Bhubaneswar


(Dr. Bhargava B. L.)

Guide

¹This page is to be included only for final submission after successful completion of viva voce.

STATEMENT BY AUTHOR

This dissertation has been submitted in partial fulfillment of requirements for an advanced degree at Homi Bhabha National Institute (HBNI) and is deposited in the Library to be made available to borrowers under rules of the HBNI. Brief quotations from this dissertation are allowable without special permission, provided that accurate acknowledgement of source is made. Requests for permission for extended quotation from or reproduction of this manuscript in whole or in part may be granted by the Competent Authority of HBNI when in his or her judgment the proposed use of the material is in the interests of scholarship. In all other instances, however, permission must be obtained from the author.

Sourav Palchowdhury
Sourav Palchowdhury

DECLARATION

I, hereby declare that the investigation presented in the thesis has been carried out by me. The work is original and has not been submitted earlier as a whole or in part for a degree / diploma at this or any other Institution / University.

Sourav Palchowdhury
Sourav Palchowdhury

List of Publications arising from the thesis

Journal

1. “Segregation of Ions at the Interface: Molecular Dynamics Studies of the Bulk and Liquid–vapor Interface Structure of Equimolar Binary Mixtures of Ionic Liquids”, **Palchowdhury, S.**; Bhargava, B. L., *Phys. Chem. Chem. Phys.*, **2015**, *17*, 19919-19928.
2. “Surface Structure and Dynamics of Ions at the Liquid–Vapor Interface of Binary Ionic Liquid Mixtures: Molecular Dynamics Studies”, **Palchowdhury, S.**; Bhargava, B. L., *J. Phys. Chem. C*, **2016**, *120*, 5430-5441.
3. “Effect of Cation Asymmetry on the Aggregation in Aqueous 1-Alkyl-3-decylimidazolium Bromide Solutions: Molecular Dynamics Studies”. **Palchowdhury, S.**; Bhargava, B. L., *J. Phys. Chem. B*, **2014**, *118*, 6241-6249.
4. “Self-Assembly of Cations in Aqueous Solutions of Hydroxyl-Functionalized Ionic Liquids: Molecular Dynamics Studies”. **Palchowdhury, S.**; Bhargava, B. L., *J. Phys. Chem. B*, **2015**, *119*, 11815-11824.
5. “Effect of Spacer Chain Length on the Liquid Structure of Aqueous Dicationic Ionic Liquid Solutions: Molecular Dynamics Studies”, **Palchowdhury, S.**; Bhargava, B. L., *Phys. Chem. Chem. Phys.*, **2015**, *17*, 11627-11637.
6. “Ionic Liquids at Nonane–Water Interfaces: Molecular Dynamics Studies”, **Palchowdhury, S.**; Bhargava, B. L., *J. Phys. Chem. B*, **2014**, *118*, 13930-13939.
7. “Glycine Molecules in Ionic Liquid Based Reverse Micelles: Investigation of Structure and Dynamics Using Molecular Dynamics studies”. **Palchowdhury, S.**; Bhargava, B. L., *J. Mol. Liq.*, **2017**, *230*, 384-394.

8. "Insights into the Structure and Dynamics at the Hexadecane Droplet–Water Interface in the Presence of 1-Alkanols as Emulsifiers", **Palchowdhury, S.**; Bhargava, B. L., *J. Mol. Liq.*, **2017**, *234*, 249-259.

Conferences

1. **MD@50 Conference, Bengaluru.** Jawaharlal Nehru Centre for Advanced Scientific Research (JNCASR), August 26-28, 2017, "Effect of Cation Asymmetry on the Aggregation in Aqueous 1-Alkyl-3-decylimidazolium Bromide Solutions: Molecular Dynamics Studies". **Palchowdhury, S.**; Bhargava, B. L. (**Poster Presentation**).
2. **TCS 2014, 14th Indian Theoretical Chemistry Symposium.** CSIR-National Chemical Laboratory, December 18-21, 2014, "Effect of Cation Asymmetry on the Aggregation in Aqueous 1-Alkyl-3-decylimidazolium Bromide Solutions: Molecular Dynamics Studies". **Palchowdhury, S.**; Bhargava, B. L. (**Poster Presentation**).
3. **CCP2015, XXVII IUPAP Conference on Computational Physics.** Indian Institute of Technology Guwahati, December 2-5, 2015. "Self-Assembly of Cations in Aqueous Solutions of Hydroxyl-Functionalized Ionic Liquids: Molecular Dynamics Studies". **Palchowdhury, S.**; Bhargava, B. L. Duration: 20 minutes (**Oral Presentation**).
4. **TCS 2016, 15th Indian Theoretical Chemistry Symposium.** University of Hyderabad, December 14-16, 2016. "Glycine Molecules in Ionic Liquid Based Reverse Micelles: Investigation of Structure and Dynamics Using Molecular Dynamics studies". **Palchowdhury, S.**; Bhargava, B. L. (**Poster Presentation**)

Sourav Palchowdhury,
Sourav Palchowdhury

To my family and teachers

ACKNOWLEDGEMENTS

First and above all, I praise God, the almighty for providing me this opportunity and granting me the capability to proceed successfully. This thesis appears in its current form due to the assistance and guidance of several people. I would therefore like to offer my sincere thanks to all of them. First of all, I would like to thank my supervisor Dr. Bhargava B. L. for providing me the opportunity to work on this exciting and inventive project. Also, I would like to express my gratitude to him for his guidance, patience, knowledge, advice and support during this long-standing learning period of my life. I appreciate all his contributions of valuable time, stimulating ideas, and funding to make my project experience interesting and productive. My sincere gratitude goes to the Prof. T. K. Chandrashekar, founder-Director (NISER), Prof. V. Chandrasekhar, Director (NISER) and Dr. Moloy Sarkar (former HOD, SCS). I would like to thank my doctoral committee members, Prof. A. Srinivasan, Dr. U. Lourderaj, Dr. J. N. Behera and Dr. Rudresh Acharya for their support and suggestions. I would also like to thank Dr. Arindam Ghosh and Dr. Himansu Sekhar Biswal for valuable discussions. I gratefully acknowledge NISER, Bhubaneswar for providing the computational facilities.

This would not have been possible without the continuous, unconditional help from my lab-mates Rituparna and Amol. I would also like to thank my friends and well wishers for their kind suggestion and help. Financial assistance (fellowship) by NISER is gratefully acknowledged. I would also like to acknowledge DST, New Delhi, Govt. of India for research funding. Finally, I would like to thank my parents, and family who were a witness to every step of the way and provided me support and confidence whenever I needed it the most. Thank you all so much for your unconditional love and untiring support.

Sourav Palchowdhury
Sourav Palchowdhury

Contents

Synopsis	13
List of Figures	20
List of Tables	39
Acronyms	41
1 Introduction	43
1.1 Ionic Liquids	43
1.1.1 Properties of Ionic Liquids	45
1.2 Motivation and Purpose	47
1.3 Literature Review.	50
1.4 Methods and Models	54
2 Segregation of Ions at the Interface: Molecular Dynamics Studies of Bulk and Liquid–vapor Interface Structure of Equimolar Binary Mixtures of Ionic Liquids	67
2.1 Introduction	68
2.2 Methodology and simulation details	70
2.3 Results and Discussion	71
2.3.1 Radial Distribution Functions (RDFs)	71
2.3.2 Spatial Distribution Functions (SDFs)	75

2.3.3	Hydrogen Bonding	77
2.3.4	Density Profiles	78
2.3.5	Surface composition	80
2.3.6	Intermolecular orientation	81
2.3.7	Interface Organization	83
2.4	Conclusions	87
A	Appendix A	89
3	Surface structure and dynamics of ions at the liquid – vapor interface of binary ionic liquid mixtures : Molecular dynamics studies	100
3.1	Introduction	101
3.2	Methodology and simulation details.	102
3.2.1	Identification of the truly interfacial molecule method (ITIM)	103
3.3	Results and Discussion	103
3.3.1	Density profiles	103
3.3.2	Surface composition	107
3.3.3	Surface tension	109
3.3.4	Surface roughness	109
3.3.5	Survival probability.	111
3.3.6	Re-orientation Dynamics	114
3.3.7	Dynamics of rotation	118
3.3.8	Interface organization	122
3.4	Conclusion	123
B	Appendix B	126
4	Effect of Cation Asymmetry on the Aggregation in Aqueous 1-Alkyl-3-Decylimidazolium Bromide Solutions: Molecular Dynamics Studies	133

4.1	Introduction	134
4.2	Methodology and simulation details	135
4.3	Results and discussion	136
4.3.1	Intramolecular structure	136
4.3.2	Hydrogen bonding	137
4.3.3	Radial distribution function	139
4.3.4	Spatial distribution	139
4.3.5	Diffusion of ions	141
4.3.6	Formation of aggregates	142
4.3.7	Aggregation number	143
4.3.8	Structure of aggregates	145
4.3.9	Number density	148
4.3.10	Organization at the interface	149
4.4	Conclusions	152
C	Appendix C	154
5	Self-Assembly of Cations in Aqueous Solutions of Hydroxyl-Functionalized Ionic Liquids: Molecular Dynamics Studies	160
5.1	Introduction	161
5.2	Methodology and simulation details	162
5.3	Results and Discussion	163
5.3.1	Radial Distribution Functions (RDFs)	163
5.3.2	Spatial Distribution	166
5.3.3	Hydrogen Bonding	167
5.3.4	Intramolecular Structure	170
5.3.5	Diffusion of ions and molecules	173
5.3.6	Formation of Aggregates	174

5.3.7	Aggregation Number	174
5.3.8	Structure of the Aggregates	177
5.4	Conclusions	181
D	Appendix D	183
6	Effect of spacer chain length on the liquid structure of aqueous dicationic ionic liquid solutions:	
	Molecular dynamics studies	192
6.1	Introduction	193
6.2	Methodology and Simulation Details	194
6.3	Results and Discussion	195
6.3.1	Radial Distribution Functions (RDFs)	195
6.3.2	Hydrogen Bonding	198
6.3.3	Spatial Distribution	200
6.3.4	Intramolecular Structure	200
6.3.5	Formation of Aggregates	202
6.3.6	Aggregation Number	202
6.3.7	Structure of [C ₁₆ (MIm) ₂] aggregates	203
6.3.8	Diffusion of Ions and Molecules	206
6.3.9	Number Density	207
6.3.10	Organisation of Cations at the Interface	211
6.3.11	Surface Tension.	213
6.4	Conclusions	214
E	Appendix E	215
7	Glycine Molecules in Ionic Liquid based Reverse Micelles: Investigation of Structure and Dynamics using Molecular Dynamics Simulations	229

7.1	Introduction.	230
7.2	Methodology and Simulation Details.	231
7.3	Results and Discussion	232
7.3.1	Formation of Reverse Micelles	232
7.3.2	Structure of the Reverse Micelles.	233
7.3.3	Density Profiles	239
7.3.4	Hydrogen Bond Dynamics.	240
7.3.5	Translational Mobility	242
7.3.6	Re-orientation Dynamics	244
7.4	Conclusions	247
F	Appendix F	249
8	Ionic Liquids at Nonane – Water Interfaces: Molecular Dynamics Studies	258
8.1	Introduction	259
8.2	Methodology and Simulation Details	259
8.3	Results and Discussions	261
8.3.1	Number Density	262
8.3.2	Hydrogen Bonding	265
8.3.3	Radial Distribution Functions (RDFs)	267
8.3.4	Spatial Distribution	270
8.3.5	Orientation of Ions and Molecules	271
8.3.6	Interfacial Tension and Interface Composition	274
8.4	Conclusions	275
G	Appendix G	277
9	Insights into the Structure and Dynamics at the Hexadecane Droplet–water Interface in the Presence of 1-alkanols as Emulsifiers: Molecular Dynamics Studies	284

9.1	Introduction	285
9.2	Methodology and Simulation Details	286
9.3	Results and Discussion	287
9.3.1	Density Profiles	287
9.3.2	Interface Organization	290
9.3.3	Conformational Analysis of Hydrocarbon Chains.	296
9.3.4	Survival Probability and Hydrogen Bond Dynamics	298
9.4	Conclusions	301
H	Appendix H	303
	Summary	309

Synopsis

Name of the Student:	Sourav Palchowdhury
Name of the Constituent Institution:	National Institute of Science Education and Research (NISER), Bhubaneswar.
Enrollment No. :	CHEM11201204006
Title of the Thesis:	Molecular Dynamics Studies of Molecular and Ionic Liquids in Aqueous and Non-aqueous Multi-component Systems.
Board of Studies:	Chemical Sciences

Chapter 1: Introduction

Molecular liquids are ubiquitous in nature. Water, benzene, ethanol etc. are some very common examples of molecular liquids. Now, what is an ionic liquid? Ionic liquids are liquid salts composed of ions with melting point (T_m) < 373 K [1, 2]. Due to wide liquid range, high thermal and electrochemical stability, low vapor pressure and many other interesting properties [3, 4], they have potential applications in the field of solvents, biomolecule stabilization, heat and energy storage, etc [5, 6]. To understand their function, atomic level investigation of the structure and dynamics in bulk and liquid–vapor interfacial layer for aqueous and non-aqueous multi-component systems containing ionic liquids is essential. We have applied atomistic molecular dynamics simulation technique and adapted the force field parameters developed under the OPLS (Optimized Potential for Liquid Simulation) framework [7]. Bonded and non-bonded interactions contributed to the

total potential energy whose functional form is given by the equation,

$$U_{\text{Total}} = \sum_b \frac{K_{r,b}}{2} (r_b - r_{0,b})^2 + \sum_a \frac{K_{\theta,a}}{2} (\theta_a - \theta_{0,a})^2 + \sum_d \sum_{m=1}^n \frac{V_{m,d}}{2} [1 + (-1)^{m+1} \cos(m\phi_d)] \\ + \sum_i \sum_j \left\{ 4\epsilon_{ij} \left[\left(\frac{\sigma_{ij}}{r_{ij}} \right)^{12} - \left(\frac{\sigma_{ij}}{r_{ij}} \right)^6 \right] - \frac{1}{4\pi\epsilon_0} \frac{q_i q_j}{r_{ij}} \right\}$$

where the total potential energy U_{Total} consists of the sum over the energy terms involving all the bonds, angles, dihedrals and non-bonded interactions. The $r_{0,b}$ and $\theta_{0,a}$ represents the equilibrium bond length and bond angle respectively, whereas the $K_{r,b}$ and $K_{\theta,a}$ are the corresponding force constants. The $V_{m,d}$ terms are the fourier coefficients involved in the dihedral interactions. q_i is the partial charge on the i -th atom, σ and ϵ are the Lennard-Jones interaction parameters.

Chapter 2: Segregation of Ions at the Interface: Molecular Dynamics Studies of the Bulk and Liquid–vapor Interface Structure of Equimolar Binary Mixtures of Ionic Liquids. [8]

The structures of three different equimolar binary ionic liquid mixtures and their liquid–vapor interface have been studied using atomistic molecular dynamics simulations. Two of these binary mixtures were composed of a common cation 1-*n*-butyl-3-methylimidazolium and varying anions (chloride and hexafluorophosphate in one of the mixtures and chloride and trifluoromethanesulfonate in the other) and the third binary mixture was composed of a common anion, trifluoromethanesulfonate and two imidazolium cations with ethyl and octyl side chains. Binary mixtures with common cations are found to be homogeneous. The anions are preferentially located near the ring hydrogen atoms due to H-bonding interactions. Segregation of ions is observed at the interface with an enrichment of the liquid–vapor interface layer by longer alkyl chains and bigger anions with a distributed charge. The surface composition is drastically different from that of the bulk composition, with the longer alkyl tail groups and bigger anions populating the outermost layer of the interface. The longer alkyl chains of the cations and trifluoromethanesulfonate anions with a smaller charge density show orientational ordering at the liquid–vapor interface.

Chapter 3: Surface Structure and Dynamics of Ions at the Liquid–Vapor Interface of Binary Ionic Liquid Mixtures. [9]

The surface structure and dynamics of ions at the liquid–vapor interface of binary mixtures of ionic liquids 1-*n*-octyl-3-methylimidazolium trifluoromethanesulfonate ([omim][TfO]) and 1-ethyl-3-methylimidazolium trifluoromethanesulfonate ([emim][TfO]) of varying composition have been studied using atomistic molecular dynamics simulations. Global definition of the interface and the identification of the truly interfacial molecule method (ITIM) have been used to analyze the structure and dynamics of the ions at the interface. We have seen enhancement in the density of the longer alkyl chain cation ([omim]) at the liquid-vapor interface compared to the bulk. The surface is mainly enriched with the [omim] cation, and it becomes smoother with a decrease in mole fraction of [omim] cations in the mixtures. The [omim] cation shows greater survival probability at the liquid-vapor interface than other ions, and this probability increases with a decrease in mole fraction of [omim] cations. The reorientational correlation function suggests that the [omim] cations prefer to retain their orientation with respect to the interface normal for a longer time. The movement of ions in and out of the interface is facilitated by the out-of-plane rotation of the ions with respect to the interface.

Chapter 4: Effect of Cation Asymmetry on the Aggregation in Aqueous 1-Alkyl-3-decylimidazolium Bromide Solutions. [10]

Self-assembly of cations in aqueous solutions of 1-alkyl-3-decylimidazolium bromide (with four different alkyl chains, methyl, butyl, heptyl, and decyl chain) have been studied using atomistic molecular dynamics simulations. Polydisperse aggregates of cations are formed in the solution with alkyl tails in the core and the polar head groups present at the surface of the aggregates. The shape of the aggregates is dictated by the length of the alkyl chain. Aggregation numbers increase steadily with the increasing alkyl chain length. The greater asymmetry in the two-substituent chain length leads to a different surface structure compared to that of the cations with alkyl chains of similar length.

Chapter 5: Self-Assembly of Cations in Aqueous Solutions of Hydroxyl-Functionalized Ionic Liquids. [11]

The effect of presence of a hydroxyl-functionalized alkyl chain of varying carbon number on the self-assembly of cations in aqueous solutions of 1-(*n*-hydroxyalkyl)-3-decylimidazolium bromide (where the alkyl groups are ethyl, butyl, heptyl, and decyl) has been studied using atomistic molecular dynamics simulations. Spontaneous self-assembly of cations to form aggregates with hydrophobic core and hydrophilic surface is observed. The shape of the aggregates changes from quasispherical in the case of cations with hydroxyheptyl or smaller substituent chain, to a thin film like intercalated aggregate in the case of cations with hydroxydecyl chain. Cations with hydroxydecyl substituent chain exhibit long-range spatial correlations, and the anions are associated with cations to a greater extent due to the higher surface charge density of the aggregate. The ordered film like aggregate is stabilized by the dispersion interactions between the intercalated substituent chains and the intermolecular hydrogen bonds formed between the alkoxy oxygen atoms and the hydrogen atoms of the imidazolium ring. The cations form less compact aggregates with lower aggregation number than their nonhydroxyl analogues in the corresponding aqueous solutions. The intracationic and aggregate structures are governed by the length of the hydroxyalkyl chain.

Chapter 6: Effect of Spacer Chain Length on the Liquid Structure of Aqueous Dicationic Ionic Liquid Solutions. [12]

The liquid structure of aqueous solutions of five different imidazolium based gemini dicationic ionic liquids 1-*n*-bis(3-methylimidazolium-1-yl) alkane bromide (*n* being the length of the spacer alkyl chain), with propyl, pentyl, octyl, decyl and hexadecyl spacer chains has been studied using atomistic molecular dynamics simulations. While solutions with propyl and pentyl spacers are homogeneous, those with octyl and decyl spacers show spatial heterogeneity. Microscopic inhomogeneity in the bulk solution phase increases with an increase in the length of the spacer chain leading to polydisperse aggregates in the solution with a hexadecyl spacer. Organization of the

cations at the solution–vapor interface also depends upon the length of the spacer chain with the most organized interfacial layer observed in the solution with a hexadecyl spacer chain.

Chapter 7: Glycine Molecules in Ionic Liquid Based Reverse Micelles: Investigation of Structure and Dynamics Using Molecular Dynamics studies. [13]

Amino acids, the building blocks of proteins, are probed in reverse micellar encapsulation processes of biological molecules. To understand the effect of confinement of amino acids on the structure and dynamics of reverse micellar aqueous core, a water/[C₁C₁₀Im][Br] reverse micelles containing variable number of glycine molecules (0 to 8), dispersed in pure nonane has been studied using atomistic molecular dynamics simulations. The size of the central water pool was found to become stable with increase in the number of glycine molecules. Confinement in nano-space region stabilizes the H-bonds formed between glycine molecules compared to bulk aqueous solution. Increase in the number of glycine molecules within the reverse micellar aqueous core increases the survival time of H-bonds among glycine molecules as well as among water molecules. Translational and reorientational motion of glycine and water molecules are found to be directly related to the survival probability of intermolecular glycine-glycine and water-water H-bonds suggesting the correlation between the mobility of molecules with rearrangement of the H-bonding network.

Chapter 8: Ionic Liquids at Nonane–Water Interfaces. [10]

The structures of ternary systems with water, nonane, and an ionic liquid, with the ionic liquid placed between water and nonane, have been studied using atomistic molecular dynamics simulations. Three different ionic liquids with 1-*n*-butyl-3-methylimidazolium cation and bromide, tetrafluoroborate, and trifluoromethanesulfonate anions have been studied. The ionic liquids disperse into the aqueous phase quickly and are solubilized in water within 15 ns to form two equivalent nonane-aqueous ionic liquid interfaces. The interfacial region is enriched with ionic liquids due to the amphiphilicity of the cations. The presence of ionic liquids at the interface reduces the interfacial tension between the nonane and water, thus facilitating the mixing of aqueous and

nonane phases. The reduction in the interfacial tension is found to be inversely related to the solubility of the corresponding ionic liquid in water. The butyl chains of the cations and the trifluoromethanesulfonate anions present in the interfacial region are found to be preferentially oriented parallel to the interface normal.

Chapter 9: Insights into the Structure and Dynamics at the Hexadecane Droplet–Water Interface in the Presence of 1-Alkanols as Emulsifiers. [15]

The structure and dynamics at the surface of nanoscopic hexadecane droplets immersed in aqueous phase with and without emulsifiers (1-alkanols of varying chain length; pentanol, heptanol, decanol and dodecanol) have been studied using atomistic molecular dynamics simulations. The nature of layering of alcohol molecules on the oil droplet is governed by the hydrophobicity of alkanols. Longer chain alkanols are more likely to penetrate into the oil droplet. The probability of tangential orientation of hexadecane molecules at the interface decreases with decreasing hydrophobic environment around the droplet. The interfacial hexadecane molecules show greater probability to obtain a puckered conformation in binary oil–water system than in ternary oil–water–alkanol systems. Decrease in hydrophobic interaction between hexadecane and water molecules due to the efficient screening of oil surface by longer chain alkanols in ternary oil–water–alkanol systems leads to greater survival probability of water molecules in the oil–water interfacial layer and enhancement in life time of H-bonds formed between alcohol and water molecules.

Bibliography

- [1] Rogers, R. D.; Seddon, K. R. *Science* **2003**, *302*, 792-793.
- [2] Hayes, R.; Warr, G. G., Atkin, R. *Chem. Rev.* **2015**, *115*, 6357-6426.
- [3] Tong, J.; Liu, Q.; Xu, W.; Fang, D.; Yang, J. *J. Phys. Chem. B* **2008**, *112*, 4381-4386.
- [4] Huddleston, J. G.; Visser, A. E.; Reichert, W. M.; Willauer, H. D.; Broker, G. A.; Rogers, R. D. *Green Chem.* **2001**, *3*, 156-164.
- [5] van Rantwijk, F.; Sheldon, R. A. *Chem. Rev.* **2007**, *107*, 2757-2785.
- [6] Greaves, T. L.; Drummond, C. J. *Chem. Rev.* **2008**, *108*, 206-237.
- [7] W. L. Jorgensen, D. S. Maxwell, J. Tirado-Rives, *J. Am. Chem. Soc.* 1996, **118**, 11225-11236.
- [8] Palchowdhury, S.; Bhargava, B. L. *Phys. Chem. Chem. Phys.* **2015**, *17*, 19919-19928.
- [9] Palchowdhury, S.; Bhargava, B. L. *J. Phys. Chem. C* **2016**, *120*, 5430-5441.
- [10] Palchowdhury, S.; Bhargava, B. L. *J. Phys. Chem. B* **2014**, *118*, 6241-6249.
- [11] Palchowdhury, S.; Bhargava, B. L. *J. Phys. Chem. B* **2015**, *119*, 11815-11824.
- [12] Palchowdhury, S.; Bhargava, B. L. *Phys. Chem. Chem. Phys.* **2015**, *17*, 11627-11637.
- [13] Palchowdhury, S.; Bhargava, B. L. *J. Mol. Liq.* **2017**, *230*, 384-394.
- [14] Palchowdhury, S.; Bhargava, B. L. *J. Phys. Chem. B* **2014**, *118*, 13930-13939.
- [15] Palchowdhury, S.; Bhargava, B. L. *J. Mol. Liq.* **2017**, *234*, 249-259.

List of Figures

1.1	Schematic representation of structures of some common constituent cations and anions.	44
1.2	Properties and applications of ionic liquids.	45
2.1	Schematic drawings of the ions in the IL mixtures.	72
2.2	RDFs between (a) different anion sites in [Cl] – [TfO] and (b) imidazolium ring centers in [emim] – [omim] at 500 K.	73
2.3	RDFs of the most negatively charged atom of the anions around (a) the most acidic hydrogen of the imidazolium ring and (b) the terminal carbon atom of the alkyl chain of the cations at 500 K in binary IL mixtures.	74
2.4	SDFs of (a) triflate oxygen atoms (in yellow) around the octylmethylimidazolium cation in [emim] – [omim] mixture and (b) chloride ions (in red), phosphorus (in cyan) and fluorine atoms (in yellow) of the [PF ₆] ions around the imidazolium cation in [Cl] – [PF ₆] at 500 K. Few carbon atoms of the octyl chain and the hydrogen atoms of the alkyl chains are not shown.	76
2.5	Distribution of the angles between the ring normal vector and the vector connecting the geometric center of the imidazolium ring and the chloride ion or the phosphorus atom of the [PF ₆] anion in [Cl] – [PF ₆] mixture at 500 K. Only those anions that are within 6Å from the cation are considered.	77

2.6	Density profiles of head and tail groups of cations and atoms of anions in (a) [Cl] – [PF ₆] (b) [Cl] – [TfO] and (c) [emim] – [omim] mixtures along the interface normal (z-axis) at 500 K.	79
2.7	Distribution of the angles between (a) alkyl chain vectors (butyl chains of mixtures with common cation and octyl chains of [emim] – [omim] mixture) of the cations and (b) CS bond vectors of triflate anions that are present in the interfacial region of IL mixtures at 500 K.	82
2.8	Snapshot of the liquid – vapor interface of the [emim] – [omim] system after 20 ns simulation. [omim] cations are shown in red, [emim] cations in yellow and [TfO] anions in blue.	83
2.9	Distribution of the angles between the interface normal (z-axis) and (a) butyl and octyl chains and (b) the NN vector (vector connecting the two nitrogen atoms of the imidazolium ring) of [bmim] and [omim] cations present in the interfacial region of IL mixtures.	84
2.10	Distribution of the angles between the interface normal (z-axis) and (a) the alkyl chains of the cations and (b) the carbon – sulfur bond vectors of the triflate anions in various slabs along the interface normal in the [emim] – [omim] mixture at 500 K.	85
2.11	Average $P_2(\cos \theta)$ of the angle between (a) alkyl chain of the cation and the surface normal (b) CS bond vector of the triflate anion and the surface normal for IL mixtures at 500 K.	86
A.1	RDFs of the chloride anions and the sulfur atoms of the triflate anions around the geometric center of the imidazolium ring in [Cl] – [TfO] mixture at 500 K.	89
A.2	RDFs of (a) different anion sites in [Cl] – [PF ₆] and (b) terminal carbon atoms of the alkyl chains belonging to distinct types of cations in [emim] – [omim] mixture at 500 K.	90

A.3	RDFs of (a) sulfur atoms of triflate anions around chloride anions in [Cl] – [TfO] system and (b) head group of [emim] cations around head groups of [omim] cations in [emim] – [omim] system at different temperatures.	90
A.4	RDFs of (a) the chloride anions around the most acidic hydrogen atom of the imidazolium ring in [Cl] – [TfO] system and (b) oxygen atoms of the triflate anions around the terminal carbon atoms of the ethyl chain [emim] – [omim] system at different temperatures.	91
A.5	SDFs of chloride anions (in red), oxygen atoms (in yellow) and sulfur atom (in cyan) of the [TfO] anions, that are within 6Å from the cation, around the geometric center of the imidazolium ring in [Cl] – [TfO] mixture at 500 K. The isosurface density shown corresponds to 8.5, 4 and 2 times the average density of chloride ions, oxygen atoms and sulfur atom of the triflate anions respectively. Hydrogen atoms on the alkyl groups are not shown.	91
A.6	Distribution of the angles between the ring normal vector and the vector connecting the geometric center of the imidazolium ring and the chloride ion or the sulfur atom of the [TfO] anion in [Cl] – [TfO] mixture at 500 K. Only those anions that are within 6Å from the cation are considered.	92
A.7	RDFs of oxygen and fluorine atoms of the triflate anions around the imidazolium ring hydrogen atoms in [emim] – [omim] system at 500 K.	92
A.8	Mass density profiles along the interface normal (z-axis) in binary ionic liquid mixtures at 500 K.	93
A.9	Number density profiles of terminal carbon atoms of the octyl chains in [emim] – [omim] mixture along the interface normal (z-axis) at different temperatures.	93
A.10	Orientation of ethyl and octyl chains of cations that are present in the interfacial region of [emim] – [omim] mixture at 500 K.	94

A.11	Distribution of the angles between the alkyl chains of the cations and the carbon – sulfur bond vectors of the triflate anions present in the interfacial layer of IL mixtures at 500 K.	94
A.12	Distribution of the angles between the interface normal (z-axis) and the alkyl chains of the [emim] – [omim] mixture at 500 K.	95
A.13	Distribution of the angles between the interface normal (z-axis) and (a) the butyl chains of the cations and (b) carbon – sulfur bond vectors of the triflate anions in various slabs along the interface normal in [Cl] – [TfO] mixture at 500 K.	95
3.1	Number density profiles of terminal carbon atoms (CT) of [omim] cations in binary IL mixtures obtained from (a) the global definition of the interface and (b) ITIM analysis. The zero value at the horizontal axis in figure (a) represent the center of the simulation cell whereas in figure (b), it corresponds to the position of the probe sphere along the test line where it was stopped for the first time by an atom at the liquid – vapor interface	104
3.2	Number density profiles of the terminal carbon atoms (CE) of [emim] cations in binary IL mixtures, obtained from (a) the global definition and (b) ITIM analysis. The zero value at the horizontal axis in figure (a) represents the center of the simulation cell whereas in figure (b), it corresponds to the position of the probe sphere along the test line where it was stopped for the first time by an atom at the liquid – vapor interface	106
3.3	Number density profiles of sulfur atoms (S) of [TfO] anions in binary IL mixtures obtained from (a) the global definition and (b) ITIM analysis. The zero value at the horizontal axis in figure (a) represents the center of the simulation cell whereas in figure (b), it corresponds to the position of the probe sphere along the test line where it was stopped for the first time by an atom at the liquid – vapor interface	107
3.4	Surface tension(γ) of binary mixtures at various mole fraction of [omim] cations.	109

3.5	Variation of normal distance of two surface points, $\langle d \rangle$ with their lateral separation l in different binary IL mixtures studied.	110
3.6	Bivariate distribution of the probability of the lateral distance l and the normal distance d of two surface points for (a) 9:1 (b) 1:1 and (c) 1:9 binary IL mixture.	112
3.7	Survival probability of (a) [omim] (b) [emim] and (c) [TfO] in the interfacial layer of the systems of varying composition.	113
3.8	Survival probability of (a)[omim] (b)[emim] and (c)[TfO] in the interfacial layer for the 1:1 IL mixture.	115
3.9	Different re-orientation TCFs of (a)[omim] (b)[emim] and (c)[TfO] in the interfacial layer for the 1:1 IL mixture.	117
3.10	Variation of $C_{zx}(t)$ (a) for octyl chain of [omim] cation across the entire composition range and (b) octyl chain of [omim] cation, ethyl chain of [emim] cation and carbon – sulfur bond vector of [TfO] anion for the 1:1 IL mixture in the interfacial layer.	118
3.11	Dynamical correlation function of (a)[omim] (b)[emim] and (c)[TfO] in the interfacial layer for the 1:1 IL mixture.	119
3.12	$C_z(t)$ for (a)[omim] (b)[emim] and (c)[TfO] in the interfacial layer for the systems of varying composition.	120
3.13	Variation in $C_{xy}(t)$ for (a)[omim] (b)[emim] and (c)[TfO] in the interfacial layer for the systems of varying composition.	121
3.14	Bivariate distribution of probability of $P_1(\cos \theta)$ and distance along the interface normal for (a) octyl chain of [omim] cation (b) ethyl chain of [emim] cation and (c) carbon – sulfur bond vector of [TfO] anion in 1:1 IL mixture.	123
3.15	Bivariate distribution of probability between $P_1(\cos \theta)$ and distance along the interface normal for (a) NN vector of [omim] cation and (b) NN vector of [emim] cation in 1:1 IL mixture.	124

B.1	Bivariate distribution of probability of the lateral distance l and the normal distance d of two surface points for (a) pure [omim][TfO] (b) 3:1 (c) 1:3 and (d) pure [emim][TfO] systems.	126
B.2	Variation of $C_{yz}(t)$ (a) for octyl chain of [omim] cation across the entire composition range and (b) octyl chain of [omim] cation, ethyl chain of [emim] cation and carbon – sulfur bond vector of [TfO] anion for the 1:1 IL mixture in the interfacial layer.	127
B.3	Variation of (a) $C_{yz}(t)$ and (b) $C_{xz}(t)$ for ethyl chain of [emim] cation across the entire composition range in the interfacial layer.	127
B.4	Variation of (a) $C_{yz}(t)$ and (b) $C_{xz}(t)$ for carbon–sulfur bond vector of [TfO] anion across the entire composition range in the interfacial layer.	128
4.1	Distribution of angle between the two alkyl chains attached to the head group. . .	137
4.2	Radial distribution functions of (a) terminal carbon atoms of shorter alkyl chain around themselves (b) geometric centers of imidazolium rings around themselves.	140
4.3	(a) Spatial density of anions and water molecules around cations in [C ₁ C ₁₀ Im][Br] solution and anions around cations in pure IL [C ₁ C ₁₀ Im][Br]. Density of anions in pure IL is shown in Yellow, red represents the density of anions in solution and cyan represents density of water. Hydrogen atoms present on the decyl chain are not shown. (b) Another view of the same figure. Water density is shown in transparent cyan.	141
4.4	Self-diffusion coefficients of cations in alkyldecylimidazolium bromide solutions.	142
4.5	Snapshot of the aqueous solution after 25 ns simulation. (a)[C ₁ C ₁₀ Im][Br] (b) [C ₄ C ₁₀ Im][Br] (c) [C ₇ C ₁₀ Im][Br] (d) [C ₁₀ C ₁₀ Im][Br]. Hydrophilic region of head group is shown in yellow whereas atoms belonging to hydrophobic alkyl chains are shown in magenta. Anions, water molecules and hydrogen atoms on the cations are not shown for the ease of visualization.	143

4.6	Fraction of cations involved in the formation of aggregates of size N in (a) $[C_1C_{10}Im][Br]$ solution (b) $[C_4C_{10}Im][Br]$ solution (c) $[C_7C_{10}Im][Br]$ solution (d) $[C_{10}C_{10}Im][Br]$ solution.	144
4.7	Structure of an aggregate in (a) $[C_1C_{10}Im][Br]$ solution (b) $[C_{10}C_{10}Im][Br]$ solution. Atoms belonging to head groups are shown in yellow, those belonging to alkyl chains are represented as magenta beads. Anions, water molecules and hydrogen atoms belonging to cations are not shown for the ease of visualization.	146
4.8	Hydration index for various carbon atoms on the decyl chain in $[C_{10}C_{10}Im][Br]$ solution.	147
4.9	Number density profiles of head and tail group of cations, anion and water along interface normal (z-axis) in $[C_{10}C_{10}Im][Br]$ solution.	148
4.10	Distribution of (a) angle between the alkyl chains and the interface normal (z-axis) (b) angle between the vector connecting the two nitrogen atoms and the interface normal.	150
4.11	Snapshot of vapor-liquid interface of (a) $[C_1C_{10}Im][Br]$ solution and (b) $[C_{10}C_{10}Im][Br]$ solution at the end of 25 ns simulation. The head groups of cations are shown as density in yellow, tail groups as density in magenta and water density is shown in transparent cyan.	151
C.1	Distribution of angle between the imidazolium rings of the cations that belong to the same aggregate and are within 8.0\AA from each other.	154
C.2	Mass density profile along interfacial normal for aqueous solutions of $[C_nC_{10}Im][Br]$ with $n = 1, 4, 7$ and 10	154
C.3	Distribution of angle between the imidazolium ring normal and the interface normal for aqueous solutions of $[C_nC_{10}Im][Br]$ with $n = 1, 4, 7$ and 10	155
5.1	Schematic diagram of the cations, mentioning the distinct atom types.	163

5.2	RDFs of (a) terminal carbon atoms (C_T) of the non-hydroxylated decyl chains around themselves and (b) alkyl chain carbon atoms (C_S) around themselves in different aqueous solutions.	164
5.3	RDFs of (a) bromide ions (Br^-) and (b) water oxygen atoms around the geometric center of the imidazolium ring in different $[HOC_nC_{10}][Br]$ solutions.	165
5.4	(a) Spatial density of anions (in yellow), water (in red) and alkoxy oxygen atoms (in green) around the imidazolium rings in $[HOC_{10}C_{10}Im][Br]$ solution (b) Another view of the same figure.	167
5.5	RDFs of hydroxyl oxygen atoms around the ring hydrogen atoms in aqueous solutions of $[HOC_nC_{10}Im][Br]$	170
5.6	Distribution of (a) angles between the two substituent chains (decyl and hydroxyalkyl) attached to the head group and (b) dihedrals formed by the nitrogen atom and successive three non-hydrogen atoms (heavier) of the hydroxyalkyl chain in different $[HOC_nC_{10}Im][Br]$ solutions.	171
5.7	Self-diffusion coefficients of cations in different $[HOC_nC_{10}Im][Br]$ solutions. . .	173
5.8	Snapshot of (a) the aqueous $[HOC_2C_{10}Im][Br]$ solution after 35 ns (b) the aqueous $[HOC_{10}C_{10}Im][Br]$ solution after 50 ns.	175
5.9	Fraction of cations involved in the formation of aggregates of size N in (a) $[HOC_{10}C_{10}Im][Br]$ (b) $[HOC_7C_{10}Im][Br]$ (c) $[HOC_4C_{10}Im][Br]$ and (d) $[HOC_2C_{10}Im][Br]$ solutions.	176
5.10	Structure of an aggregate in (a) $[HOC_{10}C_{10}Im][Br]$ (b) $[HOC_7C_{10}Im][Br]$ (c) $[HOC_4C_{10}Im][Br]$ and (d) $[HOC_2C_{10}Im][Br]$ solutions . The polar head groups are shown in yellow, the carbon atoms of the alkyl chains are shown in magenta, the oxygen atom is shown in green and the hydroxyl hydrogen atom is shown in red.	177
5.11	Distribution of intramolecular angles formed between the ring normal and the principal vector representing the decyl chain in aqueous $[HOC_nC_{10}Im][Br]$ solutions.	179
5.12	Hydration index of various carbon atoms along the hydroxydecyl and decyl chains in aqueous solution of $[HOC_{10}C_{10}Im][Br]$	180

D.1	RDFs of the bromide anions around the imidazolium ring hydrogen atoms in [HOC ₁₀ C ₁₀ Im][Br] solution.	183
D.2	RDFs of the water oxygen atoms around the imidazolium ring hydrogen atoms in [HOC ₁₀ C ₁₀ Im][Br] solution.	183
D.3	RDFs of the hydroxyl oxygen atoms around the imidazolium ring hydrogen atoms in [HOC ₁₀ C ₁₀ Im][Br] solution.	184
D.4	RDFs of the bromide anions around the hydroxyl hydrogen atom in different [HOC _n C ₁₀ Im][Br] solutions.	184
D.5	Distribution of angles made by the donor (ring carbon), hydrogen (attached to the ring carbon) and the acceptor (hydroxyl oxygen) atoms of [HOC ₂ C ₁₀ Im] cations in aqueous solution.	184
D.6	Intermolecular RDFs of hydroxyl oxygen atoms around the ring hydrogen atoms in aqueous solutions of [HOC _n C ₁₀ Im][Br].	185
D.7	Pictorial representation of the normal vector to the imidazolium ring and the vectors representing the decyl chain and the hydroxyalkyl chain. Blue, cyan and red beads represent nitrogen, carbon and oxygen atoms respectively. Hydrogen atoms are not shown.	185
D.8	Distribution of the dihedrals formed by the nitrogen atom of the imidazolium ring and successive three non-hydrogen atoms (heavier) of the decyl chains of the cations in different [HOC _n C ₁₀ Im][Br] solutions.	185
D.9	Distribution of angles formed between (a) the NN vectors and the principal axis representing the decyl chains (b) the NN vectors and the principal axis representing the hydroxyalkyl chains of the cations in their corresponding aqueous solutions.	186
D.10	Gauche defect probability of each C-C-C-C dihedral in the decyl chain of [HOC _n C ₁₀ Im] cations in their corresponding aqueous solutions.	186
D.11	Hydration index of the carbon atoms along the decyl chain in different [HOC _n C ₁₀ Im][Br] solutions.	187

6.1	Schematic representation of the $[C_n(\text{MIm})_2]$ cation.	195
6.2	RDFs of (a) anions and (b) water molecules around the geometric center of the imidazolium rings in different aqueous solutions.	196
6.3	RDFs of (a) different carbon atoms of the hexadecyl spacer around themselves in aqueous solution of $[C_{16}(\text{MIm})_2][2\text{Br}]$ (b) central carbon atom of the spacer chain around themselves in the aqueous solutions of $[C_n(\text{MIm})_2][2\text{Br}]$ systems.	197
6.4	(a) Spatial density of anions and water molecules around the imidazolium rings in $[C_{16}(\text{MIm})_2][2\text{Br}]$ solution (b) Another view of the same figure.	200
6.5	Distribution of angles between (a) the normal vectors of the two imidazolium rings separated by the alkyl spacer and (b) the two vectors joining the central carbon atom of the spacer with the imidazolium nitrogen atoms connected to the spacer, in aqueous solutions of DILs.	201
6.6	Fraction of cations involved in forming aggregates of size N in an aqueous solution of $[C_{16}(\text{MIm})_2][2\text{Br}]$	203
6.7	Structure of an aggregate in aqueous solution of $[C_{16}(\text{MIm})_2][2\text{Br}]$. Atoms belonging to head groups are shown in yellow, and those belonging to the spacer chain are represented as magenta beads. Anions, water molecules and hydrogen atoms belonging to cations are not shown for the ease of visualization.	204
6.8	Probability distribution of radii of (a) aggregates and (b) hydrophobic core for the aggregates in aqueous solution of $[C_{16}(\text{MIm})_2][2\text{Br}]$	205
6.9	Hydration index of various carbon atoms of the hexadecyl spacer in aqueous solution of $[C_{16}(\text{MIm})_2][2\text{Br}]$	206
6.10	Self-diffusion coefficients of cations and anions in $[C_n(\text{MIm})_2][2\text{Br}]$ (n=3, 5, 8, 10 and 16) solution.	206
6.11	Atom number density profiles of different carbon atoms of the (a) hexadecyl spacer of $[C_{16}(\text{MIm})_2]$ cations and (b) propyl spacers of $[C_3(\text{MIm})_2]$ cations, along the interface normal (z-axis) in their respective solution–vapor interfaces.	208

6.12	Atom number density profiles of (a) central carbon atom of hexadecyl, decyl, octyl, pentyl and propyl spacers in their corresponding aqueous solutions and (b) head groups, central spacer carbon of $[C_{16}(\text{MIm})_2]$ cations, anions and water along the interface normal (z-axis) in aqueous solution.	209
6.13	Distribution of angle between (a) the spacer vectors (connecting the two nitrogen atoms of the imidazolium rings separated by the spacer) of cations present in the interface (b) the spacer vector and the interface normal (z-axis).	211
6.14	Distribution of angle between (a) the vectors connecting the two nitrogen atoms of the imidazolium rings and the interface normal (z-axis) (b) the two vectors joining the central spacer carbon atom with the nitrogen atoms of the imidazolium rings separated by the spacer.	213
E.1	RDFs of anions around the geometric center of the imidazolium rings in aqueous solutions	215
E.2	RDFs of water molecules around the geometric center of the imidazolium rings in aqueous solutions	216
E.3	RDFs of different carbon atoms of the decyl spacer around themselves in aqueous solution of $[C_{10}(\text{MIm})_2][2\text{Br}]$	216
E.4	RDFs of different carbon atoms of the octyl spacer around themselves in aqueous solution of $[C_8(\text{MIm})_2][2\text{Br}]$	217
E.5	RDFs of different carbon atoms of the pentyl spacer around themselves in aqueous solution of $[C_5(\text{MIm})_2][2\text{Br}]$	217
E.6	RDFs of different carbon atoms of the propyl spacer around themselves in aqueous solution of $[C_3(\text{MIm})_2][2\text{Br}]$	218
E.7	RDFs of central carbon atom of the spacer chain around themselves in aqueous solutions of $[C_{10}(\text{MIm})_2][2\text{Br}]$ and $[C_8(\text{MIm})_2][2\text{Br}]$	218

E.8	Distribution of angles between the normal vectors of two imidazolium rings, and two vectors joining the central carbon atom of the spacer with the imidazolium nitrogen atoms connected to the spacer in $[C_{16}(MIm)_2][2Br]$ in gas phase.	219
E.9	Snapshot of the aqueous solution of $[C_{16}(MIm)_2][2Br]$ after 50 ns simulations. Head groups are shown in yellow and the tail groups are shown in magenta. Anions, water and hydrogen atoms on the cation are not shown for the ease of visualization.	219
E.10	Atom number density profiles of different carbon atoms of the hexadecyl spacer along the interface normal (z-axis) in the liquid–vapor interface of $[C_{16}(MIm)_2][2Br]$ solution.	220
E.11	Atom number density profiles of different carbon atoms of the decyl spacer along the interface normal (z-axis) in the liquid–vapor interface of $[C_{10}(MIm)_2][2Br]$ solution.	220
E.12	Atom number density profiles of different carbon atoms of the octyl spacer along the interface normal (z-axis) in the liquid–vapor interface of $[C_8(MIm)_2][2Br]$ solution.	221
E.13	Atom number density profiles of different carbon atoms of the pentyl spacer along the interface normal (z-axis) for the $[C_5(MIm)_2]$ cations in aqueous solution.	221
E.14	Snapshot of the liquid–vapor interface of the aqueous solution of $[C_{16}(MIm)_2][2Br]$ after 25 ns simulations. Head groups are shown in yellow and the tail groups are shown in magenta. Anions, water and hydrogen atoms on the cation are not shown for the ease of visualization.	222
E.15	Snapshot of the liquid–vapor interface of aqueous solution of $[C_{10}(MIm)_2][2Br]$ after 25 ns simulations. Head groups are shown in yellow and the tail groups are shown in magenta. Anions, water and hydrogen atoms on the cation are not shown for the ease of visualization.	222

E.16	Distribution of angles between the two vectors joining the central carbon atom of the spacer with the imidazolium nitrogen atoms connected to the spacer in the aqueous solution of $[C_{16}(MIm)_2][2Br]$	223
E.17	Distribution of angles between the two vectors joining the central carbon atom of the spacer with the imidazolium nitrogen atoms connected to the spacer in the aqueous solution of DILs.	223
7.1	Schematic representation of the $[C_1C_{10}Im]$ cation, glycine, nonane and water molecule.	233
7.2	The snapshots of different stages of aggregation of various species to form the reverse micelle in the system containing 8 glycine molecules. The water molecules, the glycine molecules and the bromide ions are shown in pink, blue and black respectively and the imidazolium rings and alkyl carbon atoms of $[C_1C_{10}Im]$ cations are shown in red and green respectively. The oil phase (nonane) and hydrogen atoms of $[C_1C_{10}Im]$ cations are not shown for the ease of visualization.	234
7.3	Structures of the reverse micelles containing (a) 1 (b) 2 (c) 4 and (d) 8 glycine molecules. The water molecules are shown in pink, the glycine molecules are shown in blue, the imidazolium rings and alkyl chain carbon atoms of $[C_1C_{10}Im]$ cations are shown in red and green respectively. The oil phase (nonane), hydrogen atoms of $[C_1C_{10}Im]$ cations and bromide anions are not shown for the ease of visualization.	235
7.4	Snapshot of glycine molecules within the reverse micellar aqueous core containing (a) 2 (b) 4 and (c) 8 glycine molecules. The oxygen, carbon and nitrogen atoms are shown in red, cyan and blue respectively and the hydrogen atoms attached to the α -C atom, and the amino hydrogen atoms are shown in pink and green respectively.	235
7.5	Spatial density of amino hydrogens (in yellow) and carboxylate oxygens (in green) around the α -C atom of glycine molecule.	235

7.6	Probability distribution of R_g of aqueous core of the reverse micellar systems containing (a)1 (b)2 (c)4 and (d)8 glycine molecules.	236
7.7	Snapshot of the reverse micellar aqueous core containing 8 glycine molecules. The water phase is shown as a continuous medium (in cyan), the glycine molecules are shown in blue, the imidazolium rings along with the first two carbon atoms attached to the ring of $[C_1C_{10}Im]$ cations are shown in red and the bromide anions are shown in black.	237
7.8	Probability distribution of the tetrahedral order parameter around those water molecules which are present in the first solvation shell of the α carbon atom of the glycine molecule.	238
7.9	Radial density profiles of (a) α -C atoms of glycine molecules and (b) water oxygen atoms for the reverse micelles containing varying number of glycine molecules.	240
7.10	Survival autocorrelation function, $C_{HB}(t)$ for H-bonds between (a) glycine molecules and (b) water molecules in different systems studied.	242
7.11	Mean squared displacement (MSD) of (a) glycine and (b) water in the center of mass frame of the reverse micelle in different systems studied.	243
7.12	Different vectors of interest for orientational relaxation in a glycine molecule.	245
7.13	Variation of $C_l(t)$ for (a) vectors characterizing the glycine molecule in reverse micelle with 8 glycine molecules and (b) M–P vector of glycine molecules across the systems studied.	245
7.14	Variation of $C_l(t)$ for the unit vector along the dipole moment of a water molecule across the reverse micellar systems studied.	247
F.1	Probability distribution of (a) R_g and (b) radius of aqueous core of the model reverse micelle.	249
F.2	Probability distribution of radius of aqueous core of the reverse micellar systems containing (a)1 (b)2 (c)4 and (d)8 glycine molecules respectively.	250

F.3	Radial density profiles of (a) geometric center of imidazolium ring and (b) bromide anions for the reverse micelles containing varying number of glycine molecules.	250
F.4	Mean squared displacement (MSD) of glycine molecules in binary glycine–water bulk solution.	251
F.5	Variation of reorientational time correlation function ($C_i(t)$) for different molecular vectors of glycine molecule in reverse micelle with single glycine molecule.	251
F.6	Variation of reorientational time correlation function ($C_i(t)$) for different molecular vectors of glycine molecule in reverse micelle with two glycine molecules.	252
F.7	Variation of reorientational time correlation function ($C_i(t)$) for different molecular vectors of glycine molecule in reverse micelle with four glycine molecules.	252
F.8	Variation of reorientational time correlation function ($C_i(t)$) for different molecular vectors of glycine molecule in binary glycine–water bulk solution.	253
8.1	Schematic representation of the $[C_4C_1Im]$ cation and nonane showing the atom types used in the discussion.	261
8.2	Snapshots of the ternary system with bromide anion. (a) initial configuration (b) after 1 ns simulation (c) after 30 ns simulation. Carbon atoms of nonane are shown in orange and the oxygen atoms of water are shown in red. Anions are represented as magenta beads.	262
8.3	(a) Number density profiles of different moieties along interface normal (z-axis) in nonane- $[C_4C_1Im][Br]$ -water system. (b) Atom number density profiles of nonane-water binary system and ternary systems along z-axis.	263
8.4	(a) Anion number density profiles along z-axis, in ternary systems. (b) Tail number density profiles in ternary systems along the interface normal.	264
8.5	RDFs of (a) nonane (C_{AT}) around different carbon atoms of $[C_4C_1Im]$ cation in the ternary system with bromide anion. (b) nonane (C_{AT}) around tail group (C_T) in ternary systems.	268

8.6	RDFs of (a) nonane (C_{AT}) around the central atoms of anions in ternary systems. (b) nonane (C_{AT}) around water in the binary and ternary systems.	269
8.7	(a) Spatial density of anions (in yellow), water (in cyan) and nonane (C_{AT}) (in red) around the cations that are in the interfacial region, in the ternary system with bromide anion. Hydrogen atoms on the butyl chain are not shown for the ease of visualization. (b) Another view of the same figure.	270
8.8	Distribution of angle between (a) the vector connecting the nitrogen atoms of the imidazolium ring (NN vector) and the interface normal (z-axis), for the cations that are present in the interfacial region. (b) the butyl chain of cations present at the interface and the interface normal.	271
8.9	Distribution of angle between (a) the butyl chains in the interfacial region and in the bulk that are within 8 Å of each other. (b) carbon-sulfur bond vector and the interface normal, for the anions that are present in the interfacial region.	272
8.10	Snapshot of the interfacial region in the ternary system with $CF_3SO_3^-$ anion. Only the atoms that are present in the interfacial region are shown. Carbon atoms of nonane are shown in pink color and oxygen atoms of water are shown in red color. Fluorine, sulfur and oxygen atoms of anions are shown in magenta, orange and cyan, respectively.	273
G.1	Number density profiles of different moieties along interface normal (z-axis) in nonane- $[C_4C_1Im][BF_4]$ -water system. Water and nonane densities have been scaled according to their ratio with respect to the cation numbers for ease of comparison.	277
G.2	Number density profiles of different moieties along interface normal (z-axis) in nonane- $[C_4C_1Im][CF_3SO_3]$ -water system. Water and nonane densities have been scaled according to their ratio with respect to the cation numbers for ease of comparison.	278

G.3	Radial distribution functions of (a) hydrogen bond acceptor on anions around the ring hydrogen atoms (b) hydrogen bond acceptor on water (oxygen atom) around the ring hydrogen atoms.	278
G.4	Water number density profiles along interface normal (z-axis) in different ternary systems.	279
9.1	Schematic representation of the hexadecane, alkanols and water molecule showing the atom types used in the discussion.	288
9.2	Radial number density profiles of (a) different chemical species in binary hexadecane–water and ternary hexadecane–dodecanol–water systems and (b) terminal carbon atoms (CT) of different alkanols in their respective ternary systems with hexadecane and water.	289
9.3	Bivariate distribution of the probability $P_1(\cos \theta)$ and the distance from the center of mass of the oil droplet in ternary systems containing (a) pentanol (b) heptanol (c) decanol (d) dodecanol and in (e) binary hexadecane–water system. θ is the angle between the radial vector and the principal axis of the hexadecane chain.	291
9.4	Hexadecane molecules in oil droplets of ternary systems containing (a) pentanol (b) heptanol (c) decanol and (d) dodecanol and in (e) binary hexadecane–water system. The hexadecane molecules near the water rich side and oil rich core are shown in magenta and yellow respectively. Hydrogen atoms are not shown for clarity.	292
9.5	Bivariate distribution of the probability $P_1(\cos \theta)$ and the distance from the center of mass of the oil droplet in ternary systems containing (a) pentanol (b) heptanol (c) decanol (d) dodecanol. θ is the angle between the radial vector and the principal axis of the alkoxy chain.	293

9.6	Alcohol molecules present near water rich region (magenta) and near oil rich region (yellow) of the ternary systems containing (a) pentanol (b) heptanol (c) decanol and (d) dodecanol. The oil and water phases are not shown for the ease of visualization	294
9.7	Bivariate distribution of the probability $P_1(\cos \theta)$ and the distance from the center of mass of the oil droplet in ternary systems containing (a) pentanol (b) heptanol (c) decanol (d) dodecanol and in (e) binary hexadecane–water system. θ is the angle between the radial vector and the dipole moment vector of the water molecule	295
9.8	Water molecules near the droplet surface in ternary systems containing (a) pentanol (b) heptanol (c) decanol and (d) dodecanol and in (e) binary hexadecane–water system. The hexadecane molecules are shown in blue, the alcohol molecules are shown in green, the oxygen and hydrogen atoms of the water molecules are shown in red and white respectively.	296
9.9	(a) Gauche population of C-C-C-C dihedrals of the hexadecane molecules (averaged over both termini (C_{AT})) present in the interfacial layer. Dihedral around the bond connecting 2nd and 3rd carbon atoms of the hexadecane chain from the terminal are plotted between 2 and 3 in the graph. (b) the average end to end distance of the hexadecane molecules present at a given distance from the center of mass of the oil droplet in binary hexadecane–water and ternary hexadecane–alkanol–water systems.	297
9.10	Survival probability of water molecules in the oil–water interfacial layer of binary hexadecane–water and different ternary hexadecane–water–alkanol systems. . . .	299
9.11	Survival autocorrelation function, $C_{HB}(t)$ for H-bonds between alcohol and water molecules in different ternary hexadecane–water–alkanol systems.	300
H.1	Radial number density profiles of terminal carbon atoms of the hexadecane molecules (C_{AT}) and the oxygen atoms of the water molecules (OW) in the ternary systems containing different alkanols.	303

H.2	Distribution of $\langle P_2(\cos \theta) \rangle$ with distance from the center of the mass of the oil droplet in binary and ternary systems studied. θ is the angle between the radial vector and the principal axis of the hexadecane molecule.	303
H.3	Distribution of $\langle P_2(\cos \theta) \rangle$ with distance from the center of the mass of the oil droplet in binary and ternary systems studied. θ is the angle between the radial vector and the principal axis of the alkoxy chain.	304
H.4	Distribution of $\langle P_2(\cos \theta) \rangle$ with distance from the center of the mass of the oil droplet in binary and ternary systems studied. θ is the angle between the radial vector and the dipole moment vector of the water molecule.	304
H.5	Percentage of gauche population of each C-C-C-C dihedral along the alkoxy chain from the terminal (CT) of various alkanol molecules present in the interfacial layer for the ternary hexadecane–water–alkanol systems.	305
H.6	Probability distribution of the length of the alkoxy chains as a function of distance from the center of mass of the oil droplet in ternary hexadecane–alkanol–water systems containing pentanol, heptanol, decanol and dodecanol molecules.	305

List of Tables

2.1	Details of simulations of ILs mixtures, where the systems are represented by differing anions or cations.	71
2.2	Average number of H-bonds formed per head group in IL mixtures at 500 K. . . .	78
2.3	Surface fractions of ions in the interfacial region in IL mixtures at 500 K.	80
3.1	Details of simulations of systems studied (the IL mixtures are presented by the ratio of mole numbers of[omim][TfO] and [emim][TfO]).	102
3.2	Surface fractions of ions in the interfacial region of IL mixtures of varying composition.	108
3.3	Amplitude of the surface roughness, a and frequency-like parameters of the surface roughness, ξ and b of the $\langle d \rangle$ versus l curve of the liquid – vapor interface for binary IL mixtures.	111
3.4	Parameters of the stretched exponential fit to the average survival time correlation function.	114
3.5	Average reorientation time $\langle \tau_r \rangle$ for the ions obtained from the reorientational TCFs.	116
4.1	Details of simulations of aqueous $[C_nC_{10}Im][Br]$ solutions, where n is the length of alkyl chain substituent.	136
4.2	Details of the properties of aggregates in $[C_nC_{10}Im][Br]$ solution	148
5.1	Details of the simulated systems; n represents the number of carbon atoms in the hydroxyl functionalized hydrocarbon chain.	162

5.2	Average number of H-bonds formed per cations	168
6.1	Details of the simulated bulk systems; n represents the number of carbon atoms in the spacer chain.	194
6.2	Average number of H-bonds formed per head group	199
7.1	Details of the simulated systems.	231
7.2	Mean lifetimes (τ_{HB}) for H-bonds between species of the same kinds in different systems studied.	241
7.3	Parameters of the stretched exponential fit to the reorientation time correlation function.	246
7.4	Parameters of the stretched exponential fit to the reorientation time correlation function.	247
8.1	Details of the Simulated Systems	260
8.2	Average number of H-bonds formed per cation	266
9.1	Details of the simulated systems.	287

Acronyms

AIMD *ab initio* molecular dynamics.

AIQC *ab initio* Quantum Chemical.

CMC Critical Micelle Concentration.

DIL Dicationic Ionic Liquid.

DLS Dynamic Light Scattering.

EAN Ethyl ammonium nitrate.

EOR Enhanced Oil Recovery.

HFIL Hydroxyl Functionalized Ionic Liquid.

IL Ionic Liquids.

ILBS Ionic Liquid Based Surfactant.

LAMMPS Large-scale Atomic/Molecular Massively Paralle Simulator.

MBEC Minimum Biofilm Eradication Concentration.

MC Monte Carlo.

MD Molecular Dynamics.

NATO North Atlantic Treaty Organization.

NMR Nuclear Magnetic Resonance.

OPLS Optimized Potential for Liquid Simulation.

PPPM Particle particle particle-mesh solver.

SANS Small Angle Neutron Scattering.

SFS Sum Frequency Scattering.

SHG Second Harmonic Generation.

TEM Transmission Electron Microscopy.

TOF-SIMS Time of Flight–Secondary Ionization Mass Spectrometry.

VMD Visual Molecular Dynamics.

XPS Xray Phototoelectron Spectroscopy.

Chapter 1

Introduction

1.1. Ionic Liquids *“Considered from the standpoint of chemistry, living bodies appear to us as laboratories of chemical processes, for they undergo perpetual changes in their material substrate. They draw materials from the outside world and combine them with the mass of their liquid and solid parts”.*

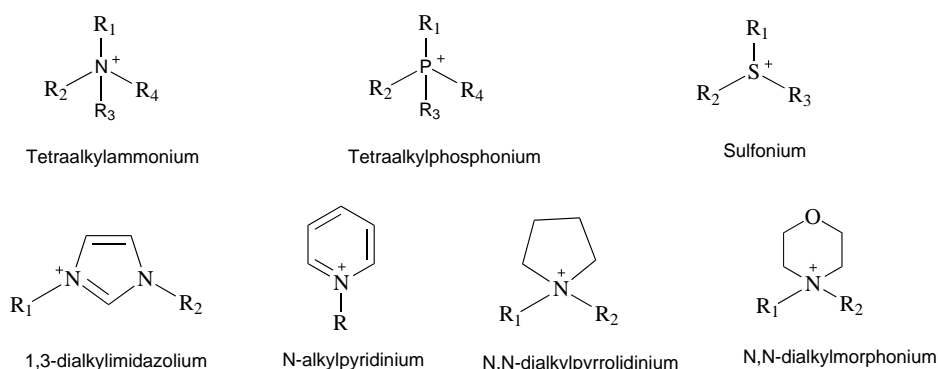
Friedrich Tiedemann

Life probably evolved in the liquid phase, and our bodies are kept alive by chemical reactions occurring in liquids. Molecular liquids are most ubiquitous in nature. Water, benzene, ethanol etc. are some very common examples of molecular liquids. Now, what is an ionic liquid (IL)? Ionic liquids are liquid salts composed of ions with melting point (T_m) $< 100^\circ\text{C}$. This definition was reaffirmed and codified in a NATO workshop in Crete in 2000 [1]. A hundred years back startling discovery by the German chemist Walden of a pure liquid salt (ethylammonium nitrate, EAN) at ambient temperatures gave birth the saga of ionic liquids [2]. In his original paper on EAN, Walden described a class of materials as “water-free salts...which melt at relatively low temperatures, about upto 100°C ”. Since the days of Walden, a drastic progress has been observed in the science of liquid salts or “ionic liquids”. In particular, there has been an exponential growth in number of publications and patents in the field of ionic liquids in the last three decades [3, 4, 5].

Ionic liquids consist of bulky organic cations and usually inorganic anions. Asymmetry in the molecular structures of constituent cations and anions destabilizes the solid-phase crystals of ILs and hence, they exist as liquids in a large window of temperature. Although the first IL,

ethyl ammonium nitrate, was identified in 1914, the invention did not receive great attention at that time. Significant attentions towards these systems were imposed in early 1980s after the development of chloroaluminate anions (AlCl_4^- or Al_2Cl_7^-) based ionic liquids [6, 7]. Now a days, a number of well known cations such as ammonium, pyridinium, imidazolium, pyrrolidinium, phosphonium, pipyridinium, morpholium, etc. are combined with anions such as halides (F^- , Cl^- , Br^- , I^-), tetrafluoroborate (BF_4^-), hexafluorophosphate (PF_6^-), nitrate (NO_3^-), triflate (CF_3SO_3^-), bis(trifluoromethanesulfonyl)imide ($[\text{NTf}_2]^-$) etc. to design ionic liquids having desired properties. Because of this, they are also known as “designer solvents” [3]. Also, at least a million binary ionic liquids, and 10^8 ternary ionic liquids are potentially possible [8]. Figure 1.1 represents structures of some common constituent cations and anions of ILs.

Cations:



Anions:

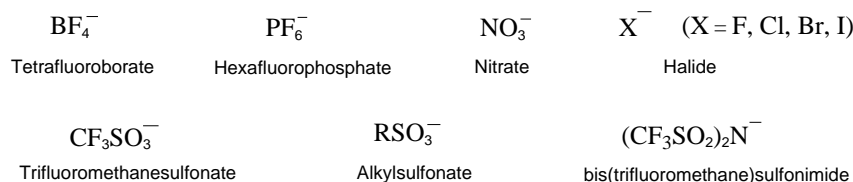


Figure 1.1: Schematic representation of structures of some common constituent cations and anions.

1.1.1 Properties of Ionic Liquids

Several inherent and unique physicochemical properties of ILs make them attractive for being used in different areas of research and industry. Figure 1.2 represents some of the most important characteristics of ILs.

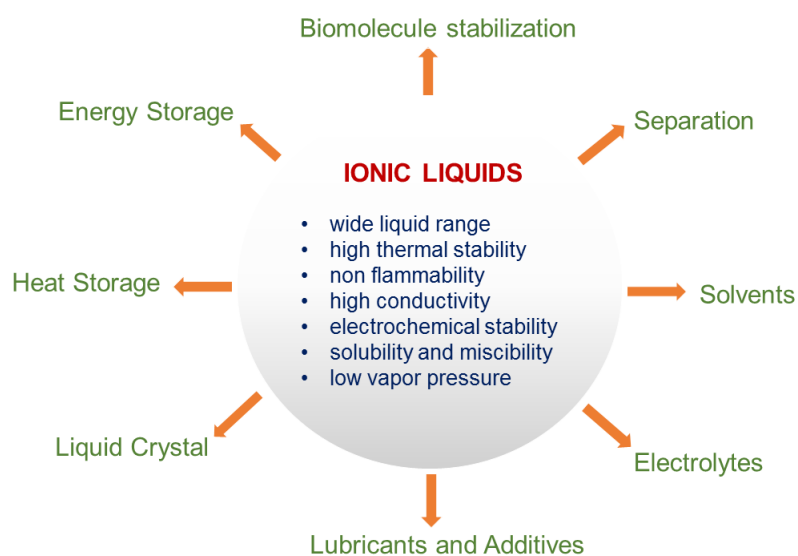


Figure 1.2: Properties and applications of ionic liquids.

- **Melting points:** Melting point plays a crucial role in determining the liquidous range and solubility of ILs in water or organic solvents. Correlating the melting points of ILs to the nature of the constituent cations and anions [9], it has been found that symmetric cations impose high melting point to ILs [10] and it decreases gradually with increase in radius of anions [11].
- **Density:** ILs are denser than water. The density of ILs depends on the efficiency of packing among the constituent ions and hence, on the size and shape of the ions and inter-ion interaction. Alkylammonium and alkylimidazolium based ILs show gradual decrease in their density values with the increase in alkyl chain length. For ammonium cation based ILs, it is expected that number of alkyl/aryl substituents around the nitrogen atom will lead to decrease in density and indeed, tributylammonium nitrate is known to have lowest density

because of its bulky size [12, 13]. The density of heterocyclic amine cations based ILs are generally more than alkylammonium based ILs.

- **Low vapor pressure:** Due to the presence of strong Coulombic interactions between ions within an IL, they have very low vapor pressure at temperatures upto their decomposition temperatures. Therefore, they contribute negligible amount of volatile organic compounds (VOCs) unlike traditional industrial solvents to the atmosphere. This also leads to ease of distillation and recyclability of ionic liquids [14, 15].
- **Viscosity:** ILs are highly viscous (ranging between 10 and 1000 cP) than conventional molecular solvents (e. g., 0.890 cP for water, at NTP). Strong electrostatic interaction among the constituent ions, van der Waals interaction and hydrogen bonding interaction within the ionic species lead to high viscous nature of ionic liquids. It has been revealed that viscosity of ILs increases with increase in the alkyl chain length of the cationic moiety [16] and decreases with charge delocalization in anionic species. The temperature dependence of viscosities of ILs is governed by Vogel-Tammann-Fulcher (VFT) equation [17]

$$\ln(\eta) = \ln(\eta_0) + \frac{DT_C}{T - T_C}$$

where, η_0 , D and T_C are constants.

- **Wide liquid range and thermal stability:** ILs remain in liquid state in a wider range of temperatures than conventional molecular solvents. The thermal decomposition temperature (T_d) can reach the value up to 250°C for many of the ILs [18]. Although cations have no significant contribution in the thermal stability of ILs, decomposition temperature decreases with increase in hydrophilicity of anions employed in the order $[\text{PF}_6] > [\text{NTf}_2] > [\text{CF}_3\text{SO}_3] > [\text{BF}_4]$ [19]. In addition, the typical glass transition temperatures (T_g) of ILs are close to -80°C. As a result, they can be used in many high-temperature and low-temperature applications without significant solvent degradation.
- **High ionic conductivity and high electrochemical stability:** Ionic liquids, being solely composed of ions, show intrinsic ionic conductivity. The ionic conductivity of ILs is gov-

erned by the number of mobile charge carriers and viscosity of the medium. Although the number of charge carriers found in ILs is greater than conventional electrolyte solutions and other ionic fluids, the usual higher viscosity of the medium hinders the mobility of ions leading to lower conductivity (of the order of 10^{-1} S/m) than that of conventional electrolytes [20, 21]. The ionic conductivity of ILs containing alkylammonium and alkyimidazolium cations decreases as the alkyl chain length of cations increases. However, the ILs are redox stable across a wide electrochemical window of voltages between 2.0 to 6.0 V [22, 23, 24].

- **Solubility and miscibility:** Since 1950s, ILs are known to dissolve both polar and apolar compounds. This is incompatible to the dictum “like dissolves like”. The ability of a solvent to dissolve a solute is governed by its polarity. Although the static dielectric constant (ϵ) which dictates the bulk polarity of ILs, falls in a narrow range between 9.0 to 13.0 (25°C), the high microscopic polarity parameter such as E_T and E_T^N justifies their ability to dissolve polar compounds. On the otherhand, being an amphiphile, ILs can dissolve apolar substances also.

1.2. Motivation and Purpose *“If you want to understand function, study structure!”*

Francis H. Crick

The main purpose of this thesis is to analyze the structure and dynamics in the bulk and at the interface of molecular and ionic liquids in multicomponent aqueous and non-aqueous systems by using computer simulation techniques. Binary mixtures of ionic liquids (ILs) are used as solvents in the field of catalysis [25, 26, 27, 28, 29], extraction layers [30], dispersive liquid – liquid micro-extraction [31], supercapacitor electrolytes in lithium batteries [32] and dye-sensitized solar cells[33]. So a detailed understanding of the bulk and liquid – vapor interface structure of binary mixtures of ILs is necessary to elucidate their role as reaction and extraction media as well as electrolytes. With this aim, the Chapter 2 of my thesis deals with all-atom classical MD simulations on a series of equimolar binary mixtures of ILs with common anion, $[\text{C}_2\text{C}_1\text{Im}][\text{C}_8\text{C}_1\text{Im}][\text{CF}_3\text{SO}_3]$, and common cation, $[\text{C}_4\text{C}_1\text{Im}][\text{Cl}][\text{PF}_6]$ and $[\text{C}_4\text{C}_1\text{Im}][\text{Cl}][\text{CF}_3\text{SO}_3]$, to get insights into the sur-

face structure of the liquid – vapor interface as well as the bulk phase organization. On the otherhand, the Chapter 3 discusses the computational studies on a series of binary IL mixtures $[\text{C}_2\text{C}_1\text{Im}][\text{C}_8\text{C}_1\text{Im}][\text{CF}_3\text{SO}_3]$ to get insights into the effect of composition on the surface structure and dynamics of ions in the liquid–vapor interfacial layer.

Understanding the aggregation behavior of ILs in solution is very important from the perspective of academic and applied aspects. Knowledge of the antibacterial properties of ionic liquid based surfactants (ILBSs) is essential to demonstrate their effects on aquatic organisms and environments [40, 41, 42]. It has been reported that there is a linear correlation between the critical micelle concentration (CMC) and minimum biofilm eradication concentration (MBEC) of ILBSs, i.e., CMC appears to be an appropriate index to estimate the efficiency of ILBSs as antimicrobial agents. Also, the transport and distribution of ILs through soil is mainly dependent on the size and structure of the aggregates formed [43]. Studies have been reported to show that MBEC of ILBSs showed an inverse dependence on the length of hydrocarbon chain which makes them potentially effective to be used for improved infection control within the hospital environment. So, investigation of structure/activity relationships (SAR), in particular to the length of the alkyl group, the heterocycle employed, and the counterion governing the properties of micellar solutions of ILBSs emerges to be essential for the better use of ILs as surfactants. The aqueous solution of ILs with single alkyl chain is well studied using experimental and theoretical methods. The presence of second alkyl chain on the imidazolium ring may alter the structure of the aggregates and aggregation numbers. Recently, double tailed imidazolium based ionic liquids have been reported to show interesting aggregation properties in their aqueous solution [44]. Based on experimental data, it is predicted that the cations in aqueous solution of dioctylimidazolium bromide form aggregates with hydrophobic core and hydrophilic surface consisting of cation rings in a staggered parallel orientation. In the present thesis, Chapter 4 is investigating atomic level details of the bulk and vapor–liquid interface of aqueous solutions of dialkylimidazolium bromide. We have carried out atomistic molecular dynamics (MD) simulations on 1-alkyl-3-decylimidazolium bromide solutions with the alkyl chain ranging from methyl to decyl. The antibacterial and antifungal active

properties of these ILs depend upon the structure of the functional group and the alkyl chain length. ILs with a hydroxyethyl group showed broad spectrum of antimicrobial activity [45]. Chapter 5 discusses the atomic-level details of the effect of the presence of a hydroxyl group attached to one of the two alkyl chains in dialkylimidazolium based ILs, on the bulk solution structure. The solution structure has been studied using atomistic molecular dynamics (MD) simulations performed on a series of 1-(*n*-hydroxyalkyl)-3-decylimidazolium bromide ILs (where the alkyl chain is ranging from ethyl to decyl) in their aqueous solutions. Compared to conventional monochain surfactants, gemini surfactants show lower CMC, higher adsorption efficiency, better foaming and limber-soap dispersing properties. The length and polarity of the spacer length plays an important role in determining the liquid structure of imidazolium based DILs in aqueous solution. Chapter 6 presents atomistic MD simulations on aqueous $[C_n(\text{MIm})_2][2\text{Br}]$ solutions to gain insights into the structure of the solution at atomic level.

Dispersions made of water, oil, and amphiphiles that are thermodynamically stable are often coined as microemulsions. The domains of the dispersed phase are either globular or bicontinuous in a microemulsion. Reverse micelles are nanometer-sized (1-10 nm) water droplets dispersed in organic media obtained by the action of surfactants. Reverse micelles have potential applications in the field of downstream processes and enzyme recovery due to their ability to encapsulate and probe biological molecules [46, 47, 48]. In Chapter 7, we have discussed the atomistic molecular dynamics simulations of reverse micelles consist of imidazolium based ionic liquids and encapsulating variable number of glycine molecules in zwitterionic forms with the aim of exploring the effect of increase in the number of amino acids on the structure of the aqueous core of the reverse micelles as well as dynamics of species confined in the aqueous core. Microemulsions are also widely used to mobilize petroleum trapped in porous sandstone for enhanced oil recovery (EOR) [58, 59, 60] and solubilization of sparingly soluble drugs [61]. In an attempt to gain insights about the adsorption and orientation of amphiphilic ILs at the planar interface of a ternary system composed of water, 1-*n*-butyl-3-methylimidazolium ($[C_4C_1\text{Im}]$) cation based IL and nonane, Chapter 8 discusses the effect of anions using MD simulations on three different

systems by varying the counter anion (Br^- , BF_4^- and CF_3SO_3^-) associated with the cation.

Oil-in-water droplet systems or emulsions are supramolecular assemblies which act as artificial life models representing the hydrophobic domains in contact with aqueous regions (with oil corresponding to the lipid membranes of the cell) [62]. SFS and SHG studies have been performed to gain molecular level insights into the structural aspects of the transition from a hydrophobic to an aqueous phase on hexadecane droplet by employing different chain length alkanols as emulsifiers [77]. The aforementioned study primarily focuses on interfacial alkyl chain conformation of the oil and various alcohol molecules and the orientational alignment of water molecules in a qualitative manner. Chapter 9 deals with the atomistic molecular dynamics simulation studies to get insights into structural transition from hydrophobic to aqueous region around the hexadecane droplet and the organization of the hexadecane, water and alkanols near the oil-water spherical interface in presence of 1-alkanols of varying chain length as emulsifiers.

1.3. Literature Review. Surface composition of binary mixtures of ionic liquids has been studied using various experimental methods [18, 19, 20, 21]. Classical molecular dynamics (MD) simulations on an equimolar mixture of $[\text{C}_2\text{C}_1\text{Im}][\text{C}_6\text{C}_1\text{Im}][\text{NTf}_2]$ have shown the microscopic phase segregation of polar and non-polar domains, which is not observed in pure components [34]. The mixture shows very small positive excess of molar volume and thus ensures ideal behavior of mixing. *Ab initio* MD simulations [35, 37] of $[\text{C}_2\text{C}_1\text{Im}][\text{SCN}][\text{Cl}]$ correlates the tendency of the anion to coordinate with the most acidic hydrogen of the cation to its basicity. The $[\text{C}_2\text{C}_1\text{Im}]$ cations show weaker ordering in their spatial arrangements due to $\pi - \pi$ stacking of the imidazolium rings. The self-diffusion coefficients of various moieties of the IL mixtures were found to depend on the compositions of the mixtures studied. It has also been found that the binary mixtures are well mixed at the molecular level [38]. Classical MD studies on the IL mixture $[\text{b}_3\text{mpy}][\text{BF}_4][\text{N}(\text{CN})_2]$ over a range of composition conclude that the diffusion coefficients of cations and anions in the mixture depend upon the interaction between them [39].

Small angle neutron scattering (SANS), transmission electron microscopy (TEM), nuclear

magnetic resonance (NMR), and molecular dynamics (MD) simulation techniques are extensively used to study the microstructure of IL aggregates in solutions. SANS investigation [91] of microstructure of the aggregates of $[\text{C}_8\text{C}_1\text{Im}][\text{Cl}]$, $[\text{C}_8\text{C}_1\text{Im}][\text{I}]$ and $[\text{C}_4\text{C}_1\text{Im}][\text{BF}_4]$ in aqueous solutions revealed that above CMC, $[\text{C}_4\text{C}_1\text{Im}][\text{BF}_4]$ formed polydisperse spherical aggregates, $[\text{C}_8\text{C}_1\text{Im}][\text{I}]$ behaved as regularly sized near-spherical charged micelles whereas $[\text{C}_8\text{C}_1\text{Im}][\text{Cl}]$ formed disklike particles showing weak long-range ordering. Goodchild et al. [92] had carried out SANS experiment to study the solution structure of $[\text{C}_n\text{C}_1\text{Im}][\text{X}]$ ($n=2, 4, 6, 8, 10$; $\text{X} = \text{Cl}, \text{Br}$) in water and reported that $[\text{C}_2\text{C}_1\text{Im}]$ and $[\text{C}_4\text{C}_1\text{Im}]$ cations did not show any sign of aggregate formation whereas $[\text{C}_6\text{C}_1\text{Im}]$ cation, above its CMC, formed oblate aggregates with radius $\sim 9 \text{ \AA}$ and the radius increases with increase in concentration of the ionic liquid. $[\text{C}_8\text{C}_1\text{Im}]$ and $[\text{C}_{10}\text{C}_1\text{Im}]$ based ILs formed near-spherical aggregates with core radii of $10.5 \pm 0.5 \text{ \AA}$ and $13.2 \pm 0.5 \text{ \AA}$ respectively just above the CMC. With increase in concentration, $[\text{C}_{10}\text{C}_1][\text{Br}]$ system formed elongated (prolate) micelles. TEM and DLS (dynamic light scattering) experiments [93] on $[\text{C}_8\text{C}_1\text{Im}][\text{X}]$ ($\text{X} = \text{Cl}, \text{Br}, \text{NO}_3, \text{CH}_3\text{COO}$ and CF_3COO), $[\text{C}_8\text{mpyr}][\text{Br}]$ and 4 m- $[\text{C}_8\text{pyr}][\text{Br}]$ aggregates in water concluded that the types of anions and cations have a very weak effect on the morphology but the size of the spherical aggregates increases with increase in hydrophobicity of the anions. NMR study based on the chemical shift of various protons of $[\text{C}_4\text{C}_1\text{Im}][\text{Cl}]$, $[\text{C}_4\text{C}_1\text{Im}][\text{BF}_4]$, $[\text{C}_8\text{C}_1\text{Im}][\text{Cl}]$ and $[\text{C}_4\text{mpy}][\text{Cl}]$ in water as a function of IL concentrations proposed that the imidazolium and pyridinium rings of $[\text{C}_4\text{C}_1\text{Im}][\text{BF}_4]$ $[\text{C}_4\text{mpy}][\text{Cl}]$ are oriented at the surface in a configuration which favors the π - π ring stacking interaction, whereas the imidazolium rings of $[\text{C}_4\text{C}_1\text{Im}][\text{BF}_4]$ and $[\text{C}_8\text{C}_1\text{Im}][\text{Cl}]$ ILs do not show such conformation [94]. Experimental studies on the aggregation behavior of HFILs in aqueous solutions indicate the formation of loosely bound aggregates with lower aggregation number [95, 96]. The first atomistic MD simulation on IL–water mixture was carried out by Hanke and Lynden-Bell in 2003 [97], where they observed differences in the signs of both excess volumes and the enthalpies of mixing for $[\text{C}_1\text{C}_1\text{Im}][\text{Cl}]$ and hydrophobic $[\text{C}_1\text{C}_1\text{Im}][\text{PF}_6]$ with water. A percolating network of water molecules was found as well as some isolated molecules and small clusters. The ionic mobility

was found to increase linearly with the mole fraction of water in the mixtures. MD simulations of [C₆C₁Im][PF₆]-water binary mixture [98] showed close association between water and anions and the authors deduced that the experimentally observed decrease in viscosity is a consequence of the faster and rotational dynamics of ions in the presence of water. Computer simulation study in mixture of [C₈C₁Im][NO₃] and water revealed nanostructural organization in the solution [99]. The calculated static structure factors with different water contents indicated the disruption of the polar network as the amount of water increased by intruding water, while the structural organization of the water network and the micelle exhibited a turnover. MD studies of [C_nC₁Im][Br] (n = 10, 12, 14, 16) in water [100, 101] found that in all the systems, quasi-spherical polydisperse aggregates were formed with the alkyl tails buried deep inside the aggregates and the polar imidazolium group exposed to water. The aggregation numbers steadily increase with increase in the hydrocarbon chain length. Molecular dynamics (MD) studies have probed the effects of spacer length and anions on the liquid structure and dynamical properties of imidazolium based DILs [102, 103]. The length and polarity of the spacer length plays an important role in determining the liquid structure of imidazolium based DILs in aqueous solution [104, 105, 106]. Only few computational studies are available on the aggregation properties of imidazolium based DILs in aqueous solutions [107, 108]. The dicationic IL 1,3-bis(3-decylimidazolium-1-yl)propane bromide in its aqueous solution formed interconnected cationic micellar aggregates mediated by head groups, a phenomenon which is not observed in monocationic ionic liquids.

Molecular dynamics simulations on model α -helical peptide encapsulated in a reverse micelle has shown the preferential residence of the peptide at the interface of the reverse micelle [109]. Computer simulation studies on ubiquitin encapsulated in a reverse micelle concluded that the backbone dynamics of the protein in reverse micelle is similar to that in bulk [110]. Computer simulation studies have also shown that the octalanine is stable in small size reverse micelle [46]. The peptide's partial helical structure has been found to be stable in reverse micellar confinement [111]. Recent computational studies have explored the role of charge and solvation in the structure of alanine-rich AKA₂ in AOT reverse micelles [112]. There are numerous experimen-

tal [49, 50, 51, 52] and computational studies [53, 54, 55, 56, 57] reported on the structure and water dynamics in reverse micellar confinement.

The first study of the phase behavior of ternary systems composed of water, surfactant and oil was reported in 1948 by Winsor [113]. Experiments [114, 115, 116] have been carried out to determine the optimum formulation of ternary systems that leads to minimum interfacial tension. Spectroscopic studies [117] of such ternary systems with anionic and cationic amphiphiles have provided insights into the ion effect on the interface structure of the system. The phase equilibria of a water – ionic liquid – oil ternary system have been investigated [118, 119, 120]. Comparative studies of thermodynamic properties between ionic liquid (IL) – oil and water – oil systems have been reported [121]. Effect of ILs on interfacial tension between heavy crude oil and water [122, 123] has been investigated. Molecular dynamics (MD) studies of adsorption and orientation of ionic surfactants at heptane – water interface have also been reported [124].

Vibrational sum frequency scattering (SFS) study on sodium dodecyl sulfate (SDS)-stabilized nanoscopic *n*-hexadecane droplets dispersed in D₂O has shown that the effect on interfacial tension due to SDS surfactant is negligible compared to a planar interface [73]. SFS and molecular dynamics studies on oil emulsions have shown that water orientation on a neat oil droplet/water interface resembles the water orientation on a negatively charged interface [74]. SFS spectra on a kinetically stabilized emulsion with SDS, consisting of nanoscopic oil droplets in water shows that the oil molecules are preferentially orienting parallel to the plane of the droplet–water interface with less number of chain defects than that in SDS molecules [75]. Second harmonic generation (SHG) study has proved that the adsorption free energy of malachite green on the surface of oil droplet in surfactant stabilized hexadecane–water emulsion is mediated by competition between the adsorption and charge–charge interaction [76]. SFS and SHG studies have been performed to gain molecular level insights into the structural aspects of the transition from a hydrophobic to an aqueous phase on hexadecane droplet by employing different chain length alkanols as emulsifiers [77]. The aforementioned study primarily focuses on interfacial alkyl chain conformation of the oil and various alcohol molecules and the orientational alignment of water molecules in a

qualitative manner.

1.4. Methods and Models Determination of properties of liquids at a microscopic level by experimental methods comes out to be inadequate both from resolution of length scale and time scale. Computer simulation techniques are considered as a fundamental tool for understanding the properties and behavior of liquids at this level. The physical characterization of molecular and ionic liquids by means of simulations has been significantly developed over the last decades and enormous progress has been achieved in the design of new potentials and more powerful computational tools. There are several computational techniques employed for studying the characteristics of materials, such as *ab initio* quantum chemical (AIQC), *ab initio* molecular dynamics (AIMD), Monte Carlo (MC) and molecular dynamics (MD). Each of them handles specific problems when dealing with molecules. For example, whereas AIQC methods include polarization and charge transfer and are very suitable to accurately describe the electronic structure, they are computationally expensive and therefore not useful when it comes to analyze a great number of molecules. On the other hand, MC and MD methods are appropriate for describing the liquid state, since they are capable of simulating a great number of ions interacting with each other. However, they can not be expected to adequately model the motion of the electrons within this kind of systems. AIMD methods fall somewhere in between, since they provide information about the electronic structure but can not be used to investigate a large number of molecules. Thus, in order to obtain a reasonably good analysis of liquids, it is of fundamental importance to deeply understand both the advantages and disadvantages of each and every technique and choose the most appropriate one depending on the size and time scales of the problem.

All the studies concerning in this thesis were performed using classical MD simulations. So, a deeper discussion of the theory behind MD is essential. The microscopic state of a system is specified in terms of the positions and momenta of a constituent set of particles. Classically, the Hamiltonian H of a system of N particles can be written as a sum of kinetic and potential energy functions of the set of coordinates \vec{r}_i and momenta \vec{p}_i of each particle i . Using a condensed

notation,

$$\vec{r} = (\vec{r}_1, \vec{r}_2, \dots, \vec{r}_N)$$

$$\vec{p} = (\vec{p}_1, \vec{p}_2, \dots, \vec{p}_N)$$

$$H(\vec{r}, \vec{p}) = K(\vec{p}) + V(\vec{r})$$

The kinetic energy K takes the form

$$K = \sum_{i=1}^N \sum_{\alpha} \frac{p_{i\alpha}^2}{2m_i}$$

where m_i is the mass of the particle and the index α runs over the different (x, y, z) components of the momentum of particle i . The potential energy V can be splitted into terms which are functions of coordinates of individual atoms, pairs, triplets etc.:

$$V = \sum_i v_1(\vec{r}_i) + \sum_i \sum_{j>i} v_2(\vec{r}_i, \vec{r}_j) + \sum_i \sum_{j>i} \sum_{k>j} v_3(\vec{r}_i, \vec{r}_j, \vec{r}_k) + \dots$$

The first term in the above equation, $v_1(\vec{r}_i)$ stands for effect of an external field on the system and depends on the coordinates of the individual atoms. The second term, $v_2(r_{ij})$ represents the pair potential and depends on the inter-particle pair separation, $r_{ij} = |\vec{r}_i - \vec{r}_j|$. For liquid properties, the pairwise approximation works really well and the above equation is reduced to

$$V \approx \sum_i v_1(\vec{r}_i) + \sum_i \sum_{j>i} v_2(\vec{r}_i, \vec{r}_j)$$

Once the form of the potential energy function is known, the force \vec{f}_i acting on the i -th particle is calculated from the gradient of the potential energy as

$$\vec{f}_i = -\frac{\delta V}{\delta r_{i\alpha}}$$

The index α runs over the different (x, y, z) coordinates of particle i . Now, by solving the Newton's equation of motion for the system of N interacting particles from the equation

$$m_i \frac{\delta^2 \vec{r}_i}{\delta t^2} = \vec{f}_i, \quad i = 1, \dots, N.$$

we get the trajectory describing the positions, velocities and accelerations of the particles as a function of time. We have used the Verlet method to integrate the equations of motion. The position of a particle in the next step, $\vec{r}(t + \delta t)$ is calculated from its current position, $\vec{r}(t)$, acceleration, $\vec{a}(t)$ and the position from the previous step, $\vec{r}(t - \delta t)$ by using the following equation:

$$\vec{r}(t + \delta t) = 2\vec{r}(t) - \vec{r}(t - \delta t) + \delta t^2 \vec{a}(t)$$

The potential energy function is constructed under the framework of Optimized Potential for Liquid Simulation (OPLS) model defined by Jorgensen et. al [125]. Bonded and non-bonded interactions contributed to the total potential energy whose functional form is given by the equation,

$$U_{\text{Total}} = \sum_b \frac{K_{r,b}}{2} (r_b - r_{0,b})^2 + \sum_a \frac{K_{\theta,a}}{2} (\theta_a - \theta_{0,a})^2 + \sum_d \sum_{m=1}^n \frac{V_{m,d}}{2} [1 + (-1)^{m+1} \cos(m\phi_d)] \\ + \sum_i \sum_j \left\{ 4\epsilon_{ij} \left[\left(\frac{\sigma_{ij}}{r_{ij}} \right)^{12} - \left(\frac{\sigma_{ij}}{r_{ij}} \right)^6 \right] - \frac{1}{4\pi\epsilon_0} \frac{q_i q_j}{r_{ij}} \right\}$$

where the total potential energy U_{Total} consists of the sum over the energy terms involving all the bonds, angles, dihedrals and non-bonded interactions. The $r_{0,b}$ and $\theta_{0,a}$ represents the equilibrium bond length and bond angle respectively, whereas the $K_{r,b}$ and $K_{\theta,a}$ are the corresponding force constants. The $V_{m,d}$ terms are the fourier coefficients involved in the dihedral interactions. q_i is the partial charge on the i -th atom, σ and ϵ are the Lennard-Jones interaction parameters. All the simulations have been performed using the LAMMPS [126] and visualization software VMD [127] has been used to render the images. The problem arising due to edge effects caused by the finite size of the central simulation cell was solved by using the periodic boundary conditions (PBC), i.e. an infinite system can be mimicked by rolling the central simulation cell in three dimensional space, which means that if any atom leaves the box by the right-hand face, its periodic image enters the box by the left-hand face. This artifact was combined with the minimum image convention, with which short-range non-bonded interactions only takes into account the nearest image of each particle. Additionally, in order to get accurate long-range electrostatic interactions we employed lattice sum methods. 13\AA cutoff was used to calculate the non-bonded interactions. Long range electrostatic interactions [128] were handled using particle-particle particle-mesh solver (PPPM)

with an accuracy of 10^{-5} . The temperature and pressure were controlled using N ose-Hoover thermostat and barostat with time constants of 1000.0 and 500.0 fs respectively. The SHAKE [129] algorithm was used to constrain the stretching and bending interactions in water molecules.

Bibliography

- [1] Rogers, R. D.; Seddon, K. R.; Volkov, S. *Green Industrial Applications of Ionic Liquids*; Kluwer Academic: Dordrecht, Netherlands, 2002.
- [2] Walden, P. *Bull. Acad. Imp. Sci. St.-Petersbourg* **1914**,8, 405-422.
- [3] Rogers, R. D.; Seddon, K. R. *Science* **2003**, 302, 792-793.
- [4] Rogers, R. D. *Nature* **2007**, 447, 917-918.
- [5] Deetlefs, M.; Fanselow, M.; Seddon, K. R. *RSC Adv.* **2016**, 6, 4280-4289.
- [6] Wilks, J. S.; Levinsky, J. A.; Wilson, R. A.; Hussey, C. L. *Inorg. Chem.* **1982**, 21, 1263-1264.
- [7] Boon, J. A.; Levinsky, J. A.; Pflug, J. L.; Wilks, J. S. *J. Org. Chem.* **1986**, 51, 480-483.
- [8] Seddon, k. R. *The International George papatheodorou Symposium: Proceedings*, S. Boghosian et al. Eds.; Institute of Chemical Engineering and High Temperature Chemical Processes; Patras, Greece, 1999. pp. 131-135.
- [9] Dzyuba, S.; Bartsch, R. A. *Chem. Phys. Chem* **2002**, 3, 161-166.
- [10] Carda-Broch, S.; Berthold, A.; Armstrong, D. W. *Anal. Bioanal. Chem.* **2003**, 375, 191-199.
- [11] Zhang, s.; Sun, N.; He, X.; Lu, X.; Zhang, X. *J. Phys. Chem. Ref. Data.* **2006**, 35, 1475-1518.
- [12] Zhou, Z. B.; Matsumoto, H.; Tatsumi, K. *Chem. Eur. J.* **2005**, 11, 752-766.
- [13] Zhou, Z. B.; Matsumoto, H.; Tatsumi, K. *Chem. Lett.* **2004**, 33, 1636-1637.

- [14] Earle, M. J.; Esperanca, J. M. S. S.; Gilea, M. A.; Lopes, J. N. C.; Rebelo, L. P. N.; Magee, J. W.; Seddon, K. R.; Widegren, J. A. *Nature* **2006**, *439*, 831-834.
- [15] Taylor, A. W.; Lovelock, K. R. J.; Deyko, A.; Licence, P.; Jones, R. G. *Phys. Chem. Chem. Phys.* **2010**, *12*, 1772-1783.
- [16] Bonhote, P.; Dias, A.; Papageorgiou, N.; Kalyanasundaram, K.; Gratzel, M. *Inorg. Chem.* **1996**, *35*, 1168-1178.
- [17] Santosh, K.; Banerjee, S.; Rangaraj, N.; Samanta, A. *J. Phys. Chem. B* **2010**, *114*, 1967-1974.
- [18] Cao, Y.; Mu, T. *Ind. Eng. Chem. Res.* **2014**, *53*, 8651-8664.
- [19] Ngo, H. L.; LeCompte, K.; Hargens, L.; McEwen, A. *Thermochim. Acta* **2010**, *357*, 97-102.
- [20] Sato, T.; Maruo, T.; Marukane, S.; Takagi, K. *J. Power Sources* **2004**, *138*, 253-261.
- [21] Lee, J. S.; Bae, J. Y.; Lee, H.; Quan, N. D.; Kim, H. S. *J. Ind. Eng. Chem.* **2004**, *10*, 1086-1089.
- [22] Buzzeo, M. C.; Evans, R. G.; Compton, R. G. *Chem. Phys. Chem.* **2004**, 1106-1120.
- [23] Endres, F.; Abedin, S. Z. E. *Phys. Chem. Chem. Phys.* **2006**, *8*, 2101-2116.
- [24] Galinski, M.; Lewandowski, A.; Stepniak, I. *Electrochim. Acta* **2006**, *51*, 5567-5580.
- [25] Chauvin, Y.; Gilbert, B.; Guibard, I. *J. Chem. Soc., Chem. Commun.* **1990**, 1715-1716.
- [26] Chauvin, Y.; Einloft, S.; Olivier, H. *Ind. Eng. Chem. Res.* **1995**, *34*, 1149-1155.
- [27] L. C. Simon, J. Dupont and R. F. de Souza, *Appl. Catal., A*, 1998, **175**, 215-220.
- [28] Lee, S. H.; Ha, S. H.; Hiep, N. M.; Chang, W.; Koo, Y. *J. Biotechnol.* **2008** *133*, 486-489.
- [29] Ha, S. H.; Hiep, N. M.; Koo, Y. *Biotechnol. Bioprocess Eng.* **2010**, *15*, 126-130.
- [30] Katsuta, S.; Yoshimoto, Y.; Okai, M.; Takeda, Y.; Bessho, K. *Ind. Eng. Chem. Res.* **2011**, *50*, 12735-12740.

- [31] Zhao, R.; Wang, X.; Zhang, L.; Wang, S.; Yuan, J. *Anal. Methods* **2011**, *3*, 831-836.
- [32] Lin, R.; Taberna, P.; Fantini, S.; Presser, V.; Pérez, C. R.; Malbosc, F.; Rupesinghe, N. L.; Teo, K. B. K.; Gogotsi, Y.; Simon, P. *J. Phys. Chem. Lett.* **2011**, *2*, 2396-2401.
- [33] Armel, V.; Pringle, J. M.; Forsyth, M.; MacFarlane, D. R.; Officer, D. L.; Wagner, P. *Chem. Commun.* **2010**, *46*, 3146-3148.
- [34] Shimizu, K.; Tariq, M.; Rebelo, L. P. N.; Lopes, J. N. C. *J. Mol. Liq.* **2010**, *153*, 52-56.
- [35] Brüssel, M.; Brehm, M.; Voigt, T.; Kirchner, B. *Phys. Chem. Chem. Phys.* **2011**, *13*, 13617-13620.
- [36] Lui, M. Y.; Crowhurst, L.; Hallett, J. P.; Hunt, P. A.; Niedermeyer, H.; Welton, *Chem. Sci.* **2011**, *2*, 1491-1496.
- [37] Brüssel, M.; Brehm, M.; Pensado, S.; Malberg, F.; Stark, A.; Kirchner, B. *Phys. Chem. Chem. Phys.* **2012**, *14*, 13204-13215.
- [38] Payal, R. S.; Balasubramanian, S. *Phys. Chem. Chem. Phys.* **2013**, *15*, 21077-21083.
- [39] Aparicio, S.; Atilhan, M. *J. Phys. Chem. B* **2012**, *116*, 2526-2537.
- [40] Bernot, R. J.; Brueseke, M. A.; Evans-White, M. A.; Lamberti, G. A. *Environ. Toxicol. Chem.* **2005**, *24*, 87-92.
- [41] Bernot, R. J.; Kennedy, E. E.; Lamberti, G. A. *Environ. Toxicol. Chem.* **2005**, *24*, 87-92.
- [42] Docherty, K. M.; Charles, F.; Kulpa, J. *Green Chem.* **2005**, *7*, 185-189.
- [43] Stepnowski, P.; Mrozik, W.; Nichthauser, J. *Environ. Sci. Technol.* **2007**, *41*, 511-516.
- [44] Ge, L.; Wang, Q.; Wei, D.; Zhang, X.; Guo, R. *J. Phys. Chem. B* **2013**, *117*, 15014-15022.
- [45] DembereNyamba, D.; Kim, K. S.; Choi, S.; Park, S. Y.; Lee, H.; Kim, C. J. *Bioorg. Med. Chem.* **2004**, *12*, 853-857.

- [46] Abel, S.; Waks, M.; Urbach, W.; Marchi, M. *J. Am. Chem. Soc.* **2006**, *128*, 382-383.
- [47] Mukherjee, S.; Chowdhury, P.; Gai, F. *J. Phys. Chem. B* **2006**, *110*, 11615-11619.
- [48] Mukherjee, S.; Chowdhury, P.; Gai, F. *J. Phys. Chem. B* **2009**, *113*, 531-535.
- [49] Fayer, M. D.; Levinger, N. E. *Annu. Rev. Anal. Chem.* **2010**, *3*, 89-107.
- [50] Levinger, N. E. *Science* **2002**, *298*, 1722-1723.
- [51] Riter, R. E.; Undiks, E. P.; Levinger, N. E. *J. Am. Chem. Soc.* **1998**, *120*, 6062-6067.
- [52] Pieniazek, P. A.; Lin, Y.; Chowdhury, J.; Ladanyi, B.; Skinner, J. L. *J. Phys. Chem. B* **2009**, *113*, 15017-15028.
- [53] Faeder, J.; Ladanyi, B. M. *J. Phys. Chem. B* **2000**, *104*, 1033-1046.
- [54] Chowdhury, J.; Ladanyi, B. M. *J. Phys. Chem. A* **2009**, *115*, 6306-6316.
- [55] Biswas, R.; Chakraborti, T.; Bagchi, B.; Ayappa, K. G. *J. Chem. Phys.* **2012**, *137*, 14515-14524.
- [56] Chandran, A.; Prakash, K.; Senapati, S. *J. Am. Chem. Soc.* **2010**, *132*, 12511-12516.
- [57] Agazzi, F. M.; Correa, N. M.; Rodriguez, J. *Langmuir* **2014**, *30*, 9643-9653.
- [58] Rosen, M. J.; Wang, H.; Shen, P.; Zhu, Y. *Langmuir* **2005**, *21*, 3749-3756.
- [59] Prochaska, K.; Staszak, K. *J. Colloid Interface Sci.* **2005**, *285*, 1-8.
- [60] Sabhapondit, A.; Borthakur, A.; Haque, I. *Energy Fuels* **2003**, *17*, 683-688.
- [61] Dobler, D.; Schmidts, T.; Klingenhöfer, I.; Runkel, F. *Int. J. Pharma.* **2013**, *441*, 620-627.
- [62] Tu, Y.; Peng, F.; Adawy, A.; Men, Y.; Abdelmohsen, L. K. E. A.; Wilson, D. A. *Chem. Rev.* **2016**, *116*, 2023-2078.
- [63] Beaman, D. K.; Robertson, E. J.; Richmond, G. L. *J. Phys. Chem. C* **2011**, *115*, 12508-12516.

- [64] Wu, W.; Fang, H.; Yang, F.; Chen, S.; Zhu, X.; Yuan, Q.; Gan, W. *J. Phys. Chem. C* **2016**, *120*, 6515-6523.
- [65] Pradilla, D.; Simon, S.; Sjöblom, J.; Samaniuk, J.; Skrzypiec, M.; Vernant, J. *Langmuir* **2016**, *32*, 2900-2911.
- [66] Pichot, R.; Watson, R. L.; Norton, I. N. *Int. J. Mol. Sci.* **2013**, *14*, 11767-11794.
- [67] Levin, Y.; Santos, A. P. D. *J. Phys.: Condens. Matter* **2014**, *26*, 203101-203111.
- [68] Bresme, F.; Chacón, E.; Tarazona, P.; Tay, K. *Phys. Rev. Lett.* **2008**, *101*, 056102-1-4.
- [69] Vácha, R.; Roke, S. *J. Phys. Chem. B* **2012**, *116*, 11936-11942.
- [70] Palchowdhury, S.; Bhargava, B. L. *J. Phys. Chem. B* **2014**, *118*, 13930-13939.
- [71] Vazdar, M.; Pluhařová, E.; Mason, P. E.; Vácha, R.; Jungwirth, P. *J. Phys. Chem. Lett.* **2012**, *3*, 2087-2091.
- [72] Valley, N. A.; Robertson, E. J.; Richmond, G. L. *Langmuir* **2014**, *30*, 14226-14233.
- [73] Aguiar, H. B. D.; Beer, A. G. F. D.; Strader, M. L.; Roke, S. *J. Am. Chem. Soc.* **2010**, *132*, 2122-2123.
- [74] Vácha, R.; Rick, S. W.; Jungwirth, P.; Beer, A. G. F. D.; Aguiar, H. B.; Samson, J.; Roke, S. *J. Am. Chem. Soc.* **2011**, *133*, 10204-10210.
- [75] Aguiar, H. B. D.; Strader, M. L.; Beer, A. G. F. D.; Roke, S. *J. Phys. Chem. B* **2011**, *115*, 2970-2978.
- [76] Sang, Y.; Yang, F.; Chen, S.; Xu, H.; Zhang, S.; Yuan, Q.; Gan, W. *J. Chem. Phys.* **2015**, *142*, 22704-1-6.
- [77] Chen, Y.; Jena, K. C.; Roke, S. *J. Phys. Chem. C* **2015**, *119*, 17725-17734.
- [78] Lopes, J. N. C.; Cordeiro, T. C.; Esperança, J. M. S. S.; Guedes, H. J. R.; Huq, S.; Rebelo, L. P. N.; Seddon, K. R.; *J. Phys. Chem. B* **2005**, *109*, 3519-3525.

- [79] Stoppa, A.; Buchner, R.; Hefter, G. *J. Mol. Liq.* **2010**, *153*, 46-51.
- [80] Abbott, A. P.; Dsouza, N.; Withey, P.; Ryder, K. S. *Trans. Inst. Met. Finish.* **2012**, *90*, 9-14.
- [81] Li, N.; Zhang, S.; Zheng, L.; Dong, B.; Li, X.; Yu, L. *Phys. Chem. Chem. Phys.* **2008**, *10*, 4375-4377.
- [82] Kang, W.; Dong, B.; Gao, Y.; Zheng, L. *Colloid Polym. Sci.* **2010**, *288*, 1225-1232.
- [83] Shi, L.; Li, N.; Zheng, L. *J. Phys. Chem. C* **2011**, *115*, 18295-18301.
- [84] Inoue, T.; Kawashima, K.; Miyagawa, Y. *J. Colloid. Interface. Sci.* **2011**, *363*, 295-300.
- [85] Maier, F.; Cremer, T.; Kolbeck, C.; Lovelock, K. R. J.; Paape, N.; Schulz, P. S.; Wasserschied, P.; Steinrück, H. P. *Phys. Chem. Chem. Phys.* **2010**, *12*, 1905-1915.
- [86] Souda, R. *Surf. Sci.* **2010**, *604*, 1694-1697.
- [87] Nakajima, K.; Oshima, S.; Suzuki, M.; Kimura, K. *Surf. Sci.* **2012**, *606*, 1693-1699.
- [88] Nakajima, K.; Miyashita, M.; Suzuki, M.; Kimura, K. *J. Chem. Phys.* **2013**, *139*, 224701.
- [89] Niedermeyer, H.; Hallett, J. P.; Villar-Garcia, I. J.; Hunt, P. A.; Welton, T. *Chem. Soc. Rev.* **2012**, *41*, 7780-7802.
- [90] Li, S.; Feng, G.; Fulvio, P. F.; Hillesheim, P. C.; Liao, C. Dai, S.; Cummings, T. *J. Phys. Chem. Lett.* **2012**, *3*, 2465-2469.
- [91] Bowers, J. P.; Butts, C. J.; Martin, P. C.; Vergara-Gutierrez, M. *Langmuir* **2004**, *20*, 2191-2198.
- [92] Goodchild, I.; Collier, L.; Millar, S. L.; Prokšes, I.; Lord, J. C. D.; Butts, C. P. B.; Bowers, J. *J. Colloid Interface Sci.* **2007**, *307*, 45-468.
- [93] Wang, H.; Wang, J.; Zhang, S.; Xuan, X. *J. Phys. Chem. B* **2008**, *112*, 16682-16689.
- [94] Singh, T.; Kumar, A. *J. Phys. Chem. B* **2007**, *111*, 7843-7851.

- [95] Liu, X.; Dong, L.; Fang, Y. *J. Surfact. Deterg.* **2011**, *14*, 203-210.
- [96] Kamboj, R.; Singh, S.; Chauhan, V. *Colloids Surf., A* **2014**, *441*, 233-241.
- [97] Hanke, C. G.; Lynden-Bell, R. M. *J. Phys. Chem. B* **2003**, *107*, 10873-10878.
- [98] Annapureddy, H. V. R.; Hu, Z.; Xia, J.; Margulis, C. J. *J. Phys. Chem. B* **2008**, *112*, 1770-1776.
- [99] Jiang, W.; Wang, Y.; Voth, G. A. *J. Phys. Chem. B* **2007**, *111*, 4812-4818.
- [100] Bhargava, B. L.; Klein, M. L. *J. Phys. Chem. A* **2009** *113*, 1898-1904.
- [101] Bhargava, B. L.; Klein, M. L. *J. Phys. Chem. B* **2009**, *113*, 9499-9505.
- [102] Ishida, T.; Shirota, H. *J. Phys. Chem. B* **2013**, *117*, 1136-1150.
- [103] Yeganegi, S.; Soltanabadi, A.; Farmanzadeh, D. *J. Phys. Chem. B* **2012**, *116*, 11517-11526.
- [104] Baltazar, A. A.; Chandawalla, J.; Sawyer, K.; Anderson, J. L. *Colloids Surf., A* **2007**, *302*, 150-156.
- [105] Ao, M.; Huang, P.; Xu, G.; Yang, X.; Wang, Y. *Colloid Polym. Sci.* **2009**, *287*, 395-402.
- [106] Bhadani, A.; Singh, S. *Langmuir* **2011**, *27*, 14033-14044.
- [107] Bhargava, B. L.; Klein, M. L. *J. Chem. Theory. Comput.* **2010** *6*, 873-879.
- [108] Bhargava, B. L.; Klein, M. L. *J. Phys. Chem. B* **2011**, *115*, 10439-10446.
- [109] Tian, J.; Garcia, A. E. *Biophys. J.* **2009**, *96*, 57-59.
- [110] Tian, J.; Garcia, A. E. *J. Chem. Phys.* **2011**, *134*, 225101-225111.
- [111] Martinez, A. V.; Desensi, S. C.; Dominguez, L.; Rivera, E.; Straub, J. E. *J. Chem. Phys.* **2011**, *135*, 055107-055109.
- [112] Martinez, A. V.; Malolepsza, E.; Dominguez, L.; Lu, Q.; Straub, J. E. *J. Phys. Chem. B* **2015**, *119*, 9084-9090.

- [113] Winsor, P.A. *Trans. Faraday Soc.* **1948**, *44*, 376-398.
- [114] Sottmann, T.; Strey, R. *J. Chem. Phys.* **1997**, *106*, 8606-8615.
- [115] Salager, J. L.; Manchego, L.; Márquez, L.; Bullón, J.;Forgiarini, A. *J. Surfactants Deterg.* **2014**, *17*, 199-213.
- [116] Tichelkamp, T.; Vu, Y.; Nourani, M.; Øye, G. *Energy Fuels* **2014**, *28*, 2408-2414.
- [117] Scheu, R.; Chen, Y.; Aguiar; H. B. D.; Rankin, B. M. ; Ben-Amotz, D; Roke, S. *J. Am. Chem. Soc.* **2014**, *136*, 2040-2047.
- [118] Lago, S.; Rodríguez, H.; Khoshkbarchi, M. K.; Soto, A.; Arce, A. *RSC Adv.* **2012**, *2*, 9392-9397.
- [119] Lago, S.; Francisco, M.; Arce, A.; Soto, A. *Energy Fuels* **2013**, *27*, 5806-5810.
- [120] Lago, S.; Rodríguez-Cabo, B.; Arce, A.; Soto, A. *J. Chem. Thermodyn.* **2014**, *75*, 63-68.
- [121] Chai, J.; Xu, L.; Liu, W.; Zhu, M. *J. Chem. Eng. Data* **2012**, *57*, 2394-2400.
- [122] Hezave, A. Z.; Dorostkar, S.; Ayatollahi, S.; Nabipour, M.; Hemmateenejad, B. *J. Mol. Liq.* **2013**, *187*, 83-89.
- [123] Hezave, A. Z.; Dorostkar, S.; Ayatollahi, S.; Nabipour, M.; Hemmateenejad, B. *Fluid Phase Equil.* **2013**, *360*, 139-145.
- [124] Zolghadr, A. R.; Ghatee, M. H.; Zolghadr, A. *J. Phys. Chem. C* **2014**, *118*, 19889-19903.
- [125] Jorgensen, W. L.; Maxwell, D. S.; Tirado-Rives, J. *J. Am. Chem. Soc.* **1996**, *118*, 11225-11236.
- [126] Plimpton, S. *J. Comput. Phys.* **1995**, *117*, 1-19; web: <http://lammps.sandia.gov>.
- [127] Humphrey, W.; Dalke, A.; Schulten, K. *J. Mol. Graphics* **1996**, *14*, 33-38.
- [128] Allen, M. P. and Tildesley, D. J. *Computer Simulation of Liquids*; Clarendon Press: Oxford, U.K., **1987**.

[129] Ryckaert, J. P.; Ciccotti, J.; Berendsen, H. J. C. Numerical Integration of the Cartesian Equations of Motion of a System with Constraints: Molecular Dynamics of n-Alkanes.

Chapter 2

Segregation of Ions at the Interface: Molecular Dynamics Studies of Bulk and Liquid–vapor Interface Structure of Equimolar Binary Mixtures of Ionic Liquids

Abstract:

The structure of three different equimolar binary ionic liquid mixtures and their liquid – vapor interface has been studied using atomistic molecular dynamics simulations. Two of these binary mixtures were composed of a common cation 1-*n*-butyl-3-methylimidazolium, and varying anions (chloride and hexafluorophosphate in one of the mixtures and chloride and trifluoromethanesulfonate in the other) and the third binary mixture was composed of a common anion, trifluoromethanesulfonate and two imidazolium cations with ethyl and octyl side chains. Binary mixtures with common cation are found to be homogeneous. The anions are preferentially located near the ring hydrogen atoms due to H-bonding interactions. Segregation of ions is observed at the interface with enrichment of the liquid – vapor interface layer by longer alkyl chains and bigger anions with distributed charge. Surface composition is drastically different compared to the bulk composition, with the longer alkyl tail groups and bigger anions populating the outermost layer of the interface. The longer alkyl chains of the cations and trifluoromethanesulfonate anions with smaller charge density show orientational ordering at the liquid – vapor interface.

2.1. Introduction Binary mixtures of ionic liquids (ILs) are used as solvents in the field of catalysis, such as catalytic dimerisation and oligomerization of alkenes [1, 2, 3]. Experimental results have shed light on the higher catalytic activity of a Ru catalyst in a mixed ionic liquid solvent, $[C_4C_1Im][Cl][NTf_2]$ in the hydroformylation reaction [4], and the ease of recycling of the reaction media. It was found that mixed anion ILs impose selectivity on the product morphology of metal organic frameworks by controlling the solvent polarity or hydrophobicity [5]. One of the most important findings is the single-pot ~100% dissolution and degradation of cellulose using the IL mixture $[C_4C_1Im][HO_3S][Cl]$ [6]. IL mixtures are also found to be efficient in providing optimum enzyme activity and stability for enzyme-catalysed biomolecular reactions [7, 8]. The applications of IL mixtures are not restricted to the periphery of solvents in catalytic reactions. Recently binary and ternary mixtures of ILs are widely used as extraction layers [9] and in dispersive liquid – liquid micro-extraction [10]. Due to their lower glass transition temperature, wider liquid range and higher conductivity at low temperature compared to pure room-temperature ionic liquids (RTILs) [11, 12, 13], the binary mixtures of ILs are used as supercapacitor electrolytes in lithium batteries [14] and dye-sensitized solar cells [15]. So a vivid understanding of the bulk and liquid – vapor interface structure of binary mixtures of ILs is necessary to elucidate their role as reaction and extraction media as well as electrolytes.

The first detailed experimental investigations regarding the ideality in mixtures of two ionic liquids containing a common ion was carried out on six binary mixtures containing a common anion $[C_mC_1Im][C_nC_1Im][NTf_2]$ (m and n ranging from 2 to 10) and three binary mixtures containing a common cation $[C_4C_1Im][NTf_2][PF_6]$, $[C_4C_1Im][NTf_2][BF_4]$ and $[C_4C_1Im][NTf_2][PF_6]$. It has been reported that the mixture showed *quasi*-ideal behavior of mixing, which becomes non-ideal as the size difference between the cations increases [16, 17, 18]. From the structural point of view, long chain imidazolium based ILs are found to form aggregates in a comparatively shorter chain ILs [19, 20, 21]. IL mixture has also served the role as a medium for the aggregation of a nonionic surfactant [22] when individual pure components have failed to serve the purpose. The earlier study on the surface composition of the IL mixture $[C_2C_1Im][C_{12}C_1Im][NTf_2]$ by XPS

method [23] revealed no preferential accumulation of the longer chain cation at the outer surface, hence diminishing the greater surfactant property of the [C₁₂C₁Im] in the IL-mixture. TOF-SIMS study [24] on ionic liquid mixtures [C₈C₁Im][C₂C₁Im][BF₄] and [C₄C₁Im][NTf₂][PF₆] have shown that larger and polarizable ions tend to occupy the surface layer. Surface enrichment of longer chain [C₁₀C₁Im] cation in IL-mixture [C₂C₁Im][C₁₀C₁Im][TFSI] has also been reported [25, 26] using high-resolution Rutherford backscattering spectroscopy.

Even though a number of experimental studies have been reported on the IL mixtures, only few computational studies are available in the literature [27, 28, 29, 30, 31]. Classical molecular dynamics (MD) simulations on an equimolar mixture of [C₂C₁Im][C₆C₁Im][NTf₂] have shown the microscopic phase segregation of polar and non-polar domains, which is not observed in pure components [29]. The mixture shows very small positive excess of molar volume and thus ensures ideal behavior of mixing. *Ab initio* MD simulations [30, 31] of [C₂C₁Im][SCN][Cl] correlates the tendency of the anion to coordinate with the most acidic hydrogen of the cation to its basicity. The [C₂C₁Im] cations show weaker ordering in their spatial arrangements due to $\pi - \pi$ stacking of the imidazolium rings. The self-diffusion coefficients of various moieties of the IL mixtures were found to depend on the compositions of the mixtures studied. It has also been found that the binary mixtures are well mixed at the molecular level [32]. Classical MD studies on the IL mixture [b₃mpy][BF₄][N(CN)₂] over a range of composition conclude that the diffusion coefficients of cations and anions in the mixture depend upon the interaction between them [33]. Computational studies of capacitive performance of binary mixture of ILs and their mutual miscibility have also been reported [34]. To the best of our knowledge, no computational studies of the surface structure of IL mixtures are reported.

In the present work, we have carried out all-atom classical MD simulations on a series of equimolar binary mixtures of ILs with common anion, [C₂C₁Im][C₈C₁Im][CF₃SO₃], and common cation, [C₄C₁Im][Cl][PF₆] and [C₄C₁Im][Cl][CF₃SO₃], to get insights into the surface structure of the liquid – vapor interface as well as the bulk phase organization.

2.2. Methodology and simulation details Classical MD simulations have been carried out on 1:1 mixtures of ILs. Three different systems have been studied, with two of them containing a common cation, 1-*n*-butyl-3-methylimidazolium ([bmim]) and one with a common anion, trifluoromethanesulfonate (triflate, [TfO]). One of the systems, with a common cation had chloride ([Cl]) and hexafluorophosphate ([PF₆]) and the other had chloride and triflate ([TfO]) anions. The system containing the common anion had 1-*n*-ethyl-3-methylimidazolium ([emim]) and 1-*n*-octyl-3-methylimidazolium ([omim]) cations. In the following discussion, we use the notation [Cl] – [PF₆] to represent the [bmim][Cl] – [bmim][PF₆] mixture, [Cl] – [TfO] to represent [bmim][Cl] – [bmim][CF₃SO₃] mixture and [emim] – [omim] to represent [emim][CF₃SO₃] – [omim][CF₃SO₃] mixture.

The simulations were carried out using LAMMPS software [35] using the all atom force field developed by Pádúa and co-workers [36, 37]. The transferable force field with unit charge on ions is extensively used in the MD studies of ionic liquids. Since we are studying mixtures of ionic liquids, we have used the transferable force field model where the parameters are derived independently for the anions and the cations. The model has been known to predict the density, thermodynamic properties and the structure of the condensed phase and the crystalline phase fairly accurately [38].

For one of the systems with common cation, 200 ion pairs of [bmim][Cl] and 200 ion pairs of [bmim][PF₆] were randomly placed within a cubic box and isothermal-isobaric ensemble simulations were carried out for 2 ns at 350 K and 1 atmospheric pressure. Subsequent canonical ensemble simulations were carried out with the volume taken as the average over the last one nanosecond simulation at constant NPT conditions. The second system consisted of 256 ion pairs of [bmim][Cl] and 256 ion pairs of [bmim][CF₃SO₃]. The third system with a common triflate anion consisted of 256 ion pairs of [emim][TfO] and 256 ion pairs of [omim][TfO]. From the equilibrated configurations at 350 K, constant NPT simulations were carried out at higher temperatures of 400 K and 500 K for all the systems. These simulations were followed by constant NVT simulations with the volume fixed from the NPT simulations. The details of the systems are

Table 2.1: Details of simulations of ILs mixtures, where the systems are represented by differing anions or cations.

system	No. of IL1	No. of IL2	No. of atoms	Run length (ns)	Box length (at 500 K) (Å)
[Cl] – [PF ₆]	200	200	11600	30.0	51.76
[Cl] – [TfO]	256	256	15104	30.0	56.59
[emim] – [omim]	256	256	18432	30.0	59.96

provided in the table 2.1. The NVT simulations at 350 K were performed in cubic boxes with lengths 50.36, 54.96 and 58.21 Å for [Cl] – [PF₆], [Cl] – [TfO] and [emim] – [omim] mixtures respectively. At 400 K, the corresponding numbers were 50.74, 55.48 and 58.96 Å. A timestep of 0.5 fs was used to integrate the equations of motion.

Liquid – vapor interface simulations were performed for 20 ns by placing the equilibrated box in the center of the supercell which was extended along the z-axis to 100.0 Å for systems with common cation and 120.0 Å for the [emim] – [omim] system. These simulations were also performed at 350, 400 and 500 K. Positions of the atoms were stored every 5 ps. The mixtures have very high viscosity at low temperatures and the mixtures may not have sampled the phase space properly in the 30 ns simulations. Hence we are mainly using the results based on 500 K data in the discussion.

2.3. Results and Discussion The schematic drawings of the ions in the IL mixtures are provided in figure 2.1 to aid the discussion.

2.3.1 Radial Distribution Functions (RDFs)

The liquid structure in the binary mixtures of ILs can be obtained from the corresponding RDFs. Figure 2.2(a) presents the RDFs between the different anion sites for the mixture [Cl] – [TfO] at 500 K. We observe the first maxima for Cl – Cl, Cl – S and S – S pairs at around 6.7 Å, 7.2 Å and 7.7 Å respectively. The amplitude of the first maxima is highest for the Cl – Cl pair and is lowest for the S – S pair. This trend is consistent with the organisation of the chloride ions and central sulfur atoms of the triflate ions around the imidazolium rings in the [Cl] – [TfO] mixture

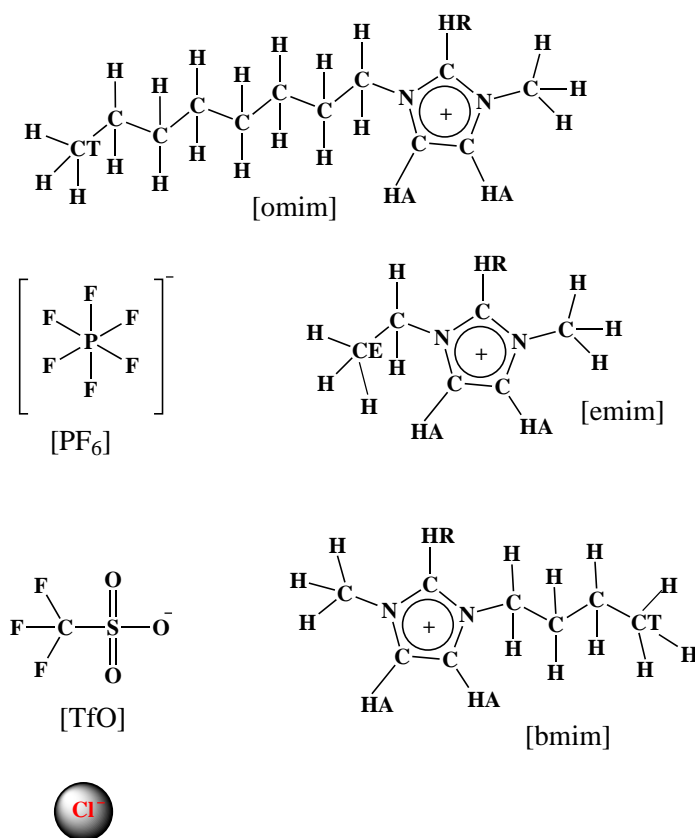


Figure 2.1: Schematic drawings of the ions in the IL mixtures.

(Figure A.1, Appendix A). It has been reported [41] that for a given alkyimidazolium cation, the cation – anion interaction strength decreases on going from bromide to triflate anion. Chloride, being smaller in size and having greater charge density than the bromide, must have greater cation – anion interaction strength than the bromide ion. So it is not surprising that the organisation of the the chloride ions is more pronounced than the organisation of the triflate anions around the imidazolium rings. This in turn will lead to better organization of the chloride ions around themselves compared to the sulfur atoms of the triflate ions around themselves, due to the presence of more chloride ions in any of the coordination shell of the imidazolium rings than the number of the sulfur atoms (data are not shown here). The amplitude of the first maximum of the Cl –

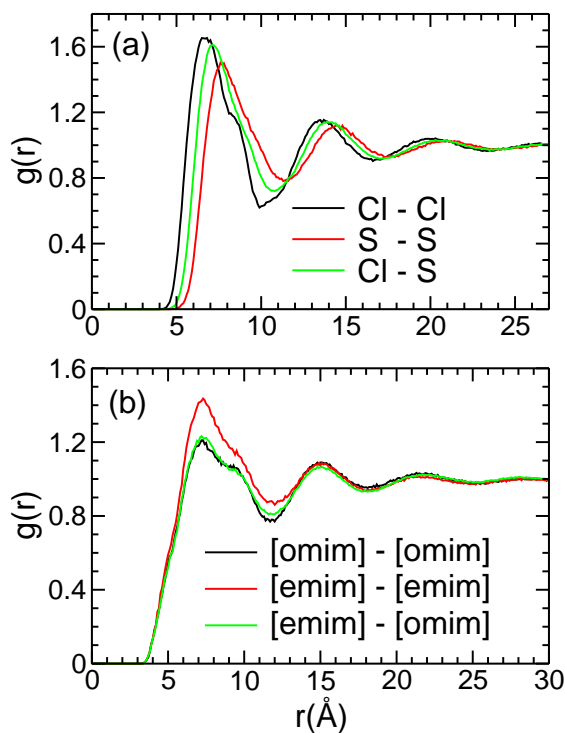


Figure 2.2: RDFs between (a) different anion sites in [Cl] – [TfO] and (b) imidazolium ring centers in [emim] – [omim] at 500 K.

S peak (arising from the cross interaction) is in between those of Cl – Cl and S – S amplitude due to the electrostatic attraction between the negative charge of the chloride ion and positive charge center (S atom) of the triflate anion. Similar trend is observed in [Cl] – [PF₆] mixture (Figure A.2, Appendix A), with the exception that Cl – P peak height is comparable with the Cl – Cl peak height as the phosphorous atom of [PF₆] anion has more positive charge than the sulfur atom of the [CF₃SO₃] anion. Simulations at lower temperatures also show similar trends in radial distribution functions (Figure A.3, Appendix A).

Figure 2.2(b) presents the RDFs between the geometric center of the imidazolium rings belonging to all possible distinct combinations of cations in the [emim] – [omim] mixture at 500 K. All the three plots have their first peak at around 6.6 Å. We observe that the imidazolium rings belonging to the [emim] cations are organised more around themselves than the imidazolium rings belonging to the [omim] cations. The amplitude of the first peak of the RDF between the imidazolium rings belonging to different type of cations (responsible for the cross interaction) is comparable to the amplitude of the peak in [omim] – [omim] RDF. We have also computed the

RDFs between the terminal carbon atoms of the alkyl chains of all distinct types of cation pairs and observed that the organisation of the terminal carbon atoms around themselves is highest for [omim] cations and lowest for [emim] cations, while the organisation between the terminal carbon atoms belonging to different types of cations is comparable with the organisation for the [emim] cations (Figure A.4, Appendix A). Based on these observations, we can conclude that in the [emim] – [omim] system, the organisation of the polar part of the cations increases with decrease in the hydrocarbon chain length whereas the trend is reversed for the organisation of the non-polar part of the cations. Also the cross RDFs of the polar domain and non-polar domain resemble that of [omim] cation and [emim] cation respectively. Similar results have been observed at lower temperatures (Figure A.5, Appendix A).

Figure 2.3(a) shows the RDFs between the most acidic hydrogen atom of the imidazolium ring and most negatively charged atom of the anion in IL mixtures. In both mixtures with common

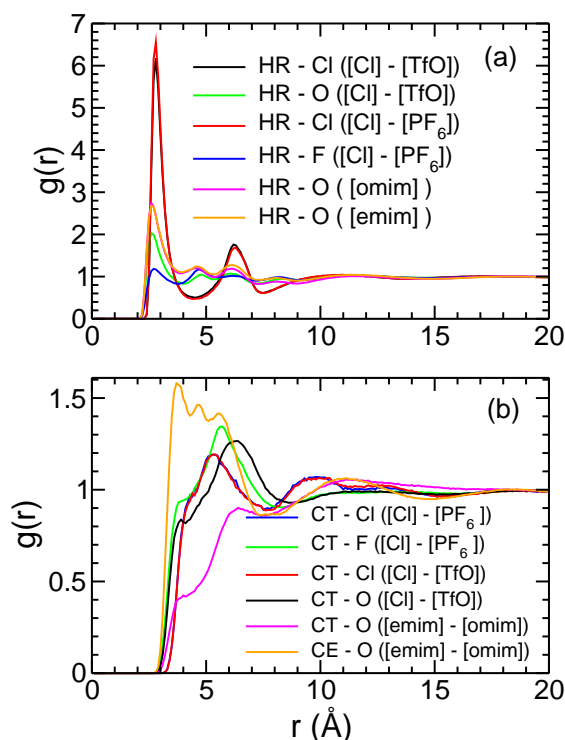


Figure 2.3: RDFs of the most negatively charged atom of the anions around (a) the most acidic hydrogen of the imidazolium ring and (b) the terminal carbon atom of the alkyl chain of the cations at 500 K in binary IL mixtures.

cation, i.e., [Cl] – [PF₆] and [Cl] – [TfO], the amplitude of the first maxima is higher for chloride

ion around the most acidic hydrogen and is lower for the most negative atom of the other anion (fluorine atom of $[\text{PF}_6]$ and oxygen atom of $[\text{TfO}]$) in the mixture. This variation is consistent with the cation – anion interaction strength [41], i.e., greater interaction strength will lead to better organisation of the anion around the most acidic hydrogen of the alkylimidazolium cation. In $[\text{emim}] - [\text{omim}]$ mixture, the RDFs between the most acidic hydrogen of the imidazolium ring belonging to either type of the cations and the oxygen atoms of the triflate anions show same intensity profile.

Figure 2.3(b) shows the RDFs of the most negatively charged atom of the anion around the terminal carbon atom of the cation in binary IL mixtures. In IL mixtures with common cation, anions ($[\text{PF}_6]$, $[\text{TfO}]$) having less cation – anion interaction strength with the $[\text{bmim}]$ cation show higher peak intensity than the $[\text{Cl}]$ anion which has greater interaction strength with $[\text{bmim}]$ cation. However, comparing the intensity of the first maxima of the RDF of the terminal carbon around fluorine atom (of $[\text{PF}_6]$) to that of around oxygen atom (of $[\text{TfO}]$), it is observed that the former shows higher intensity than the latter. This is also consistent with the variation in cation – anion interaction strength. In $[\text{emim}] - [\text{omim}]$ mixture, the anion is better organized around the terminal carbon atom of the more polar $[\text{emim}]$ cation than the $[\text{omim}]$ cations. RDFs obtained from the simulations at lower temperatures are similar to those at 500 K (Figure A.4, Appendix A).

2.3.2 Spatial Distribution Functions (SDFs)

Spatial distribution function provides information of the three dimensional arrangement of atoms or groups around others. Figure 2.4(a) shows the spatial density of oxygen atoms belonging to the triflate anions around the imidazolium cation in $[\text{emim}] - [\text{omim}]$ mixture at 500 K. Only those anions that are within 6\AA from the ring center are considered. The isosurface density value corresponds to ~ 4.5 times the average density of triflate oxygens in the system. We observe that the oxygen atoms are preferably located near the ring hydrogen atoms due to H-bonding interaction. Figure 2.4(b) represents the spatial density of the chloride anions, phosphorus atom and the fluorine atoms of the $[\text{PF}_6]$ anions around the imidazolium rings. The isosurface shown corresponds to 8.5, 6 and 3 times the average density of chloride ions, phosphorus atoms and fluorine atoms

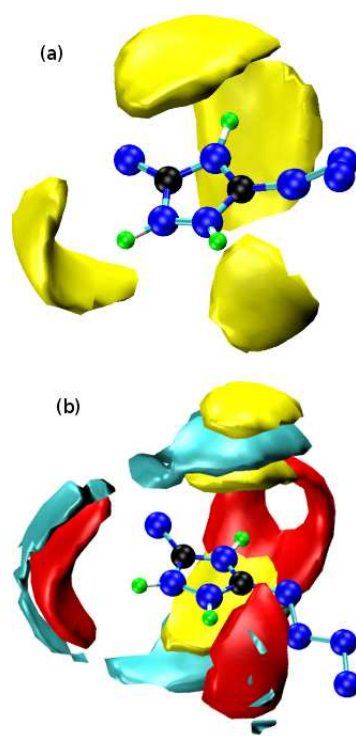


Figure 2.4: SDFs of (a) triflate oxygen atoms (in yellow) around the octylmethylimidazolium cation in [emim] – [omim] mixture and (b) chloride ions (in red), phosphorus (in cyan) and fluorine atoms (in yellow) of the [PF₆] ions around the imidazolium cation in [Cl] – [PF₆] at 500 K. Few carbon atoms of the octyl chain and the hydrogen atoms of the alkyl chains are not shown.

respectively. It can be observed from the figure that the chloride ions are predominantly located near the ring hydrogen atoms. The density of the chloride ions above and below the ring is lower compared to its density in the ring plane. If we look at the density of phosphorus and fluorine atoms of the [PF₆] anions, it is evident that they are more likely to be found above and below the imidazolium ring compared to the ring plane. This observation is also supported by the distribution of the angles formed by the normal vector to the imidazolium ring and the vector connecting the geometric center of the imidazolium ring and the chloride ion or the phosphorus atom of the [PF₆] ions shown in figure 2.5. From the figure, it is evident that the chloride ions are more probable to be present in the ring plane whereas the [PF₆] ions are more likely to be found above and below the ring. The distribution of anions around the cations in the [Cl] – [TfO] mixture is also found to be similar (Figure A.5 and Figure A.6, Appendix A).

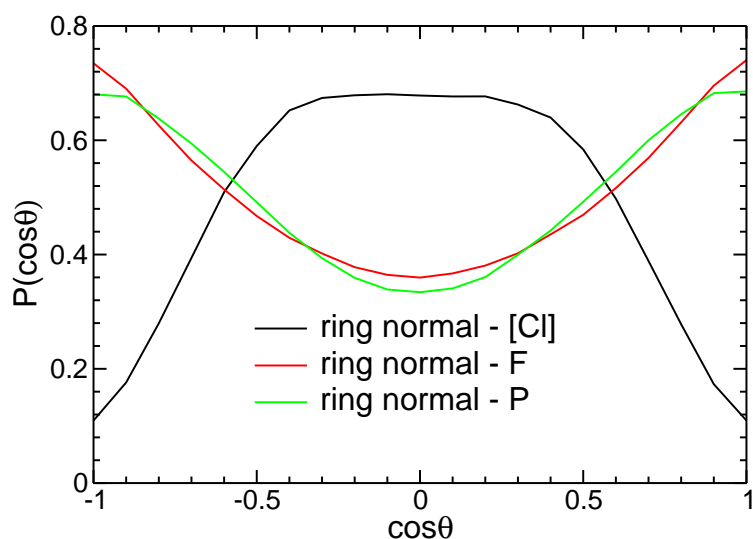


Figure 2.5: Distribution of the angles between the ring normal vector and the vector connecting the geometric center of the imidazolium ring and the chloride ion or the phosphorus atom of the $[PF_6]$ anion in $[Cl] - [PF_6]$ mixture at 500 K. Only those anions that are within 6\AA from the cation are considered.

2.3.3 Hydrogen Bonding

Hydrogen bonding is a key factor in determining the liquid structure of ILs in both pure form and aqueous solutions [42]. In our study, we recognize the imidazolium ring carbon atoms as the H-bond donors and negatively polarized atoms of the anions as the H-bond acceptor. We have adapted the geometric criteria [43] to identify H-bonds. If the distance of separation between the H-atom and the acceptor is less than 2.2\AA and the angle made by the donor, H-atom and the acceptor falls within the range of $130 - 180^\circ$, the H-bond formed is classified as strong one. The corresponding distance and angular range are $2.0 - 3.0\text{\AA}$ and $90 - 180^\circ$ respectively, for a weak hydrogen bond. Table 2.2 presents the average number of head – anion H-bonds observed in different IL mixtures at 500 K. The number of H-bonds per head group in the $[emim] - [omim]$ mixture are averaged over all the imidazolium rings belonging to both type of cations. We see that the number of H-bonds between the imidazolium ring and triflate oxygen atoms is almost three times that of the corresponding number with the fluorine atoms of triflate anion. This is due to the fact that the more negatively charged oxygen atoms are strongly interacting with the ring hydrogen atoms than the less negatively charged fluorine atoms do, which is also evidenced from

Table 2.2: Average number of H-bonds formed per head group in IL mixtures at 500 K.

System	acceptor	head-anion
[Cl] – [PF ₆]	Cl	1.11
[Cl] – [PF ₆]	F	1.76
[Cl] – [TfO]	Cl	1.08
[Cl] – [TfO]	O	1.30
[Cl] – [TfO]	F	0.46
[emim] – [omim]	O	2.90
[emim] – [omim]	F	1.15

the corresponding radial distribution plots (Figure A.7, Appendix A). In [Cl] – [PF₆] and [Cl] – [TfO] mixtures, we see that the chloride ions are competing with the other type of anions, present in the mixture, to form H-bonds with the imidazolium hydrogen atoms. The numbers shown in the table are consistent with the number of acceptor atoms present in the first coordination shell of the ring hydrogen atoms (data are not shown here).

2.3.4 Density Profiles

Density profiles of head and tail groups of cations and atoms of anions, along the interface normal (z-axis) at 500 K are shown in figure 2.6. As the number of cations and anions are different, the profiles are scaled accordingly for comparison. The density profiles of the systems with a common cation ([bmim]) are shown in figure 2.6(a) (with [Cl] and [PF₆] anions) and 2.6(b) (with [Cl] and [TfO] anions). It is evident from the figure 2.6(a) and 2.6(b), that the tail group of the cation is present closest to the interface, whereas the head group lies towards the bulk region. The peaks in the density profiles of the head and the tail groups are separated by 5 Å in both systems with a common cation. The peaks in the density profiles of chloride and hexafluorophosphate are observed close to that of the head group. While the chloride ion is more probable to be located towards the bulk region compared to the head group, the [PF₆] anion is more likely to be located towards the interface compared to the head group. In the system with chloride and triflate anions, the triflate anion is closer to interface and the CF₃ group of the anion shows similar enrichment in the interface as that of the alkyl tail. The difference in the location of the peak for the tail group

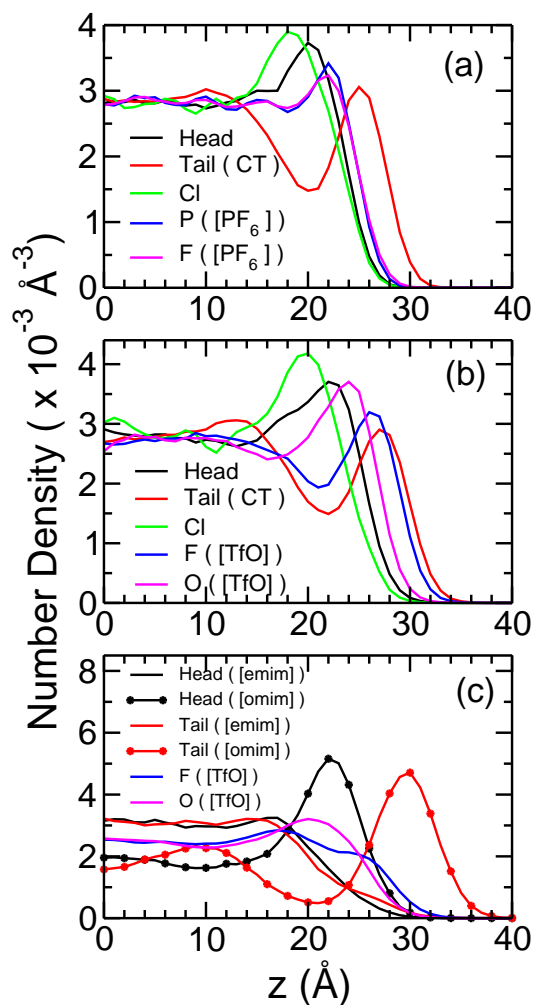


Figure 2.6: Density profiles of head and tail groups of cations and atoms of anions in (a) [Cl] – [PF₆] (b) [Cl] – [TfO] and (c) [emim] – [omim] mixtures along the interface normal (z -axis) at 500 K.

of cation and the CF₃ group of anion is just 1 Å. Well defined first minima in the density profiles are also observed in case of the tail group of cation and the CF₃ group of the anion. This suggests that the liquid – vapor interface of the mixture is enriched with larger anion consistent with the experimental observations [24]. The chloride ion, in which the whole charge is concentrated on a single atom, will be attracted to the head group and stays close to it, whereas [PF₆], in which the charge is diffused, feels relatively lesser attraction from the head group. In case of triflate, the dispersion interaction between the CF₃ group of anion and the alkyl tail of the cation makes the anion stay closer to the interface.

Figure 2.6(c) shows the density profiles in the [emim] – [omim] mixture at 500 K. In this binary mixture, the peaks in the density profiles of tail group and head group of [omim] cation are separated by 8Å. The peaks in the profiles of tail groups of [omim] and [emim] cations are separated by 16Å. In this case, the surface is clearly enriched with [omim] cations in agreement with the experimental findings [24]. The triflate anions are closer to the head group of the cations unlike in the case of the system with common cation ([bmim]).

The tail number density shows a well defined minima in all the studied systems. We define the interface as the region beyond this point towards the vapor phase. If at least one of the atoms of an ion (anion or cation) is within this region, then that ion is considered to be present in the interface. The mass density was found to be increased near the interface compared to the bulk (Figure A.8, Appendix A). The region along the z-axis between the points where the mass density of the system starts decreasing from its maximum value and where it reaches zero also coincides with the interface defined earlier. The density profiles at lower temperatures are qualitatively similar (Figure A.9, Appendix A)

2.3.5 Surface composition

The surface fractions of different ions present in the interfacial region at 500 K calculated as an average over the last 5 ns of the trajectory are shown in table 2.3. The surface fractions of the ions in the top half of the layer (layer towards the vapor phase) are given in parenthesis.

Table 2.3: Surface fractions of ions in the interfacial region in IL mixtures at 500 K.

System	Ion	Surface fraction
[Cl] - [PF ₆]	[bmim]	0.56 (0.77)
	[Cl]	0.18 (0.03)
	[PF ₆]	0.26 (0.20)
[Cl] - [TfO]	[bmim]	0.56 (0.66)
	[Cl]	0.15 (0.02)
	[TfO]	0.29 (0.32)
[emim] - [omim]	[emim]	0.13 (0.04)
	[omim]	0.40 (0.71)
	[TfO]	0.47 (0.25)

If we look at the surface fraction of the ions in the interfacial region as well as the outer half of the interface in the [Cl] – [PF₆] system, it is evident that the interface is slightly enriched with cations and the [PF₆] ions compared to the bulk fraction of the cations (0.5) and the anions (0.25). If we look at the outermost layer of the interface, it is highly enriched with the cations (0.77), whereas the presence of chloride ions is negligible. Similar trend is observed in [Cl] – [TfO] system, where the interface is enriched with cations and [TfO] anions. However, in this case we see that in the outermost layer of the interface, the surface fraction of [TfO] ions (0.32) is higher than that of [PF₆] ions in the [Cl] – [PF₆] system. When we look at the [emim] – [omim] system, we see that the interface is predominantly occupied by the [omim] cations. The surface fraction of [emim], [omim] and [TfO] ions are 0.13, 0.40 and 0.47 respectively compared to the bulk fraction of 0.25, 0.25 and 0.50. In the outermost layer, the composition is even more drastic with the surface fraction of [omim] being 0.71 and negligible presence of [emim] (0.04), i.e., surface fraction of [omim] is about 3 times its value in bulk region and that of [emim] is just 16% of its bulk value.. To summarise, there is surface segregation in the IL mixtures, with the longer alkyl chains at the outermost layer of the interface, followed by hydrophobic anions ([TfO] and [PF₆]). In case of systems with two anions, the interface is enriched with the larger (with distributed charge) anion, and in systems with two cations, the interface is enriched with cation with longer alkyl chain.

2.3.6 Intermolecular orientation

The orientation of the alkyl chains of the cations and the CS bond vectors (vector connecting carbon and sulfur atoms of the triflate anion) of anions among themselves that are present in the interfacial region are shown in figure 2.7. It is evident from the figure 2.7(a) that the longer alkyl chains of cations are predominantly oriented parallel to each other in the interfacial region in all three IL mixtures studied. In the bulk region, the orientation is almost random. Such an arrangement is favored by the dispersion interaction between the alkyl tails at the planar interface. In [emim] – [omim] interface, the octyl chains show a high degree of parallel orientation and ethyl chains are slightly oriented parallel to octyl chains whereas the ethyl chains show a very small degree of parallel orientation with other ethyl chains (Figure A.10, Appendix A). Triflate

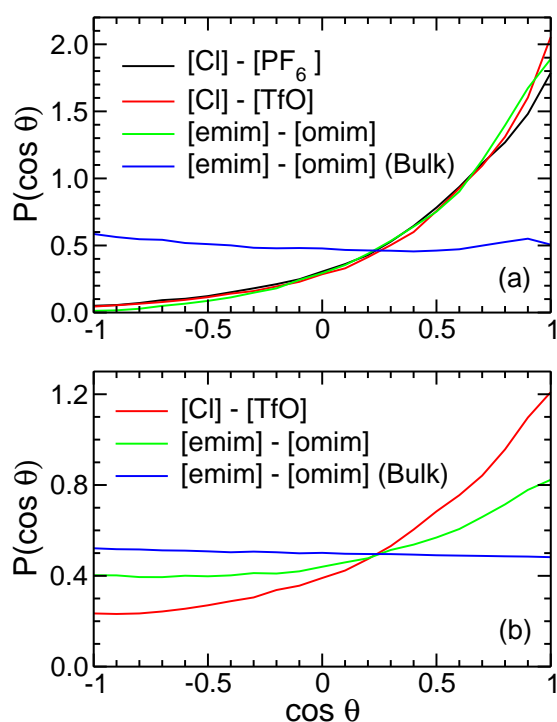


Figure 2.7: Distribution of the angles between (a) alkyl chain vectors (butyl chains of mixtures with common cation and octyl chains of [emim] – [omim] mixture) of the cations and (b) CS bond vectors of triflate anions that are present in the interfacial region of IL mixtures at 500 K.

anions also show orientational ordering at the interface as is evidenced from the figure 2.7(b). The carbon – sulfur bond vectors of the triflate anions are more likely to be oriented parallel to each other and the parallel orientation probability is higher in the [Cl] – [TfO] system. In the [emim] – [omim] system, the orientation is not pronounced as the interface is enriched with octyl chains of the cations and the triflate anions are not completely exposed to the interface. Parallel orientation of the anions allows the polar and nonpolar regions of the anions to interact with the head and the tail groups of the [bmim] cation respectively. As expected the interionic orientation in the bulk region is almost random. The carbon – sulfur bond vector of the triflate anions are also likely to be oriented parallel to the butyl chain and this preference is not seen with either the octyl or the ethyl chain (Figure A.11, Appendix A).

A snapshot of the liquid – vapor interface of the [emim] – [omim] system at 500 K after 20 ns simulation is shown in figure 2.8. From the figure, it can be seen that the octyl chains of the [omim] cation are protruding out towards the vapor phase. The segregation of ions near the interface is

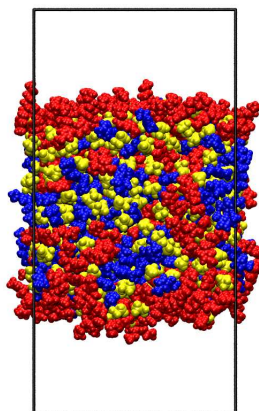


Figure 2.8: Snapshot of the liquid – vapor interface of the [emim] – [omim] system after 20 ns simulation. [omim] cations are shown in red, [emim] cations in yellow and [TfO] anions in blue.

clearly visible. The interface is predominantly populated by the [omim] cations and we see the [TfO] anions and [emim] cations towards the bulk liquid phase of the interface. Segregation of anions at the liquid – vapor interface to a greater extent in [Cl] – [TfO] mixture and to a small extent in [Cl] – [PF₆] mixture is also observed.

2.3.7 Interface Organization

The orientation of the butyl and octyl chains of the cations that are present in the interfacial region along the interface normal (z-axis) is shown in figure 2.9(a). From the figure, it can be observed that alkyl chains are more likely to be oriented parallel to the interface normal which is also reported in previous studies of pure ionic liquid – vapor interface [44]. The probability of the octyl chain to be parallel to the interface normal is slightly higher in the [emim] – [omim] system and is lower to be oriented in antiparallel direction to the interface normal compared to the systems with [bmim] cations. Also the probability of ethyl chains to be oriented parallel to the z-axis is lower compared to either the butyl or the octyl chains (Figure A.12, Appendix A). Note that, the parallel orientation of the alkyl chains along the interface normal is the most probable orientation. Other orientations are also observed in the interfacial region, although with smaller probabilities. These observations are consistent with the results derived based on the definition of the intrinsic interface [45] in the liquid – vapor interfaces of ionic liquids [46, 47], where multiple orientations

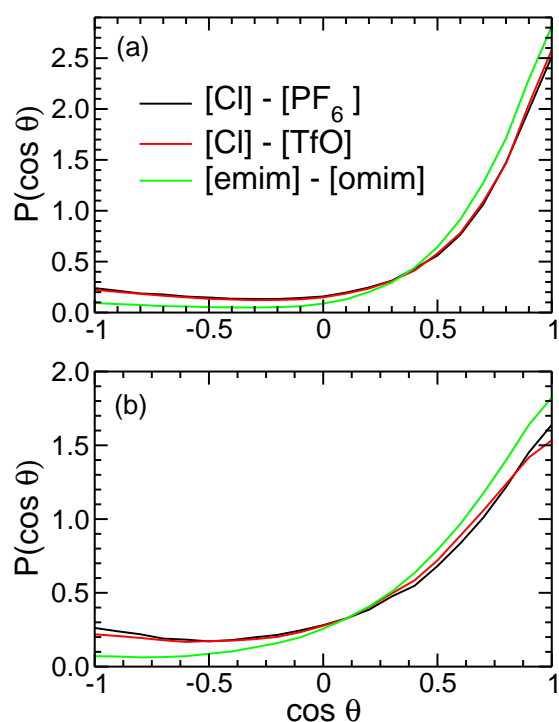


Figure 2.9: Distribution of the angles between the interface normal (z-axis) and (a) butyl and octyl chains and (b) the NN vector (vector connecting the two nitrogen atoms of the imidazolium ring) of [bmim] and [omim] cations present in the interfacial region of IL mixtures.

of the cations along the interface normal have been reported.

Figure 2.9(b) shows the distribution of the angles between the interface normal and the NN vector (vector connecting two nitrogen atoms of the imidazolium ring) of the [bmim] and [omim] cations that are present in the interfacial layer. In this case also it is observed that they are more likely to be oriented parallel to the interface normal. The NN vector of [omim] cation shows similar behavior as the corresponding chain - showing higher and lower probability to be parallel and antiparallel to the interface normal respectively, compared to the systems with [bmim] cation. The orientation of the cations along the z-axis shows that the cations are organized in the interfacial region.

The IL mixtures were divided into slabs of thickness 6 \AA along the interface normal from the center of the box and the orientation of the alkyl chain of the [omim] cations and the CS bond vector of the triflate anion along the interface normal were calculated. Figure 2.10(a) shows the orientation of octyl chains along the z-axis in various slabs along the interface normal in [emim]

– [omim] mixture. Slab 1, is the first slab from the center of box and represents the bulk region,

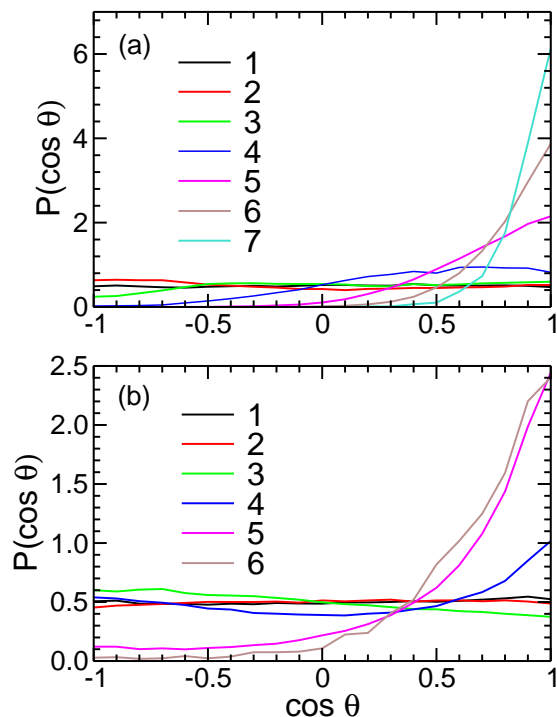


Figure 2.10: Distribution of the angles between the interface normal (z-axis) and (a) the alkyl chains of the cations and (b) the carbon – sulfur bond vectors of the triflate anions in various slabs along the interface normal in the [emim] – [omim] mixture at 500 K.

slab 2 is the next and so on. It can be noticed that in the first three slabs, the chains are randomly oriented along z-axis. However, from the fourth slab as we move towards the interface, octyl chains are increasingly likely to be oriented parallel to the interface normal. The probability to observe these chains in the antiparallel orientation with respect to the interface normal is absolutely nil from the fifth slab.

The orientation of CS bond vector of the triflate anion along z-axis in various slabs is shown in figure 2.10(b). It is seen that in first three slabs from the center of the box the anions are randomly oriented. In the fourth slab anions show an increased probability to be oriented along the interface normal and this probability increases as we move towards the interface. Also notice that there are no anions in the 7th slab. This also shows that there is segregation of ions at the interface. The outermost layer is composed of the octyl chain and then we find the triflate ions. The orientation of the butyl chains and the [TfO] anions in different slabs along the interface normal in [Cl] – [TfO]

mixture is found to be similar (Figure A.13, Appendix A).

The orientation of the ions in the IL mixtures can be described by Legendre polynomials which are defined as $P_1(\cos \theta) = \cos \theta$ and $P_2(\cos \theta) = (1/2)(3 \cos^2 \theta - 1)$. These functions provide an idea of orientational preferences at the interface. The averages of $\langle P_2(\cos \theta) \rangle$ for the alkyl chains of the cations and the CS bond vectors of the triflate anions along z-axis in the IL mixtures are shown in figure 2.11. Average P_2 for the alkyl chain of the cation along z-axis is shown in figure 2.11(a).

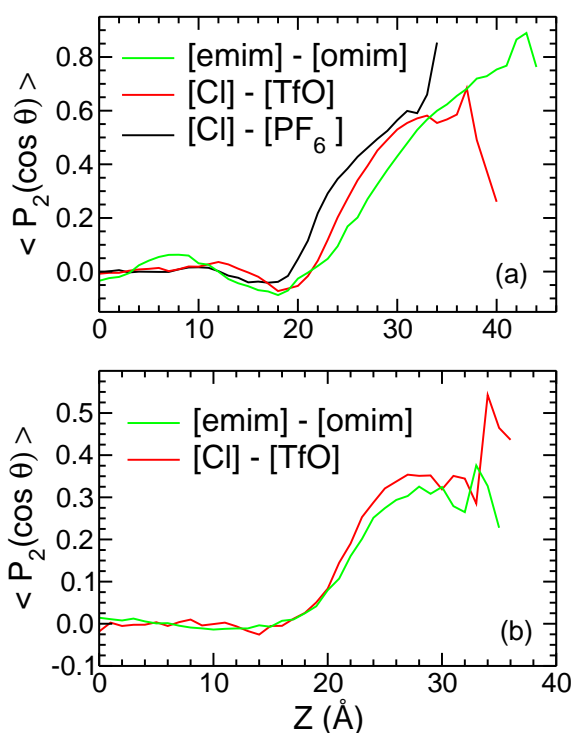


Figure 2.11: Average $P_2(\cos \theta)$ of the angle between (a) alkyl chain of the cation and the surface normal (b) CS bond vector of the triflate anion and the surface normal for IL mixtures at 500 K.

From the figure, one can notice that the orientation is random in the bulk region of the mixture and it gradually increases from about 20Å from the center of the box. The maximum value of $\langle P_2 \rangle$ observed is about 0.7, 0.85 and 0.9 in case of [Cl] – [TfO], [Cl] – [PF₆] and [emim] – [omim] mixtures, respectively. The perfect parallel orientation (where all the chains are oriented parallel to the interface normal) will give the $\langle P_2 \rangle$ of unity. So it is evident that there is very high degree of ordering of the chains in the interfacial region. Figure 2.11(b) shows the average $\langle P_2(\cos \theta) \rangle$ for the CS bond vector of the triflate anion along z-axis. In this case, it is evident that the anions

are randomly oriented in the bulk region and some ordering is seen beyond 15Å from the center of the box. The ordering increases gradually moving towards the interface and the value of $\langle P_2 \rangle$ reaches about 0.3 – 0.35 in the interfacial region. In [[Cl] – [TfO] mixture the $\langle P_2 \rangle$ reaches a maximum of 0.55 which is not seen in [emim] – [omim]. Nevertheless, the ordering of anions is not as pronounced as in the case of the alkyl chains. It is also important to note that the triflate anions are more ordered in the [Cl] – [TfO] mixture compared to [emim] – [omim] mixture.

2.4. Conclusions Atomistic MD simulations have been carried out on binary IL mixtures with a common cation and a common anion. The analysis of RDFs suggests that IL mixtures with a common cation are homogeneous. Strong interactions leading to the hydrogen bonding between the anions and the imidazolium ring hydrogen atoms are observed. The anions tend to concentrate near the ring hydrogen atoms as evidenced from the corresponding SDFs. In IL mixtures with two different anions, the anion with higher charge density ([Cl]) is more likely to be present in the ring plane whereas the bigger anions (with lower charge density), [PF₆] and [TfO], are more probable to be found above and below the plane of the imidazolium ring.

The liquid – vapor interface of the IL mixtures with a common cation, unlike the bulk region is not homogeneous. Segregation of ions is observed at the interface. In the IL mixtures, the alkyl chain protrudes towards the vapor phase with the head group present towards the liquid phase. The [Cl] and [PF₆] anions at the interface are closer to the imidazolium ring of the cation, whereas the [TfO] anion is oriented in such a way that the CF₃ group is present towards the interface whereas the SO₃ group interacts with the head group of the cation. Composition of the interface of [emim] – [omim] mixture provides an interesting picture of the interfacial layer with nonpolar alkyl groups at the edge of the interface towards the vapor phase with the [TfO] anions and [emim] cations interspersed as we move towards the bulk region, making the surface of the mixture hydrophobic. [Cl] anions and [emim] cations are completely excluded from the outermost layer of the interface. The bigger anions with distributed charge are found towards the vapor phase of the interface whereas the ions with concentrated charge ([Cl]) are found towards the liquid phase. Unlike the bulk IL mixture, the liquid – vapor interface shows the segregation of ions and enrichment of the

interface with specific ions.

The alkyl chains of the cations, and the triflate anions exhibit ordered orientation at the interface and are more likely to be oriented parallel to themselves. In addition, they are also found to be preferentially oriented parallel to the surface normal. The surface of the mixture predominantly consists of alkyl chains that are protruding out and perpendicular to the surface. The polar imidazolium ring lies towards the liquid phase along with the anions having higher charge density. In the presence of two types anions that are not similar, the anions with lower charge density are found near the interface while those with higher charge density stays closer to the head group towards the bulk region. In the presence of two types of cations, the cations with longer alkyl chain are found near the interface while the cations with shorter alkyl chain are located towards the liquid phase. The alkyl chains of the cation and the CS bond vectors of the triflate anions show a gradual increase in their orientational ordering as we proceed from bulk region to the interface.

Chapter A

Appendix A

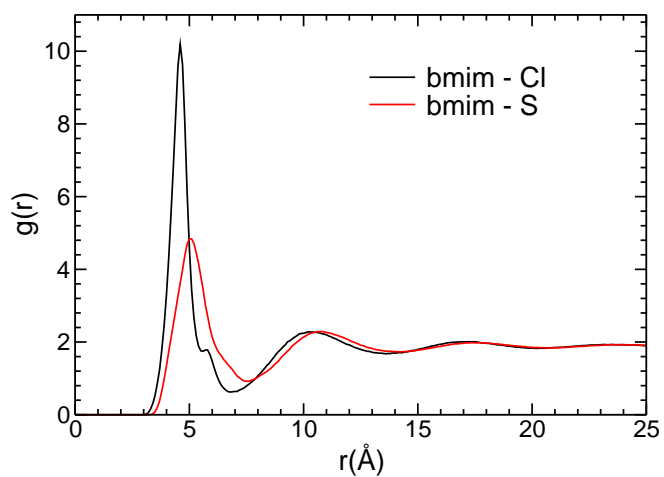


Figure A.1: RDFs of the chloride anions and the sulfur atoms of the triflate anions around the geometric center of the imidazolium ring in [Cl] – [TfO] mixture at 500 K.

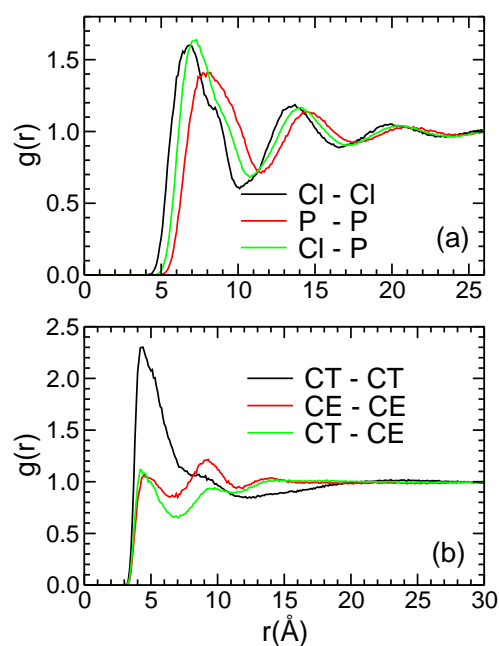


Figure A.2: RDFs of (a) different anion sites in [Cl] – [PF₆] and (b) terminal carbon atoms of the alkyl chains belonging to distinct types of cations in [emim] – [omim] mixture at 500 K.

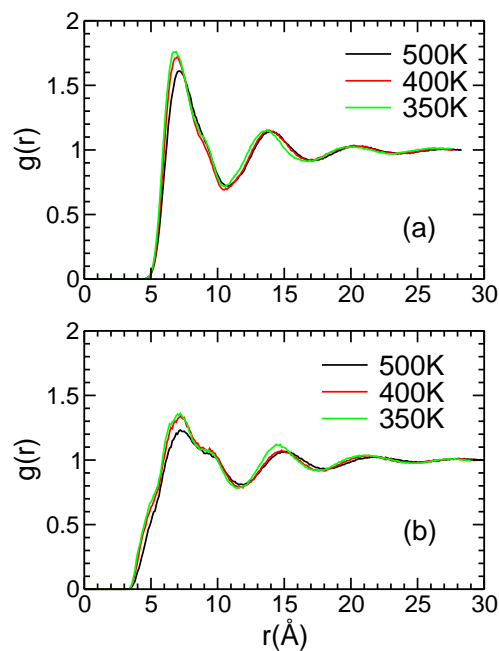


Figure A.3: RDFs of (a) sulfur atoms of triflate anions around chloride anions in [Cl] – [TfO] system and (b) head group of [emim] cations around head groups of [omim] cations in [emim] – [omim] system at different temperatures.

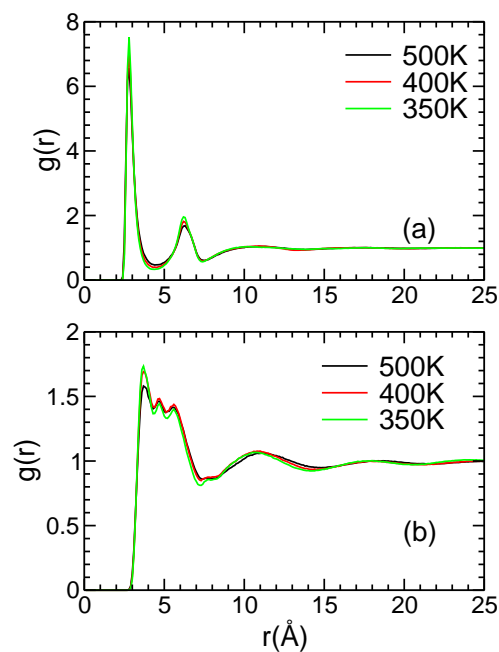


Figure A.4: RDFs of (a) the chloride anions around the most acidic hydrogen atom of the imidazolium ring in [Cl] – [TfO] system and (b) oxygen atoms of the triflate anions around the terminal carbon atoms of the ethyl chain [emim] – [omim] system at different temperatures.

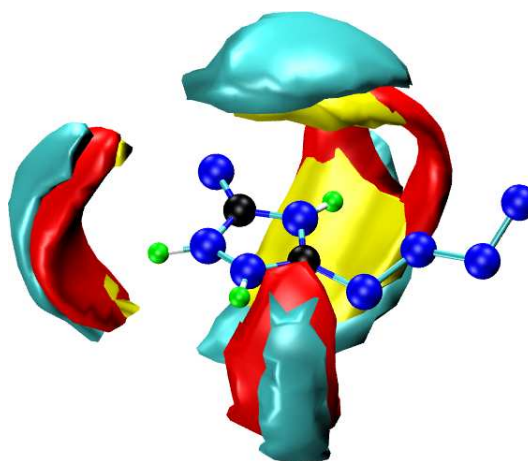


Figure A.5: SDFs of chloride anions (in red), oxygen atoms (in yellow) and sulfur atom (in cyan) of the [TfO] anions, that are within 6 \AA from the cation, around the geometric center of the imidazolium ring in [Cl] – [TfO] mixture at 500 K. The isosurface density shown corresponds to 8.5, 4 and 2 times the average density of chloride ions, oxygen atoms and sulfur atom of the triflate anions respectively. Hydrogen atoms on the alkyl groups are not shown.

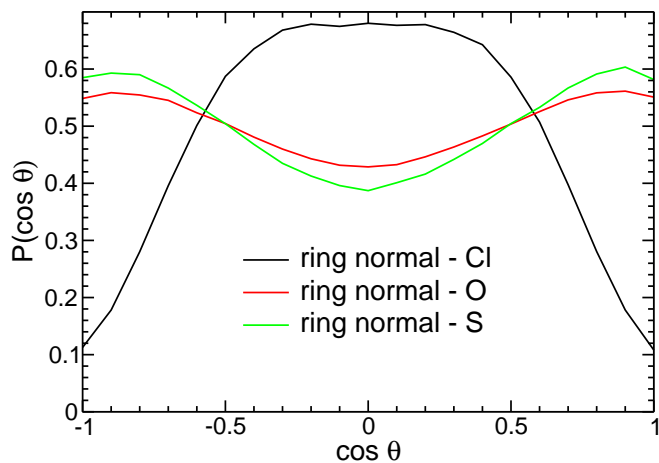


Figure A.6: Distribution of the angles between the ring normal vector and the vector connecting the geometric center of the imidazolium ring and the chloride ion or the sulfur atom of the [TfO] anion in [Cl] – [TfO] mixture at 500 K. Only those anions that are within 6\AA from the cation are considered.

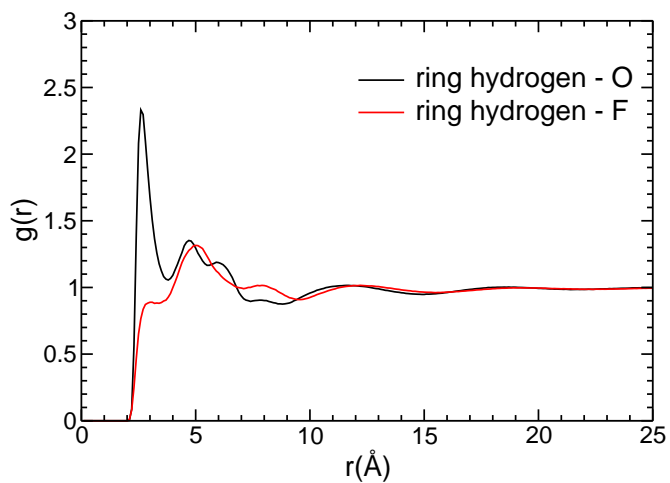


Figure A.7: RDFs of oxygen and fluorine atoms of the triflate anions around the imidazolium ring hydrogen atoms in [emim] – [omim] system at 500 K.

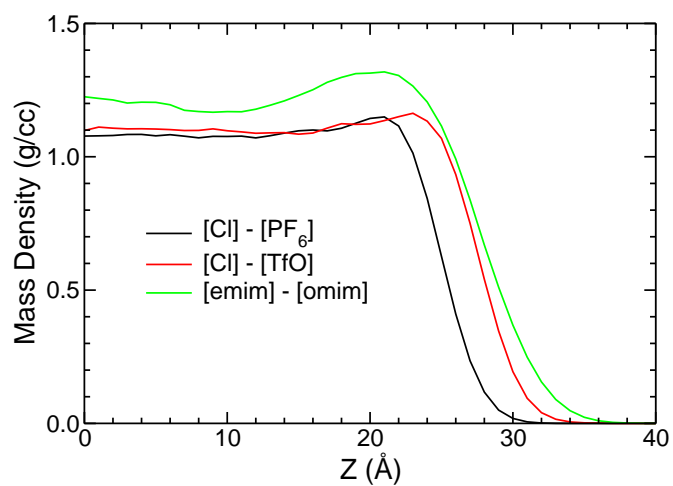


Figure A.8: Mass density profiles along the interface normal (z -axis) in binary ionic liquid mixtures at 500 K.

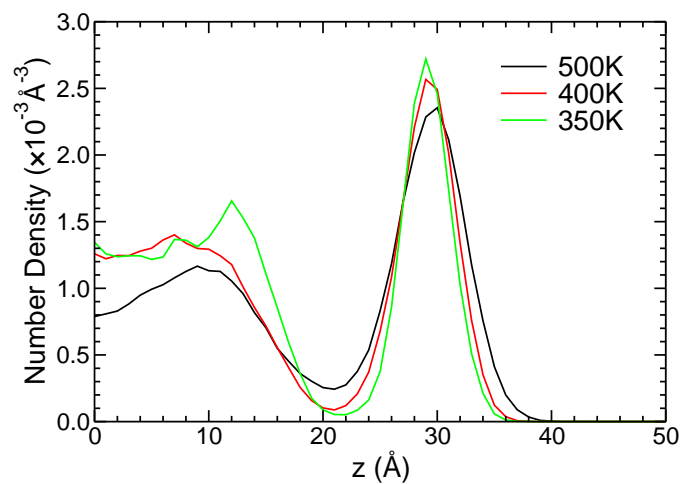


Figure A.9: Number density profiles of terminal carbon atoms of the octyl chains in [emim] – [omim] mixture along the interface normal (z -axis) at different temperatures.

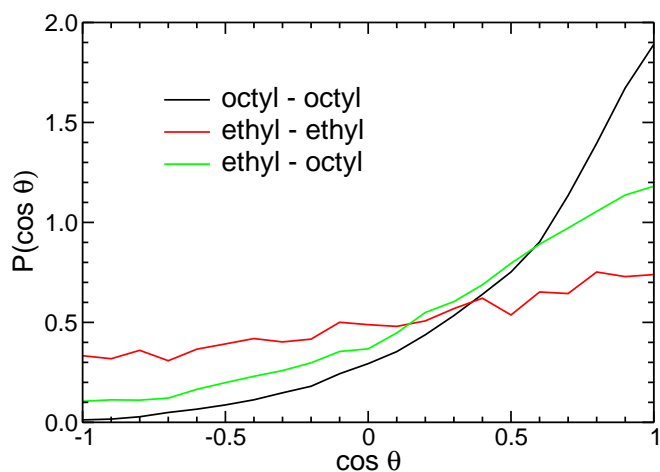


Figure A.10: Orientation of ethyl and octyl chains of cations that are present in the interfacial region of [emim] – [omim] mixture at 500 K.

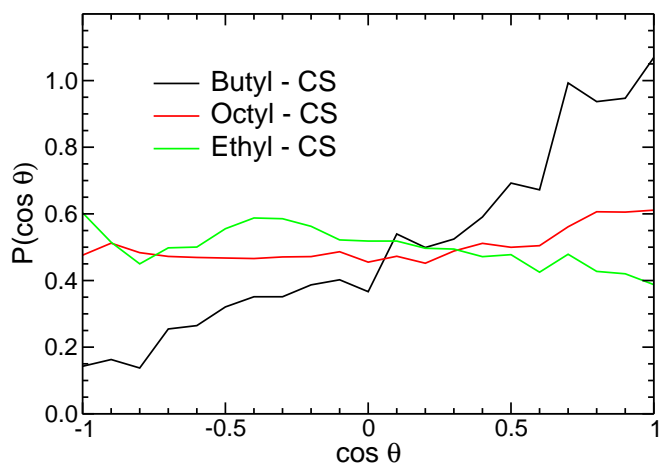


Figure A.11: Distribution of the angles between the alkyl chains of the cations and the carbon – sulfur bond vectors of the triflate anions present in the interfacial layer of IL mixtures at 500 K.

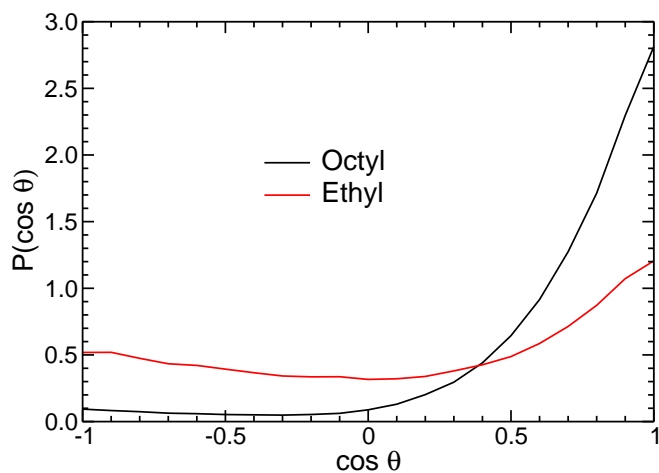


Figure A.12: Distribution of the angles between the interface normal (z-axis) and the alkyl chains of the [emim] – [omim] mixture at 500 K.

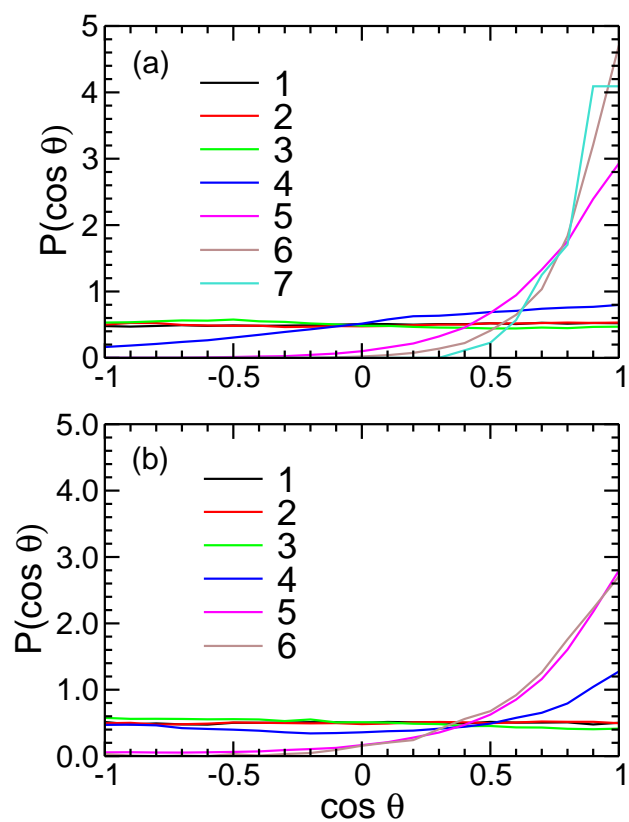


Figure A.13: Distribution of the angles between the interface normal (z-axis) and (a) the butyl chains of the cations and (b) carbon – sulfur bond vectors of the triflate anions in various slabs along the interface normal in [Cl] – [TfO] mixture at 500 K.

Bibliography

- [1] Chauvin, Y.; Gilbert, B.; Guibard, I. *J. Chem. Soc., Chem. Commun.* **1990**, 1715-1716.
- [2] Chauvin, Y.; Einloft, S.; Olivier, H. *Ind. Eng. Chem. Res.* **1995**, *34*, 1149-1155.
- [3] Simon, L. C.; Dupont, J. and de Souza, R. F. *Appl. Catal., A* **1998**, *175*, 215-220.
- [4] Tominaga, K. *Catal. Today* **2006**, *115*, 70-72.
- [5] Lin, Z. ; Wragg, D. S.; Warren, J. E. and Morris, R. E. *J. Am. Chem. Soc.* **2007**, *129*, 10334-10335.
- [6] Long, J. ; Guo, B. ; Li, X. ; Jiang, Y. ; Wang, F. ; Tsang, S. C.; Wang, L. and Yu, K. M. K. *Green Chem.* **2011**, *13*, 2334-2338.
- [7] Lee, S. H. ; Ha, S. H. ; Hiep, N. M. ; Chang, W. and Koo, Y. *J. Biotechnol.* **2008**, *133*, 486-489.
- [8] Ha, S. H. ; Hiep, N. M. and Koo, Y. *Biotechnol. Bioprocess Eng.* **2010**, *15*, 126-130.
- [9] Katsuta, S. ; Yoshimoto, Y. ; Okai, M. ; Takeda, Y. and Bessho, K. *Ind. Eng. Chem. Res.* **2011**, *50*, 12735-12740.
- [10] Zhao, R. ; Wang, X. ; Zhang, L. ; Wang, S. and Yuan, J. *Anal. Methods* **2011**, *3*, 831-836.
- [11] Kunze, M. ; Jeong, S. ; Paillard, E. ; Winter, M. and Passerini, S. *J. Phys. Chem. C* **2010**, *114*, 12364-12369.
- [12] Annat, G. ; Forsyth, M. and MacFarlane, D. R. *J. Phys. Chem. B* **2012**, *116*, 8251-8258.

- [13] Fox, E. T. ; Weaver, J. E. F. and Henderson, W. A. *J. Phys. Chem. C* **2012**, *116*, 5270-5274.
- [14] Lin, R. ; Taberna, P. ; Fantini, S. ; Presser, V. Pérez, C. R. ; Malbosc, F. ; Rupesinghe, N. L. ; Teo, K. B. K. ; Gogotsi, Y. and Simon, P. *J. Phys. Chem. Lett.* **2011**, *2*, 2396-2401.
- [15] Armel, V. ; Pringle, J. M. ; Forsyth, M. MacFarlane, D. R. ; Officer, D. L. and Wagner, P. *Chem. Commun.* **2010**, *46*, 3146-3148.
- [16] Lopes, J. N. C. ; Cordeiro, T. C. Esperança, J. M. S. S. ; Guedes, H. J. R. ; Huq, S. ; Rebelo, L. P. N. and Seddon, K. R. *J. Phys. Chem. B* **2005**, *109*, 3519-3525.
- [17] Stoppa, A. ; Buchner, R. and Hefter, G. *J. Mol. Liq.* **2010**, *153*, 46-51.
- [18] Abbott, A. P. ; Dsouza, N. ; Withey, P. and Ryder, K. S. *Trans. Inst. Met. Finish.* **2012**, *90*, 9-14.
- [19] Li, N. ; Zhang, S. ; Zheng, L. ; Dong, B. ; Li, X. and Yu, L. *Phys. Chem. Chem. Phys.* **2008**, *10*, 4375-4377.
- [20] Kang, W. ; Dong, B. ; Gao, Y. and Zheng, L. *Colloid Polym.Sci.* **2010**, *288*, 1225-1232.
- [21] Shi, L. ; Li, N. and Zheng, L. *J. Phys. Chem. C* **2011**, *115*, 18295-18301.
- [22] Inoue, T. ; Kawashima, K. and Miyagawa, Y. *J. Colloid. Interface. Sci.* **2011**, *363*, 295-300.
- [23] Maier, F. ; Cremer, T. ; Kolbeck, C. ; Lovelock, K. R. J. Paape, N. ; Schulz, P. S. ; Wasserschied, P. and Steinrück, H. P. *Phys. Chem. Chem. Phys.* **2010**, *12*, 1905-1915.
- [24] Souda, R. *Surf. Sci.* **2010**, *604*, 1694-1697.
- [25] Nakajima, K.; Oshima, S. ; Suzuki, M. and Kimura, K. *Surf. Sci.* **2012**, *606*, 1693-1699.
- [26] Nakajima, K. ; Miyashita, M. ; Suzuki, M. and Kimura, K. *J. Chem. Phys.* **2013**, *139*, 224701.
- [27] Lui, M. Y. ; Crowhurst, L. ; Hallett, J. P. Hunt, P. A. ; Niedermeyer, H. and Welton, T. *Chem. Sci.* **2011**, *2*, 1491-1496.

- [28] Niedermeyer, H. ; Hallett, J. P. ; Villar-Garcia, I. J. ; Hunt, P. A. and Welton, T. *Chem. Soc. Rev.* **2012**, *41*, 7780-7802.
- [29] Shimizu, K. ; Tariq, M. ; Rebelo, L. P. N. and Lopes, J. N. C. *J. Mol. Liq.* **2010**, *153*, 52-56.
- [30] Brüssel, M. ; Brehm, M. ; Voigt, T. and Kirchner, B. *Phys. Chem. Chem. Phys.* **2011**, *13*, 13617-13620.
- [31] Brüssel, M. ; Brehm, M. ; Pensado, S. ; Malberg, F. ; Stark, A. and Kirchner, B. *Phys. Chem. Chem. Phys.* **2012**, *14*, 13204-13215.
- [32] Payal, R. S. and Balasubramanian, S. *Phys. Chem. Chem. Phys.* **2013**, *15*, 21077-21083.
- [33] Aparicio, S. and Atilhan, M. *J. Phys. Chem. B* **2012**, *116*, 2526-2537.
- [34] Li, S. ; Feng, G. ; Fulvio, P. F. ;Hillesheim, P. C. ; Liao, C. ; Dai, S. and Cummings, T. J. *Phys. Chem. Lett.* **2012**, *3*, 2465-2469.
- [35] Plimpton, S. *J. Comput. Phys.* **1995**, *117*, 1-19 (<http://lammps.sandia.gov>).
- [36] Lopes, J. N. C. and Pádua, A. A. H. *J. Phys. Chem. B* **2004**, *108*, 16893-16898.
- [37] Lopes, J. N. C. and Pádua, A. A. H. *J. Phys. Chem. B* **2006**, *110*, 19586-19592.
- [38] Lopes, J. N. C. and Pádua, A. A. H. *Theor. Chem. Acc.* **2012**, *131*, 1129.
- [39] Allen, M. P. and Tildesley, D. J. *Computer Simulation of Liquids*; Clarendon Press: Oxford, U.K., **1987**.
- [40] Humphrey, W. ; Dalke, A. and Schulten, K. *J. Mol. Graphics* **1996**, *14*, 33-38.
- [41] Bini, R. ; Bortolini, O. ; Chiappe, C. ; Pieraccini, D. and Siciliano, T. *J. Phys. Chem. B* **2007**, *111*, 598-604.
- [42] Hunt, P. A. ; Ashworth, C. R. and Matthews, R. P. *Chem. Soc. Rev.* **2015**, *44*, 1257-1288.
- [43] Desiraju, G. R. and Steiner, T. *The Weak Hydrogen Bond, In Structural Chemistry and Biology*; Oxford University Press: New York, **2001**.

- [44] Bhargava, B. L. and Balasubramanian, S. *J. Am. Chem. Soc.* **2006**, *128*, 10073-10078.
- [45] Pártay, L. B. ; Hantal, G. ; Jedlovszky, P. ; Vincze, A. and Horvai, G. *J. Comput. Chem.* **2008**, *29*, 945-956.
- [46] Hantal, G. ; Cordeiro, M. N. D. S. and Jorge, M. *Phys. Chem. Chem. Phys.* **2011**, *13*, 21230-21232.
- [47] Hantal, G. ; Voroshylova, I. ; Cordeiro, M. N. D. S. and Jorge, M. *Phys. Chem. Chem. Phys.* **2012**, *14*, 5200-5213.

Chapter 3

Surface structure and dynamics of ions at the liquid – vapor interface of binary ionic liquid mixtures : Molecular dynamics studies

Abstract:

The surface structure and dynamics of ions at the liquid – vapor interface of binary mixtures of ionic liquids 1-*n*-octyl-3-methylimidazolium trifluoromethanesulfonate ([omim][TfO]) and 1-ethyl-3-methylimidazolium trifluoromethanesulfonate ([emim][TfO]) of varying composition have been studied using atomistic molecular dynamics simulations. Global definition of the interface and the identification of the truly interfacial molecule method (ITIM) have been used to analyze the structure and dynamics of the ions at the interface. We have seen enhancement in density of longer alkyl chain cation ([omim]) at the liquid – vapor interface compared to the bulk. The surface is mainly enriched with [omim] cation and it becomes smoother with decrease in the mole fraction of [omim] cations in the mixtures. The [omim] cation shows greater survival probability at the liquid – vapor interface than other ions and this probability increases with decrease in the mole fraction of [omim] cations. The re-orientational correlation function suggests that the [omim] cations prefer to retain their orientation with respect to the interface normal for a longer time. The movement of ions in and out of the interface is facilitated by the out of plane rotation of the ions with respect to the interface.

3.1. Introduction Ionic liquid (IL) mixtures are receiving increasing attention from academia and industry due to their interesting properties and potential applications [1, 2]. IL mixtures are used as solvents in organic and biomolecular catalytic reactions [3, 4, 5, 6, 7, 8], supercapacitor electrolytes in lithium ion batteries [9] and dye-sensitized solar cells [10], reactive media for biomass processing [11, 12], extraction media [13, 14], etc. Varying the composition of IL mixtures can also improve CO₂ absorption [15, 16, 17]. Since many of the processes take place at the interface of the IL mixtures, understanding the surface structure as well as the dynamics of the ions at the interface is of potential interest from the academic point of view.

Surface composition of binary mixtures of ionic liquids has been studied using various experimental methods [18, 19, 20, 21]. An XPS study [18] on the IL mixture [C₂C₁Im][C₁₂C₁Im][NTf₂] revealed no preferential accumulation of the longer chain cations at the outer surface. However, TOF-SIMS study [19] on IL mixtures [C₈C₁Im][C₂C₁Im][BF₄] and [C₄C₁Im][NTf₂][PF₆] showed the presence of larger and polarizable ions at the surface layer. High-resolution Rutherford back-scattering spectroscopy [20, 21] also reported the surface enrichment of longer chain [C₁₀C₁Im] cations in the IL-mixture [C₂C₁Im][C₁₀C₁Im][TFSI].

Although a few computational studies are available in the literature regarding structure [22, 23, 24, 25, 26, 27, 28] and dynamics [29] of ions in bulk region of the binary IL mixtures, computational studies of the liquid – vapor interface are rare [27]. In our recent work [27], we have shown the surface enrichment and orientational ordering of cations with the longer alkyl chain and bigger anions with a distributed charge at the liquid – vapor interface.

To the best of our knowledge, no computational studies of the surface structure and dynamics of ions at the liquid – vapor interface of binary mixtures of ionic liquids of varying composition have been reported. In the present work, we have carried out all-atom classical MD simulations on a series of IL mixtures [C₂C₁Im][C₈C₁Im][CF₃SO₃] to get insights into the effect of composition on the surface structure and dynamics of ions in the liquid – vapor interfacial layer.

3.2. Methodology and simulation details. We have carried out atomistic MD simulations on a series of IL mixtures consisting of 1-*n*-octyl-3-methylimidazolium trifluoromethanesulfonate ([omim][TfO]) and 1-ethyl-3-methylimidazolium trifluoromethanesulfonate ([emim][TfO]) of varying composition. The mole fraction of either of the ILs in the mixtures varies from 0 (implying the absence of that component in the system) to 1 (corresponds to the pure component). Molecular dynamics software LAMMPS [30] has been used to perform the simulations. The force field parameters are adapted from the works of Pádua and co-workers [31, 32]. Ion pairs were randomly placed within a cubic box. Isothermal-isobaric ensemble (constant NPT) simulations were carried out at 500 K and 1-atmosphere pressure for 2 ns. Liquid – vapor interfaces were simulated by extending the supercell along z-axis to 120.0 Å for mixtures and placing the corresponding equilibrated box at the center of the extended supercell. As the pure IL systems were smaller, the supercell was extended to 100 Å along z-axis. Canonical ensemble simulations (constant NVT) on all the interfacial systems were performed for 35 ns. The details of the simulated systems are tabulated in Table 3.1. The atomic positions were

Table 3.1: Details of simulations of systems studied (the IL mixtures are presented by the ratio of mole numbers of [omim][TfO] and [emim][TfO]).

system	No. of [omim][TfO]	No. of [emim][TfO]	No. of atoms	Run length (ns)	Box length (at 500 K) (Å)
pure [omim][TfO]	256	–	11520	35.0	51.71
9:1	580	64	27828	35.0	68.97
3:1	375	125	20250	35.0	62.28
1:1	256	256	18432	35.0	59.96
1:3	125	375	15750	35.0	57.71
1:9	64	580	18540	35.0	61.36
pure [emim][TfO]	–	256	6912	35.0	44.31

stored at a regular interval of 5 ps which were used for further analyses. The surface tension was calculated from the pressure tensor that was stored at each step during the last 1 ns of the liquid – vapor interface simulations. Structural properties of the interfaces have been averaged over the last 5 ns of trajectory unless mentioned otherwise. The dynamical properties are calculated from the last 15 ns of trajectory. In some tables pure [omim][TfO] and pure [emim][TfO] systems are

represented by "1:0" and "0:1" respectively. The studies on the structural properties of the 1:1 binary mixture can be found elsewhere [27].

We use the term "global" interface to indicate the interface defined in the Cartesian frame of reference using a cutoff distance for interface boundary. The "intrinsic" interface is used to indicate an instantaneous interface frame of reference.

3.2.1 Identification of the truly interfacial molecule method (ITIM)

We employed the ITIM method [35, 36, 37] for the analysis of the intrinsic liquid – vapor interface. The basic principle behind the ITIM method is based on moving probe spheres of a given radius along the straight lines parallel to the interface normal, i.e., z-axis (perpendicular to the interface, i.e., xy-plane) from the vacuum side. Once the distance between the center of the probe sphere and the first atom on the surface becomes less or equal to the sum of the radius of the probe sphere and the Lennard-Jones σ of the atom, the probe sphere is stopped and the atom is identified as truly interfacial one. Through thorough scanning of the interface by moving the probe spheres along all the test lines, we obtain the complete set of truly interfacial atoms and the corresponding molecules. The positions where the probe spheres are stopped along the test lines are regarded as surface points. We used a probe radius of 2.5 Å and each grid on the xy-plane has dimension 1.0×1.0 Å. The instantaneous interface determined is not sensitive to probe sphere radius when we choose 2.5 Å.

3.3. Results and Discussion

3.3.1 Density profiles

In the discussion of density profiles of different moieties along the interface normal (z-axis), from the global definition of the interface, the zero value at the horizontal axis represents the center of the simulation cell. However, the zero value at the horizontal axis in the density profiles obtained from ITIM analysis corresponds to the position of the probe sphere along the test line where it was stopped for the first time by an atom at the liquid – vapor interface. The density profiles of the terminal carbon atoms (CT) of the octyl chains of [omim] cations along the interface normal

(z-axis) in different systems studied are presented in Figure 3.1. As the number of [omim] cations vary with changing composition of the binary mixtures studied, the density profiles are scaled accordingly.

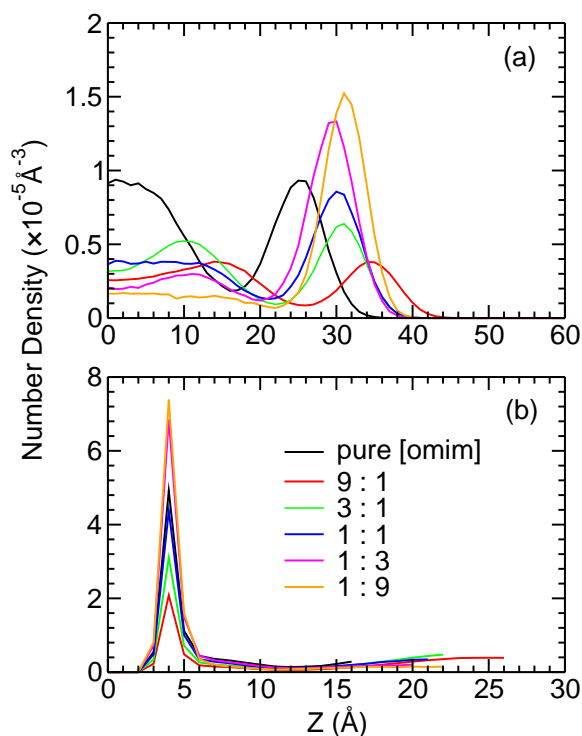


Figure 3.1: Number density profiles of terminal carbon atoms (CT) of [omim] cations in binary IL mixtures obtained from (a) the global definition of the interface and (b) ITIM analysis. The zero value at the horizontal axis in figure (a) represent the center of the simulation cell whereas in figure (b), it corresponds to the position of the probe sphere along the test line where it was stopped for the first time by an atom at the liquid – vapor interface

The number density profiles of CT atoms from the global definition of the interface in Figure 3.1(a) show well-defined minima and maxima across the entire composition range. We observe that there is enrichment of the interface with [omim] cations. The presence of octyl chain at the interface facilitates the dispersion interactions between the alkyl chains which is supported by the preferred parallel orientation of the octyl chains (present in the interfacial region) with each other [27] while simultaneously reducing the surface energy density. Comparing the bulk number density of CT atoms to the number density at the first maxima, we found that there is a greater increase in the number density of CT atoms at the liquid – vapor interface with decrease in the mole fraction of the [omim] cations. The ratio of the number density of CT atoms at the first

maxima to the bulk number density increases from 1.0 in case of pure [omim][TfO] to 9.0 in case of 1:9 [omim][TfO] – [emim][TfO] binary mixture. The number density profiles of CT atoms obtained from the ITIM method (Figure 3.1(b)) also supports the enrichment of [omim] cations at the liquid – vapor interface compared to the bulk region with decrease in the mole fraction of [omim] cations. Using intrinsic interface, the ratio of the number density of CT atoms at the first maxima to the bulk number density was found to increase from ~ 9.0 for 9:1 binary mixture to ~ 55.0 for 1:9 binary mixture. From these observations, it is evident that the probability of an octyl chain of the [omim] cation to be present at the surface increases with decrease in the mole fraction of the [omim] cation in the binary IL mixtures. This observation can be attributed to the decrease in competition among the [omim] cations to occupy the interfacial region with decrease in their numbers in the mixtures. The number density profile of CT atoms in pure [omim][TfO] obtained from the ITIM method shows ~ 25.0 times enhancement at the liquid – vapor interface compared to the bulk region. The number density enhancement at the liquid – vapor interface is less when the global definition is used as it is averaged over the fixed Cartesian frame of reference. ITIM method in which instantaneous interface is considered provides a better picture of the interface.

The number density profiles of the terminal carbon atoms (CE) of the ethyl chains of [emim] cations in binary IL mixtures of various composition, obtained from both the global definition of the interface and the ITIM method are shown in Figure 3.2.

The number density profiles of CE atoms obtained from the global definition (Figure 3.2(a)) show very less fluctuation at the liquid – vapor interface compared to the bulk region, leading to the absence of any distinguishable minima and maxima. However, the density profiles of CE atoms obtained from the ITIM method (Figure 3.2(b)) show gradual increase in the number density at the liquid – vapor interface compared to the bulk region with increase in the mole fraction of [emim] cations in the binary mixtures. The ratio of the number density of CE atoms at the liquid – vapor interface to the bulk number density increases from ~ 0.4 for 9:1 binary IL mixture to ~ 3.5 for pure [emim][TfO], leading to the gradual pronouncement in the formation of well-defined minima and maxima.

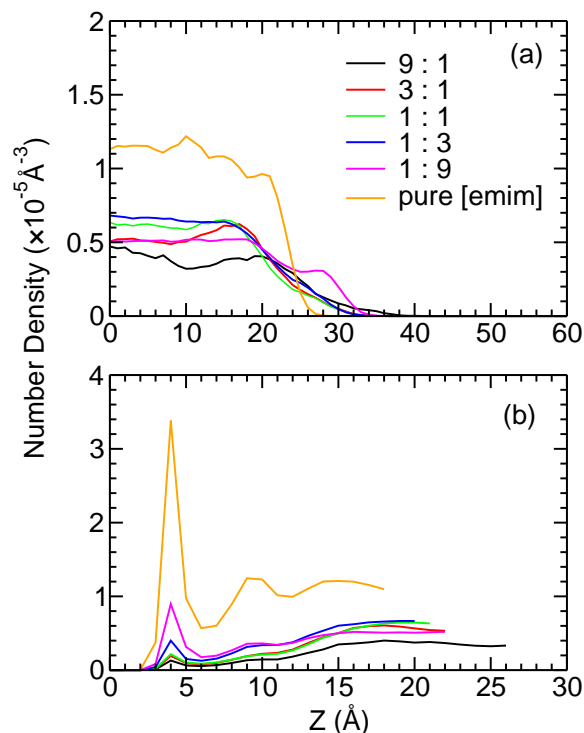


Figure 3.2: Number density profiles of the terminal carbon atoms (CE) of [emim] cations in binary IL mixtures, obtained from (a) the global definition and (b) ITIM analysis. The zero value at the horizontal axis in figure (a) represents the center of the simulation cell whereas in figure (b), it corresponds to the position of the probe sphere along the test line where it was stopped for the first time by an atom at the liquid – vapor interface

The number density profiles of sulfur atoms (S) of triflate anions based on the global definition of the interface (Figure 3.3(a)) show almost similar trend as those of CE atoms. In pure [omim][TfO] system there is ~ 2.0 times increase in density at the liquid – vapor interface compared to the bulk region. However, the ITIM analysis (Figure 3.3(b)) has shown a gradual increase in the ratio of the number density of S atoms at the liquid – vapor interface to the bulk number density from ~ 0.6 for pure [omim][TfO] to ~ 3.0 for pure [emim][TfO]. The increase in the ratio of the number density at the interface to the bulk number density for [emim] and [TfO] moieties with decrease in the mole fraction of [omim] cations can be attributed to the decrease in competition with longer alkyl chain cations to occupy the liquid – vapor interface.

The CT number density profiles, in the Cartesian frame of reference with the center of mass at the origin, show well defined minima in all the systems. We have defined the region beyond this point towards the vapor phase as interfacial region. For pure [emim][TfO] system, although

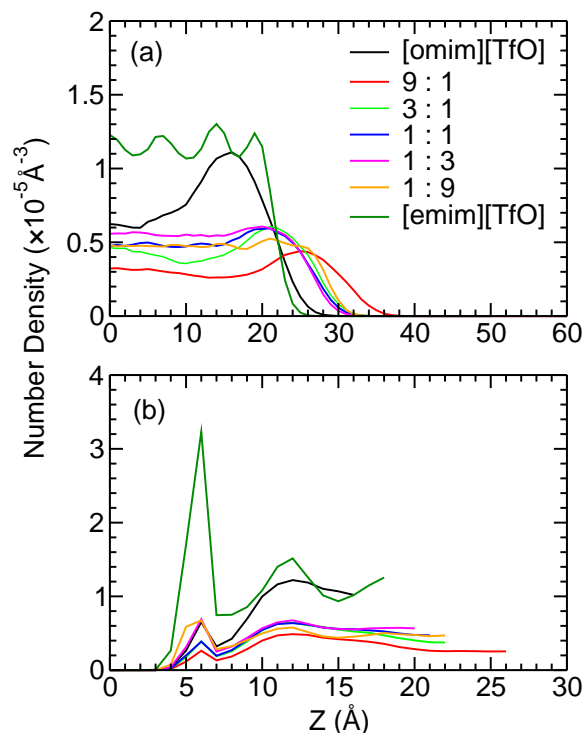


Figure 3.3: Number density profiles of sulfur atoms (S) of [TfO] anions in binary IL mixtures obtained from (a) the global definition and (b) ITIM analysis. The zero value at the horizontal axis in figure (a) represents the center of the simulation cell whereas in figure (b), it corresponds to the position of the probe sphere along the test line where it was stopped for the first time by an atom at the liquid – vapor interface

we do not observe such well defined minima in the CE number density profile from the global definition of the interface, we see the presence of a very weak minima at 18.0 Å. So we have defined the interfacial region for pure [emim][TfO] system as the region beyond 18.0 Å towards the vapor phase. If any of the atoms of an ion (anion or cation) is within this region, then the ion is considered to be present in the interface.

3.3.2 Surface composition

The surface composition of different systems studied is expressed in terms of the mole fractions of different ions present at the interface. Table 3.2 presents the surface fraction of different ions present in the interfacial region calculated as an average over the last 5 ns of the trajectory in binary IL mixtures of varying composition. The surface fractions of the ions determined from the ITIM analysis are given in parentheses.

Table 3.2: Surface fractions of ions in the interfacial region of IL mixtures of varying composition.

System	[omim]	[emim]	[TfO]
pure [omim][TfO]	0.54(0.77)	–	0.46(0.23)
9:1	0.53(0.75)	0.02(0.01)	0.45(0.24)
3:1	0.48(0.56)	0.06(0.06)	0.46(0.38)
1:1	0.41(0.50)	0.12(0.11)	0.47(0.39)
1:3	0.27(0.33)	0.25(0.24)	0.48(0.43)
1:9	0.13(0.16)	0.39(0.40)	0.48(0.44)
pure [emim][TfO]	–	0.52(0.53)	0.48(0.47)

The surface fractions of ions in the 1:1 binary mixture computed from last 5 ns of 30 ns trajectory by using the dividing surface definition of the interface were similar to those reported here [27]. We see that the surface fraction of [omim] cations decreases from 0.54 in pure [omim][TfO] system to 0.13 in 1:9 binary IL mixture, based on the global definition of the interface. This trend is also observed from ITIM method but the values of surface fractions obtained from ITIM analysis are higher. With decrease in number of [omim] cations in the system, the difference in surface fraction of [omim] cations obtained from ITIM method and the global interface definition decreases. The surface fraction of [emim] cations increases from 0.02 in 9:1 IL mixture to 0.52 in pure [emim][TfO]. In case of [emim] cations, the surface fraction values obtained using the global definition and ITIM method are almost same. Although the surface fraction of [TfO] anions obtained using the global definition remains almost constant across the composition range, ITIM method shows a gradual increase in the surface fraction of [TfO] anions from 0.23 in pure [omim][TfO] to 0.47 in pure [emim][TfO]. Also in case of [TfO] anions, the difference in surface fraction of [TfO] anions obtained from ITIM method and using the global definition decreases with decrease in the mole fraction of [omim] cations in the system. In a nutshell, we can conclude that the surface fraction of [omim] cations increases while the surface fraction of [emim] cations and [TfO] anions decreases with increase in the mole fraction of [omim] cations in the system. This observation can be attributed to the greater availability of interfacial region for [emim] cations and [TfO] anions with decrease in the number of [omim] cations in the system.

3.3.3 Surface tension

The surface tension γ of the liquid – vapor interface was calculated from the diagonal components of pressure tensor P_{ii} using the formula [38]

$$\gamma = -b_z(P_{xx} + P_{yy} - 2P_{zz})/4 \quad (3.1)$$

where b_z is the length of the super-cell along the interface normal (z-axis). The factor 2 has been introduced in the denominator to account for the presence of two equivalent interfaces. Figure 3.4 shows the surface tension of the binary mixtures at various mole fraction of [omim] cations. The

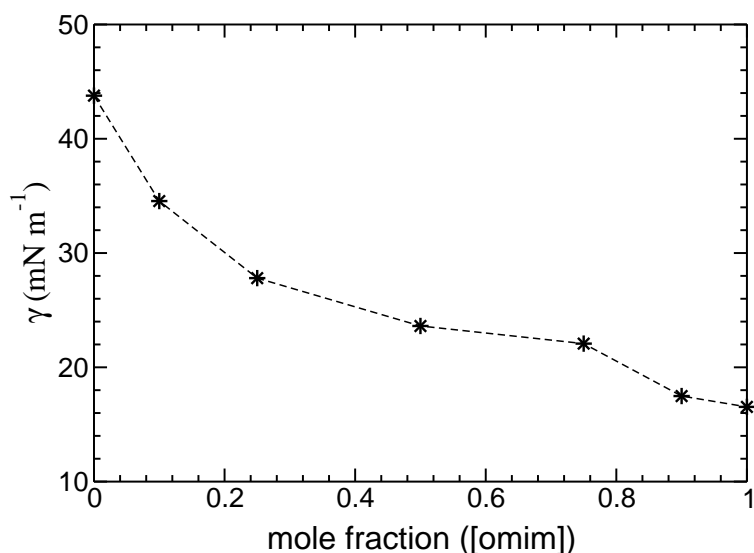


Figure 3.4: Surface tension(γ) of binary mixtures at various mole fraction of [omim] cations.

surface tension of pure [emim][TfO] and pure [omim][TfO] were calculated to be 43.8 mN m^{-1} and 16.5 mN m^{-1} respectively. If we look at figure 3.4, we see the decrease in surface tension of the IL mixtures with increase in the mole fraction of [omim] cations. This decrease is consistent with the increase in surface fraction of [omim] cations with increase in their mole fraction as seen from Table 3.2. In other words, surface enrichment by longer alkyl chain [omim] cations causes decrease in surface tension of the liquid – vapor interface.

3.3.4 Surface roughness

In ITIM analysis, the surface points are defined as the positions of the probe spheres along the test lines where they are stopped for the first time by atoms at the liquid – vapor interface. The

dependence of average normal distance of two surface points, $\langle d \rangle$ in the z -axis, on their lateral separation, l in the xy -plane characterizes the surface roughness of the liquid – vapor interface [35, 39, 40]. Figure 3.5 presents the variation of vertical separation of two surface points, $\langle d \rangle$, with their lateral separation, l in binary IL mixtures of varying composition. Observing the initial sharp

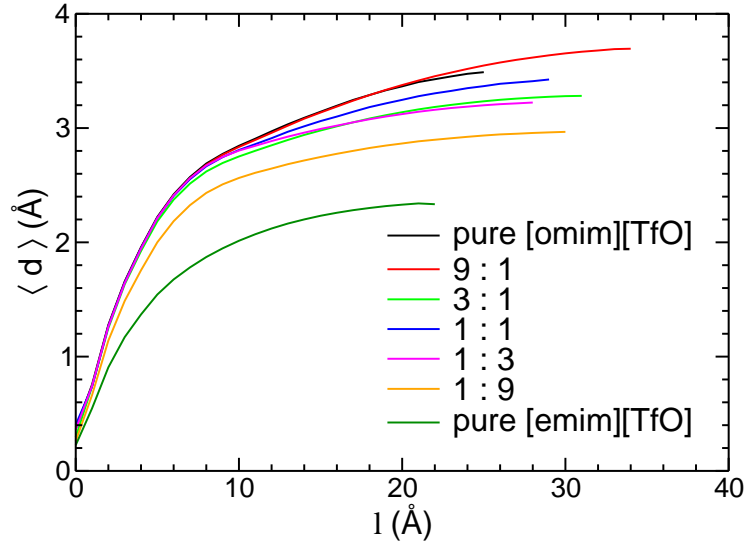


Figure 3.5: Variation of normal distance of two surface points, $\langle d \rangle$ with their lateral separation l in different binary IL mixtures studied.

increase of $\langle d \rangle$ at small l followed by the appearance of plateau like region at large l , the following equation has been employed to fit the $\langle d \rangle$ versus l curve [39, 40].

$$\langle d \rangle = \frac{a\xi l^b}{a + \xi l^b} \quad (3.2)$$

where a represents the amplitude of the surface roughness and ξ and b are frequency like parameters of the surface roughness. Table 3.3 summarizes the parameters associated with the surface roughness of the different systems studied. From Table 3.3, we see that the surface of pure [emim][TfO] is smoother than pure [omim][TfO] which implies that the presence of longer alkyl chain of [omim] cation makes the surface rougher compared to the presence of shorter alkyl chain of [emim] cation. Comparing the surface roughness parameters, it is evident that the surface roughness of the interface of 9:1 IL mixture is close to that of pure [omim][TfO] system and that of 1:9 IL mixture is close to that pure [emim][TfO] system. The values of the surface roughness parameters for the rest of the systems fall in between pure [omim][TfO] and pure [emim][TfO].

Table 3.3: Amplitude of the surface roughness, a and frequency-like parameters of the surface roughness, ξ and b of the $\langle d \rangle$ versus l curve of the liquid – vapor interface for binary IL mixtures.

System	$a(\text{\AA})$	ξ	b
pure [omim][TfO]	4.052	0.938	1.014
9:1	4.306	0.969	0.934
3:1	3.555	0.898	1.133
1:1	3.789	0.921	1.072
1:3	3.430	0.860	1.230
1:9	3.162	0.761	1.234
pure [emim][TfO]	2.754	0.645	1.06

Investigation of the various ripples of surface gives a vivid picture of the surface roughness of the liquid – vapor interface [39, 40]. For this purpose, we have evaluated the probability $P(l, d)$ of bivariate distribution between lateral distance l and normal distance d of two surface points. Figure 3.6 presents the $P(l, d)$ distribution of 9:1, 1:1 and 1:9 IL mixture. We observe that with increase in lateral distance l between two surface points, the spread in their vertical separation also increases. Nevertheless, we observe that at larger lateral separation, the most probable vertical separation is lying in the range of 2.5 – 4.0 Å irrespective of the composition of the systems studied (Figure B.1, Appendix B).

3.3.5 Survival probability.

The probability, $L(t)$, of a cation ([omim] or [emim]) or an anion ([TfO]) to be found in the interfacial layer at time t_0 and t_0+t gives an idea about the mean lifetime of that ion in the interfacial layer [39, 40]. $L(t)$ corresponds to the intermittent survival probability [41]. $L(t)$ for the cations([omim] or [emim]) and anion([TfO]) are shown in Figure 3.7. We observe a sharp fall in all the time correlation functions (TCFs) for a very short period of 5 – 10 ps followed by a steady fall at larger observation time. The computed TCFs are fitted by a sum of two stretched exponential decay functions [42]

$$L(t) = a_1 \exp(-(t/\tau_1)^{\beta_1}) + a_2 \exp(-(t/\tau_2)^{\beta_2}) \quad (3.3)$$

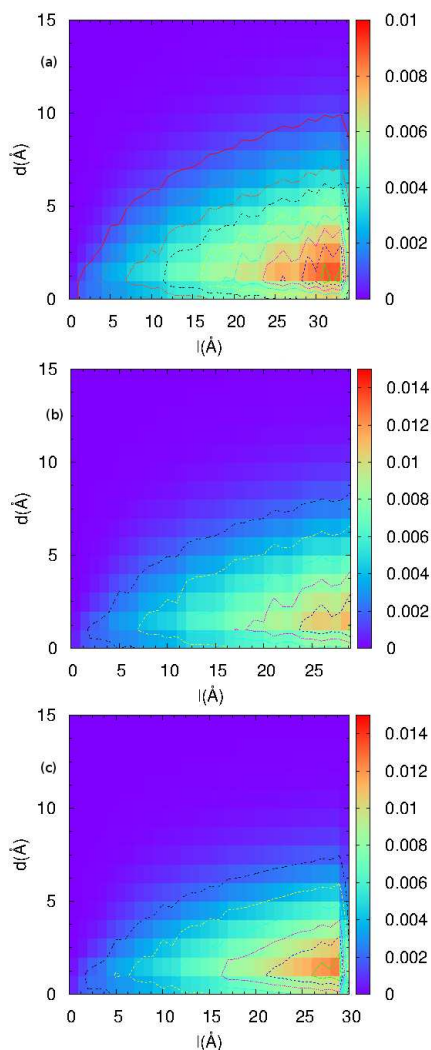


Figure 3.6: Bivariate distribution of the probability of the lateral distance l and the normal distance d of two surface points for (a) 9:1 (b) 1:1 and (c) 1:9 binary IL mixture.

where τ_1 and τ_2 are the residence time associated with two exponential functions, a_1 and a_2 are the contributions from the individual terms and β s stand for stretched exponents. The average residence time $\langle \tau_s \rangle$ can be expressed as the weighted average of τ_1 and τ_2 as follows:

$$\langle \tau_s \rangle = a_1 \tau_1 + a_2 \tau_2 \quad (3.4)$$

We have fitted the curves up to 10 ns of elapsed time. The fitted parameters are listed in Table 3.4.

For binary IL mixtures of varying composition, we observe a gradual increase in the average survival time of [omim] cation in the interfacial layer with decrease in the mole fraction of [omim]

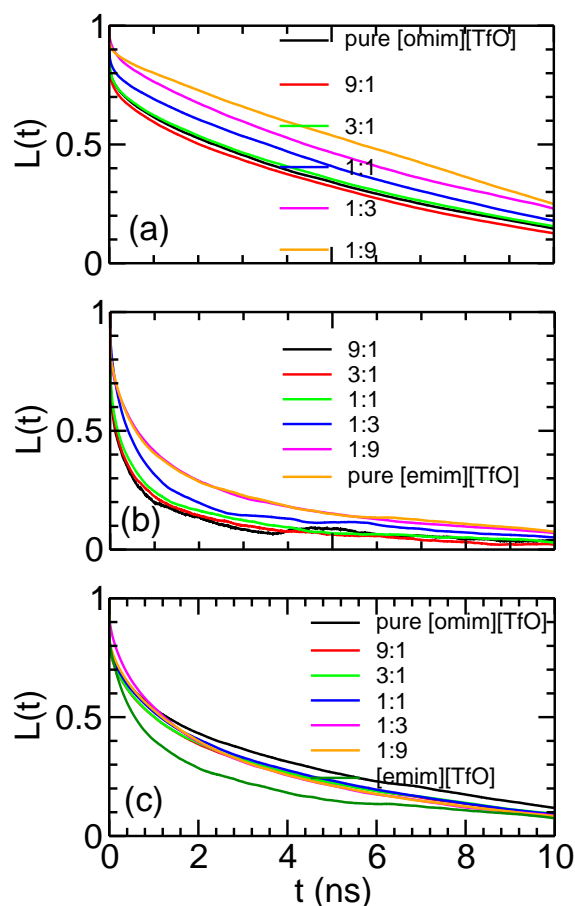


Figure 3.7: Survival probability of (a) [omim] (b) [emim] and (c) [TfO] in the interfacial layer of the systems of varying composition.

cation. As the number of [omim] cations in the IL mixture decreases, the probability of an [omim] cation to get displaced from the interfacial layer by another [omim] cation which is beneath the interfacial layer decreases, leading to a greater probability to see an [omim] cation in the interfacial layer for a longer time. The average residence time of [omim] cation in pure [omim][TfO] was calculated to be 4.75 ns. The shorter lifetime term (τ_1) along with its contribution (a_1) to the total survival time ($\langle\tau_s\rangle$) decreases whereas the longer lifetime term (τ_2) along with its contribution (a_2) to the total survival time ($\langle\tau_s\rangle$) increases with decrease in [omim] mole fraction in the IL mixtures studied.

The average lifetime of [emim] cation gradually increases from 0.28 ns for 9:1 IL mixture to 1.94 ns in pure [emim][TfO] system. [emim] cation, being more polar than [omim] cation, shows less tendency to occupy the liquid – vapor interface. However, with decrease in mole fraction of

Table 3.4: Parameters of the stretched exponential fit to the average survival time correlation function.

Ion	System	a_1	τ_1 (ns)	β_1	a_2	τ_2 (ns)	β_2	$\langle\tau_s\rangle$ (ns)
[omim]	1:0	0.27	0.03	0.36	0.71	6.67	1.0	4.75
	9:1	0.28	0.02	0.38	0.70	6.25	1.0	4.38
	3:1	0.26	0.02	0.38	0.72	6.87	1.0	4.97
	1:1	0.19	0.01	0.47	0.81	7.15	1.0	5.77
	1:3	0.18	0.009	0.33	0.87	7.83	1.0	6.81
	1:9	0.09	0.003	0.60	0.91	8.88	1.0	8.10
[emim]	9:1	0.79	0.21	0.28	0.19	0.61	1.0	0.28
	3:1	0.14	3.0×10^{-5}	0.79	0.87	0.51	0.43	0.45
	1:1	0.19	2.0×10^{-5}	0.06	0.81	0.59	0.47	0.47
	1:3	0.21	0.1	0.05	0.9	0.65	0.56	0.61
	1:9	0.16	3.0×10^{-6}	0.03	0.84	1.46	0.57	1.23
	0:1	0.70	0.21	0.49	0.20	8.91	1.0	1.94
[TfO]	1:0	0.42	0.67	0.47	0.47	7.24	1.0	3.67
	9:1	0.45	0.73	0.51	0.42	6.34	1.0	2.99
	3:1	0.52	1.0	0.49	0.36	6.41	1.0	2.82
	1:1	0.44	0.80	0.50	0.44	6.05	1.0	3.01
	1:3	0.11	0.005	0.19	0.89	2.72	0.64	2.41
	1:9	0.19	0.0002	0.17	0.81	3.26	0.70	2.64
	0:1	0.15	0.87	0.89	0.78	1.76	0.46	1.50

[omim] cation in the system, the interfacial layer offers more unoccupied surface area to [emim] cation. As a result, the average lifetime of [emim] cation increases with increase in mole fraction of [emim] cation in the systems studied. The average residence time of [TfO] anion remains in the range of 2.45 – 3.7 ns in all the mixtures studied. The average lifetime $\langle\tau_s\rangle$, for the different ions present in any of the the IL mixtures follows the order as [omim] > [TfO] > [emim] as exemplified by the 1:1 mixture in Figure 3.8.

3.3.6 Re-orientation Dynamics

Orientational relaxation is quantified by orientational TCFs, $C_I(t)$. Usually, $C_I(t)$ is defined as

$$C_I(t) = \frac{1}{N} \sum_{i=1}^N \langle e_i(t) \cdot e_i(0) \rangle \quad (3.5)$$

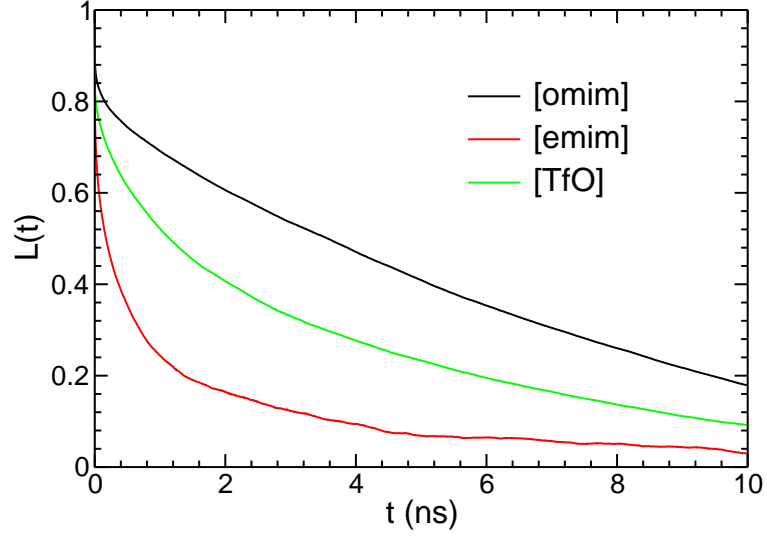


Figure 3.8: Survival probability of (a)[omim] (b)[emim] and (c)[TfO] in the interfacial layer for the 1:1 IL mixture.

where e_i stands for an unit vector corresponding to the i -th species. In our present study, we have decomposed the three dimensional rotation of an unit vector belonging to a species present in the interfacial layer into three orthogonal components, i.e., on the xy -, yz - and zx - planes in the Cartesian coordinate system. We have computed three distinct TCFs (C_{xy} , C_{yz} and C_{zx}) corresponding to the rotation on three orthogonal planes along with the TCF (C_{xyz}) taking care of the rotation in the three dimensional space. In calculating the TCFs, we have considered the species that are in the interfacial layer at $t = 0$. The computed TCFs are best fitted by the combination of two stretched exponential decay functions [43]

$$C_l(t) = a_1 \exp(-(t/\tau_1)^{\beta_1}) + a_2 \exp(-(t/\tau_2)^{\beta_2}) \quad (3.6)$$

where τ_1 and τ_2 are the re-orientation time or relaxation time associated with two exponential functions, a_1 and a_2 are the contributions from the individual terms and β s stand for stretched exponents. The curves have been fitted up to 10 ns of elapsed time. The average re-orientation time, $\langle \tau_r \rangle$ can be expressed as the weighted average of τ_1 and τ_2 (from equation 3.6) as follows:

$$\langle \tau_r \rangle = a_1 \tau_1 + a_2 \tau_2 \quad (3.7)$$

The fitted parameters for $C_{xyz}(t)$, $C_{xy}(t)$, $C_{yz}(t)$ and $C_{zx}(t)$ are provided as supporting information (Tables S1, S2, S3 and S4. Electronic supplementary information).

Table 3.5: Average reorientation time $\langle \tau_r \rangle$ for the ions obtained from the reorientational TCFs.

Ion	System	$\langle \tau_r \rangle$ (ns)			
		$C_{xyz}(t)$	$C_{xy}(t)$	$C_{yz}(t)$	$C_{zx}(t)$
[omim]	1:0	0.18	0.06	3.34	3.02
	9:1	0.12	0.07	3.19	3.15
	3:1	0.09	0.07	4.18	3.82
	1:1	0.10	0.06	11.95	11.80
	1:3	0.03	0.02	15.55	13.19
	1:9	0.05	0.03	60.33	71.98
	0:1	0.01	0.01	0.02	0.02
[emim]	9:1	0.04	0.03	0.04	0.06
	3:1	0.03	0.03	0.05	0.06
	1:1	0.03	0.03	0.04	0.06
	1:3	0.02	0.02	0.03	0.03
	1:9	0.03	0.02	0.04	0.05
	0:1	0.01	0.01	0.02	0.02
	0:1	0.01	0.01	0.02	0.02
[TfO]	1:0	0.01	0.02	0.12	0.12
	9:1	0.04	0.02	0.12	0.10
	3:1	0.01	0.01	0.07	0.10
	1:1	0.01	0.02	0.04	0.04
	1:3	0.01	0.01	0.03	0.02
	1:9	0.005	0.003	0.17	0.10
	0:1	0.003	0.01	0.87	0.90

Figure 3.9 shows time evolution of $C_{xyz}(t)$, $C_{xy}(t)$, $C_{yz}(t)$ and $C_{zx}(t)$ of different vectors for 1:1 IL mixture. The major contribution to the decay of the TCFs $C_{xyz}(t)$ and $C_{xy}(t)$ for octyl chain vector of [omim] cation (Figure 3.9(a)) is from the rapid initial decay with a very short relaxation time. Relatively slower decay with a longer relaxation time accounts for the remaining decay of these TCFs. The slower re-orientation on the yz- and zx-planes can be attributed to the tendency of the octyl chains to retain the parallel orientation with respect to the interface normal for a longer time. However, rotation on the interface (xy-plane) does not hinder the retention of orientation of the octyl chains with respect to the interface normal. As a result, $C_{xy}(t)$ relaxes rapidly and the total rotation is mainly governed by the rotation on the interface. We see that all the four re-orientation TCFs for ethyl chain of [emim] cation (Figure 3.9(b)) relaxes very rapidly with slightly longer $\langle \tau_r \rangle$ associated with rotation on yz- and zx-planes. It is evident that the ethyl chain vectors

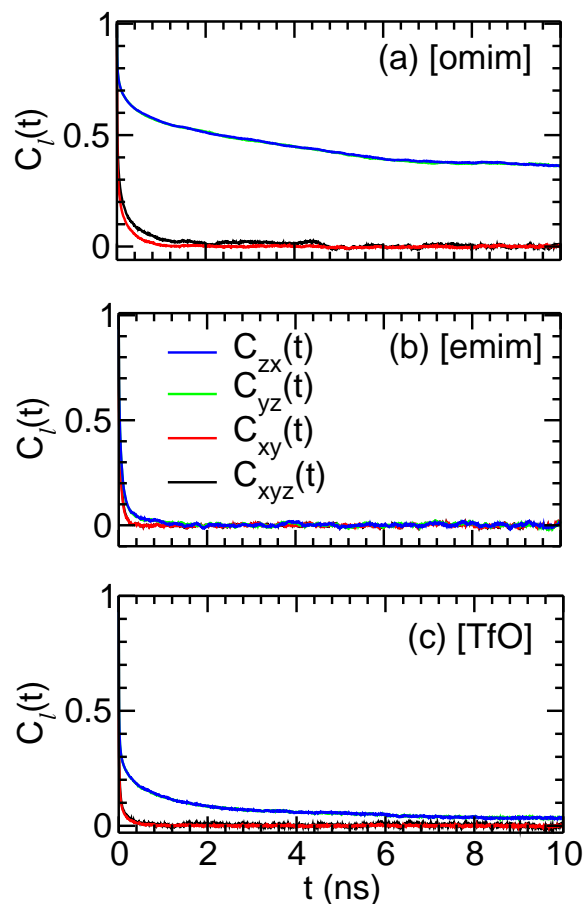


Figure 3.9: Different re-orientation TCFs of (a)[omim] (b)[emim] and (c)[TfO] in the interfacial layer for the 1:1 IL mixture.

undergo very rapid rotation in all directions. The TCFs for carbon – sulfur bond vectors of [TfO] anions (Figure 3.9(c)) show similar behavior as the [omim] cations, except that the rotation of the vectors on the planes orthogonal to the interface is less restricted compared to [omim] cations. The re-orientational TCFs in other binary mixtures with different composition also exhibit similar behavior.

Figure 3.10(a) shows the rotational relaxation ($C_{zx}(t)$) of octyl chain of [omim] cation in systems of varying composition on the zx plane. We observe that $C_{zx}(t)$ for [omim] cation in all the systems is mainly characterized by a very slow relaxation. The average re-orientation time $\langle\tau_r\rangle$ for rotation of octyl chain on zx -plane increases with decrease in mole fraction of [omim] cations in the systems studied (Table 3.5). There is a direct correlation between $\langle\tau_r\rangle$ and $\langle\tau_s\rangle$. [omim] cations with longer residence time at the interface have a tendency to retain their orientation with

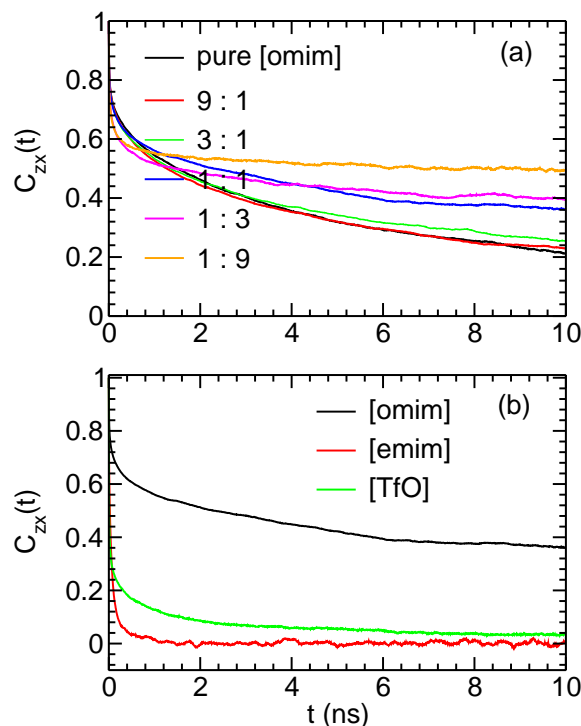


Figure 3.10: Variation of $C_{zx}(t)$ (a) for octyl chain of [omim] cation across the entire composition range and (b) octyl chain of [omim] cation, ethyl chain of [emim] cation and carbon – sulfur bond vector of [TfO] anion for the 1:1 IL mixture in the interfacial layer.

respect to the interface normal for a longer time and hence will have slower re-orientation on a plane orthogonal to the interface. Similar trend is observed in $C_{yz}(t)$ (Figure B.2, Appendix B). $\langle \tau_r \rangle$ for ethyl vectors for the rotation on orthogonal planes with respect to the interface remain almost constant across the entire composition range (Figure B.3, Appendix B). $\langle \tau_r \rangle$ for carbon – sulfur bond vector also does not vary systematically or significantly for rotation on planes orthogonal to the interface. It is observed to remain almost constant across the entire composition range (Figure B.4, Appendix B).

3.3.7 Dynamics of rotation

To investigate the dynamics of rotation, we have decomposed the rotation of an unit vector representing an ion present in the interfacial layer into two components. One of the components corresponds to the angular displacement with respect to the interface normal(z-axis) and the other one corresponds to the rotation about the z-axis, i.e., on the interface (xy-plane). For this purpose,

we have evaluated two distinct TCFs defined as

$$C_z(t) = \frac{1}{N} \sum_{i=1}^N \langle \cos \theta(t) \cos \theta(0) \rangle \quad (3.8)$$

$$C_{xy}(t) = \frac{1}{N} \sum_{i=1}^N \langle \cos \phi(t) \cos \phi(0) \rangle \quad (3.9)$$

where $\cos \theta$ corresponds to the angle formed by the unit vectors associated with the octyl chain of [omim] cation, ethyl chain of [emim] cation and carbon – sulfur bond vector of [TfO] anion with the z-axis and $\cos \phi$ corresponds to the angle formed by the projection of the aforementioned unit vectors on the xy-plane with the x-axis. In calculating TCFs we have considered the ions that were in the interfacial layer at $t = 0$. Figure 3.11 shows the $C_z(t)$ and $C_{xy}(t)$ of different vectors for 1:1 IL mixture. We see that both $C_z(t)$ and $C_{xy}(t)$ for different ions (figure 3.11) exhibit a fast exponential

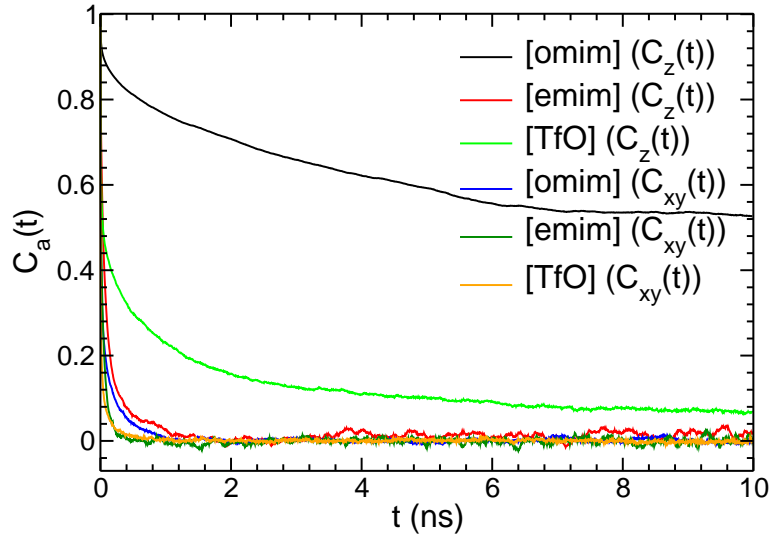


Figure 3.11: Dynamical correlation function of (a)[omim] (b)[emim] and (c)[TfO] in the interfacial layer for the 1:1 IL mixture.

decay followed by a very slow relaxation region. $C_z(t)$ for octyl chain has decayed only ~ 50 at the end of 10 ns which suggest that [omim] cation present in the interfacial layer prefer to retain the orientation of the octyl chain with respect to the interface normal for a long time. The dynamics of rotation of the carbon – sulfur bond vector of [TfO] anion with respect to the z-axis ($C_z(t)$) is faster than that observed for octyl chain and $C_z(t)$ decays to zero even faster for the ethyl chains. The trend in $C_z(t)$ for different molecular vectors in 1:1 IL mixture correlates with the average survival time of that molecular species in the interfacial layer as shown in table 3.4, i.e., larger the

survival probability, the longer will be the time required for orientational relaxation with respect to the interface normal. However, the TCFs for the rotation of the projection vectors of the octyl chain, ethyl chain and carbon – sulfur bond on the xy -plane vanishes very rapidly which suggest that these vectors can rotate freely on the interface. $C_z(t)$ for [emim] cation is only marginally higher than $C_{xy}(t)$ suggesting that [emim] cations can undergo both in-plane (on the xy -plane) and out-of-plane (perpendicular to the xy -plane) rotation quite easily. Observing the variation in $C_z(t)$ and in $C_{xy}(t)$ among the different vectors, we propose that out-of-plane rotation, i.e., rotation perpendicular to the interface, facilitates the movement of ions in and out of the interfacial layer and governs the survival probability of the ions at the interface.

Figure 3.12 shows the dynamical TCFs of octyl, ethyl and carbon – sulfur bond vectors with respect to the interface normal for binary IL mixtures of varying composition. The initial fast de-

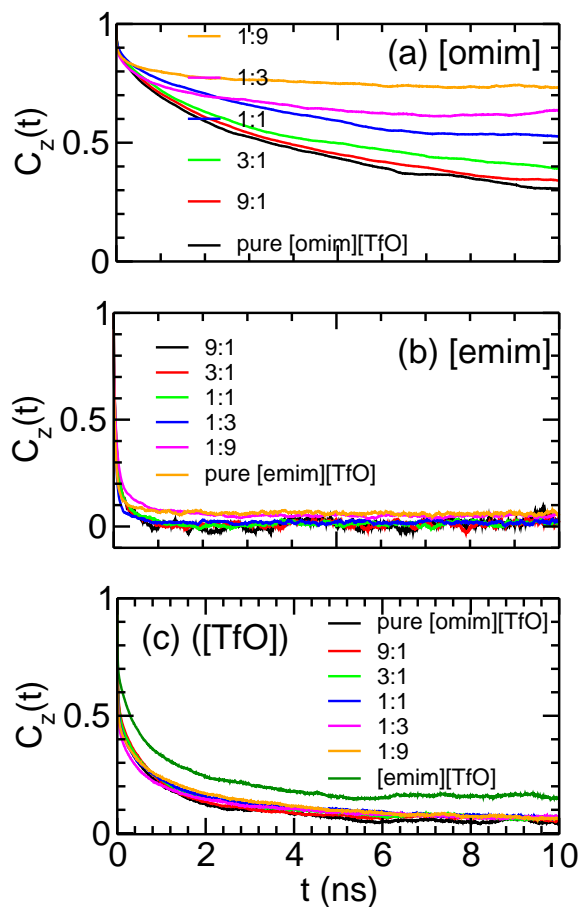


Figure 3.12: $C_z(t)$ for (a)[omim] (b)[emim] and (c)[TfO] in the interfacial layer for the systems of varying composition.

cay of $C_z(t)$ for [omim] ions in Figure 3.12(a) can be attributed to very small but rapid oscillation of octyl chain with respect to the z-axis, which is followed by a slower relaxation region responsible for inversion of the octyl chain from the side of vapor phase to the side of liquid phase with respect to the interface or vice versa. The rate of decay of $C_z(t)$ decreases with decrease in mole fraction of [omim] cation in the mixture. As the number of [omim] cations in the system decreases, there is less competition among them to occupy the interface and hence the cation stays for a longer time in the interface and thus retains its orientation with respect to the z-axis for a longer time. We have also observed that the rate of fall of $C_z(t)$ becomes slightly slower for [emim] and [TfO] with decrease in number of [omim] ions in the systems studied.

Figure 3.13 presents the TCFs, $C_{xy}(t)$ for the rotational motion on the xy plane of the octyl chain, ethyl chain and carbon – sulfur bond vector about the interface normal. We observe a

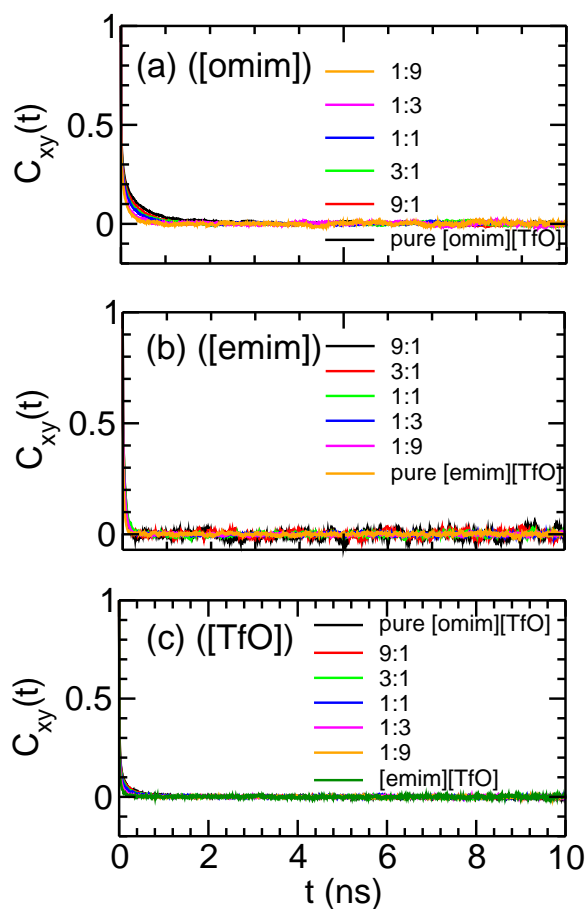


Figure 3.13: Variation in $C_{xy}(t)$ for (a)[omim] (b)[emim] and (c)[TfO] in the interfacial layer for the systems of varying composition.

very rapid decay in correlation for all the ions across the entire composition range. Nevertheless, the rate of initial rapid fall of $C_{xy}(t)$ for [omim] cation decreases with increase in the number of [omim] ions in the system as shown in Figure 3.13(a). With increase in number of [omim] cations in the system, the [omim] ions present in the interfacial layer will experience greater van der Waals interaction with other [omim] ions. Besides, the void space available around an octyl chain will also decrease due greater crowding of [omim] ions in the interfacial layer. These two effects restrict the rotational motion of the octyl chain vectors about the z-axis. The $C_{xy}(t)$ for ethyl chain and carbon – sulfur bond vector shows similar relaxation irrespective of the composition of the mixture.

3.3.8 Interface organization

The orientational profile of octyl chain of [omim] cation, ethyl chain of [emim] cation and carbon – sulfur bond vector of [TfO] anion with respect to the interface normal in 1:1 IL mixture along the interface normal from the center of the simulation cell is shown by bivariate distribution of probability of the Legendre polynomial of first kind (defined as $P_1(\cos \theta) = \cos \theta$) and distance from the center of the simulation cell along the interface normal in Figure 3.14. We see that the probability of the octyl chain, ethyl chain and carbon – sulfur bond vector to be oriented parallel to the interface normal increases as we move from the center of the box to the liquid – vapor interface. We also observe that orientational selectivity of octyl chains with respect to the interface normal is more pronounced than ethyl chains and carbon – sulfur bond vectors. Figure 3.15 shows the bivariate distribution of probability of $P_1(\cos \theta)$ for NN vectors belonging to [omim] cations and [emim] cations and distance from the center of the simulation cell along the interface normal. We find that the NN vectors belonging to [omim] cations show greater orientational selectivity to be aligned parallel to the interface normal from the box center towards the liquid – vapor interface compared to the NN vectors belonging to [emim] cations. This orientational profile is common in all the systems studied (not shown here). These observations suggests that the octyl chain, ethyl chain, carbon – sulfur bond vector and the NN vectors belonging to [omim] cations present at the liquid – vapor interface tend to point towards the vapor phase.

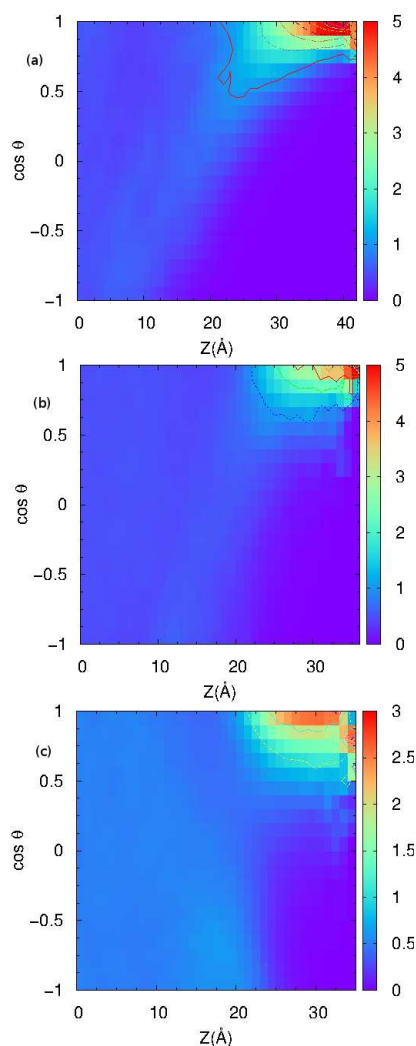


Figure 3.14: Bivariate distribution of probability of $P_1(\cos \theta)$ and distance along the interface normal for (a) octyl chain of [omim] cation (b) ethyl chain of [emim] cation and (c) carbon – sulfur bond vector of [TfO] anion in 1:1 IL mixture.

3.4. Conclusion Atomistic MD simulations have been carried out on binary IL mixtures containing [omim][TfO] and [emim][TfO] of varying composition. We have found an increase in the ratio of number density of the terminal carbon atom of the octyl chain belonging to the [omim] cation at the liquid – vapor interface to its bulk number density with decrease in the mole fraction of [omim] cations. This enhancement in the ratio of the number density at the liquid – vapor interface as calculated from the ITIM method is more compared to that determined from the global definition of the interface. A very weak layering of [emim] and [TfO] ions at the liquid – vapor interface is observed in all the systems, using the global definition of the interface.

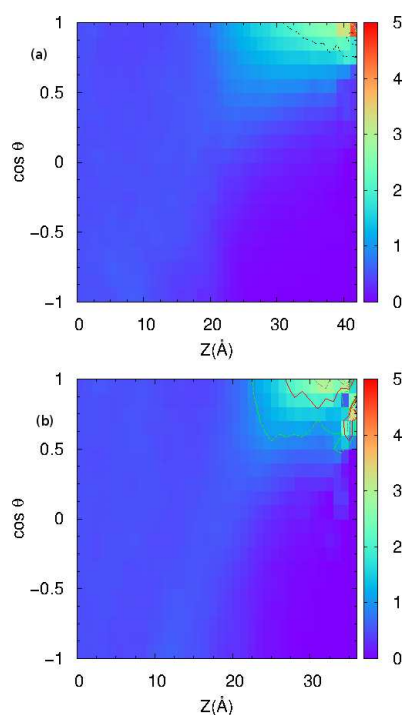


Figure 3.15: Bivariate distribution of probability between $P_1(\cos \theta)$ and distance along the interface normal for (a) NN vector of [omim] cation and (b) NN vector of [emim] cation in 1:1 IL mixture.

However, the ITIM method shows that there is a considerable enhancement in the number density of these ions at the interface compared to the bulk region in pure [emim][TfO] system. The surface roughness of the IL mixtures is determined using the ITIM method. The variation of the vertical separation of two surface points, $\langle d \rangle$, with their lateral separation, l , shows that the surface becomes smoother with increase in the mole fraction of [emim] cations. Surface tension γ of the systems is found to decrease with the increase in the surface fraction of the longer chain [omim] cation in the liquid – vapor interfacial layer. With the decrease in the mole fraction of [omim] cations, the surface fraction of the [omim] cations at the interface is found to decrease whereas that of the [emim] cations increases. The bivariate distribution of probability of the $P_1(\cos \theta)$ and distance from the center of the simulation cell along the interface normal shows that the probability of the octyl chains and NN vectors of the [omim] cations to be oriented parallel to the interface normal increases towards the liquid – vapor interface. The probability for the [omim] cations to be found in the interfacial layer at time t_0 and $t_0 + t$ shows a gradual increase in the average survival

time $\langle\tau_s\rangle$ with decrease in the mole fraction of [omim] cations in binary IL mixtures. The average survival time of [emim] cations in the interfacial layer also increase with decrease in mole fraction of [omim] cations. In all the IL mixtures studied, it was found that the survival probability is highest for the [omim] cations and least for the [emim] cations. The average re-orientation time, $\langle\tau_r\rangle$ for rotation of the projection vectors of the octyl chains of [omim] cations on the planes orthogonal (yz- and xz-planes) to the interface (xy-plane) increases with decrease in mole fraction of [omim] cations. The orientational correlation diminishes very rapidly for the rotation of the projection vectors on the interface which suggests that the octyl chains prefer to retain their orientation with respect to the interface normal for a longer time. A direct correlation is observed between $\langle\tau_r\rangle$ and $\langle\tau_s\rangle$. Analysis of the dynamics of rotation and the relation between the average survival time and the rotational relaxation time suggests that the movement of ions in and out of the interface is facilitated by the out of plane rotation of ions about the interface.

Chapter B

Appendix B

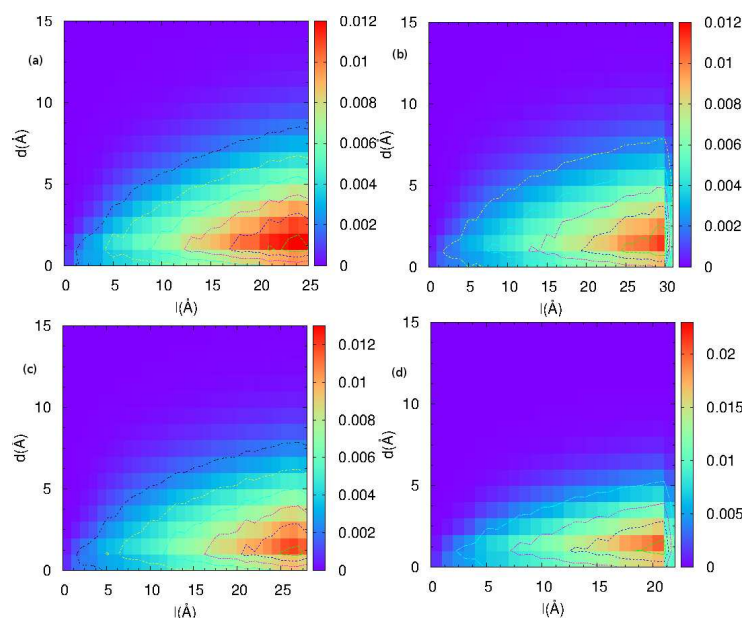


Figure B.1: Bivariate distribution of probability of the lateral distance l and the normal distance d of two surface points for (a) pure [omim][TfO] (b) 3:1 (c) 1:3 and (d) pure [emim][TfO] systems.

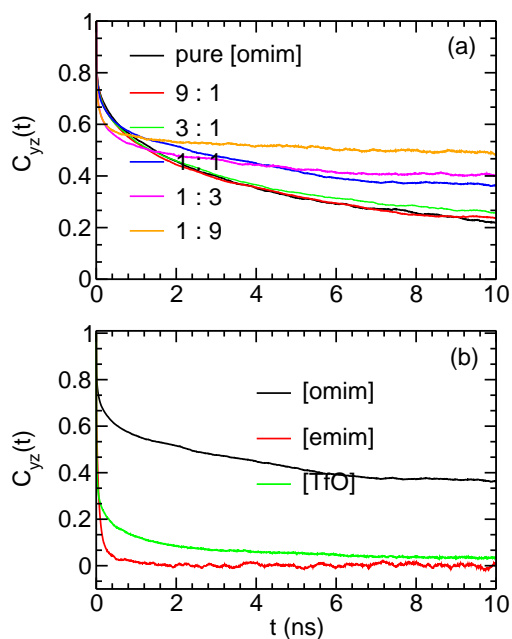


Figure B.2: Variation of $C_{yz}(t)$ (a) for octyl chain of [omim] cation across the entire composition range and (b) octyl chain of [omim] cation, ethyl chain of [emim] cation and carbon – sulfur bond vector of [TfO] anion for the 1:1 IL mixture in the interfacial layer.

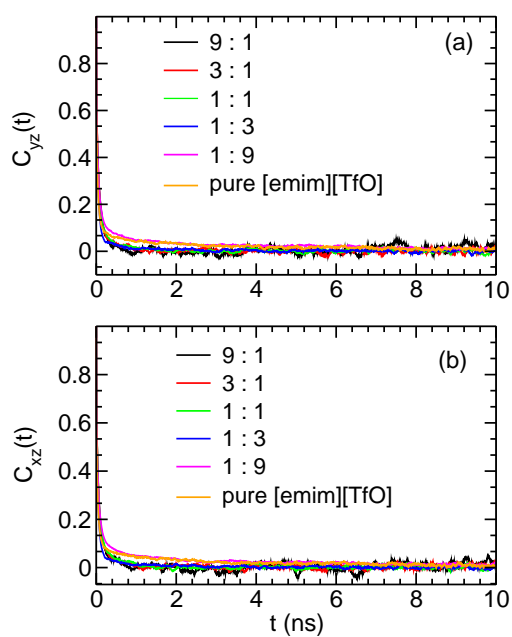


Figure B.3: Variation of (a) $C_{yz}(t)$ and (b) $C_{xz}(t)$ for ethyl chain of [emim] cation across the entire composition range in the interfacial layer.

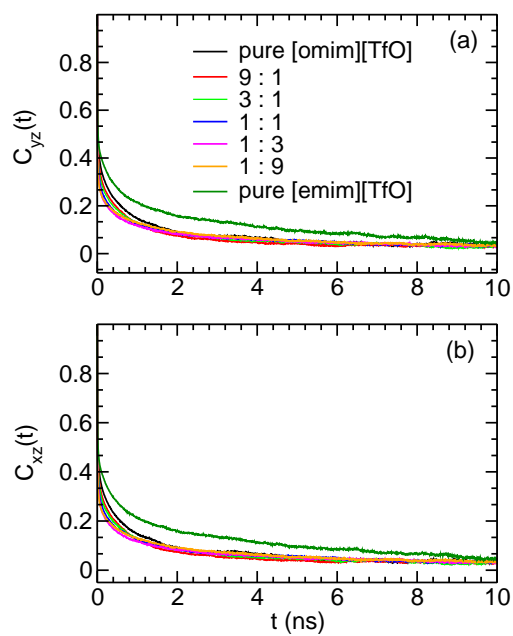


Figure B.4: Variation of (a) $C_{yz}(t)$ and (b) $C_{xz}(t)$ for carbon–sulfur bond vector of [TfO] anion across the entire composition range in the interfacial layer.

Bibliography

- [1] Niedermeyer, H; Hallett, J. P.; Villar-Garcia, I. J.; Hunt, P. A.; Welton, T. *Chem. Soc. Rev.* **2012**, *41*, 7780-7802.
- [2] Chatel, G; Pereira, J. F. B.; Debbeti, V.; Wang, H; Rogers, R. D. *Green Chem.* **2014**, *16*, 2051-2083.
- [3] Chauvin, Y.; Gilbert, B.; Guibard, I. *J. Chem. Soc., Chem. Commun.* **1990**, 1715-1716.
- [4] Chauvin, Y.; Einloft, S.; Olivier, H. *Ind. Eng. Chem. Res.* **1995**, *34*, 1149-1155.
- [5] Simon, L. C.; Dupont, J.; de Souza, R. F. *Appl. Catal., A* **1998**, *175*, 215-220.
- [6] Tominaga, K. *Catal. Today* **2006**, *115*, 70-72.
- [7] Lee, S. H.; Ha, S. H.; Hiep, N. M.; Chang, W.; Koo, Y. *J. Biotechnol.* **2008**, *133*, 486-489.
- [8] Ha, S. H.; Hiep, N. M.; Koo, Y. *Biotechnol. Bioprocess Eng.* **2010**, *15*, 126-130.
- [9] Lin, R.; Taberna, P.; Fantini, S.; Presser, V.; Pérez, C. R.; Malbosc, F.; Rupesinghe, N. L.; Teo, K. B. K.; Gogotsi, Y.; Simon, P. *J. Phys. Chem. Lett.* **2011**, *2*, 2396-2401.
- [10] Armel, V.; Pringle, J. M.; Forsyth, M.; MacFarlane, D. R.; Officer, D. L.; Wagner, P. *Chem. Commun.* **2010**, *46*, 3146-3148.
- [11] Long, J.; Guo, B.; Li, X.; Jiang, Y.; Wang, F.; Tsang, S. C.; Wang, L.; Yu, K. M. K. One Step Catalytic *Green Chem.* **2011**, *13*, 2334-2338.

- [12] Gurau, G.; Wang, H.; Qiao, Y.; Lu, X.; Zhang, S.; Rogers, R. D. *Pure Appl. Chem.* **2012**, *84*, 745-754.
- [13] Katsuta, S.; Yoshimoto, Y.; Okai, M.; Takeda, Y.; Bessho, K. *Ind. Eng. Chem. Res.* **2011**, *50*, 12735-12740.
- [14] Zhao, R.; Wang, X.; Zhang, L.; Wang, S.; Yuan, J. *Anal. Methods* **2011**, *3*, 831-836.
- [15] Pinto, A. M.; Rodríguez, H.; Colón, Y. J.; Arce Jr. A.; Arce, A.; Soto, A. *Ind. Eng. Chem. Res.* **2013**, *52*, 5975-5984.
- [16] Lei, Z.; Han, J.; Zhang, B.; Li, Q.; Zhu, J.; Chen, B. *J. Chem. Eng. Data* **2012**, *57*, 2153-2159.
- [17] Wang, M.; Zhang, L.; Gao, L.; Pi, K.; Zhang, J.; Zheng, C. *Energy Fuels* **2013**, *27*, 461-466.
- [18] Maier, F.; Cremer, T.; Kolbeck, C.; Lovelock, K. R. J.; Paape, N.; Schulz, P. S.; Wasserschied, P.; Steinrück, H. P. *Phys. Chem. Chem. Phys.* **2010**, *12*, 1905-1915.
- [19] Souda, R. *Surf. Sci.* **2010**, *604*, 1694-1697.
- [20] Nakajima, K.; Oshima, S.; Suzuki, M.; Kimura, K. *Surf. Sci.* **2012**, *606*, 1693-1699.
- [21] Nakajima, K.; Miyashita, M.; Suzuki, M.; Kimura, K. *J. Chem. Phys.* **2013**, *139*, 224701.
- [22] Shimizu, K.; Tariq, M.; Rebelo, L. P. N.; Lopes, J. N. C. *J. Mol. Liq.* **2010**, *153*, 52-56.
- [23] Brüssel, M.; Brehm, M.; Voigt, T.; Kirchner, B. *Phys. Chem. Chem. Phys.* **2011**, *13*, 13617-13620.
- [24] Lui, M. Y.; Crowhurst, L.; Hallett, J. P.; Hunt, P. A.; Niedermeyer, H.; Welton, T. *Chem. Sci.* **2011**, *2*, 1491-1496.
- [25] Brüssel, M.; Brehm, M.; Pensado, S.; Malberg, F.; Stark, A.; Kirchner, B. *Phys. Chem. Chem. Phys.* **2012**, *14*, 13204-13215.
- [26] Payal, R. S.; Balasubramanian, S. *Phys. Chem. Chem. Phys.* **2013**, *15*, 21077-21083.

- [27] Palchowdhury, S.; Bhargava, B. L. *Phys. Chem. Chem. Phys.* **2015**, *17*, 19919-19928.
- [28] Li, S.; Feng, G.; Fulvio, P. F.; Hillesheim, P. C.; Liao, C.; Dai, S.; Cummings, T. *J. Phys. Chem. Lett.* **2012**, *3*, 2465-2469.
- [29] Aparicio, S.; Atilhan, M. *J. Phys. Chem. B* **2012**, *116*, 2526-2537.
- [30] Plimpton, S. *J. Comput. Phys.* **1995**, *117*, 1-19.
- [31] Lopes, J. N. C.; Pádua, A. A. H. *J. Phys. Chem. B* **2004**, *108*, 2038-2047; *108*, 11250-11250.
- [32] Lopes, J. N. C.; Pádua, A. A. H. *J. Phys. Chem. B* **2004**, *108*, 16893-16898.
- [33] Allen, M. P.; Tildesley, D. J. *Computer Simulation of Liquids*; Clarendon Press: Oxford, U.K., 1987.
- [34] Humphrey, W.; Dalke, A.; Schulten, K. *J. Mol. Graphics* **1996**, *14*, 33-38.
- [35] Pátay, L. B.; Hantal, G.; Jedlovsky, P.; Vincze, A.; Horvai, G. *J. Comput. Chem.* **2008** *29*, 945-956.
- [36] Jorge, M.; Hantal, G.; Jedlovsky, P.; Cordeiro, M. N. D. S. *J. Phys. Chem. C* **2010**, *114*, 18656-18663.
- [37] Hantal, G.; Voroshylova, I.; Cordeiro, M. N. D. S.; Jorge, M. *Phys. Chem. Chem. Phys.* **2012**, *14*, 5200-5213.
- [38] Rao, M.; Berne, B. J. *Mol. Phys.* **1979**, *37*, 455-461.
- [39] Lisal, M.; Posel, Z.; Izák, P. *Phys. Chem. Chem. Phys.* **2012**, *14*, 5164-5177.
- [40] Lisal, M. *J. Chem. Phys.* **2013**, *139*, 214701.
- [41] Lloyd, E. *Handbook of Applicable Mathematics. Volume II: Probability*, Wiley, New York, 1st edn, 1980.
- [42] Berberan-Santos, M. N.; Bodunov, E. N.; Valeur, B. *Chem. Phys.* **2005**, *315*, 171.

[43] Roy, S; Bagchi, B. *J. Chem. Phys.* **2013**, *139*, 034308.

Chapter 4

Effect of Cation Asymmetry on the Aggregation in Aqueous 1-Alkyl-3-Decylimidazolium Bromide Solutions: Molecular Dynamics Studies

Abstract:

Self assembly of cations in aqueous solutions of 1-alkyl-3-decylimidazolium bromide (with four different alkyl chains, methyl, butyl, heptyl and decyl chain) have been studied using atomistic molecular dynamics simulations. Polydisperse aggregates of cations are formed in the solution with alkyl tails in the core and the polar head groups present at the surface of the aggregates. The shape of the aggregates is dictated by the length of the alkyl chain. Aggregation numbers increase steadily with the increasing alkyl chain length. The greater asymmetry in the two substituent chain length leads to a different surface structure compared to the cations with alkyl chains of similar length.

4.1. Introduction Room temperature ionic liquids (RTILs) have received considerable attention of researchers due to their interesting properties [1, 2] and potential applications [3, 4] in various fields including synthesis, catalysis and electrochemistry. Structure and dynamics of RTILs have been probed extensively using experimental [5, 6, 7] and computational methods [8, 9, 10, 11, 12]. Liquid-vacuum interface of RTILs has also been studied using polarizable and non-polarizable force fields [13]. Binary mixture of ionic liquids (ILs) with CO₂ and water have also been studied [14, 15, 16, 17, 18].

Imidazolium based ILs form a very interesting class due to their specific physicochemical properties [1, 19, 20]. When a hydrocarbon tail, hexyl or longer, is attached to the imidazolium ring, the cations behave as amphiphiles. Due to this structural feature they act as surfactants [21, 22]. Water miscible imidazolium ILs have been studied extensively in their aqueous solutions [23, 24]. These studies are focused on the structure of the aggregates and the properties of the solution above critical aggregation concentration (CAC). It has been found that ILs form aggregates at a lower concentration compared to alkyltrimethylammonium bromide containing similar alkyl chains [25].

Surface active behavior of long chain imidazolium ILs have been studied [21] using surface tension, conductivity and small angle neutron scattering (SANS). The association of ions at higher concentration has been reported for [C₁₀mim][Br] using potentiometric and conductometric methods [26]. Studies focused on the size and shape of the micelles have also been carried out on long chain imidazolium bromide solutions [27, 25]. It is known that ILs with very short alkyl tails (ethyl to butyl) form isotropic solutions on mixing with water whereas those with hexyl or longer chains form aggregates [28, 10]. With increase in the chain length, the aggregates are formed at lower concentration and systems with decyl and longer chains exhibit aggregation at very low concentration. The ability of these compounds to self assemble can be used in the extraction of products from systems containing ILs. The aqueous solution of ILs with single alkyl chain is well studied using experimental [21, 29, 30, 31, 32] and theoretical methods [28, 33, 34, 35].

The presence of second alkyl chain on the imidazolium ring may alter the structure of the

aggregates and aggregation numbers. Recently, double tailed imidazolium based ionic liquids have been reported to show interesting aggregation properties in their aqueous solution [36]. Based on experimental data, it is predicted that the cations in aqueous solution of dioctylimidazolium bromide form aggregates with hydrophobic core and hydrophilic surface consisting of cation rings in a staggered parallel orientation. In the present study we are investigating atomic level details of the bulk and vapor-liquid interface of aqueous solutions of dialkylimidazolium bromide. We have carried out atomistic molecular dynamics (MD) simulations on 1-alkyl,3-decylimidazolium bromide solutions with the alkyl chain ranging from methyl to decyl. We have also investigated the effect of asymmetry of the cations on the structure of the aggregates formed in the solution.

4.2. Methodology and simulation details Aqueous solutions of a series of 1-alkyl,3-decylimidazolium bromide ILs have been studied using classical MD simulations. The simulations were performed using the LAMMPS [37] software with an all atom force field model developed by Pádua and co-workers [38, 39]. The force field parameters for water molecules were adapted from the simple point charge (SPC) model [40]. All the systems studied contained the imidazolium head group with two alkyl chains attached to each of the nitrogen atoms. One of the chains was decyl in all the cases, whereas the other chain was varied to have four different systems with methyl, butyl, heptyl and decyl chains. Table 4.1 presents the details of the systems that have been investigated.

The positions of the atoms were stored every 5 ps which were used for analyses. Initial configurations were prepared by replicating the coordinates of a single ion pair along the three dimensions, which were then combined with a water box with random orientation of water molecules at the experimental density. The water molecules that were within 2.5\AA from any of the atoms of the cation or anion were removed. Isothermal-isobaric ensemble simulations (constant NPT) were performed at 1 atmosphere and 300 K for a period of 2 ns. Volume averaged over the last 1 ns was used to perform canonical ensemble simulations (constant NVT) at 300 K. Vapor-liquid interfaces of the solutions were simulated by extending the box along the z-direction. Initial configurations for these simulations were prepared by taking the final configuration from the re-

Table 4.1: Details of simulations of aqueous $[C_nC_{10}Im][Br]$ solutions, where n is the length of alkyl chain substituent.

n	No. of ion-pairs	No. of water	No. of atoms	Run length (ns)	Box length (Å)	Conc. of IL (M)
10	100	14390	50270	25.0	79.965	0.3247
7	100	12590	43970	25.0	76.491	0.3710
4	100	13373	45419	25.0	77.440	0.3575
1	100	10492	35876	25.0	71.516	0.4539
10	1	1889	5738	25.0	38.892	0.0282
1	100	0	4400	25.0	40.000	–

spective isothermal-isobaric ensemble simulations and extending the box along the z -direction to 120.0Å. Three dimensional periodic boundary conditions were used, simulating the thin liquid film of aqueous IL solutions separated by vacuum. To study the vapor-liquid interface of dilute solution, the box along z -direction was extended to 80.0Å.

Radial distribution functions have been calculated with a fine binwidth of 0.1Å. In the figures, a short hand notation is used to mention a system. For example, C_1 - C_{10} is used instead of $[C_1C_{10}Im][Br]$ solution.

4.3. Results and discussion

4.3.1 Intramolecular structure

Distribution of the angle between the two alkyl chains attached to the nitrogen atoms of the imidazolium ring is shown in figure 4.1. The angle reported in the figure is the angle between the vectors connecting the nitrogen atom and the terminal carbon atom of the alkyl chain attached to it. It is interesting to note that in case of $[C_1C_{10}Im][Br]$ solution, the alkyl chains are preferred to be oriented along opposite direction (making 180° with each other). While in $[C_4C_{10}Im][Br]$ solution the alkyl chains show a very small preference to be oriented either in same or opposite direction, in $[C_7C_{10}Im][Br]$ and $[C_{10}C_{10}Im][Br]$ solutions a very high preference is seen for the chains to be aligned parallel to each other in the same direction (making an angle of 0°) and negligible preference to be aligned in opposite direction. The reasons for such preferences will be discussed in the later section.

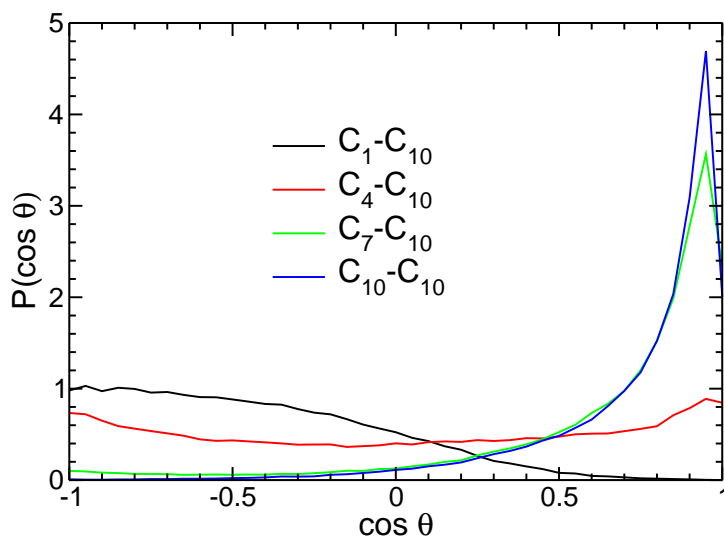


Figure 4.1: Distribution of angle between the two alkyl chains attached to the head group.

4.3.2 Hydrogen bonding

In aqueous solutions of ILs, the dominant interaction between the cations and the anions will be of coulombic nature. Nevertheless, the hydrogen bonding interactions play a significant role in determining the structure of ILs and their solutions. Hydrogen bonds are usually defined by either energetic criteria or geometric criteria. In this study we are using the geometric criteria [44], i.e., the hydrogen atom and acceptor are within a certain distance of each other and the angle made by the donor, hydrogen atom and the acceptor are within a certain range. For strong hydrogen bond, the distance cutoff is taken to be 2.2\AA , whereas the range for the angle is taken to be 130° to 180° . For weak H-bonds the range of distance is taken to be 2.2 to 3.0\AA , and the range of angle is between 90° and 180° .¹ The results presented here are averaged over the last 5 ns of the trajectory unless mentioned otherwise.

It was observed that around 4-5% of cations in the system are H-bonded to anions *via* the ring hydrogen atoms and the hydrogen atoms attached to the first carbon atom of the alkyl chain. In case of $[\text{C}_1\text{C}_{10}\text{Im}][\text{Br}]$, $[\text{C}_4\text{C}_{10}\text{Im}][\text{Br}]$ and $[\text{C}_7\text{C}_{10}\text{Im}][\text{Br}]$ solutions 5.2%, 3.9% and 3.9% of cations respectively, are bound to anions. The preference for hydrogen bonding between anion and cations *via* ring hydrogen atoms decreases gradually as the length of the chain increases from

¹H-bonds are classified as weak if the distance is less than 2.2\AA and the angle is between 90° and 130°

methyl to heptyl. However, in $[\text{C}_{10}\text{C}_{10}\text{Im}][\text{Br}]$ solution the percentage of cations bound to anion through H-bonds increases to 4.6%, while those formed *via* ring hydrogen atoms is 2.5%. The reason for this increase is the formation of more ordered aggregates in $[\text{C}_{10}\text{C}_{10}\text{Im}][\text{Br}]$ solution with symmetric cation. It was also observed that the percentage of cations H-bonded to anions increases slightly during the course of simulation. The fraction of cations H-bonded with anions at the initial stages of simulations (with cations randomly dispersed in aqueous solution) is around 0.4 to 0.7% lower compared to the final numbers presented above. (The results for the initial stages are averaged over first 1 ns of trajectory). The numbers can be compared with those in pure ionic liquid, $[\text{C}_1\text{C}_{10}\text{Im}][\text{Br}]$ where, at room temperature one in three cations are hydrogen bonded with anions and 20% of these are strong H-bonds. Strong hydrogen bonds between anion and cation were not observed in the aqueous solution.

Cations also form H-bonds with water molecules. On average each cation forms weak H-bond with about 8 to 10 water molecules. While the ring hydrogen atoms are involved in 3 to 4 H-bonds, the hydrogen atoms on the first carbon of the chain are involved in 5 to 6 H-bonds in each cation. The $[\text{C}_1\text{C}_{10}\text{Im}]$ cation forms 10 H-bonds with water, where as the other systems studied form about 8 weak H-bonds per cation. In imidazolium cations, the positive charge is distributed in the ring and methyl/methylene groups attached to the ring [38]. The exposure of this methyl group (attached to ring) to water, in $[\text{C}_1\text{C}_{10}\text{Im}][\text{Br}]$ solution is the reason for the marginal increase in the average number of H-bonds per cation compared to other solutions studied.

Bromide anions in all the systems are found to form on an average 7 H-bonds with water out of which 30% may be classified as strong H-bonds. The H-bonding propensity for the anions with water is similar across all the systems studied.

In summary, the aqueous solutions of ILs with two alkyl chains show the presence of extended hydrogen bonding network between cations, anions and water. In cations, the most preferred donor are the ring carbon atoms. The anions are more strongly bound to cations in the aggregates compared to a cation randomly dispersed in the solution (which did not show any H-bonds in our studies).

4.3.3 Radial distribution function

The organization of molecules can be determined using radial distribution function (RDF). The RDFs provide insights into the molecular structure, despite the fact that the angular information is lost. The RDF for the terminal carbon atoms of the shorter chain around themselves is shown in figure 4.2a. It can be noticed from the figure that the peak corresponding to the tail group in $[C_{10}C_{10}Im][Br]$ solution is very prominent, and the intensity of the peak decreases as the length of the differing alkyl chain decreases. In $[C_1C_{10}Im][Br]$ solution there is no peak in the region where the others show a maximum. The RDFs for the alkyl tails in $[C_4C_{10}Im][Br]$, $[C_7C_{10}Im][Br]$ and $[C_{10}C_{10}Im][Br]$ solutions show the first maxima at 4.2\AA and the first minima around 7\AA . While the tail-tail RDFs in $[C_7C_{10}Im][Br]$ and $[C_{10}C_{10}Im][Br]$ solutions show a noticeable second maxima around 8.6\AA , it is not so in case of $[C_4C_{10}Im][Br]$ solution. The terminal carbon atom of the methyl chain does not show any organization around similar carbon atoms of other molecules.

Radial distribution of the geometric center of the head groups around themselves for various systems studied is shown in figure 4.2b. The RDFs show first maxima at 9.3, 9.3, 10.0 and 10.0\AA respectively for the $[C_1C_{10}Im][Br]$, $[C_4C_{10}Im][Br]$, $[C_7C_{10}Im][Br]$ and $[C_{10}C_{10}Im][Br]$ solutions. It is evident from observing the amplitude of the peaks in the figure, that the head groups are more organized around themselves in $[C_{10}C_{10}Im][Br]$ solution and the organization decreases as the length of the second chain decreases. The first minima are present around 15\AA in systems with chains longer than butyl but is not noticeable for the system with methyl chain. The first minima in the former three systems is followed by a very broad second maxima. The organization of the head groups can be attributed to the well defined structure in the case of symmetric $[C_{10}C_{10}Im][Br]$ solution.

4.3.4 Spatial distribution

RDFs do not describe the three dimensional distribution of an atom or group around another. In order to gain insights into the distribution of anions and water around the cation in three dimensional space, spatial distribution functions (SDF) can be used. The spatial distribution of water and anions around cations in aqueous solution and anions around cations in pure IL are shown in

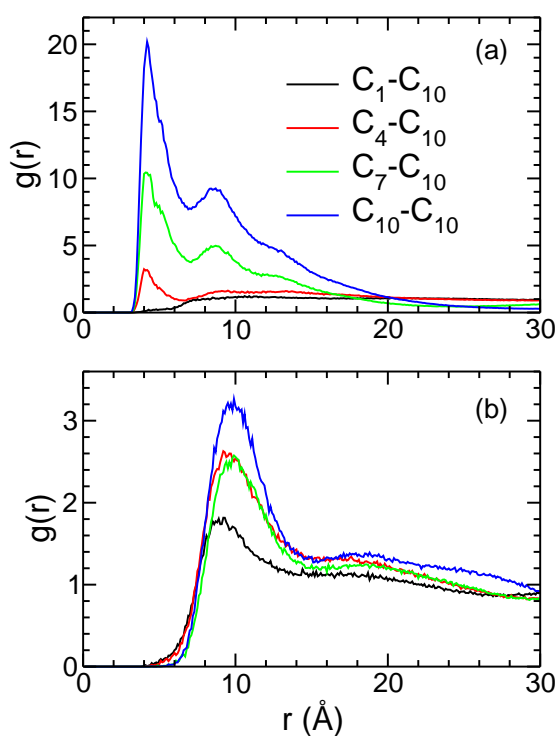


Figure 4.2: Radial distribution functions of (a) terminal carbon atoms of shorter alkyl chain around themselves (b) geometric centers of imidazolium rings around themselves.

figure 4.3. The isodensity surface shown corresponds to 5 times the average density for anions in solution and 10 times the average density for the anions in pure IL. In case of water the isosurface corresponds to 2.5 times the average density. It is evident from the figure that the anions in the pure liquid are predominantly located near the ring hydrogen atoms and the highest density is present in the vicinity of the unique hydrogen atom of the ring (attached to the carbon atom between the two nitrogen atoms). The anions are also likely to be present near the methyl group. However, in aqueous solution it was observed that there were no regions where the density is 10 times the average density. A very small region near ring hydrogens exhibited 5 times the average density. In solution, we can notice that the water partially replaces the anion to interact with ring hydrogen atoms which is evident from the spatial density at 2.5 times the average density of water. This will also corroborate the breakage of anion-cation hydrogen bonds in the solution to form cation-water H-bonds.

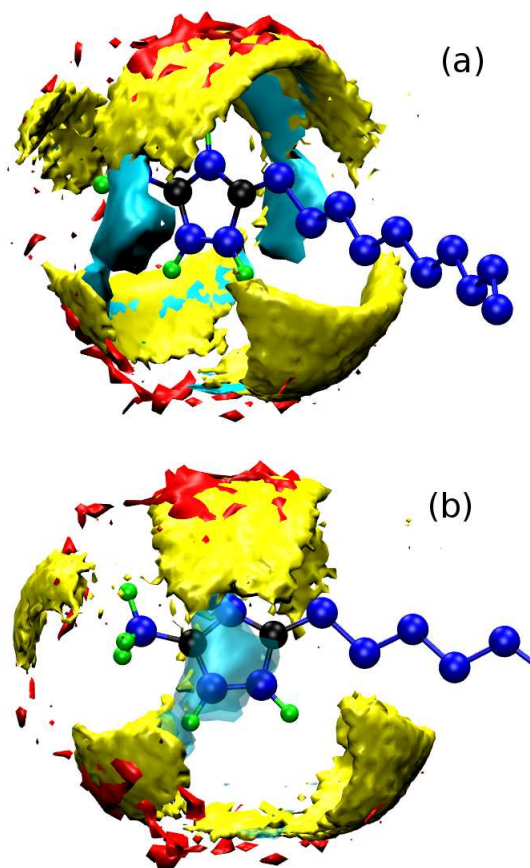


Figure 4.3: (a) Spatial density of anions and water molecules around cations in $[C_1C_{10}Im][Br]$ solution and anions around cations in pure IL $[C_1C_{10}Im][Br]$. Density of anions in pure IL is shown in Yellow, red represents the density of anions in solution and cyan represents density of water. Hydrogen atoms present on the decyl chain are not shown. (b) Another view of the same figure. Water density is shown in transparent cyan.

4.3.5 Diffusion of ions

The self diffusion coefficients of the cations in solution are computed from the slope of mean squared displacements. Even though the model used in this study is known to underestimate the diffusion of ions, the computed self diffusion coefficients can be used to compare the diffusion in different systems with varying alkyl chains. It is known that the diffusion in pure ionic liquids is very low [45]. It is also known from experiments that the self-diffusion coefficients of the ions in ionic liquids increase upon addition of water [46]. Increase in the mole fraction of water is known to increase the diffusion coefficients of ions [28]. This increase in diffusion due to the electrostatic screening of the charges of IL molecules by water is also observed in our current

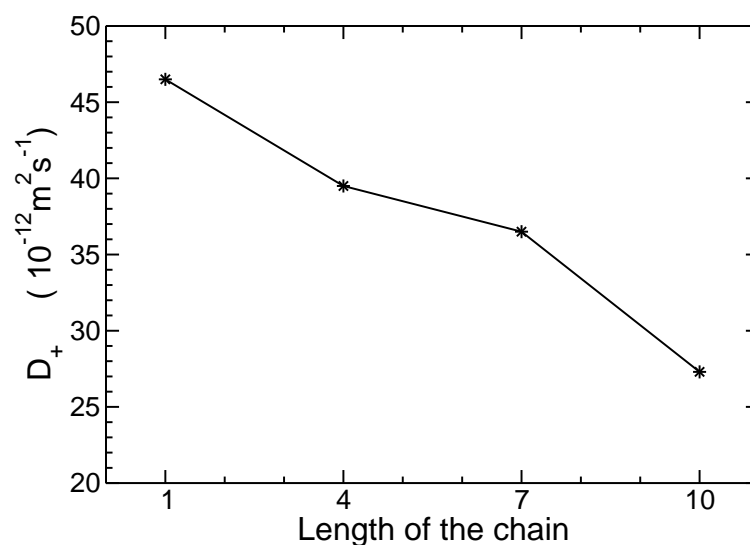


Figure 4.4: Self-diffusion coefficients of cations in alkyldecylimidazolium bromide solutions.

study which shows order of magnitude higher diffusion in case of aqueous solutions of ILs. We can also see that the diffusion co-efficients decrease (figure 4.4) by 70% going from $[\text{C}_1\text{C}_{10}\text{Im}]$ to $[\text{C}_{10}\text{C}_{10}\text{Im}]$ even though the increase in the mass contribute to about 25% decrease in the self diffusion coefficients only. The rapid decrease in the diffusion can be attributed to the aggregation of the cations which in turn increases the apparent mass of the cations, since they are now part of the aggregate. Anions are more mobile in the solution compared to cations but the association of anions with the aggregates is also evident from the fact that despite being the same, the bromide anion shows decreasing diffusion when present in systems with longer alkyl chains.

4.3.6 Formation of aggregates

The MD simulations were started from uniform distribution of cations in the aqueous solution with the bromide anion placed near the head group. During the course of simulation, we observed that cations grouped together to form oligomers. With time, monomers were absorbed into the oligomers increasing their size. In the beginning small oligomers fused to form bigger ones. But as the size of the oligomer increased, they took a more organized structure, with the hydrophobic alkyl chains at the core and the polar head groups at the surface of these oligomeric aggregates. Once the quasispherical aggregates with charged head groups at the surface are formed, the fusion

of aggregates becomes difficult as there will be repulsion between the charged layers of the two aggregates. Anions though likely to be present near the head group were found to be present through out the solution.

Snapshots of different systems after 25 ns are shown in figure 4.5. The atoms belonging to the head groups are shown in yellow color whereas the atoms belonging to the alkyl tail are shown as magenta beads. We can notice that in $[C_1C_{10}Im][Br]$ solution, the cations form quasi-spherical aggregates but are not having well defined structure. As the length of the second alkyl chain increases the aggregates become more spherical in structure. The increase in the size of the aggregates with increase in the alkyl chain length can also be noticed.

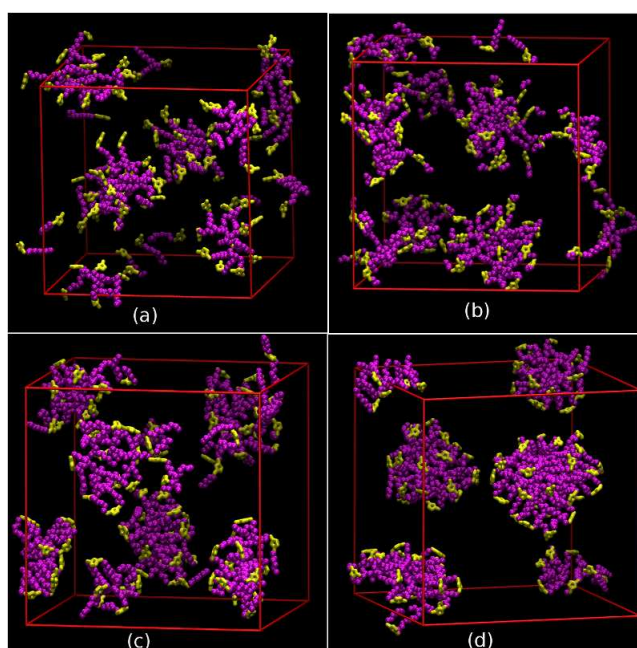


Figure 4.5: Snapshot of the aqueous solution after 25 ns simulation. (a) $[C_1C_{10}Im][Br]$ (b) $[C_4C_{10}Im][Br]$ (c) $[C_7C_{10}Im][Br]$ (d) $[C_{10}C_{10}Im][Br]$. Hydrophilic region of head group is shown in yellow whereas atoms belonging to hydrophobic alkyl chains are shown in magenta. Anions, water molecules and hydrogen atoms on the cations are not shown for the ease of visualization.

4.3.7 Aggregation number

The polydispersity of the aggregates is evident from figure 4.5. If the terminal carbon atoms of either of the alkyl chains (except for methyl chain) are present within a distance of 12.0\AA then the two cations are considered to belong to the same aggregate. With this definition, the distribution

of fraction of cations involved in forming an aggregate of a given size is shown in figure 4.6. The data presented are the average over the last 5 ns of the trajectory. In case of $[C_1C_{10}Im][Br]$ solution, most of the cations are involved in the formation of aggregates of size between 10 to 18. This number can be compared with experimentally determined aggregation number of 27 based on monodisperse aggregate model using NMR [47] and the computational reports of most probable aggregation number of 16 [48]. As the length of the alkyl chain increases we can notice that the most probable aggregation number also increases. In $[C_4C_{10}Im][Br]$ and $[C_7C_{10}Im][Br]$ solutions, the most probable aggregation number is 19 and 25 respectively. The spread in the aggregation number is between 14 to 23 in $[C_4C_{10}Im][Br]$ solution whereas in $[C_7C_{10}Im][Br]$ solution we can see that there are aggregates of 15, 18 and 25 cations. In $[C_{10}C_{10}Im][Br]$ solution aggregates of size 22, 30 and 48 are formed. The number of monomers present in the solution also decreases with the increase in the length of the second alkyl chain. It was noticed that the aggregates were dynamic, i.e., monomers were getting absorbed into the aggregates as well as leaving the aggregates to become free monomers during the course of the simulation.

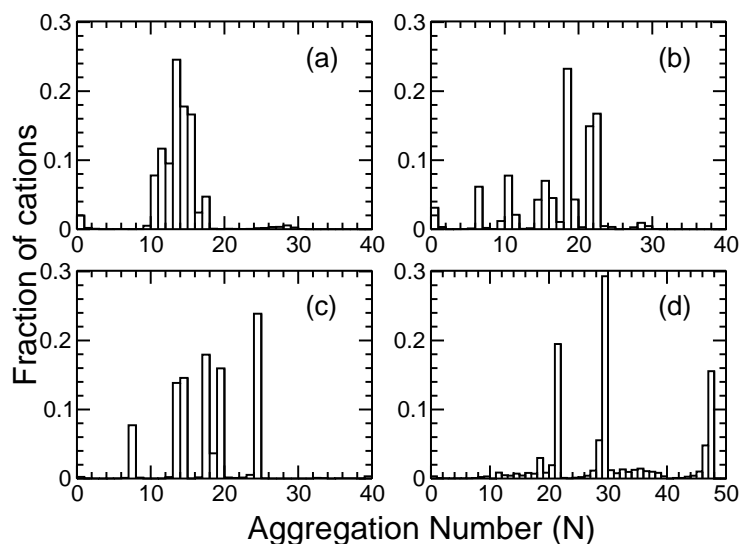


Figure 4.6: Fraction of cations involved in the formation of aggregates of size N in (a) $[C_1C_{10}Im][Br]$ solution (b) $[C_4C_{10}Im][Br]$ solution (c) $[C_7C_{10}Im][Br]$ solution (d) $[C_{10}C_{10}Im][Br]$ solution.

The aggregation number of 27 for $[C_1C_{10}Im][Br]$ solution arrived from NMR data has been

obtained using a model which assumes equilibrium between the monomers and monodisperse aggregates just above the critical micelle concentration (CMC). It is also reported [27] that the aggregation number increases with the concentration of the surfactant and was found to saturate at 47 at a concentration of 0.6M. Our $[C_1C_{10}Im][Br]$ solution is of concentration 0.45 M and should exhibit aggregation number of 45. Even though the initial formation of aggregates is quick, due to the charged surfaces of aggregates, growth of the aggregates by fusion has substantial activation barrier and hence requires longer times. Nevertheless, the initial formation of aggregates shows a definite trend of increasing number of aggregates with the increase in the length of the second alkyl chain. This is also observed experimentally in ILs with single alkyl chain substituent [27, 25].

4.3.8 Structure of aggregates

The structure of the aggregates in $[C_1C_{10}Im][Br]$ and $[C_{10}C_{10}Im][Br]$ solutions are shown in figure 4.7. In the figure, only the heavy atoms belonging to the cations are shown. Hydrogen atoms on cations, anions and water are not shown for the ease of visualization. The polar head group is shown in yellow whereas the carbon atoms belonging to the alkyl chains are shown in magenta. Figure 4.7a depicts the structure of a single aggregate in $[C_1C_{10}Im][Br]$ solution. We can notice that the aggregate is quasi-spherical in shape, with the hydrophobic alkyl chains buried inside, so as to minimize their unfavorable interactions with water and to maximize the dispersion interactions with each other. The polar head groups are at the surface of the aggregate so as to maximize the favorable interaction with water. We can also notice that most of the head groups are oriented in such a way that the ring normal is tangential to the spherical surface.

The aggregate formed in $[C_{10}C_{10}Im][Br]$ solution (figure 4.7b) is also of similar structure, with the hydrophobic core and hydrophilic surface, but the difference lies in the orientation of the imidazolium rings at the surface of the aggregate. Unlike in $[C_1C_{10}Im][Br]$ solution, the imidazolium ring plane is more likely to be oriented tangential to the spherical surface, i.e., the ring normal is directed radially outwards. In addition, the aggregate is bigger in size and also more spherical compared to that in $[C_1C_{10}Im][Br]$ solution. The aggregates in $[C_7C_{10}Im][Br]$ solution also exhibit similar behavior as those in $[C_{10}C_{10}Im][Br]$ solution. The distribution of

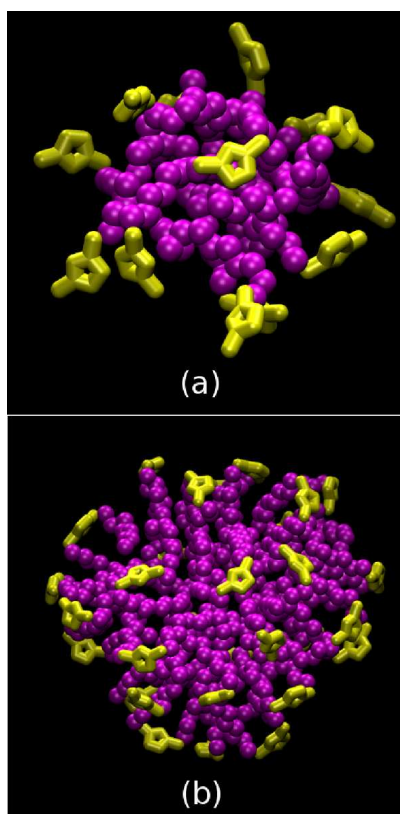


Figure 4.7: Structure of an aggregate in (a) $[C_1C_{10}Im][Br]$ solution (b) $[C_{10}C_{10}Im][Br]$ solution. Atoms belonging to head groups are shown in yellow, those belonging to alkyl chains are represented as magenta beads. Anions, water molecules and hydrogen atoms belonging to cations are not shown for the ease of visualization.

angle between the two imidazolium rings belonging to an aggregate that are within 8.0\AA of each other (Figure C.1, Appendix C) shows that the rings are more probable to be parallel to each other consistent with the experimental report on 1,3-dioctylimidazolium bromide solution [36].

The extent of penetration of water into the aggregates is studied using hydration index, which is defined as the ratio of average number of water molecules in the first solvation shell of the carbon atom of the chain, in the aggregate to that which is completely exposed to water. Figure 4.8 shows the hydration index for the decyl chain in $[C_{10}C_{10}Im][Br]$ solution. We can note that water penetration gradually decreases as we move towards the core of the aggregate. It drops from 0.76 for the first carbon atom of the decyl chain to around 0.1 at the terminal carbon atom. Visualization of the trajectory also confirms the penetration of water until the second carbon atom of the chain. Ideally, the hydration index should be zero for the atoms at the free end of the alkyl chain. But

since we are also accounting for the monomers and small oligomers, the deviation is seen. The

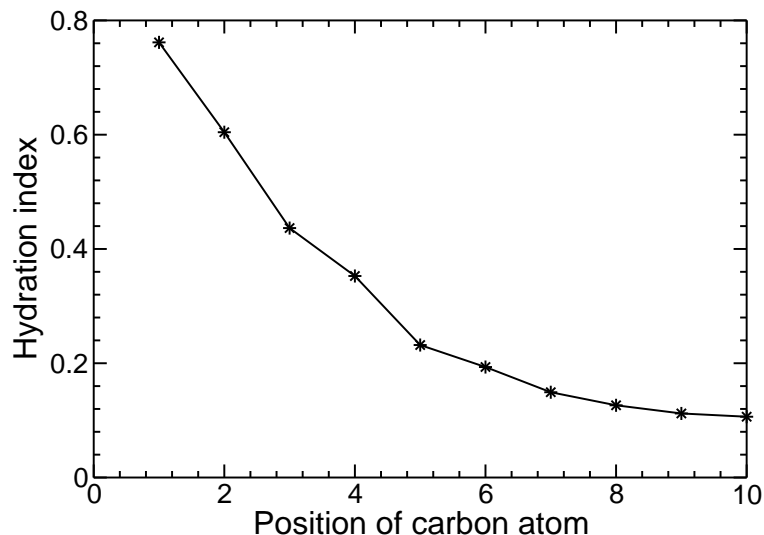


Figure 4.8: Hydration index for various carbon atoms on the decyl chain in $[C_{10}C_{10}Im][Br]$ solution.

mean radii of the aggregates and the hydrophobic core have been calculated for all the systems. In order to calculate the radius of the hydrophobic core, the center of the aggregate was defined as the geometric center of all the terminal carbon atoms of the alkyl chains forming the aggregate. Then, for each of the cations in the aggregate, the distance between the center of that aggregate and the second carbon atom from the fixed end of the alkyl chain was computed. This distance was averaged over all the cations of the aggregate to get the hydrophobic core radius of that aggregate. The mean hydrophobic core radius was obtained by averaging over all the aggregates and also over time.

Similarly the radius of the aggregate was calculated by using the distance between the center of the aggregate and the geometric center of the imidazolium ring, and averaging over all the aggregates. Properties characterizing the size and shape of the aggregates are tabulated in table 4.2. From the table, it is evident that the aggregation number increases with the length of the alkyl chain. The mean radii of the aggregate and the hydrophobic core also show similar trend.

Table 4.2: Details of the properties of aggregates in $[C_nC_{10}Im][Br]$ solution

cation	mode aggregation number	mean radius of the aggregate	mean radius of hydrophobic core
$[C_1C_{10}Im]$	14	12.89	8.88
$[C_4C_{10}Im]$	19	12.96	9.38
$[C_7C_{10}Im]$	25	13.39	10.42
$[C_{10}C_{10}Im]$	30	16.70	13.96

4.3.9 Number density

The number density profiles of the head group, tail group, anion and water in the $[C_{10}C_{10}Im][Br]$ solution are shown in figure 4.9. In the figure, the head group represents the geometric center of the imidazolium ring and the tail group represents the terminal carbon atom of the decyl chain. Since the number of water molecules in the solution is different than that of cations and anions, the water number density is scaled accordingly to match the bulk number density of the cations. From the figure, we can notice that the number density profile of the tail group show a tall peak

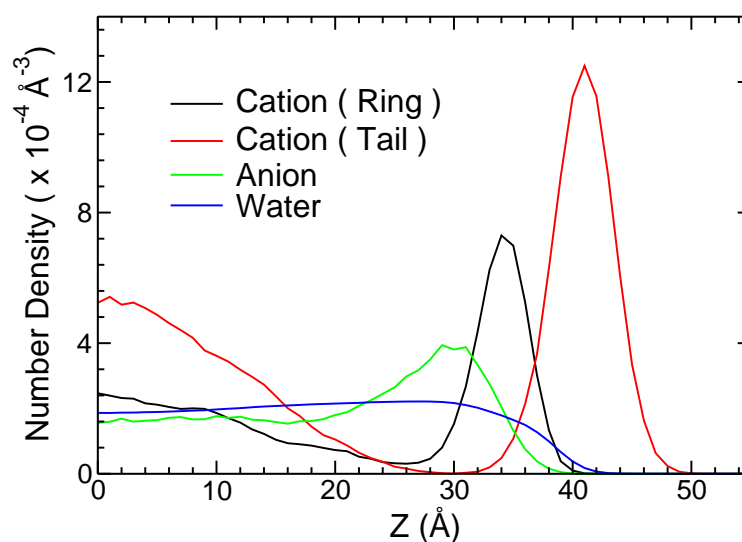


Figure 4.9: Number density profiles of head and tail group of cations, anion and water along interface normal (z -axis) in $[C_{10}C_{10}Im][Br]$ solution.

at the interface. At 30\AA from the center of the box the number density of tail group is almost zero. The density profile for head group also shows similar behavior except that the head groups are present well within the bulk region. Alkyl tails are protruding out of the interface whereas the

imidazolium rings are dispersed in the solution. The peaks of the head and tail number densities are separated by 7\AA . At the interface, the number density of tail group is 6 times higher than the average number density of the cations. The anion number density profile also exhibits peak closer to that of head group suggesting a partial association of anions with the head groups. The number densities of anions and cations varies in the bulk region, due to the formation of aggregates. In dilute $[\text{C}_{10}\text{C}_{10}\text{Im}][\text{Br}]$ solution, the cation number density profile shows the tail protruding out of the interface with imidazolium ring below the interface, and the anion mobile through out the solution. Alkyl tails protruding out of the interface has also been observed in pure IL liquid-vacuum interface using atomistic and coarse grained MD studies [13, 49].

The mass density profile (Figure C.2, Appendix C) shows 4% increase in the mass density at the interface compared to the average value in the bulk region. The maximum value in the mass density profile occurs at around 30\AA from the center of mass of the system along the z -axis. The mass density drops to 50% of its maximum value around 39\AA in $[\text{C}_{10}\text{C}_{10}\text{Im}][\text{Br}]$ solution and 35 to 38\AA in other systems. The region where the mass density is 50% of its maximum value is also near the region where the tail number density is highest. For the analysis of structure and orientation at the surface, we define the interface as the region that encloses the first peak in the tail number density profile. For example, in case of $[\text{C}_{10}\text{C}_{10}\text{Im}][\text{Br}]$ solution, the interface is defined as the region between 30\AA and 50\AA from the center of mass of the system along z -axis on either side.

4.3.10 Organization at the interface

In the following section, those cations for which the z -coordinate of the terminal carbon atom of either of the alkyl chains (except the methyl group) is present beyond a certain cutoff on either side of the z -axis are considered to be present in the interface. In other words the cations at the interface are those that are contributing to the peak in the tail number density profile near the interface. The distributions of angle between the alkyl chains (vector connecting the nitrogen atom and the terminal carbon atom of the chain linked to it) of same cation were found to be similar to those in bulk for all the systems studied. In addition, the distribution of angle between the alkyl

tails of different molecules present at the interface also showed preference to be oriented either parallel or antiparallel to each other.

The distribution of angle between, the alkyl chain (vector connecting the nitrogen atom and the terminal carbon atom connected to it) and the surface normal (positive and negative z-axis) is shown in figure 4.10a. Notice that the alkyl chains are more likely to be oriented parallel to

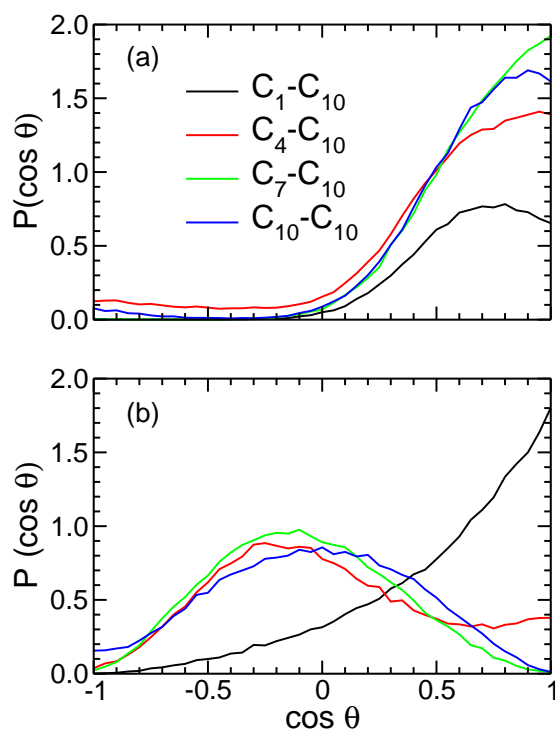


Figure 4.10: Distribution of (a) angle between the alkyl chains and the interface normal (z-axis) (b) angle between the vector connecting the two nitrogen atoms and the interface normal.

the surface normal, i.e., they prefer to be oriented perpendicular to the surface. In $[C_1C_{10}Im][Br]$ solution, the decyl tail is more probable to be tilted making an angle of 30 to 45° with the interface. In other systems, parallel orientation of chains along surface normal is most probable. Also note that in $[C_4C_{10}Im][Br]$ solution, cations show relatively more probability to be oriented antiparallel to the surface normal. This is due to the fact that the length of the butyl chain is smaller compared to heptyl and decyl chains and hence it does not behave like long linear alkyl chains.

The distribution of the angle between, the vector connecting the two nitrogen atoms (NN vector) and the interface normal for various systems studied is shown in figure 4.10b. While

cations in $[\text{C}_1\text{C}_{10}\text{Im}][\text{Br}]$ solution show preference for their NN vectors to be aligned parallel to the interface normal, the NN vector of the cations in all the other systems are more probable to be present perpendicular to the interface normal. It was observed (Figure C.3, Appendix C) that the imidazolium rings are more likely to be oriented parallel to the surface in $[\text{C}_4\text{C}_{10}\text{Im}][\text{Br}]$, $[\text{C}_7\text{C}_{10}\text{Im}][\text{Br}]$ and $[\text{C}_{10}\text{C}_{10}\text{Im}][\text{Br}]$ solutions.

From these observations, it is evident that in $[\text{C}_1\text{C}_{10}\text{Im}][\text{Br}]$ solution, the most probable alignment of the cation is such that the decyl chain is protruding away from the interface where as the methyl chain is pointing towards the bulk region. In case of $[\text{C}_4\text{C}_{10}\text{Im}][\text{Br}]$, $[\text{C}_7\text{C}_{10}\text{Im}][\text{Br}]$ and $[\text{C}_{10}\text{C}_{10}\text{Im}][\text{Br}]$ solutions, both the alkyl chains are likely to be aligned parallel to the interface normal with the imidazolium ring parallel to the interface.

Snapshots of $[\text{C}_1\text{C}_{10}\text{Im}][\text{Br}]$ and $[\text{C}_{10}\text{C}_{10}\text{Im}][\text{Br}]$ solutions are shown in figure 4.11. We can observe that the tails are protruding out of the interface in both the solutions. While the ring plane in $[\text{C}_1\text{C}_{10}\text{Im}][\text{Br}]$ solution is perpendicular to the interface, in $[\text{C}_{10}\text{C}_{10}\text{Im}][\text{Br}]$ solution, the imidazolium ring is more likely to be oriented parallel to the interface. In the bulk region of the solution, we can notice the aggregates, which are similar to those observed in bulk solution.

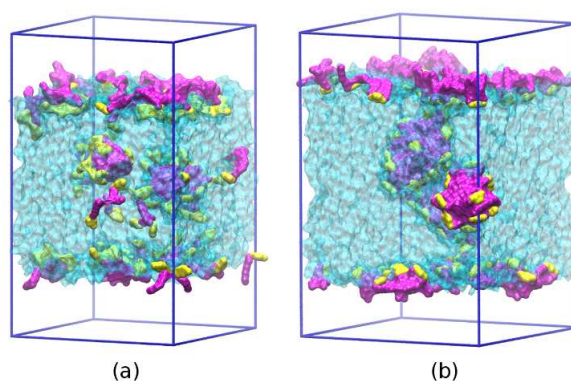


Figure 4.11: Snapshot of vapor-liquid interface of (a) $[\text{C}_1\text{C}_{10}\text{Im}][\text{Br}]$ solution and (b) $[\text{C}_{10}\text{C}_{10}\text{Im}][\text{Br}]$ solution at the end of 25 ns simulation. The head groups of cations are shown as density in yellow, tail groups as density in magenta and water density is shown in transparent cyan.

4.4. Conclusions Atomistic MD simulations have been carried out on a series of aqueous solutions of 1-alkyl-3-decylimidazolium bromide ILs at room temperature, with the alkyl chain ranging from methyl to decyl. Starting from uniform configuration of ILs in the solution, spontaneous aggregation of cations to form quasi-spherical or spherical polydisperse aggregates, depending on the length of the alkyl chain, is observed. The aggregates are formed with alkyl tails at the core, interacting favorably through van der Waals interactions while shielding themselves from the unfavorable interactions with water, and the polar head groups at the surface exposed to water. Aggregation number and the size of the aggregates increases with the increase in the length of the alkyl chain. The shape of the aggregate is more spherical in case of $[C_{10}C_{10}Im][Br]$ solution due to the presence of two similar chains.

Spatial distribution functions reveal that the anions are no longer strongly associated with cations unlike in pure ILs. In aqueous solution, water molecules compete to form hydrogen bonds with the cation replacing the anions from their preferred position. Weak association of anions with cationic head groups is evident from the fact that the diffusion of anions decreases with increase in the length of the alkyl chain despite the fact that the anions are same in all the systems. Water is found to penetrate up to a certain distance inside the aggregate. The aggregation number, radius of the hydrophobic core of the aggregates and the radius of the aggregate steadily increase with the increase in the length of one of the substituent chain on the cation. The organization of the cationic head groups in the aggregates in $[C_7C_{10}Im][Br]$ and $[C_{10}C_{10}Im][Br]$ solutions is similar to that predicted from the nuclear magnetic resonance experiment [36] in $[C_8C_8Im][Br]$ solution. The surface structure of $[C_1C_{10}Im][Br]$ solution is different from that of others with the ring plane perpendicular to the aggregate surface compared to the tangential orientation in $[C_7C_{10}Im][Br]$ and $[C_{10}C_{10}Im][Br]$ solutions.

In the vapor-liquid interface of the solution, the alkyl groups are protruding out of the interface, with head groups within the solution, and anions near the head groups. At the interface, the intermolecular alkyl chains are more probable to be aligned parallel to each other. The most probable orientation of the alkyl chains is found to be perpendicular to the interface. The vector

connecting the two nitrogen atoms is found to be preferentially oriented perpendicular to the surface in [C₁C₁₀Im][Br] solution and parallel to the surface in [C₇C₁₀Im][Br] and [C₁₀C₁₀Im][Br] solution.

Aggregation processes require time scales of microsecond or more [50] and our simulations are limited to 25 ns. Computation of statistically significant values for the aggregation number and other properties require simulations of larger systems spanning longer time scales, which can be achieved using coarse grained studies. Nevertheless, we found that the aggregation number or the structure does not change in the last 10 ns and the system is locked in a metastable state. Though the equilibrium distribution of aggregation number and the structures require simulations for a longer time, the results obtained from this study provide insights into the structure of aggregates with cations having asymmetric and symmetric substituent chains. The presence of methyl and decyl chain on the same cation leads to a completely different surface structure of the aggregates compared to the solution with two decyl substituents.

Chapter C

Appendix C

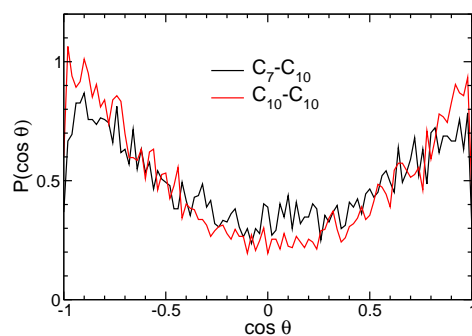


Figure C.1: Distribution of angle between the imidazolium rings of the cations that belong to the same aggregate and are within 8.0Å from each other.

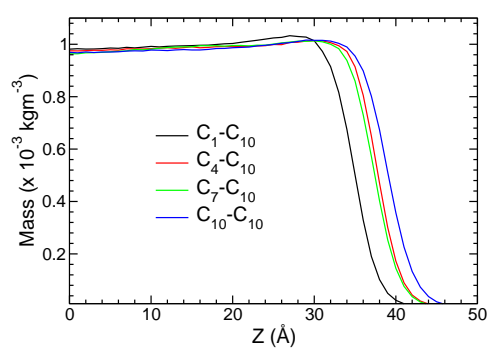


Figure C.2: Mass density profile along interfacial normal for aqueous solutions of $[C_nC_{10}\text{Im}][\text{Br}]$ with $n = 1, 4, 7$ and 10.

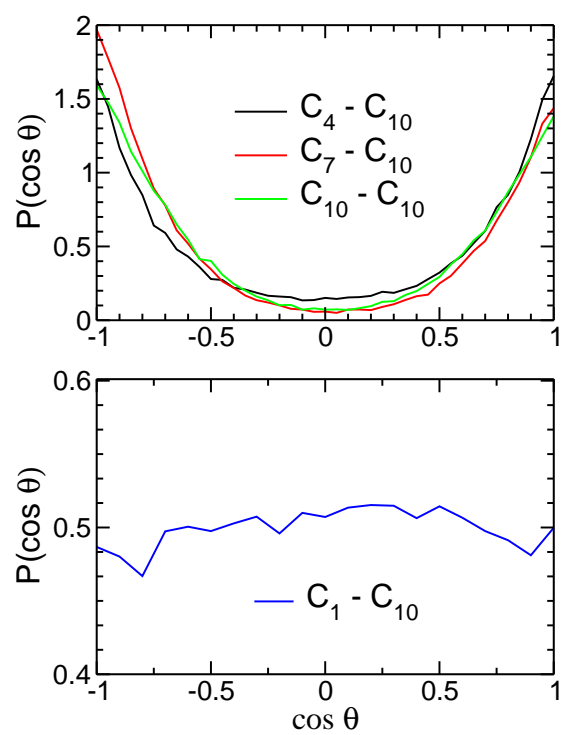


Figure C.3: Distribution of angle between the imidazolium ring normal and the interface normal for aqueous solutions of $[C_n C_{10} \text{Im}][\text{Br}]$ with $n = 1, 4, 7$ and 10 .

Bibliography

- [1] Tong, J.; Liu, Q.; Xu, W.; Fang, D.; Yang, J. *J. Phys. Chem. B* **2008**, *112*, 4381-4386.
- [2] Huddleston, J. G.; Visser, A. E.; Reichert, W. M.; Willauer, H. D.; Broker, G. A.; Rogers, R. D. *Green Chem.* **2001**, *3*, 156-164.
- [3] van Rantwijk, F.; Sheldon, R. A. *Chem. Rev.* **2007**, *107*, 2757-2785.
- [4] Greaves, T. L.; Drummond, C. J. *Chem. Rev.* **2008**, *108*, 206-237.
- [5] Triolo, A.; Mandanici, A.; Russina, O.; Rodriguez-Mora, V.; Cutroni, M.; Hardacre, C.; Nieuwenhuyzen, M.; Bleif, H.; Keller, L.; Ramos, M. A. *J. Phys. Chem. B* **2006**, *110*, 21357-21364.
- [6] Triolo, A.; Russina, O.; Bleif, H.; Di Cola, E. *J. Phys. Chem. B* **2007**, *111*, 4641-4644.
- [7] Rocha, M. A. A.; Coutinho, J. A. P.; Santos, M. N. B. F. *J. Phys. Chem. B* **2012**, *116*, 10922-10927.
- [8] Wang, Y.; Voth, G. A. *J. Am. Chem. Soc.* **2005**, *127*, 12192-12193.
- [9] Wang, Y.; Voth, G. A. *J. Phys. Chem. B* **2006**, *110*, 18601-18608.
- [10] Bhargava, B. L.; Klein, M. L. *Soft Matter* **2009**, *5*, 3475-3480.
- [11] Skarmoutsos, I.; Dellis, D.; Matthews, R. P.; Welton, T.; Hunt, P. A. *J. Phys. Chem. B* **2012**, *116*, 4921-4933.

- [12] Hettige, J. J.; Kashyap, H. K.; Annapureddy, H. V. R.; Margulis, C. J. *J. Phys. Chem. Lett.* **2013**, *4*, 105-110.
- [13] Yan, T.; Li, S.; Jiang, W.; Gao, X.; Xiang, B.; Voth, G. A. *J. Phys. Chem. B* **2006**, *110*, 1800-1806.
- [14] Kazarian, S. G.; Briscoe, B. J., Welton, T. *Chem. Commun.* **2000**, 2047-2048.
- [15] Inoue, T.; Dong, B.; Zheng, L. *J. Colloid Interface Sci.* **2007**, *307*, 578-581.
- [16] Annapureddy, H. V. R.; Hu, Z.; Xia, J.; Margulis, C. J. *J. Phys. Chem. B* **2008**, *112*, 1770-1776.
- [17] Raju, S. R.; Balasubramanian, S. *J. Phys. Chem. B* **2009**, *113*, 4799-4806.
- [18] Shi, W.; Maginn, E. J. *J. Phys. Chem. B* **2006**, *112*, 2045-2055.
- [19] Anouti, M.; Sizaret, P. Y.; Ghimbeu, C.; Galiano, H.; Lemordant, D. *Colloids Surf., A* **2012**, *395*, 190-198.
- [20] Hunt, P. A. *J. Phys. Chem. B* **2007**, *111*, 4844-4853.
- [21] Bowers, J.; Butts, C. P.; Martin J. P.; Vergara-Gutierrez M. C. *Langmuir* **2004**, *20*, 2191-2198.
- [22] Wang, X.; Yu, L.; Jiao, J.; Zhang, H.; Wang, R.; Chen, H. *J. Mol. Liq.* **2012**, *173*, 103-107.
- [23] Firestone, M. A.; Dzielawa, J. A.; Zapol, P.; Curtiss, L. A.; Seifert, S.; Dietz, M. L. *Langmuir*, **2002**, *18*, 7258-7260.
- [24] Blesic, M.; Lopes, A.; Melo, E.; Petrovski, Z.; Plechkova, N. V.; Lopes, J. N. C.; Seddon, K. R.; Rebelo, L. P. N. *J. Phys. Chem. B* **2008**, *112*, 8645-8650.
- [25] Vanyúr, R.; Biczók, L.; Miskolczy, Z. *Colloids Surf., A* **2007**, *299*, 256-261.
- [26] Sirieix-Plénet, J.; Gallion, L.; Letellier, P. *Talanta* **2004**, *63*, 979-986.

- [27] Goodchild, I.; Collier, L.; Millar, S. L.; Prokeš, I.; Lord, J. C. D.; Butts, C. P.; Bowers, J.; Webster, J. R. P.; Heenan, R. K. *J. Colloid Interface Sci.* **2007**, *307*, 455-468.
- [28] Jiang, W.; Wang, Y.; Voth, G. A. *J. Phys. Chem. B* **2007**, *111*, 4812-4818.
- [29] Miskolczy, Z.; Sebök-Nagy, K.; Biczéok, L.; Göktürk, S. *Chem. Phys. Lett.* **2004**, *400*, 296-300.
- [30] Blesic, B.; Marques, M. H.; Plechkova, N. V.; Seddon, K. R.; Rebelo, L. P. N.; Lopes, A. *Green Chem.* **2007**, *9*, 481-490.
- [31] El Seoud, O. A.; Pires, P. A. R.; Abdel-Moghny, T.; Bastos, E. L. *J. Colloid. Interface Sci.* **2007**, *313*, 296-299.
- [32] Luczak, J.; Hupka, J.; Thöming, J.; Jungnickel, C. *Colloids and Surfaces A* **2008**, *329*, 125-133.
- [33] Bhargava, B. L.; Klein, M. L. *Mol. Phys.* **2009**, *107*, 393-401.
- [34] Bhargava, B. L.; Klein, M. L. *J. Phys. Chem. B* **2009**, *113*, 9499-9505.
- [35] Bhargava, B. L.; Yasaka, Y.; Klein, M. L. *Chem. Commun.* **2011**, *47*, 6228-6241.
- [36] Ge, L.; Wang, Q.; Wei, D.; Zhang, X.; Guo, R. *J. Phys. Chem. B* **2013**, *117*, 15014-15022.
- [37] Plimpton, S. *J. Comput. Phys.* **1995**, *117*, 1-19, web: <http://lammps.sandia.gov>.
- [38] Lopes, J. N. C.; Deschamps, J.; Pádua, A. A. H. *J. Phys. Chem. B* **2004**, *108*, 2038-2047; *108*, 11250.
- [39] Lopes, J. N. C.; Pádua, A. A. H. *J. Phys. Chem. B* **2006**, *110*, 19586-19592.
- [40] H. J. C. Berendsen, J. P. M. Postma, W. F. van Gunsteren and J. Hermans, in B. Pullman (ed.), *Intermolecular Forces*; Reidel: Dordrecht, 1981, p331.
- [41] Allen, M. P.; Tildesley, D. J. *Computer Simulation of Liquids*; Clarendon Press: Oxford, 1987.

- [42] Ryckaert, J. P.; Ciccotti, J.; Berendsen, H. J. C. *J. Comput. Phys.* **1977**, *23*, 327-341.
- [43] Humphrey, W.; Dalke, A.; Schulten, K. *J. Molec. Graphics* **1996**, *14*, 33-38.
- [44] Desiraju, G. R.; Steiner, T. *The Weak Hydrogen Bond, In Structural Chemistry and Biology*; Oxford University Press: USA, 2001.
- [45] Bhargava, B. L.; Balasubramanian, S. *J. Chem. Phys.* **2005**, *123*, 144505; **2006**, *125*, 219901.
- [46] Kanakubo, M.; Umecky, T.; Hiejima, Y.; Aizawa, T.; Nanjo, H.; Kameda, Y. *J. Phys. Chem. B* **2005**, *109*, 13847-13850.
- [47] Zhao, Y.; Gao, S.; Wang, J.; Tang, J. *J. Phys. Chem. B* **2008**, *112*, 2031-2039.
- [48] Bhargava, B. L.; Klein, M. L. *J. Phys. Chem. A* **2009**, *113*, 1898-1904.
- [49] Jiang, W.; Wang, Y.; Yan, T.; Voth, G. A. *J. Phys. Chem. C* **2008**, *112*, 1132-1139.
- [50] Alexandridis, P.; Holzwarth, J. F.; Hatton, T. A. *Langmuir* **1993**, *9*, 2045-2052.

Chapter 5

Self-Assembly of Cations in Aqueous Solutions of Hydroxyl-Functionalized Ionic Liquids: Molecular Dynamics Studies

Abstract

The effect of presence of a hydroxyl functionalized alkyl chain of varying carbon number on the self-assembly of cations in aqueous solutions of 1-(*n*-hydroxyalkyl)-3-decylimidazolium bromide (where the alkyl groups are ethyl, butyl, heptyl and decyl) has been studied using atomistic molecular dynamics simulations. Spontaneous self-assembly of cations to form aggregates with hydrophobic core and hydrophilic surface is observed. The shape of the aggregates changes from quasi-spherical in case of cations with hydroxyheptyl or smaller substituent chain, to a thin film like intercalated aggregate in case of cations with hydroxydecyl chain. Cations with hydroxydecyl substituent chain exhibit long range spatial correlations and the anions are associated with cations to a greater extent due to the higher surface charge density of the aggregate. The ordered film like aggregate is stabilized by the dispersion interactions between the intercalated substituent chains and the intermolecular hydrogen bonds formed between the alkoxy oxygen atoms and the hydrogen atoms of the imidazolium ring. The cations form less compact aggregates with lower aggregation number than their non-hydroxyl analogues in the corresponding aqueous solutions. The intracationic and aggregate structures are governed by the length of the hydroxyalkyl chain.

5.1. Introduction Hydroxyl functionalized ionic liquids (HFILs) are molten salts [1] which are stable up to $\sim 300^\circ\text{C}$ [2, 3] and show a systematic variation of physicochemical properties with temperature and substituent alkyl chain length of the cations [4, 5]. Solvatochromic dyes and fluorescence probe molecules have shown anion-dependent increase in polarity of HFILs due to ionic hydrogen bonds between the hydroxyl group and the anions [6]. Due to this increase in the polarity of HFILs with respect to their nonhydroxyl analogues, they are widely used in fixation of greenhouse gases [7, 8, 9, 10, 11]. HFILs are also found to have remarkable liquid phase microextraction ability with $[\text{NTf}_2]$ and $[\text{PF}_6]$ anions [12, 13]. They also have wide range of applications, as stabilizer [14, 15, 16, 17] and template [18] in the synthesis of nanostructure material.

Hydroxyl functionalized ionic liquids with longer alkyl chains are reported to show surfactant properties [19, 20, 21, 22]. It has been reported that the catalytic behavior of HFILs for the decomposition of p-nitrophenyl esters of carbonic acids in aqueous solution is more than their corresponding nonhydroxyl analogue [21]. Experimental studies on the aggregation behavior of HFILs in aqueous solutions indicate the formation of loosely bound aggregates with lower aggregation number [20, 22]. There have been several computational studies on aqueous solutions of alkyylimidazolium ionic liquids without any functionalization [23, 24, 25, 26, 27]. Even though few computational studies are reported on the thermodynamic and structural properties of HFILs in pure liquid form [28, 29, 30], to the best of our knowledge, there have been no reports of computational studies on the solution structure of HFILs in water. In the present study, we have investigated the atomic-level details of the effect of the presence of a hydroxyl group attached to one of the two alkyl chains in dialkyylimidazolium based ILs, on the bulk solution structure. The solution structure has been studied using atomistic molecular dynamics (MD) simulations performed on a series of 1-(*n*-hydroxyalkyl)-3-decyylimidazolium bromide ILs (where the alkyl chain is ranging from ethyl to decyl) in their aqueous solutions.

5.2. Methodology and simulation details A series of aqueous solutions of 1-(*n*-hydroxyalkyl)-3-decylimidazolium bromide

([HOC_{*n*}C₁₀Im][Br], with *n*=2, 4, 7 and 10) have been studied using atomistic MD simulations. The simulations were performed using the LAMMPS [31] software. The force field parameters were adapted from the works of Lopes et. al [32, 33, 34] and Jorgensen et. al [35]. Lopes et. al model is a transferable general force field for ionic liquids based on the OPLS-AA/AMBER framework and derives several terms in the force field that were not yet defined in the literature. Lopes et. al force field has parameters derived for imidazolium ILs with hydroxyethyl substituent chain [34] and since we are studying ILs with hydroxyl functionalized alkyl groups of longer chainlength we have adapted some of the parameters from OPLS-AA force field developed by Jorgensen et. al [35]. The extended simple point charge model (SPC/E) has been used to model water molecules [36, 37]. Atomic partial charges in the force field model [32] were calculated from the electron density obtained by *ab initio* calculations using an electrostatic surface potential methodology. The simulated systems differed from each other in the length of the hydroxyl functionalized alkyl chain. Details of the systems studied have been presented in table 5.1. The initial configurations were generated by replicating the coordinates of a single ion pair along the three dimensions to form a box of uniformly placed ions, then inserting this box in a water box with randomly oriented water molecules at experimental density and removing the

Table 5.1: Details of the simulated systems; *n* represents the number of carbon atoms in the hydroxyl functionalized hydrocarbon chain.

<i>n</i>	no. of ion pairs	no. of waters	no. of atoms	run length(ns)	box length(Å)	concentration (M)
10	100	15373	53319	50	81.64	0.305
7	100	13414	46542	35	77.89	0.351
4	100	11614	40242	35	74.23	0.406
2	100	10274	35622	35	71.42	0.456
10	50	7500	26100	20	64.33	0.312
10	1	1875	5697	10	38.79	0.028
7	1	1886	5721	10	38.84	0.028
4	1	1894	5736	10	38.87	0.028
2	1	1901	5751	10	38.91	0.028

pair along the three dimensions to form a box of uniformly placed ions, then inserting this box in a water box with randomly oriented water molecules at experimental density and removing the

water molecules that were within 3.0 Å from any atoms of the cations or the anions. All simulations were performed at 300 K using the Nöse-Hoover thermostat with a temperature damping parameter of 1000 fs. The equations of motion were integrated using the verlet algorithm with a time step of 0.5 fs.

Isothermal-isobaric ensemble simulations (constant NPT) at 1 atmosphere pressure, using the Nöse-Hoover barostat with a pressure damping parameter of 500 fs, were carried out on each solution for 2 ns to get the equilibrated density. The canonical ensemble simulations (constant NVT) were then performed from the last configuration of NPT simulations with a volume averaged over last 1 ns of NPT simulations. Three dimensional periodic boundary conditions were used. The coordinates of the atoms were stored at an interval of 5 ps. In some of the figures, a short-hand notation is adapted to represent a system. For example, HOC₁₀ is used to represent [HOC₁₀C₁₀Im][Br] solution. The oxygen atom of the hydroxyalkyl chain is referred to as hydroxyl oxygen in the following discussion. The schematic of the molecular structures of the cations is shown in figure 5.1.

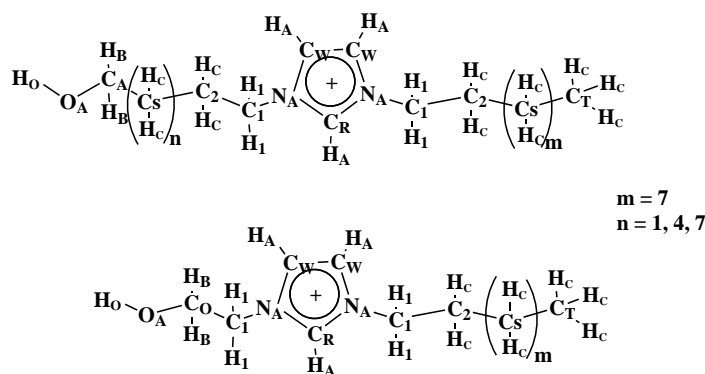


Figure 5.1: Schematic diagram of the cations, mentioning the distinct atom types.

5.3. Results and Discussion

5.3.1 Radial Distribution Functions (RDFs)

The short-range ordering in liquids at atomic level can be understood by analysing the radial distribution functions of atoms or ions around each other. Figure 5.2(a) presents the RDFs of

terminal carbon atoms (C_T) of the non-hydroxylated decyl chains around themselves. The first

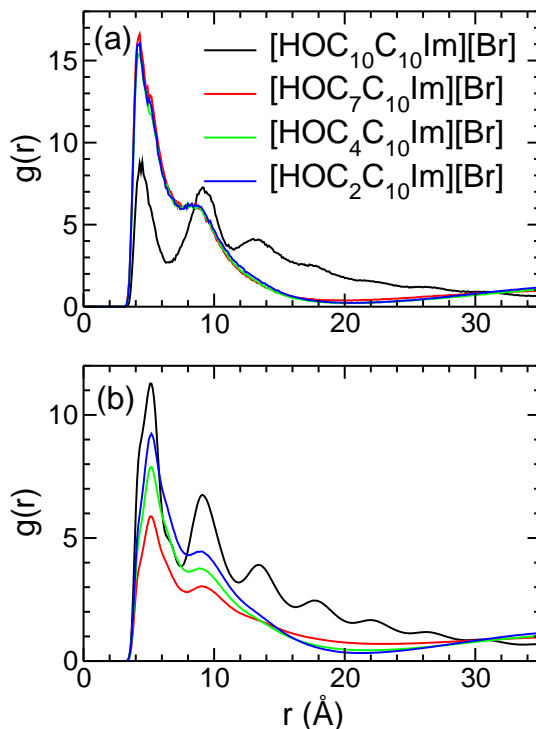


Figure 5.2: RDFs of (a) terminal carbon atoms (C_T) of the non-hydroxylated decyl chains around themselves and (b) alkyl chain carbon atoms (C_S) around themselves in different aqueous solutions.

maxima of the RDFs appear at 4.3 \AA in all the four systems whereas the first minima appear at 7.4 \AA in [HOC₇C₁₀Im][Br], [HOC₄C₁₀Im][Br] and [HOC₂C₁₀Im][Br] systems and at 6.6 \AA in [HOC₁₀C₁₀Im][Br] system. We see that at short distances the spatial correlation among the the C_T atoms is very high in [HOC₇C₁₀Im][Br], [HOC₄C₁₀Im][Br] and [HOC₂C₁₀Im][Br] systems and it is comparatively lower in [HOC₁₀C₁₀Im][Br] system. At larger distances (> 15 \AA) spatial correlation is still significant in [HOC₁₀C₁₀Im][Br] system. Figure 5.2(b) provides the intermolecular RDFs of C_S carbon atoms of the hydrocarbon tails (belonging to both hydroxylated and non-hydroxylated alkyl chains) around themselves in various solutions studied. We see that the first maxima of the RDFs appear at 5.2 \AA in all the four systems studied and the first minima appear at 7.4 \AA in [HOC₁₀C₁₀Im][Br] solution and at 8 \AA in other three solutions. The peak height of $C_S - C_S$ RDF is maximum in [HOC₁₀C₁₀Im][Br] solution. Also the $C_S - C_S$ RDF in [HOC₁₀C₁₀Im][Br] solution shows subsequent peaks with gradually diminishing peak intensities

at 9.1, 13.4, 17.7, 21.9, 26.2 Å and almost vanishing peak intensity beyond this distance. Note that these peaks are spaced equally with about 4.3 Å between them suggesting a liquid crystal like ordering of the cations in the aqueous $[\text{HOC}_{10}\text{C}_{10}\text{Im}][\text{Br}]$ solution. Although, a second maxima with a smaller intensity is observed at 9.0 Å in the remaining three solutions, the correlation is not observed at larger distances. Based on the nature of the RDFs of $\text{C}_T - \text{C}_T$ and $\text{C}_S - \text{C}_S$ pairs, we can conclude that there is long distance spatial correlation among the intermolecular decyl chains (both hydroxylated and non-hydroxylated) in $[\text{HOC}_{10}\text{C}_{10}\text{Im}]$ cations (due to the intercalation of the chains which will be discussed later), whereas in other three systems, the decyl chains are organized around their C_T atoms (due to formation of spherical or quasi-spherical aggregates).

Figure 5.3(a) shows the RDFs of bromide ions around the geometric center of the imidazolium ring of $[\text{HOC}_n\text{C}_{10}\text{Im}]$ cations in their aqueous solutions. The RDFs show the first maxima at 4.9 Å

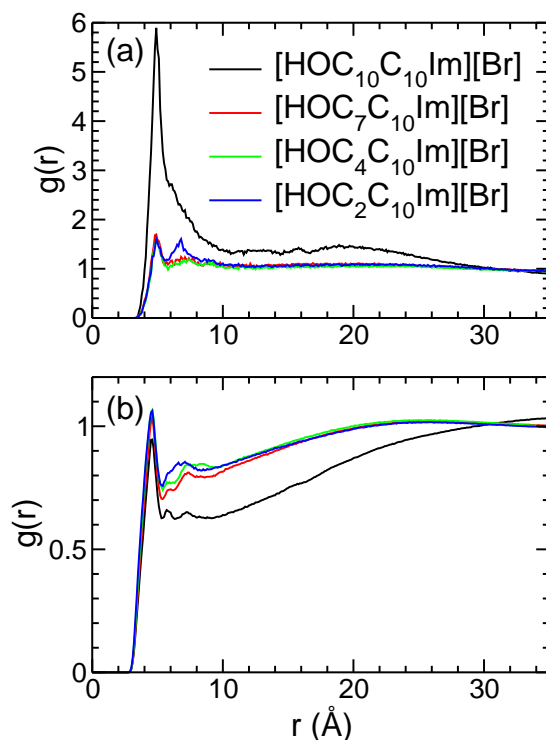


Figure 5.3: RDFs of (a) bromide ions (Br^-) and (b) water oxygen atoms around the geometric center of the imidazolium ring in different $[\text{HOC}_n\text{C}_{10}][\text{Br}]$ solutions.

in all the four systems. The intensity of the first maximum is very high in $[\text{HOC}_{10}\text{C}_{10}\text{Im}][\text{Br}]$ system. In the other three systems the intensity is significantly lower compared to the system with

hydroxydecyl substituent. In a closer view, the ring – bromide RDF in $[\text{HOC}_7\text{C}_{10}\text{Im}][\text{Br}]$ system has slightly greater intensity than the corresponding RDFs in $[\text{HOC}_4\text{C}_{10}][\text{Br}]$ and $[\text{HOC}_2\text{C}_{10}][\text{Br}]$ systems which have similar intensities. The organisation of anions around the ring center of alkylimidazolium cations should decrease with increase in the hydrocarbon chain length due to the decrease in cation – anion interaction strength [41, 42]. But in the current study, we see that the trend is exactly opposite. This anomaly can be explained on the basis of the size and shape of the aggregates formed in the corresponding aqueous solutions that will be discussed in a later section.

The organisation of water molecules around cations in various aqueous solutions studied can be deciphered from the RDFs between the geometric center of the imidazolium ring and water oxygen atoms that are shown in figure 5.3(b). We observe that the organisation of the water molecules around the imidazolium rings decreases gradually as the number of carbon atoms in the asymmetrically substituted hydroxyalkyl chain length increases. This phenomenon may be attributed to the decrease in aqueous solubility of $[\text{HOC}_n\text{C}_{10}][\text{Br}]$ salts with increase in alkyl chain length. Similar trend in the organisation of water around cations with varying alkyl chain length has been reported earlier [41].

5.3.2 Spatial Distribution

Spatial distribution functions (SDFs) provide insight into the three-dimensional probability density of atoms or groups around an atom or a group of interest. Figure 5.4 shows the spatial distribution of anions (in yellow), water (in red) and oxygen atoms of the hydroxyalkyl chains (in green) around imidazolium rings of $[\text{HOC}_{10}\text{C}_{10}\text{Im}]$ cations in their aqueous solution. The isosurface of bromide, water and hydroxyalkyl oxygen atoms correspond to 5, 2 and 20 times their average density respectively. We see that the anions, water oxygen and hydroxyalkyl oxygen atoms tend to concentrate near the ring hydrogen atoms due to formation of H-bonds. From the figure 5.4, we see that water molecules prefer to interact with the non-unique ring hydrogen atoms (attached to C_W), whereas, the anions and hydroxyalkyl oxygen atoms accumulate near the unique ring hydrogen atoms (attached to C_R). This is also evident from the site-site RDFs of bromide ions,

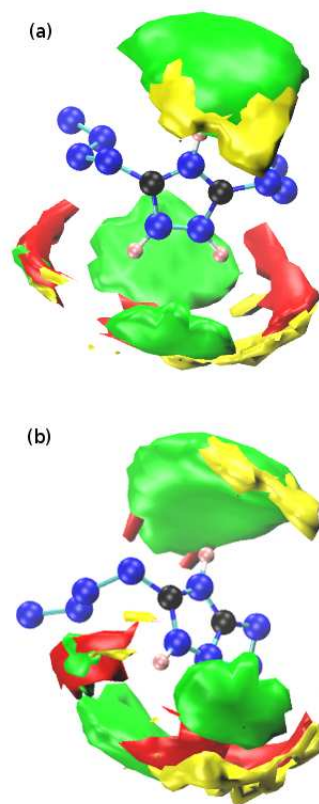


Figure 5.4: (a) Spatial density of anions (in yellow), water (in red) and alkoxy oxygen atoms (in green) around the imidazolium rings in $[\text{HOC}_{10}\text{C}_{10}\text{Im}][\text{Br}]$ solution (b) Another view of the same figure.

oxygen atoms of water and the oxygen atoms of hydroxyalkyl groups around the imidazolium ring hydrogen atoms (Figure D.1, Figure D.2, Figure D.3, Appendix D).

5.3.3 Hydrogen Bonding

Hydrogen bonding plays an important role in determining the nature of molecular association in structural chemistry and biology. Formation of hydrogen bonds in imidazolium based ionic liquids in pure state [30] and in aqueous solutions [43, 41] has been reported. In this study, we have adapted the geometric criteria [44] to classify H-bonds. In a strong H-bond, the H-atom and the acceptor are separated by a distance less than 2.2 \AA and the angle made by the donor, H-atom and the acceptor is within the range of $130 - 180^\circ$. The corresponding distance range and angular range are $2.0 - 3.0 \text{ \AA}$ and $90 - 180^\circ$ respectively, in a weak hydrogen bond.

In aqueous solutions of hydroxyalkylimidazolium bromide ILs, many types of H-bonded interactions are observed. The cation may form H-bond with bromide ions *via* the ring hydrogen atoms or the hydroxyl hydrogen atom, with the ring carbon atoms and hydroxyl oxygen atoms acting as donors respectively. The cation may also form H-bond with water molecules *via* the ring hydrogen atoms, the hydroxyl group or the π electron cloud of the imidazolium ring. The average number of different types of cation – anion and cation – water H-bonds observed in different $[\text{HOC}_n\text{C}_{10}\text{Im}][\text{Br}]$ solutions are tabulated in 5.2. We see that the average number of head – anion

Table 5.2: Average number of H-bonds formed per cations

System	head-anion	head-water	π -water	hydroxyl-anion	hydroxyl (H)-water (O)	hydroxyl (O)-water (H)
$[\text{HOC}_{10}\text{C}_{10}\text{Im}]$	0.058	3.512	0.290	0.071	1.073	0.864
$[\text{HOC}_7\text{C}_{10}\text{Im}]$	0.023	3.744	0.339	0.024	1.216	1.825
$[\text{HOC}_4\text{C}_{10}\text{Im}]$	0.025	3.837	0.348	0.043	1.288	1.913
$[\text{HOC}_2\text{C}_{10}\text{Im}]$	0.027	3.665	0.473	0.060	1.299	1.459

hydrogen bonds per cation is highest for $[\text{HOC}_{10}\text{C}_{10}\text{Im}]$ cation while it decreases by a factor of ~ 2 for rest of the cations. This observation is consistent with the number of bromide anions present in the first solvation shell of the imidazolium ring hydrogen atoms which is also evident from the intensity of the first maxima of the anion – head group RDFs.

The average numbers of H-bonds formed between water oxygen atoms and imidazolium ring hydrogen atoms per cation show a gradual increase with decrease in the hydroxyalkyl chain length from $[\text{HOC}_{10}\text{C}_{10}\text{Im}]$ to $[\text{HOC}_4\text{C}_{10}\text{Im}]$ cation. The number of water molecules in the first solvation shell of the cation correlates directly with the number of cation – water H-bonds observed (data are not shown here). However, the slight decrease in the average number of H-bonds formed between the water oxygen atoms and ring hydrogen atoms per $[\text{HOC}_2\text{C}_{10}\text{Im}]$ cation may be attributed to the formation of the intramolecular H-bonds between the ring hydrogen atoms and hydroxyl oxygen atoms (discussed in a later section) that hinders the water molecules from taking the required geometrical orientation to form H-bonds. All the cations show π -hydrogen bonding interactions with hydrogen atoms of water molecules and we see that the average number of π -hydrogen bonds

per head group increases gradually with decrease in the hydroxyalkyl chain length.

The average number of H-bonds formed between the hydroxyl hydrogen atom and bromide anions per cation follows the same trend as the average number of head – anion H-bonds per head group. We have seen that this variation in the number of hydroxyl hydrogen – bromide H-bonds correlates with the variation in the intensity of the first maxima in the RDFs of bromide anions around the hydroxyl hydrogen atoms in different $[\text{HOC}_n\text{C}_{10}\text{Im}][\text{Br}]$ solutions studied (Figure D.4, Appendix D). We have noticed that ~50% of these hydrogen bonds are strong in nature. The average number of H-bonds formed between the hydroxyl hydrogen atoms and water oxygen atoms per cation increases gradually as the hydroxyalkyl chain length decreases. As the hydrophilicity of the hydroxyalkyl chain increases with decrease in the chain length, the hydroxyl group tends to be more exposed into water leading to the formation of greater number of hydroxyl hydrogen – water H-bonds. We have found that ~62% of these hydrogen bonds are strong in nature. A gradual increase in the average number of H-bonds formed between the hydroxyl oxygen atoms and water hydrogen atoms is observed, with decrease in hydroxyalkyl chain length (from $[\text{HOC}_{10}\text{C}_{10}\text{Im}]$ to $[\text{HOC}_4\text{C}_{10}\text{Im}]$). The decrease in the average number of hydroxyl oxygen – water H-bonds per $[\text{HOC}_2\text{C}_{10}\text{Im}]$ cation compared to the higher two homologues in the present study is due to the formation of intramolecular H-bonds between the hydroxyl oxygen atoms and the ring hydrogen atoms. About 60% of these H-bonds are strong in nature.

The average number of intermolecular H-bonds formed between the ring hydrogen atoms and hydroxyl oxygen atom in $[\text{HOC}_{10}\text{C}_{10}\text{Im}][\text{Br}]$ solution is 0.378 per cation. The H-bonds are formed between the intercalated $[\text{HOC}_{10}\text{C}_{10}\text{Im}]$ cations within the aggregate. The average number of intramolecular H-bonds between the hydroxyl oxygen atom and ring hydrogen atoms is 0.524 per $[\text{HOC}_2\text{C}_{10}\text{Im}]$ cation. In a detailed analysis, we have found that these intramolecular H-bonds are formed only in the gauche conformation of the N-C-C-O dihedral (discussed later). In most of these intramolecular H-bonds, the angle made by the donor (ring carbon), the hydrogen (attached to the ring carbon) and the acceptor (hydroxyl oxygen) is found to be in the range of ~107-113° (Figure D.5, Appendix D). Formation of intramolecular hydrogen bonds is also observed in pure

hydroxyl functionalized alkylimidazolium based ILs using MD simulations [30]. The RDFs of the hydroxyl oxygen atoms (O_A) around the ring hydrogen atoms (H_A) is shown in figure 5.5. From the

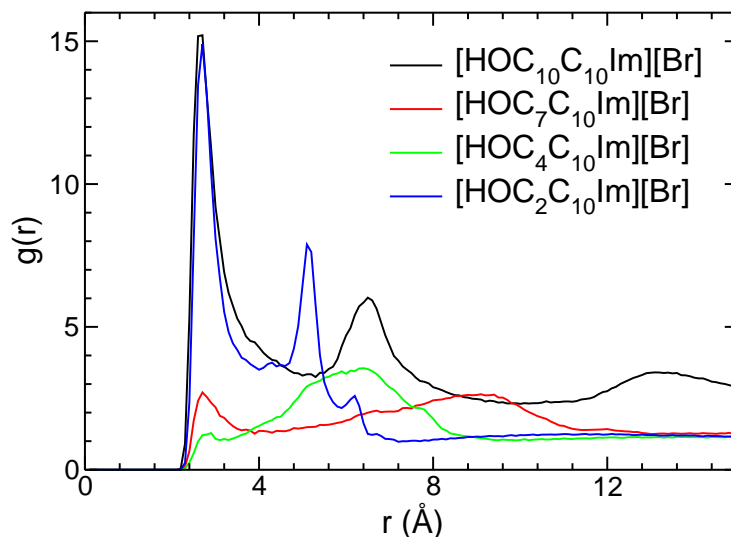


Figure 5.5: RDFs of hydroxyl oxygen atoms around the ring hydrogen atoms in aqueous solutions of $[HOC_nC_{10}Im][Br]$

figure, it is evident that the hydroxyl oxygen atoms interact with the ring hydrogen atoms to a great extent in solutions with hydroxydecyl and hydroxyethyl substituent chains, while in other two solutions such an interaction is not present. In $[HOC_{10}C_{10}Im][Br]$ solution, H-bonds formed are due to intermolecular interactions whereas in $[HOC_2C_{10}Im][Br]$, they arise due to intramolecular interactions which is evident from the greatly diminished first peak in the corresponding $O_A - H_A$ intermolecular RDF (Figure D.6, Appendix D).

5.3.4 Intramolecular Structure

The distribution of angles between the principal vectors (Figure D.7, Appendix D) representing the two intracationic substituent chains (decyl and hydroxyalkyl) in various solutions studied are shown in figure 5.6(a). From the figure, it is evident that the two substituent chains in the $[HOC_{10}C_{10}Im]$ cations show very large probability to be oriented parallel to each other. Both the hydroxydecyl and the decyl chains in the $[HOC_{10}C_{10}Im]$ cations are sufficiently hydrophobic and interact mainly through dispersion interactions, and hence are likely to be oriented parallel to each other giving rise to a very ordered structure (discussed later). Due to presence of hydroxyl group

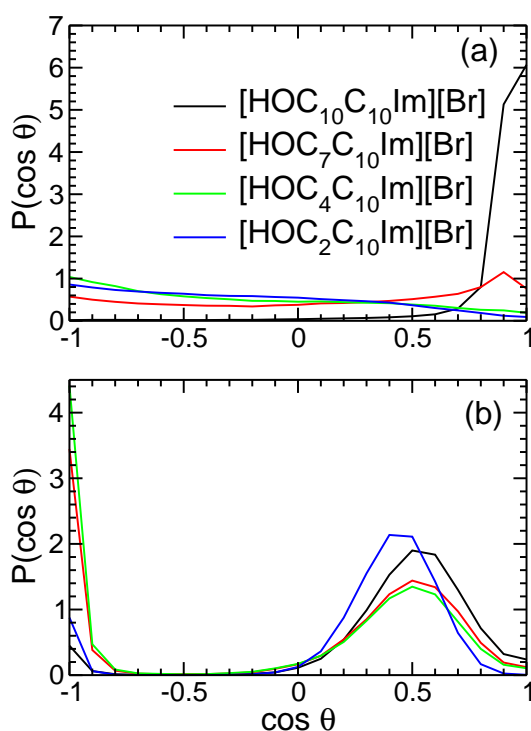


Figure 5.6: Distribution of (a) angles between the two substituent chains (decyl and hydroxyalkyl) attached to the head group and (b) dihedrals formed by the nitrogen atom and successive three non-hydrogen atoms (heavier) of the hydroxyalkyl chain in different $[\text{HOC}_n\text{C}_{10}\text{Im}][\text{Br}]$ solutions.

in the asymmetrically substituted chain, the hydroxyalkyl chains become more hydrophilic with decrease in their length. So, the interaction of the hydroxyalkyl chains with the water molecules become more favorable as the alkyl chain length decreases. As a result, the two alkyl chains in $[\text{HOC}_7\text{C}_{10}\text{Im}]$ cations show only a slight preference to be oriented parallel to each other while they prefer to be oriented antiparallel to each other in $[\text{HOC}_4\text{C}_{10}\text{Im}]$ and $[\text{HOC}_2\text{C}_{10}\text{Im}]$ cations in their respective aqueous solutions. In the absence of the hydroxyl group on the alkyl chain, it has been observed [27] previously that alkyl chains of $[\text{C}_7\text{C}_{10}\text{Im}]$ cations show very high probability to be oriented parallel to each other while the preference is very small to be oriented either in the same or opposite direction in $[\text{C}_4\text{C}_{10}\text{Im}]$ cations in their aqueous solutions. It has also been observed that the probability of finding the two intracationic alkyl chains oriented antiparallel to each other is slightly higher in $[\text{HOC}_4\text{C}_{10}\text{Im}]$ cations than in $[\text{HOC}_2\text{C}_{10}\text{Im}]$ cations. This is due to the formation of intramolecular H-bond between the hydroxyl oxygen atom and the ring hydrogen atom in $[\text{HOC}_2\text{C}_{10}\text{Im}]$ cation which causes the hydroxyethyl chain to be flipped back towards the

decyl chain. Clearly, the presence of the hydroxyl group influences the relative orientation of the two intracationic substituent chains in $[\text{HOC}_n\text{C}_{10}\text{Im}][\text{Br}]$ solutions.

Figure 5.6(b) presents the distribution of the dihedral angles formed by the ring nitrogen atom and the three successive heavier atoms (N-C-C-X, where X is oxygen atom in $[\text{HOC}_2\text{C}_{10}\text{Im}]$ cation and carbon atom in other three cations) of the hydroxyalkyl chains of $[\text{HOC}_n\text{C}_{10}\text{Im}]$ cations in their aqueous solutions. We see that the corresponding dihedrals in $[\text{HOC}_{10}\text{C}_{10}\text{Im}]$ and $[\text{HOC}_2\text{C}_{10}\text{Im}]$ cations show very large probability to adapt gauche conformation ($\sim 98\%$ and $\sim 95\%$ respectively). However, the probabilities of the N-C-C-X dihedrals in $[\text{HOC}_7\text{C}_{10}\text{Im}]$ and $[\text{HOC}_4\text{C}_{10}\text{Im}]$ cations to adapt gauche conformation are relatively lower ($\sim 78\%$ and $\sim 72\%$ respectively). We have also computed the probability distribution of the N-C-C-C dihedral of the decyl chains in all the four solutions studied (Figure D.8, Appendix D) and found that the preference of adapting gauche conformation decreases with decrease in the length of the hydroxyalkyl chain ($\sim 98\%$, $\sim 79\%$, $\sim 70\%$ and $\sim 67\%$ for $[\text{HOC}_{10}\text{C}_{10}\text{Im}]$, $[\text{HOC}_7\text{C}_{10}\text{Im}]$, $[\text{HOC}_4\text{C}_{10}\text{Im}]$ and $[\text{HOC}_2\text{C}_{10}\text{Im}]$ cations respectively). Based on these statistics, we can say that the N-C-C-C dihedrals in both the decyl chain and hydroxyalkyl chain show considerable probability to adapt gauche conformation in $[\text{HOC}_{10}\text{C}_{10}\text{Im}]$, $[\text{HOC}_7\text{C}_{10}\text{Im}]$ and $[\text{HOC}_4\text{C}_{10}\text{Im}]$ cations and this probability decreases with decrease in the hydroxyalkyl chain length.

The preference of the N-C-C-C dihedrals in these three types of cations to adapt gauche conformation arises due to preferred perpendicular orientation (Figure D.9, Appendix D) of the substituent chains (both decyl and hydroxyalkyl) relative to the imidazolium NN vector (vector connecting two nitrogen atoms of the ring). With decrease in the hydrophobicity of the hydroxyalkyl chain, the probability of both the substituent chains to be oriented perpendicular to the NN vector decreases leading to the decrease in gauche probability of the corresponding N-C-C-C dihedrals. In $[\text{HOC}_2\text{C}_{10}\text{Im}]$ cation, although the N-C-C-C dihedral of the decyl chain show lesser gauche probability, the N-C-C-O dihedral of the hydroxyethyl chain shows very high gauche probability. This is due to the formation of the intramolecular H-bond between the hydroxyl oxygen atoms and the ring hydrogen atoms. We have also computed gauche defect probability of each C-C-C-C

dihedral in the decyl chains of $[\text{HOC}_n\text{C}_{10}\text{Im}]$ cations and found that this probability is remarkably lower in $[\text{HOC}_{10}\text{C}_{10}\text{Im}]$ cations. (Figure D.10, Appendix D).

5.3.5 Diffusion of ions and molecules

The self-diffusion coefficient of ions (D) is computed from the slope of the mean-squared displacement, using the Einstein relation

$$D = \frac{1}{6} \lim_{t \rightarrow \infty} \frac{d}{dt} \langle |\vec{r}_i(t) - \vec{r}_i(0)|^2 \rangle$$

where $r_i(t)$ and $r_i(0)$ denote the position of the i -th particle at time t and at the beginning of the measurement. The self-diffusion coefficients of cations correspond to that of the center of mass of the cations. Figure 5.7 shows the self-diffusion coefficients of cations in different aqueous solutions studied. It is observed that the value of self-diffusion coefficient increases from $[\text{HOC}_2\text{C}_{10}\text{Im}]$ to

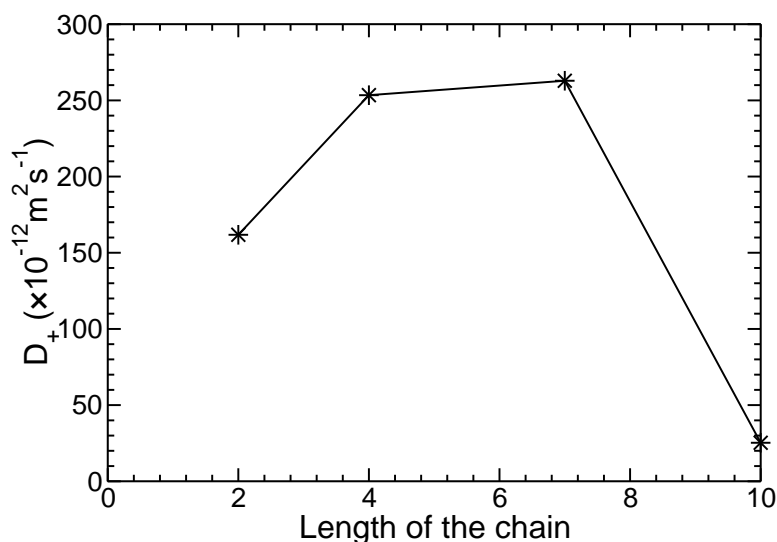


Figure 5.7: Self-diffusion coefficients of cations in different $[\text{HOC}_n\text{C}_{10}\text{Im}][\text{Br}]$ solutions.

$[\text{HOC}_4\text{C}_{10}\text{Im}]$ cations. However, the increase from $[\text{HOC}_4\text{C}_{10}\text{Im}]$ to $[\text{HOC}_7\text{C}_{10}\text{Im}]$ is very small, and further it decreases significantly in case of $[\text{HOC}_{10}\text{C}_{10}\text{Im}]$ cations which have the least value among the four cations in the present study. This variation in self-diffusion coefficient with variation of the hydroxyalkyl chain can be attributed to the formation of aggregates of different sizes in their aqueous solutions. The formation of aggregates increases the apparent mass of the cations, as they are now constituent of an aggregate, and hence hinders their diffusion. The diffusion co-

efficients suggests that the aggregation number is higher in the solution composed of cations with hydroxyethyl chain than that composed of cations with hydroxybutyl chain, and highest in aqueous solution of ILs with hydroxydecyl chain.

5.3.6 Formation of Aggregates

The simulations were started from a uniform configuration of ions. Within few nanoseconds, cations come together to form small aggregates (dimers and trimers). These small aggregates coalesce to form bigger aggregates. The monomers in the solution are also adsorbed into the bigger aggregates. At about 25 ns, in all the solutions except the one with hydroxydecyl substituent chain, the solution had reached metastable state with no further change in the size distribution of the aggregates. In these three systems the aggregates were quasi-spherical in shape with hydrophobic decyl tail buried in the aggregate and the hydrophilic region, i.e., the imidazolium headgroup and the hydroxyl group exposed to water. In the solution with hydroxydecyl substituent chain, the aggregation was still progressing after 25 ns and almost all the cations in the solution formed a single aggregate with a very ordered orientation with intercalation of the decyl and hydroxydecyl chains. Snapshots of the systems with hydroxyethyl and hydroxydecyl chains after 35 ns and 50 ns respectively are shown in figure 5.8. The solution structure in systems with hydroxybutyl and hydroxyheptyl substituent chain were similar to that of the solution with hydroxyethyl side chain

5.3.7 Aggregation Number

The fraction of $[\text{HOC}_n\text{C}_{10}\text{Im}]$ cations involved in the formation of an aggregate of size N in corresponding aqueous solutions is shown in figure 5.9. Cations in the solution were grouped into different aggregates. Two $[\text{HOC}_{10}\text{C}_{10}\text{Im}]$ cations were considered to belong to the same aggregate, if the sixth carbon atoms from the imidazolium end on the hydroxydecyl chains of these cations were present within a distance of 13.0 Å. In the remaining three systems, if the terminal carbon atoms of the decyl chains of the two cations were present within a distance of 10.0 Å, then they were considered to be the constituents of the same aggregate. In all the four systems, the cutoff

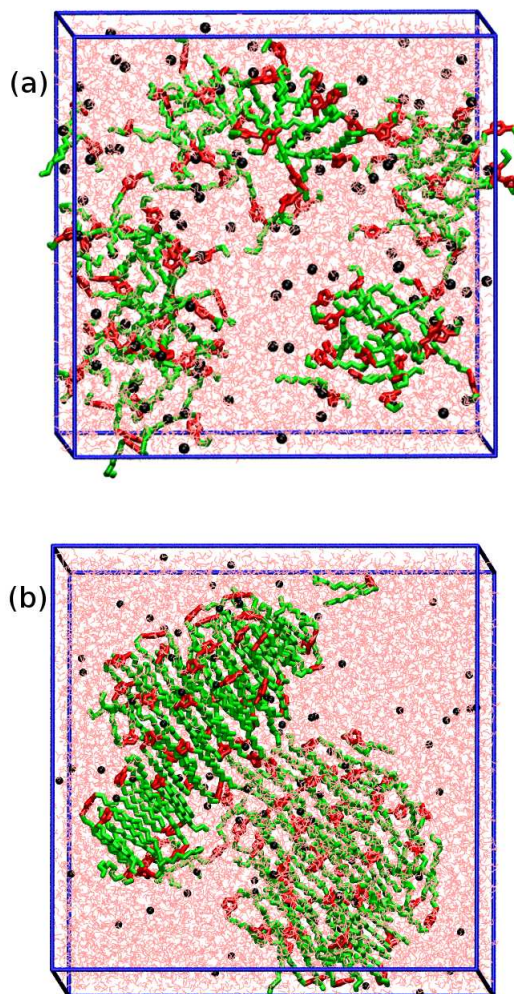


Figure 5.8: Snapshot of (a) the aqueous $[\text{HOC}_2\text{C}_{10}\text{Im}][\text{Br}]$ solution after 35 ns (b) the aqueous $[\text{HOC}_{10}\text{C}_{10}\text{Im}][\text{Br}]$ solution after 50 ns.

distances were chosen by careful inspection of the trajectory.

In $[\text{HOC}_{10}\text{C}_{10}\text{Im}][\text{Br}]$ solution, a cation is most likely to be part of an aggregate of aggregation number 98. The aggregation number fluctuated between 97 and 99 during the last 5 ns of the simulations while the number of monomers fluctuated between 1 and 3 during the same time. In $[\text{HOC}_7\text{C}_{10}\text{Im}][\text{Br}]$ solution, the maximum number of cations were involved in the formation of aggregates of size 10, but many of the cations were also found to form aggregates of size 11 to 19. The highest aggregation number of 31 was observed with a low probability. Many monomers were also present in the $[\text{HOC}_7\text{C}_{10}\text{Im}][\text{Br}]$ solution, which is evident from the probability distri-

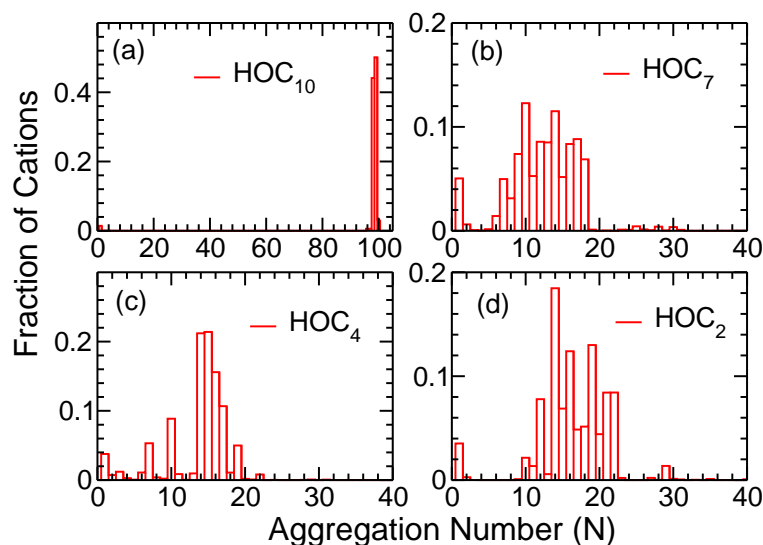


Figure 5.9: Fraction of cations involved in the formation of aggregates of size N in (a) $[\text{HOC}_{10}\text{C}_{10}\text{Im}][\text{Br}]$ (b) $[\text{HOC}_7\text{C}_{10}\text{Im}][\text{Br}]$ (c) $[\text{HOC}_4\text{C}_{10}\text{Im}][\text{Br}]$ and (d) $[\text{HOC}_2\text{C}_{10}\text{Im}][\text{Br}]$ solutions.

bution. The probability of a $[\text{HOC}_4\text{C}_{10}\text{Im}]$ cation to be found in an aggregate of size 14-15 is maximum and the highest aggregation number observed is 31 although with a very small probability. Aggregates of sizes 10, 16, 17 and 19 are also likely to be observed in the solution. In the $[\text{HOC}_2\text{C}_{10}\text{Im}][\text{Br}]$ solution, most cations belong to the aggregates of size 14 which is in good agreement with the aggregation number of 17 determined by steady-state fluorescence quenching in $[\text{HOC}_2\text{C}_{12}\text{Im}][\text{Cl}]$ solution [20]. We see the presence of an aggregate having aggregation number of 40 with very low probability in $[\text{HOC}_2\text{C}_{10}\text{Im}][\text{Br}]$ solution. Considerable number of cations are also involved in the formation of aggregates of size ranging from 15 to 22 in $[\text{HOC}_2\text{C}_{10}\text{Im}][\text{Br}]$ solution. The trend observed in the self-diffusion coefficients of different types of cations in their aqueous solutions (figure 5.7) is consistent with the most probable aggregation number of aggregates formed in the solution

Since almost all the cations in the $[\text{HOC}_{10}\text{C}_{10}\text{Im}]$ are involved in the formation of a single aggregate, the aggregation number reported is not statistically significant. The presence of the hydroxyl group on the alkyl chain increases the most probable aggregation number significantly in $[\text{HOC}_{10}\text{C}_{10}\text{Im}]$ solutions. The shape of the aggregate formed is also completely different compared to the spherical aggregates observed in didecylimidazolium bromide solutions [27]. In case

of $[\text{HOC}_7\text{C}_{10}\text{Im}][\text{Br}]$ and $[\text{HOC}_4\text{C}_{10}\text{Im}][\text{Br}]$ solutions, the most probable aggregation number is lower compared to their non-hydroxylated analogues [27]. It has also been observed experimentally that the aggregation number decreases with the introduction of hydroxyl group into the cation substituent chain in similar ionic liquid solutions [19, 22].

5.3.8 Structure of the Aggregates

The structures of the aggregates in $[\text{HOC}_n\text{C}_{10}\text{Im}][\text{Br}]$ solutions are shown in figure 5.10. In the figure, H-atoms bonded to the carbon atoms, anions and water molecules are not shown for the ease of visualization. The polar head groups of the cations are shown in yellow, the carbon atoms belonging to the alkyl chains are shown in magenta, the oxygen and hydrogen atoms of the hydroxyl group are shown in red and green respectively. Figure 5.10(a) depicts the structure of the

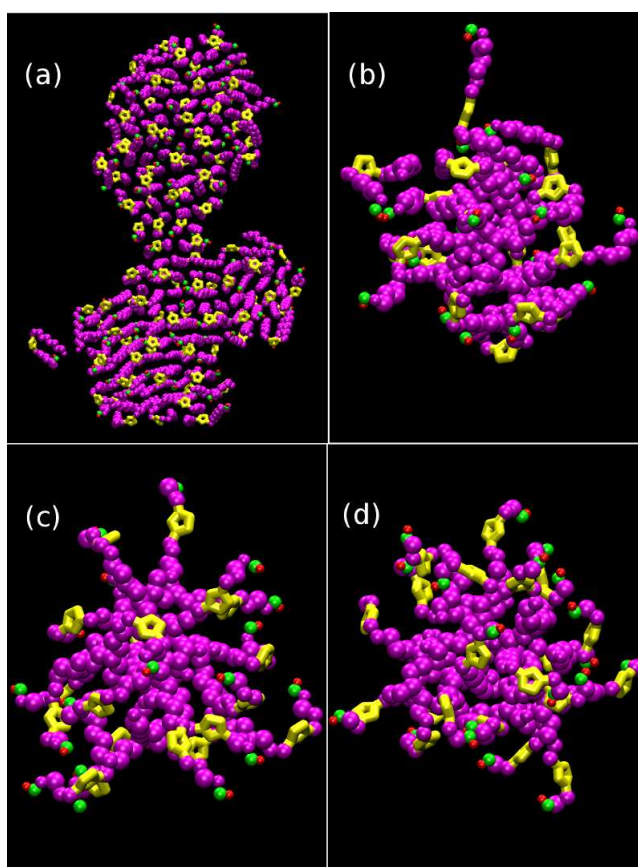


Figure 5.10: Structure of an aggregate in (a) $[\text{HOC}_{10}\text{C}_{10}\text{Im}][\text{Br}]$ (b) $[\text{HOC}_7\text{C}_{10}\text{Im}][\text{Br}]$ (c) $[\text{HOC}_4\text{C}_{10}\text{Im}][\text{Br}]$ and (d) $[\text{HOC}_2\text{C}_{10}\text{Im}][\text{Br}]$ solutions. The polar head groups are shown in yellow, the carbon atoms of the alkyl chains are shown in magenta, the oxygen atom is shown in green and the hydroxyl hydrogen atom is shown in red.

aggregate formed in $[\text{HOC}_{10}\text{C}_{10}\text{Im}][\text{Br}]$ solution. We see that the aggregate has a two dimensional film like structure with no definite geometry. The $[\text{HOC}_{10}\text{C}_{10}\text{Im}]$ cations are intercalated through their hydrocarbon chains with the formation of intermolecular H-bonds between the imidazolium ring hydrogen atoms and oxygen atoms of the hydroxyl groups. The presence of two substituent chains, decyl and hydroxydecyl, both of which are of similar length imparts a very ordered structure to the aggregates in the solution. The decyl group and the alkyl chain of the hydroxydecyl group are hydrophobic, whereas the imidazolium head group and the hydroxyl group are hydrophilic. Therefore, in their aqueous solutions, the cations form aggregates where the interaction between the hydrophilic groups and water is maximized while at the same time, the interaction between water and the hydrophobic groups is minimized. In addition, there are favorable dispersion interactions between the alkyl groups. These three factors lead to the formation of thin film like structures which are one cation thick along the normal direction of the sheet and extended along the other two dimensions. Such a structure is also stabilized by the formation of hydrogen bonds between hydroxyl oxygen atom and the ring hydrogen atoms. Both the surfaces of the thin film are hydrophilic, and the region in between these two surfaces is hydrophobic and is shielded from water by the hydrophilic surface. However, the decyl chains of the cations that are at the edge of the aggregate are exposed to water. We carried out simulations on a smaller system of similar concentration. The structure of the aggregate in the smaller system was found to be similar to that observed in the larger system.

The ordered orientation of $[\text{HOC}_{10}\text{C}_{10}\text{Im}]$ cations in their aqueous solution also results in the greater cation – anion association. The RDF of the anions around the center of the imidazolium ring (figure 5.3) shows a dramatic increase in the intensity of the first maximum compared to the other solutions studied. This is due to the formation of hydrophilic planar surface of head groups leading to a region (surface) of high positive charge density (due to the compact arrangement of cations), which in turn attracts the anions near to the surface. The number of anion – head group hydrogen bonds is also found to be increased by a factor of 2.3 compared to other solutions where the cations form quasi-spherical aggregates (table 5.2).

The aggregates in rest of the three systems are quasi-spherical in shape. The hydroxyalkyl chains of the cations are more likely to be exposed to water whereas the decyl chains are buried inside the hydrophobic core of the aggregates. The aggregates become more spherical with decrease in the length of the hydroxyalkyl chain. The mismatch in the length of the alkyl and hydroxyalkyl chain in case of $[\text{HOC}_7\text{C}_{10}\text{Im}]$ cations prohibit them from forming a more ordered structure. Even though hydroxyheptyl has considerable hydrophobic region, they cannot form a structure like hydroxydecyl cation. In some cations, the heptyl groups are exposed to water, though not completely, and hence prevents the aggregates from attaining spherical shape. The hydroxyethylimidazolium group may be considered as a single hydrophilic group and hence form more spherical aggregates with hydrophobic core and hydrophilic surface. No water molecules and anions were found to be present in the hydrophobic region of any of the aggregates.

The distributions of intracationic angles between the normal vector of the imidazolium ring and the principal vector representing the decyl chain of $[\text{HOC}_n\text{C}_{10}\text{Im}]$ cations in the corresponding aqueous solutions are shown in figure 5.11. We observe that the probability of the ring normal to be

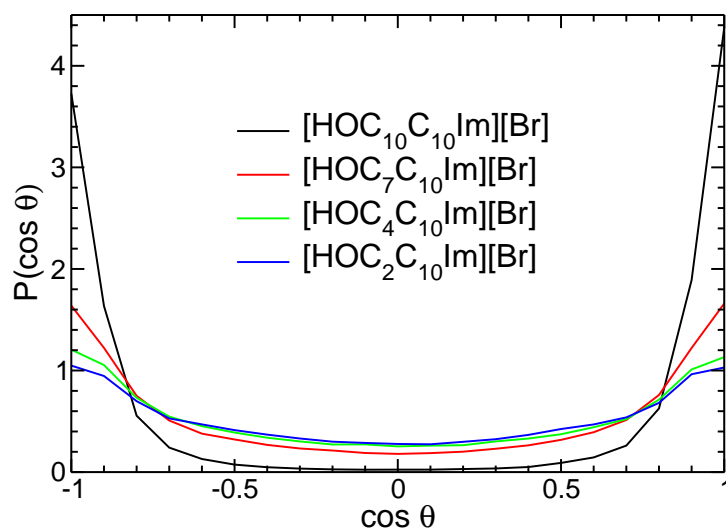


Figure 5.11: Distribution of intramolecular angles formed between the ring normal and the principal vector representing the decyl chain in aqueous $[\text{HOC}_n\text{C}_{10}\text{Im}][\text{Br}]$ solutions.

oriented parallel to the decyl chain vector is very high in $[\text{HOC}_{10}\text{C}_{10}\text{Im}]$ cation and decreases ~ 2 times in $[\text{HOC}_7\text{C}_{10}\text{Im}]$ cation. It decreases further as the length of the asymmetrically substituted hydroxyalkyl chain decreases. In other words, the imidazolium ring plane in $[\text{HOC}_{10}\text{C}_{10}\text{Im}]$ cation

is more likely to be oriented along the planar surface of the aggregate and as the length of the hydroxyalkyl chain decreases the ring planes are more likely to be directed radially outward from the quasi-spherical surface.

The hydration index provides the information about the extent of water penetration into the aggregate, along the alkyl chain of the cation. It is defined as the ratio of the average number of water molecules in the first solvation shell of the alkyl carbon atom in the aggregate, to that which is completely exposed to water. Figure 5.12 shows the hydration index of the carbon atoms on the hydroxydecyl and decyl chains of $[\text{HOC}_{10}\text{C}_{10}\text{Im}]$ cations in the aqueous solution. It can

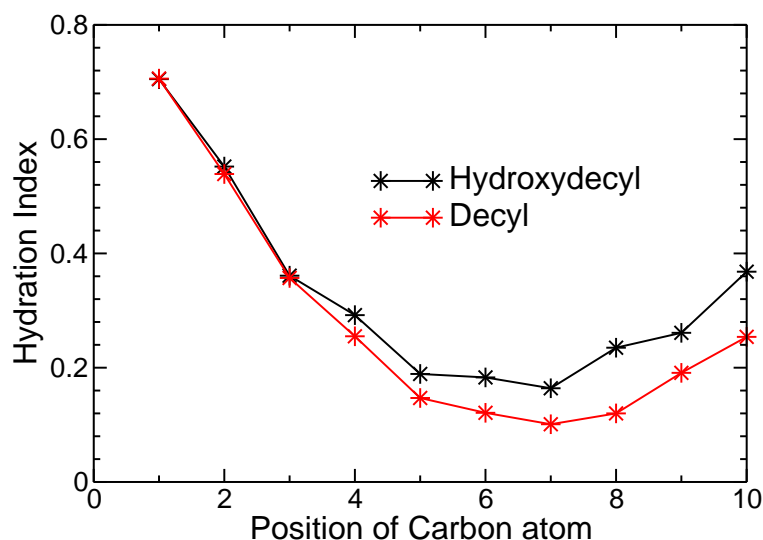


Figure 5.12: Hydration index of various carbon atoms along the hydroxydecyl and decyl chains in aqueous solution of $[\text{HOC}_{10}\text{C}_{10}\text{Im}][\text{Br}]$

be noticed that the water penetration gradually decreases up to the seventh carbon atom from the imidazolium end on both the hydroxydecyl and decyl chains and then it increases slightly. We see that the hydration index values are almost same for both decyl and hydroxydecyl chain up to the third carbon atom from the imidazolium end. Significant departure in the value of hydration index of carbon atoms of decyl chain and hydroxydecyl chain is observed starting from the fourth carbon atom, from the imidazolium ring. The hydration index of the terminal carbon atom of the hydroxydecyl chain is ~47% higher compared to that of the terminal carbon atom of the decyl chain. This is due to the presence of the hydroxyl group on the hydrophilic surface of the

aggregate which draws more number of water molecules near the carbon atom connected to the hydroxyl group. It has also been observed that the hydration index of the carbon atoms along the decyl chain are lower in case of $[\text{HOC}_{10}\text{C}_{10}\text{Im}]$ cations compared to the other cations in various solutions studied (Figure D.11, Appendix D).

5.4. Conclusions Extensive all-atom MD simulations have been carried out on a series of aqueous solutions of 1-(*n*-hydroxyalkyl)-3-decylimidazolium bromide ILs, ($[\text{HOC}_n\text{C}_{10}\text{Im}][\text{Br}]$ with $n=2, 4, 7$ and 10). Starting from a uniform configuration of ions in the solution, the cations come together spontaneously to form aggregates of different sizes. The size and shape of the aggregates depend on the length of the hydroxyl functionalized alkyl chain. The aggregate formed in the aqueous solution of $[\text{HOC}_{10}\text{C}_{10}\text{Im}][\text{Br}]$ has thin film like structure with no regular geometry. The aggregates become more spherical in shape with decrease in the hydroxyl functionalized alkyl chain length. The site – site RDFs of the carbon atoms on the alkyl and hydroxyalkyl chain confirm the difference in the structure of aggregates in $[\text{HOC}_{10}\text{C}_{10}\text{Im}][\text{Br}]$ solution compared to others. The spatial correlation observed over a long length scale in $[\text{HOC}_{10}\text{C}_{10}\text{Im}][\text{Br}]$ solution points to the ordered arrangement of cations over extended range which is not seen in other solutions. Such an aggregate is stabilized by the dispersion interactions between the intercalated alkyl chains and the intermolecular H-bonds formed between the hydroxyl oxygen atoms and the ring hydrogen atoms. Formation of an ordered aggregate is also observed from an independent simulation of aqueous $[\text{HOC}_{10}\text{C}_{10}\text{Im}][\text{Br}]$ solution with a similar concentration and fewer cations.

The SDFs reveal that the anions, water oxygen atoms and the hydroxyl groups prefer to interact with the imidazolium ring hydrogen atoms of $[\text{HOC}_{10}\text{C}_{10}\text{Im}]$ cations through H-bonding interactions. The ring planes are more likely to be oriented along the hydrophilic surface of the aggregate in $[\text{HOC}_{10}\text{C}_{10}\text{Im}][\text{Br}]$ solution. The probability of the imidazolium ring planes to be oriented tangential to the hydrophilic micellar surface (of quasi-spherical aggregates) increases with increase in the length of the substituted hydroxyalkyl chain. The extent of water penetration along the hydrocarbon chains of $[\text{HOC}_{10}\text{C}_{10}\text{Im}]$ cations is greater for the hydroxyl-functionalized decyl chain compared to the non-hydroxylated decyl chain beyond the third carbon atom from

the imidazolium ring. The probability of two intracationic alkyl chains to be oriented parallel to each other increases with increase in the length of the hydroxyl-functionalized alkyl chain. The N-C-C-O dihedral in [HOC₂C₁₀Im] cation prefers to adapt gauche conformation which facilitates the formation of intramolecular H-bond between the ring hydrogen atoms and hydroxyl oxygen atom.

Chapter D

Appendix D

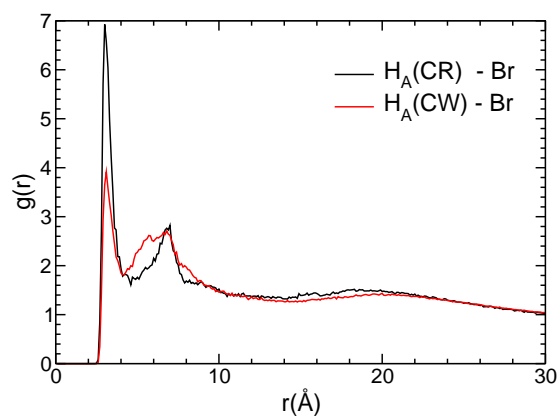


Figure D.1: RDFs of the bromide anions around the imidazolium ring hydrogen atoms in $[\text{HOC}_{10}\text{C}_{10}\text{Im}][\text{Br}]$ solution.

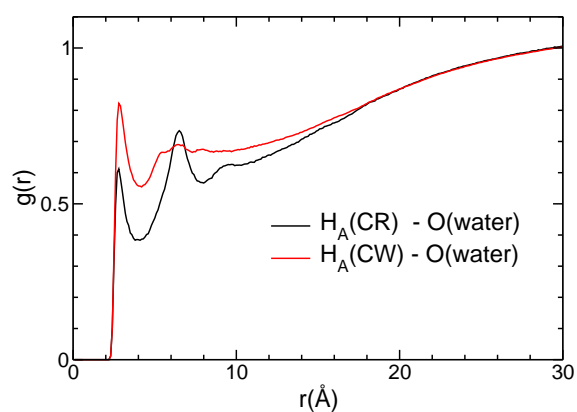


Figure D.2: RDFs of the water oxygen atoms around the imidazolium ring hydrogen atoms in $[\text{HOC}_{10}\text{C}_{10}\text{Im}][\text{Br}]$ solution.

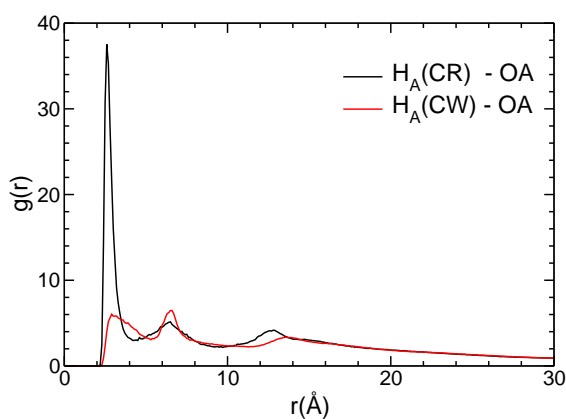


Figure D.3: RDFs of the hydroxyl oxygen atoms around the imidazolium ring hydrogen atoms in $[\text{HOC}_{10}\text{C}_{10}\text{Im}][\text{Br}]$ solution.

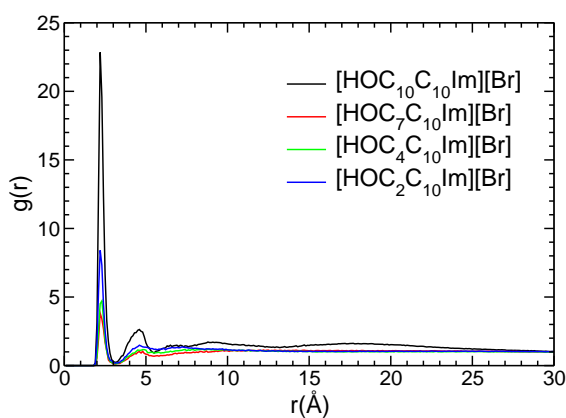


Figure D.4: RDFs of the bromide anions around the hydroxyl hydrogen atom in different $[\text{HOC}_n\text{C}_{10}\text{Im}][\text{Br}]$ solutions.

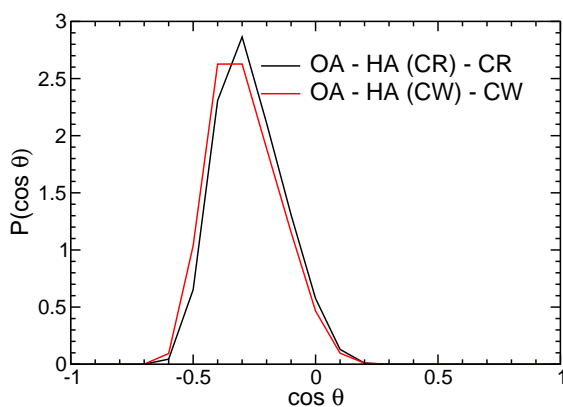


Figure D.5: Distribution of angles made by the donor (ring carbon), hydrogen (attached to the ring carbon) and the acceptor (hydroxyl oxygen) atoms of $[\text{HOC}_2\text{C}_{10}\text{Im}]$ cations in aqueous solution.

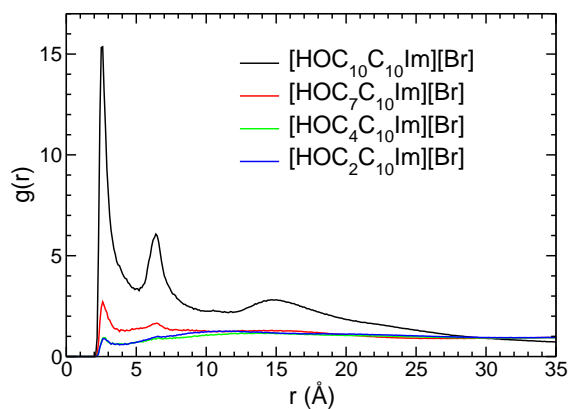


Figure D.6: Intermolecular RDFs of hydroxyl oxygen atoms around the ring hydrogen atoms in aqueous solutions of $[\text{HOC}_n\text{C}_{10}\text{Im}][\text{Br}]$.

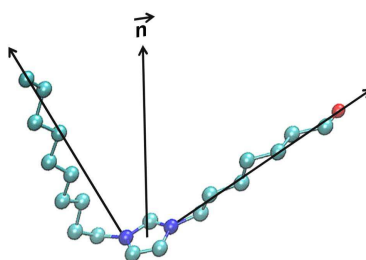


Figure D.7: Pictorial representation of the normal vector to the imidazolium ring and the vectors representing the decyl chain and the hydroxyalkyl chain. Blue, cyan and red beads represent nitrogen, carbon and oxygen atoms respectively. Hydrogen atoms are not shown.

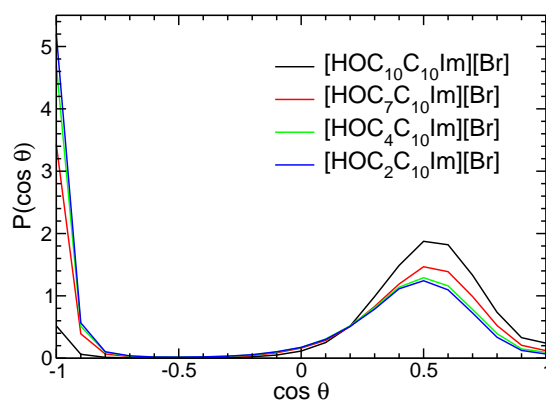


Figure D.8: Distribution of the dihedrals formed by the nitrogen atom of the imidazolium ring and successive three non-hydrogen atoms (heavier) of the decyl chains of the cations in different $[\text{HOC}_n\text{C}_{10}\text{Im}][\text{Br}]$ solutions.

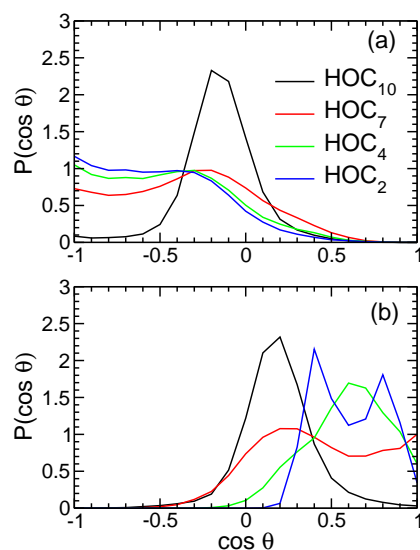


Figure D.9: Distribution of angles formed between (a) the NN vectors and the principal axis representing the decyl chains (b) the NN vectors and the principal axis representing the hydroxyalkyl chains of the cations in their corresponding aqueous solutions.

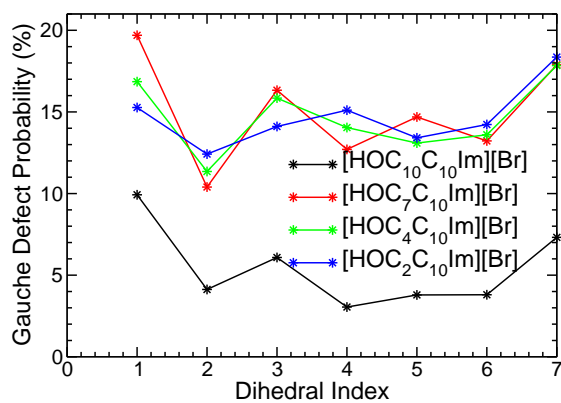


Figure D.10: Gauche defect probability of each C-C-C-C dihedral in the decyl chain of [HOC_nC₁₀Im] cations in their corresponding aqueous solutions.

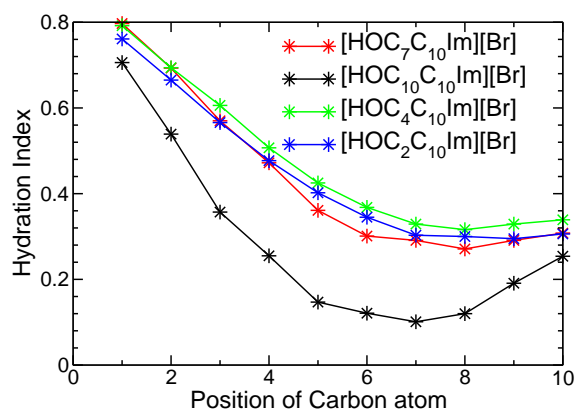


Figure D.11: Hydration index of the carbon atoms along the decyl chain in different $[\text{HOC}_n\text{C}_{10}\text{Im}][\text{Br}]$ solutions.

Bibliography

- [1] Branco, L. C.; Rosa, J. N.; Ramos, J. J. M.; Afonso, C. A. M. *Chem. Eur. J.* **2002**, *8*, 3671-3677.
- [2] Xue, Z.; Zhang, Y.; Zhou, X.; Cao, Y.; Mu, T. *Thermochim. Acta* **2014**, *578*, 59-67.
- [3] Song, Y.; Xia, Y.; Liu, Z. *Tribol. Trans.* **2012**, *55*, 738-746.
- [4] Hossain, M. I.; Babaa, M.; El-Harbawi, M.; Man, Z.; Hefter, G.; Yin, C. *J. Chem. Eng. Data* **2011**, *56*, 4188-4193.
- [5] Hossain, M. I.; El-Harbawi, M.; Alitheen, N. B. M.; Noaman, Y. A.; L ev eque, J.; Yin, C. *Ecotoxicol. Environ. Saf.* **2013**, *87*, 65-69.
- [6] Zhang, S.; Qi, X.; Ma, X.; Lu, L.; Deng, Y. *J. Phys. Chem. B* **2010**, *114*, 3912-3920.
- [7] Wang, L.; Li, P.; Jin, X.; Zhang, J.; He, H.; Zhang, S. *J. CO₂. Util.* **2015**, *10*, 113-119.
- [8] Jalili, A. H.; Mehdizadeh, A.; Skokouhi, M.; Sakhaeinia, H.; Taghikhani, V. *J. Chem. Thermodynamics* **2010**, *42*, 787-791.
- [9] Wang, L.; Jin, X.; Li, P.; Zhang, J. *Ind. Eng. Chem. Res.* **2014**, *53*, 8426-8435.
- [10] Shi, T.; Wang, J.; Sun, J.; Wang, M.; Cheng, W.; Zhang, S. *RSC Adv.* **2013**, *3*, 3726-3732.
- [11] Liu, M.; Gao, K.; Liang, L.; Wang, F.; Shi, L.; Sheng L.; Sun, J. *Phys. Chem. Chem. Phys.* **2015**, *17*, 5959-5965.
- [12] Jiang, Y.; Tang, T.; Cao, Z.; Shi, G.; Zhou, T. *J. Sep. Science* **2015**, *38*, 2158-2166.

- [13] Ebrahimi, M.; Ahmadi, A. N.; Safekordi, A. A.; Fateminasab, F.; Mehdizadeh, A. *J. Chem. Eng. Data* **2014**, *59*, 197-204.
- [14] Yang, X.; Yan, N.; Fei, Z.; Crespo-Quesada, M.; Laurency, G.; Kiwi-Minsker, L.; Kou, Y.; Li, Y.; Dyson, P. J. *Inorg. Chem.* **2008**, *47*, 7444-7446.
- [15] Huang, Z.; Meng, X.; Liu, M.; Wang, S. *Anal. Methods* **2014**, *6*, 8744-8751.
- [16] Sugioka, D.; Kameyama, T.; Kuwabata, S.; Torimoto, T. *Phys. Chem. Chem. Phys.* **2015**, *17*, 13150-13159.
- [17] Zhang, B.; Yuan, Y.; Philippot, K.; Yan, N. *Catal. Sci. Technol.* **2015**, *5*, 1683-1692.
- [18] Lonkar, S. P.; Bobenrieth, A.; Winter, J. D.; Gerbaux, P.; Raquez, J.; Dubois, P. *J. Mater. Chem.* **2012**, *22*, 18124-18126.
- [19] Li, X.; Gao, Y.; Liu, J.; Zheng, L.; Chen, B.; Wu, L.; Tung, C. *J. Colloid. Sci.* **2010**, *343*, 94-101.
- [20] Liu, X.; Dong, L.; Fang, Y. *J. Surfact. Deterg.* **2011**, *14*, 203-210.
- [21] Mirgorodskaya, A. B.; Yackevich, E. I.; Syakaev, V. V.; Zakharova, L. Y.; Latypov, S.K.; Konovalov, A. I. *J. Chem. Eng. Data* **2012**, *57*, 3153-3163.
- [22] Kamboj, R.; Singh, S.; Chauhan, V. *Colloids Surf., A* **2014**, *441*, 233-241.
- [23] Thar, J.; Lehmann, S.; Zahn, S.; Hunger, J.; Buchner, R.; Hunt, P. A.; Welton, T.; Kirchner, B. *J. Chem. Phys.* **2008**, *129*, 104505.
- [24] Bhargava, B. L.; Yasaka, Y.; Klein, M. L. *Chem. Commun.* **2011**, *47*, 6228-6241.
- [25] Frost, D. S.; Dai, L. L. *J. Chem. Phys.* **2012**, *136*, 084706.
- [26] Bhargava, B. L.; Klein, M. L. *J. Chem. Theo. Comput.* **2010**, *6*, 873-879.
- [27] Palchowdhury, S.; Bhargava, B. L. *J. Phys. Chem. B.* **2014**, *118*, 6241-6249.

- [28] Pensado, A. S.; Gomes, M. F. C.; Lopes, J. N. C.; Malfreyt, P.; Pádua, A. A. H. *Phys. Chem. Chem. Phys.* **2011**, *13*, 13518-13526.
- [29] Lísal, M. *J. Chem. Phys.* **2013**, *139*, 214701-214715.
- [30] Fakhraee, M.; Zandkarimi, B.; Salari, H.; Gholami, M. R. *J. Phys. Chem. B* **2014**, *118*, 14410-14428.
- [31] Plimpton, S. *J. Comput. Phys.* **1995**, *117*, 1-19; web: <http://lammps.sandia.gov>.
- [32] Lopes, J. N. C.; Deschamps, J.; Pádua, A. A. H. *J. Phys. Chem. B* **2004**, *108*, 2038-2047; **108**, 11250.
- [33] Lopes, J. N. C.; Pádua, A. A. H. *J. Phys. Chem. B* **2006**, *110*, 19586-19592.
- [34] Shimizu, K.; Almantariotis, D.; Gomes, M. F. C.; Pádua, A. A. H.; Lopes, J. N. C. *J. Phys. Chem. B* **2010**, *114*, 3592-3600.
- [35] Jorgensen, W. L.; Maxwell, D. S.; Tirado-Rives, J. *J. Am. Chem. Soc.* **1996**, *118*, 11225-11236.
- [36] Berendsen, H. J. C.; Postma, J. P. M.; van Gunsteren, W. F.; Hermans, J. In *Intermolecular Forces*; Pullman, B., Ed.; Reidel: Dordrecht, The Netherlands, 1981; p 331.
- [37] Berendsen, H. J. C.; Grigera, J. R.; Straatsma T. P. *J. Phys. Chem.* **1987**, *91*, 6269-6271.
- [38] Allen, M. P.; Tildesley, D. J. *Computer Simulation of Liquids*; Clarendon Press: Oxford, U.K., 1987.
- [39] Ryckaert, J. P.; Ciccotti, J.; Berendsen, H. J. C. *J. Comput. Phys.* **1977**, *23*, 327-341.
- [40] Humphrey, W.; Dalke, A.; Schulten, K. *VMD J. Mol. Graphics* **1996**, *14*, 33-38.
- [41] Palchowdhury, S.; Bhargava, B. L. *Phys. Chem. Chem. Phys.* **2015**, *17*, 11627-11637.
- [42] Bini, R.; Bortolini, O.; Chiappe, C.; Pieraccini, D.; Siciliano, T. *J. Phys. Chem. B* **2007** *111*, 598-604.

- [43] Palchowdhury, S.; Bhargava, B. L. *J. Phys. Chem. B* **2014**, *118*, 13930-13939.
- [44] Desiraju, G. R.; Steiner, T. *The Weak Hydrogen Bond, In Structural Chemistry and Biology*; Oxford University Press: New York, 2001.

Chapter 6

Effect of spacer chain length on the liquid structure of aqueous dicationic ionic liquid solutions: Molecular dynamics studies

Abstract:

The liquid structure of aqueous solutions of five different imidazolium based gemini dicationic ionic liquids 1,n-bis(3-methylimidazolium-1-yl) alkane bromide (n being the length of the spacer alkyl chain), with propyl, pentyl, octyl, decyl and hexadecyl spacer chain has been studied using atomistic molecular dynamics simulations. While solutions with propyl and pentyl spacer are homogeneous, those with octyl and decyl spacers show spatial heterogeneity. Microscopic inhomogeneity in the bulk solution phase increases with increase in the length of the spacer chain leading to polydisperse aggregates in solution with hexadecyl spacer. Organization of the cations at the solution–vapor interface also depends upon the length of the spacer chain with most organized interfacial layer observed in the solution with hexadecyl spacer chain.

6.1. Introduction Gemini surfactants have drawn the attention of researchers for their versatile use in industrial, medical and scientific applications. Gemini surfactants contain two polar head groups linked by a rigid or flexible spacer [1, 2]. They have lower critical micelle concentrations (CMCs) compared to their single head group counterpart [3, 4, 5, 6]. So, one can use small amount of gemini surfactants instead of the large amount required for conventional surfactants to achieve the same results. This makes them environment friendly and cost effective. Due to their low CMCs, slow millisecond monomer-micelle kinetics [7] and smaller aggregation number, they are extensively used in the field of biochemical research [8, 9, 10], gene delivery [11, 12, 13], drug delivery [14, 15] and antimicrobial activity [16, 17, 18]. They also have wide applications in the field of material science and nanotechnology [19, 20].

Imidazolium-based ionic liquids are a class of materials that have been extensively studied by the researchers in the past two decades due to their specific physicochemical properties [21, 22, 23, 24, 25]. This has led the surfactant chemists to design, characterize and explore surface activity of gemini surfactants containing imidazolium cations as head groups. Imidazolium based dicationic ionic liquids (DILs) are thermally more stable than their monocationic counterpart [26] and show affinity for self-aggregation in aqueous or polar media [4, 27]. They also have potential applications in nano technology [28], as carriers for therapeutic DNA [29], gene-delivery agents [30] and modulator for the growth of nanorods or 2D Langmuir films [31].

Even though considerable number of experimental investigations have been carried out on imidazolium based DILs [4, 32, 33, 34, 35], only few theoretical studies have been reported [36, 37, 38, 39, 40, 41, 42]. Computational studies on the structure of gemini imidazolium based ILs in the gas phase [36], and in the liquid phase [36, 37, 38] have been reported. Molecular dynamics (MD) studies have probed the effects of spacer length and anions on the liquid structure and dynamical properties of imidazolium based DILs [39, 40]. The length and polarity of the spacer length plays an important role in determining the liquid structure of imidazolium based DILs in aqueous solution [4, 32, 33]. Only few computational studies are available on the aggregation properties of imidazolium based DILs in aqueous solutions [41, 42]. We have carried out atom-

istic MD simulations on aqueous $[C_n(\text{MIm})_2][2\text{Br}]$ solutions to gain insights into the structure of the solution at atomic level. Simulations have been performed on a series of aqueous DIL solutions varying the spacer chain length from propyl to hexadecyl, mimicking bulk and liquid–vapor interface of the solution.

6.2. Methodology and Simulation Details We have carried out all-atom classical MD simulations on a series of aqueous 1,n-bis(3-methylimidazolium-1-yl) alkane bromide ($[C_n(\text{MIm})_2][2\text{Br}]$ (where $n= 3, 5, 8, 10, 16$)) solutions, using the LAMMPS package [43]. The simulated systems differed from each other in the length of the hydrocarbon spacer in the cation. The all-atom force field parameters for DILs are adapted from the work of Pádua and coworkers [44]. A minor modification of atomic partial charge for the $[C_3(\text{MIm})_2]$ cation was made, that is mentioned elsewhere [41]. The simple point charge model (SPC) has been used to model [45] water molecules.

$[C_8(\text{MIm})_2][2\text{Br}]$ and $[C_{10}(\text{MIm})_2][2\text{Br}]$ solutions have been simulated at two different concentrations. Details of the systems studied have been presented in the table 6.1. The initial concentration

Table 6.1: Details of the simulated bulk systems; n represents the number of carbon atoms in the spacer chain.

n	no. of ion pairs	no. of waters	no. of atoms	run length(ns)	box length(Å)	concentration (M)
3	125	1971	10288	50	47.12	1.98
5	125	2223	11794	50	49.12	1.75
8	120	6000	24000	50	62.36	0.82
8	120	3000	15000	50	53.20	1.32
10	120	6000	24720	50	62.94	0.80
10	120	3000	15720	50	53.96	1.27
16	100	8577	33131	50	69.40	0.50
16	1	3813	11513	20	49.05	—

figurations were generated by replicating the ion unit (cation and two bromide anions) along three dimensions and placing it in a water box with randomly oriented water molecules at experimental density. Water molecules that were within 3.0 \AA of any atoms of the cation or anions were removed.

All simulations were performed at 300 K. The equations of motion were integrated using the verlet algorithm with a time step of 0.5 fs. The initial configurations were equilibrated under isothermal-isobaric (constant NPT) condition at 1 atmosphere pressure using the N ose-Hoover barostat with a pressure damping parameter of 500 fs for 2 ns to get the equilibrated density. The canonical ensemble simulations (constant NVT) were performed starting from the last configuration of NPT simulation with a volume that was obtained (averaged over last 1 ns) from constant NPT simulations. Three dimensional periodic boundary conditions were used.

The box length and the run length in table 6.1 correspond to the bulk phase simulations. The solution–vapor interface simulations have been carried out by placing the equilibrated bulk system at the center of the box that was extended along the z-direction to 130.0   for [C₁₆(MIm)₂][2Br] solution and 100.0   for others. 25 ns trajectory was generated for each of these simulations. All other conditions were same as mentioned for bulk simulations. The atomic positions were stored at an interval of 5 ps. For the calculation of surface tension, pressure tensor was stored at each step during the last 1 ns of solution–vapor interface simulations. All equilibrium properties presented here have been averaged over the last 5 ns of trajectory unless mentioned otherwise. The schematic of the general structure of the cations studied is shown in figure 6.1.

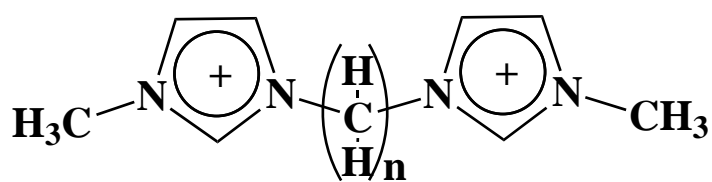


Figure 6.1: Schematic representation of the [C_n(MIm)₂] cation.

6.3. Results and Discussion

6.3.1 Radial Distribution Functions (RDFs)

RDFs provide the information about the short-range ordering in liquids. Figure 6.2(a) presents the RDFs of anions (Br[−]) around the geometric center of the imidazolium rings of the cations in various aqueous solutions. The RDFs for [C₁₀(MIm)₂][2Br] and [C₈(MIm)₂][2Br] presented in this section corresponds to the lower concentration systems, i.e., 0.8 M and 0.82 M solutions

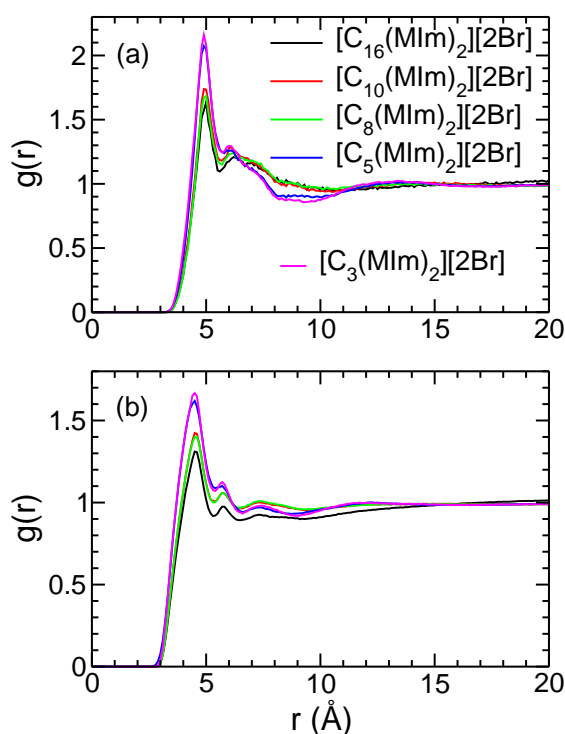


Figure 6.2: RDFs of (a) anions and (b) water molecules around the geometric center of the imidazolium rings in different aqueous solutions.

respectively. All the five curves show a sharp peak near 5 Å. This suggests that the anions are well organised around the imidazolium rings in all the aqueous systems. However, the peak height decreases with the increase in the spacer chain length, suggesting the decrease in the organisation of anions around the imidazolium rings with increase in spacer length. It has been reported that the cation-anion interaction strength decreases with increase in the substituent chain length in imidazolium based monocationic ILs [49]. Even though there is no estimation of cation-anion interaction strength in imidazolium based gemini ILs, it is expected that the interaction strength decreases with increase in the length of the spacer chain. Based on this, it can be inferred that the organisation of anions around the ring center decreases with increase in the spacer chain length. We have also observed an increase in the peak height at higher concentrations for the decyl and octyl spacer systems (Figure E.1, Appendix E).

The RDFs of oxygen atoms of water molecules around the imidazolium rings in different aqueous solutions studied are shown in figure 6.2(b). The first maxima are observed at 4.5 Å in all the RDFs. The organisation of water molecules around the imidazolium rings decreases with increase

in the spacer chain length. This observation can be attributed to the enhanced hydrophobicity of the cation with increase in the spacer chain length, which hinders the favorable interaction of water molecules with the imidazolium rings. The amplitude of the first maxima is found to increase in systems with octyl and decyl spacer at higher concentration. (Figure E.2, Appendix E).

Figure 6.3(a) illustrates the RDFs of the carbon atoms of the hexadecyl spacer around themselves in the aqueous solution. The subscript represents the position of the carbon atom from the imidazolium ring. An intense peak was observed at 5.2 Å in the RDF of eighth carbon atoms (two

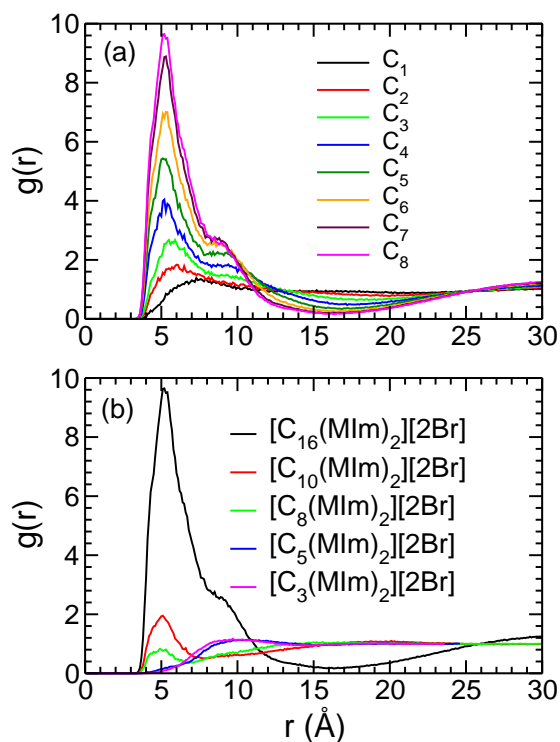


Figure 6.3: RDFs of (a) different carbon atoms of the hexadecyl spacer around themselves in aqueous solution of $[C_{16}(MIm)_2][2Br]$ (b) central carbon atom of the spacer chain around themselves in the aqueous solutions of $[C_n(MIm)_2][2Br]$ systems.

central carbon atoms of spacers) around themselves. The amplitude of the first maxima for RDFs of carbon atoms around themselves decreases as we move towards either of the imidazolium rings. For the second spacer carbon atoms from the imidazolium rings, a broad peak was observed, while the spacer carbon atoms linked to the imidazolium nitrogen atoms do not show any peak in that region. This observation demonstrates the fact that the $[C_{16}(MIm)_2]$ cations are organised mostly about their eighth carbon of the hexadecyl spacer in aqueous solution. This kind of organization

maximizes the van der Waals attractive interaction between the spacer chains while simultaneously reducing the repulsive hydrophobic interactions between the alkyl chain and water. Similar trends are observed in the RDFs of spacer carbon atoms around themselves in solutions of DILs with decyl, octyl and pentyl spacer. Nevertheless, the amplitudes are significantly higher only in case of decyl spacer. For the aqueous solution with DIL containing propyl spacer, both RDFs are similar (Figure E.3, Figure E.4, Figure E.5 and Figure E.6, Appendix E).

Figure 6.3(b) shows the pair correlation functions of the central spacer carbon atoms around themselves for the cations in their aqueous solutions. The central spacer carbons have been chosen as the eighth, fifth, fourth, third and second carbon atoms from either of the imidazolium ends for the hexadecyl, decyl, octyl, pentyl and propyl spacers respectively. It is observed that the amplitude of the first maxima is highest for the hexadecyl spacer and decreases with reduction in the length of the spacer chain. The octyl spacer shows a broad first maximum at that region while the pentyl and propyl spacers do not show any peaks. These observations suggest that the spatial correlation of spacers decreases with decrease in the van der Waals interaction between them in short spacers. and the solutions become microscopically homogeneous for the solutions of DILs with pentyl and propyl spacers. The amplitude of the peaks was observed to increase with increase in the concentration of the solution (Figure E.7, Appendix E).

6.3.2 Hydrogen Bonding

Hydrogen bonding plays an important role in molecular association and hence in structural chemistry and biology. Hydrogen bonding interactions in aqueous solution of monocationic ILs have been reported [50, 51]. In this study the geometric criteria [52] have been adapted to classify H-bonds. In a strong H-bond, the H-atom and the acceptor are separated by a distance less than 2.2 Å and the angle made by the donor, H-atom and the acceptor should fall within the range of 130-180°. The corresponding distance range and angular range are 2.0-3.0 Å and 90-180° respectively, in a weak hydrogen bond.

We have identified the cation-anion H-bonds assuming the imidazolium ring carbon atoms as the donors. H-bonds formed between ring hydrogen atoms and water oxygen atoms along with

π -hydrogen bonding interaction between the π electron cloud of the imidazolium ring and water hydrogen atoms [53, 54] are identified as cation-water H-bonds. Average number of head - anion and head - water H-bonds observed in different aqueous dicationic IL solutions are tabulated in table 6.2. From the table 6.2, we see that the average number of head - anion H-bonds per head

Table 6.2: Average number of H-bonds formed per head group

System	head-anion	ring hydrogen-water	π -water
[C ₁₆ (MIm) ₂]	0.057	4.069	0.045
[C ₁₀ (MIm) ₂](0.80 M)	0.102	4.083	0.046
[C ₁₀ (MIm) ₂](1.27 M)	0.219	3.888	0.042
[C ₈ (MIm) ₂] (0.82 M)	0.101	4.115	0.046
[C ₈ (MIm) ₂] (1.32 M)	0.220	3.926	0.042
[C ₅ (MIm) ₂]	0.320	3.852	0.064
[C ₃ (MIm) ₂]	0.349	3.973	0.041

group increases with decrease in the spacer chain length. This observation is consistent with the number of bromide anions present in the first coordination shell of the imidazolium ring (ring hydrogen atoms). Cations with higher number of anions in their first coordination shell exhibit more number of hydrogen bonds between the head group and bromide ions (data are not shown here). We have also observed an increase in average number of cation-anion H-bonds per head group for [C₁₀(MIm)₂] and [C₈(MIm)₂] cations in their aqueous solutions at higher concentration.

The average number of H-bonds formed between water oxygen atoms and imidazolium ring hydrogen atoms per head group show gradual increase with decrease in spacer length from hexadecyl to octyl spacer at comparable concentrations. There is a decrease in this number for the [C₁₀(MIm)₂] and [C₈(MIm)₂] solutions at higher concentrations. However for the [C₅(MIm)₂] and [C₃(MIm)₂] cations in their solutions, the average number of H-bonds formed per head group with water molecules decrease slightly. All these observations are consistent with the number of water molecules present in the first solvation shell of the imidazolium ring or ring hydrogen atoms of the corresponding cation, i.e., more the hydration number, more the number of hydrogen bonds between the head group and water oxygen atoms (data are not shown here).

All the cations show π -hydrogen bonding interactions with water hydrogen atoms but no spe-

cific trend is observed. Bromide anions are also found to form H-bonds with water molecules in all the systems studied. Average number of bromide-water H-bonds varied between 6-7 in different systems. Roughly 35% of these are strong H-bonds.

6.3.3 Spatial Distribution

Spatial distribution functions (SDFs) provide insight into the three dimensional arrangement of atoms or groups around other atoms or groups. Figure 6.4 shows the spatial distributions of anions (in yellow) and water (in red) around imidazolium rings of cations in $[C_{16}(MIm)_2]$ solution. The isosurface of both anions and water correspond to 2 times their average density. It is evident from the figure that anions tend to concentrate near the ring hydrogen atoms due to formation of H-bonds. The anion density is maximum near the most acidic ring hydrogen atom which is attached to the unique carbon bonded to two nitrogen atoms. The water molecules also tend to aggregate near the ring hydrogen atoms. However, we see accumulation of water molecules above and below the imidazolium ring plane.

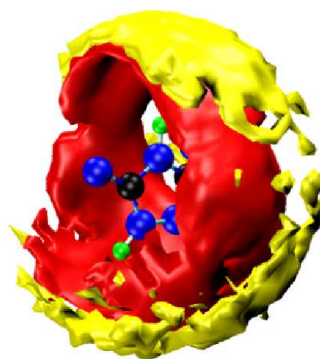


Figure 6.4: (a) Spatial density of anions and water molecules around the imidazolium rings in $[C_{16}(MIm)_2][2Br]$ solution (b) Another view of the same figure.

6.3.4 Intramolecular Structure

Figure 6.5(a) shows the angle distribution between the normal vectors of the two imidazolium rings that are connected by the alkyl spacer. We have found that the probability for the two intracationic imidazolium planes to be oriented either parallel or antiparallel to each other increases with decrease in the spacer chain length from hexadecyl to pentyl spacer in aqueous DIL solutions.

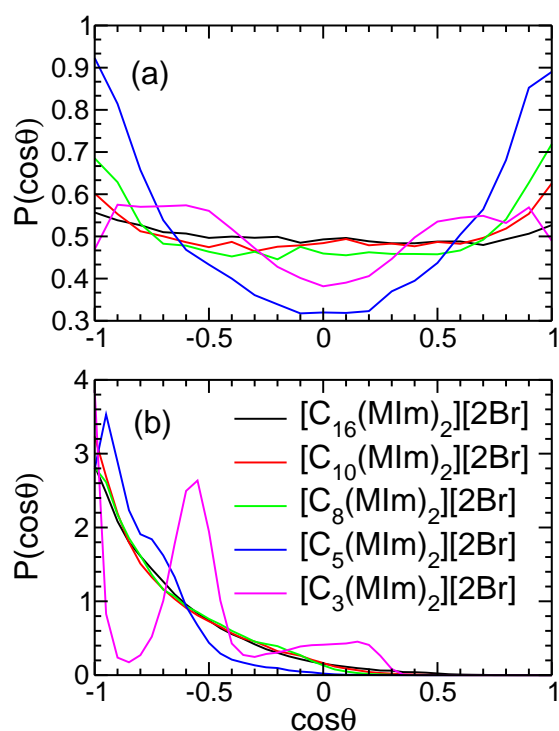


Figure 6.5: Distribution of angles between (a) the normal vectors of the two imidazolium rings separated by the alkyl spacer and (b) the two vectors joining the central carbon atom of the spacer with the imidazolium nitrogen atoms connected to the spacer, in aqueous solutions of DILs.

For the $[C_5(\text{MIm})_2]$ cation, this probability is maximum while it decreases for the propyl spacer and the rings remain in a twisted orientation from each other (125° - 160°). The parallel orientation of the two imidazolium planes is a direct consequence of $\pi - \pi$ stacking interaction between the rings. For a very long hydrocarbon spacer like hexadecyl, this interaction is very weak and hence the orientation of the two rings with respect to each other is almost random. With decrease in the spacer length, the $\pi - \pi$ stacking interaction increases, leading to a greater probability of observing the parallel or antiparallel orientation of the rings within a cation. The variation in the extent of spacer folding due to $\pi - \pi$ stacking is depicted in figure 6.5(b). The angle of folding is defined as the angle between the two vectors joining the central spacer carbon with the nitrogen atoms of the two imidazolium rings linked with the alkyl spacer. We see that the spacers remain unfolded for spacer length greater than five. For the $[C_5(\text{MIm})_2]$ cation, the most probable angle between the two vectors is 162° while for the $[C_3(\text{MIm})_2]$ cation, although the propyl chain prefers to remain unfolded, we observe a sharp peak near 123° . It is also observed that there is a high probability of

the two imidazolium rings orienting either parallel or antiparallel to each other with considerable spacer folding for $[C_{16}(MIm)_2]$ cation in gas phase (Figure E.8, Appendix E). This suggests that hydration of the imidazolium rings in aqueous solution decrease $\pi - \pi$ stacking interaction.

6.3.5 Formation of Aggregates

MD simulations were started from a uniform distribution of cations in aqueous solution. Both of the bromide anions were placed near the head groups. The $[C_3(MIm)_2][2Br]$ and $[C_5(MIm)_2][2Br]$ solutions remained almost isotropic throughout the course of the simulation. The $[C_8(MIm)_2][2Br]$ and $[C_{10}(MIm)_2][2Br]$ solutions, both in concentrated and dilute systems, showed microscopic inhomogeneity on a small length scale with the presence of few dimers and trimers. In $[C_{16}(MIm)_2][2Br]$ solution, the cations came together very rapidly to form oligomers within first 5 ns of the simulation. The oligomeric aggregates fused to form bigger aggregates (Figure E.9, Appendix E). It was observed that the cations were dynamic with few of them adsorbing into the aggregate from the free monomeric state and few cations from the aggregate entering into the solution to become free monomers. The hydrophobic hexadecyl spacers club together to form the hydrophobic core of the aggregates whereas the polar head groups form the surface of the aggregates. In aqueous solutions of monocationic ILs, cations with octyl or longer chains form well defined aggregates [50] whereas in dicationic IL solutions aggregates are not formed even with the decyl spacer chain. So, in addition to the length of the alkyl chain, its location in the cation is also important in the formation of aggregates.

6.3.6 Aggregation Number

The fraction of $[C_{16}(MIm)_2]$ cations involved in forming an aggregate of size N in aqueous solution is shown in figure 6.6. Two cations are considered to be belonging to the same aggregate if the central carbon atoms of two hydrocarbon spacers are within a specified distance cutoff. For $[C_{16}(MIm)_2]$ cations, the cutoff distance has been chosen as 12.0 Å by careful inspection of the trajectory. For the $[C_{16}(MIm)_2]$, most probable aggregation number ranges from 6 to 7. We have also found formation of aggregates of size 8, 11, and 12 with considerable probability. The highest

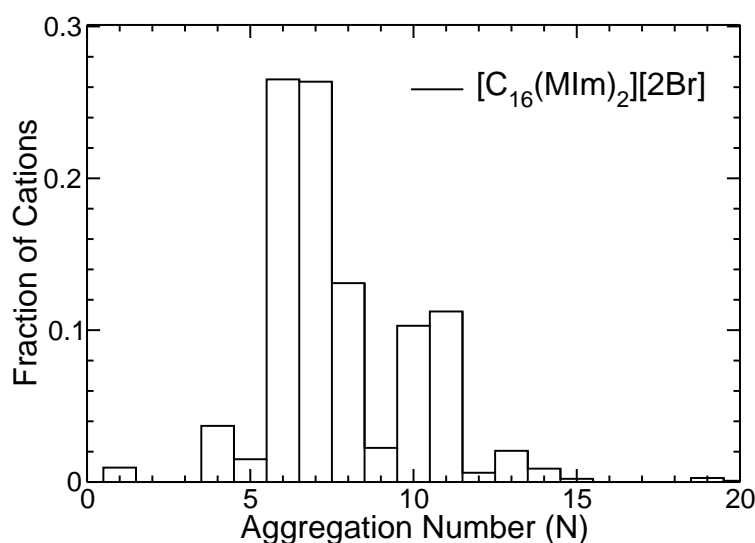


Figure 6.6: Fraction of cations involved in forming aggregates of size N in an aqueous solution of $[C_{16}(MIm)_2][2Br]$.

aggregation number was found to be 19 with very small probability for $[C_{16}(MIm)_2]$ cations. The fraction of cations that remained as monomers is quite low in aqueous solution with hexadecyl spacer. The aggregation numbers observed in aqueous DIL solution with hexadecyl spacer are lower compared to those in aqueous solution of the monocationic IL, $[C_{16}Mim][Br]$. The aggregation number in aqueous solution of $[C_{16}Mim][Br]$ is reported to be 66 [55]. The presence of the alkyl chain between two hydrophilic groups hinders the formation of aggregates in DIL solutions with smaller spacer chains and reduces the size of the aggregates in solutions of cations with longer spacer chains, compared to their monocationic counterparts. In case of $[C_n(MIm)_2]$ ($n=3,5$), most of the cations remain as monomers while only a small fraction of cations are involved in the formation of dimers (not shown here). $[C_8(MIm)_2]$ and $[C_{10}(MIm)_2]$ cations also exist primarily as monomers although they show appearance of dimers and trimers in their aqueous solutions. However, the probability of observing dimers is higher for octyl and decyl spacer and increases with increase in concentration. At higher concentration of $[C_{10}(MIm)_2]$, formation of tetrameric aggregates is observed.

6.3.7 Structure of $[C_{16}(MIm)_2]$ aggregates

The structure of an aggregate in aqueous $[C_{16}(MIm)_2][2Br]$ solution is shown in figure 6.7. Only

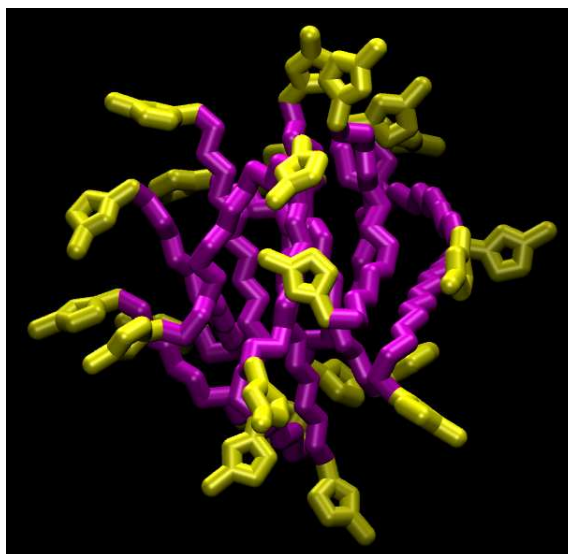


Figure 6.7: Structure of an aggregate in aqueous solution of $[C_{16}(MIm)_2][2Br]$. Atoms belonging to head groups are shown in yellow, and those belonging to the spacer chain are represented as magenta beads. Anions, water molecules and hydrogen atoms belonging to cations are not shown for the ease of visualization.

the heavy atoms of the aggregate are shown for the ease of visualization. We see that the aggregates are quasispherical in shape. The polar head groups are represented in yellow, whereas the carbon atoms are shown in magenta. Both the imidazolium rings of the cation are exposed to water, thus maximizing the favorable interaction with water. The hexadecyl spacers of cations form the hydrophobic core of the aggregate thus minimizing the unfavorable interaction of the hydrocarbon spacers with the water molecules. The spacers are extending from one end of aggregate to the other, resulting in the center of the spacer to be buried in the hydrophobic core. Both the head groups of the cation are part of the positively charged micellar surface. No anions or water molecules are found in the hydrophobic core of the aggregate. We have also characterized the aggregates by calculating the most probable radius of the aggregate and the most probable radius of the hydrophobic core from the center of mass of the aggregate. The radius of the aggregate is defined as the distance between the center of mass of the aggregate and the geometric center of the imidazolium ring. We have found that the water molecules rarely penetrate beyond the second carbon atom of the hexadecyl spacer from the imidazolium ring. Hence, we have defined the radius of the hydrophobic core as the distance between the center of mass of the aggregate and the

second carbon atom of the hexadecyl spacer mentioned above. The probability distribution of both the radii are shown in figure 6.8. The most probable radii of the aggregates and the hydrophobic

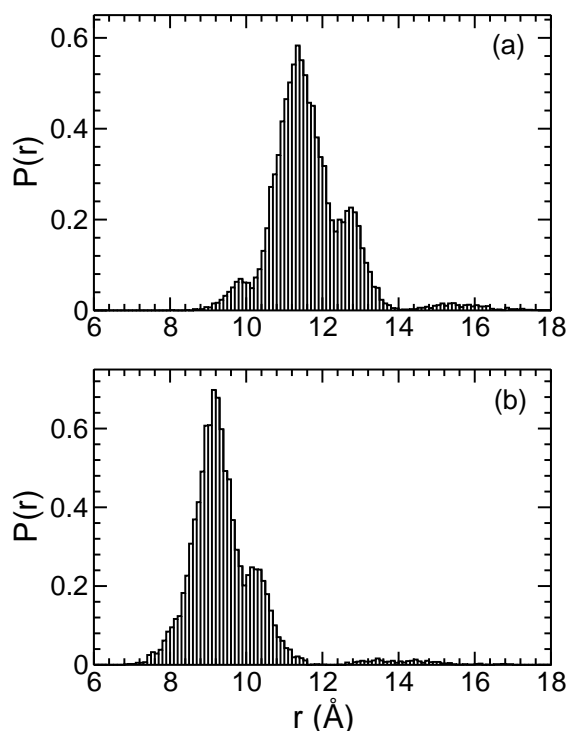


Figure 6.8: Probability distribution of radii of (a) aggregates and (b) hydrophobic core for the aggregates in aqueous solution of $[C_{16}(MIm)_2][2Br]$.

core are calculated to be 11.4 Å and 9.2 Å respectively.

Hydration index provides the information about the extent of water penetration into the aggregates. It is defined as the ratio of the average number of water molecules in first solvation shell of the spacer carbon atom in the aggregate, to that which is completely exposed to water. Figure 6.9 shows the hydration index of carbon atoms on the hexadecyl chain in aqueous $[C_{16}(MIm)_2][2Br]$ solution. We notice that water penetration gradually decreases as we move toward the central carbon atom of the spacer, i. e., toward the hydrophobic core from the imidazolium end. It decreases up to 60% from the first carbon atom of the hexadecyl spacer to the central carbon atom. The hydration index of the central spacer carbon atom does not reach the ideal value of zero because the monomers and oligomers have also been taken into account.

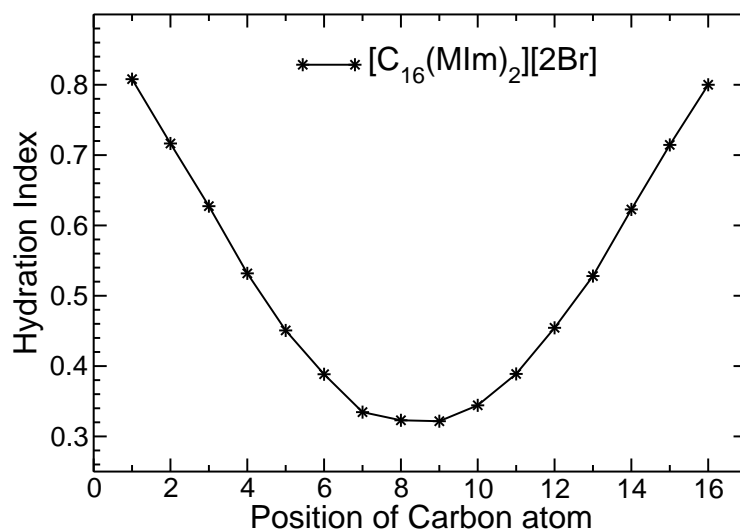


Figure 6.9: Hydration index of various carbon atoms of the hexadecyl spacer in aqueous solution of $[C_{16}(MIm)_2][2Br]$.

6.3.8 Diffusion of Ions and Molecules

The self-diffusion coefficients of cations and anions in solution are computed from the slope of mean-squared displacements using the Einstein relation. Although the model used in this study is known to underestimate [56, 57] the diffusion of ions, we can use the computed self-diffusion (D) coefficients of various moieties for qualitative comparison of different solutions of cations with varying spacer length. Figure 6.10 shows the self-diffusion coefficients of cations and anions in different aqueous solutions of cations with different spacer length. The self-diffusion coefficients

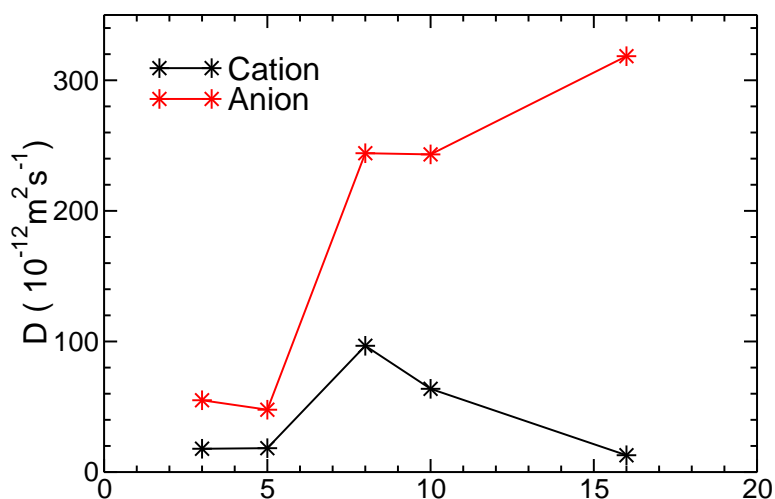


Figure 6.10: Self-diffusion coefficients of cations and anions in $[C_n(MIm)_2][2Br]$ ($n=3, 5, 8, 10$ and 16) solution.

of cations correspond to the self-diffusion coefficients of the center of mass of the cations. We have taken the 0.8 M and 0.82 M aqueous solutions of $[C_{10}(\text{MIm})_2][2\text{Br}]$ and $[C_8(\text{MIm})_2][2\text{Br}]$ systems for this comparison. The self-diffusion coefficients of cations and anions for $[C_3(\text{MIm})_2][2\text{Br}]$ in pure liquid state have already been reported [40]. We have found a remarkable increase in the diffusion of cations and anions upon addition of water. This increase in diffusion is due to the screening of the electrostatic charge between the head groups by water molecules. The diffusion of cations in their aqueous solutions increases with increase in the spacer carbon number from three to eight. This increase is consistent with the increase in the flexibility of the spacer with greater carbon number. Upon further increase in the spacer chain length, there is a decrease in diffusion of cations. This decrease can be attributed to the formation of dimers and micellar aggregates in $[C_{10}(\text{MIm})_2]$ and $[C_{16}(\text{MIm})_2]$ cations respectively, which increases the effective mass of the cations due to being part of an aggregate. The self-diffusion coefficient of anion is always higher by an order of magnitude compared to cation. We have found that the diffusion of anions increases in the aqueous solution containing cations of longer spacer. The variation of diffusion of anions is observed to correlate with the concentration of the ions in the solution.

6.3.9 Number Density

The atom number density profiles of different moieties along the interface normal (z-axis) obtained from MD simulations provide insights into the surface accumulation and ordering of molecules at the liquid–vapor interface [51, 58, 59]. Figure 6.11(a) shows the density profiles of first, third, fifth and eighth carbon atoms of the hexadecyl spacer starting from either of the imidazolium ends for the $[C_{16}(\text{MIm})_2]$ cations in aqueous solution. The minima in the density profiles along the interface normal appear at 24 Å, 24 Å, 25 Å, and 25 Å for the first, third, fifth and eighth carbon atoms of the hexadecyl spacer, respectively, while the corresponding maxima appear at 31 Å, 32 Å, 33 Å, and 34 Å from the center of the simulation box. The minimum value in the atom number density profile for eighth carbon atom of the hexadecyl spacer is the lowest among these four. The maximum of this density profile is located closest to the interface as evidenced from the figure. The peak height in the atom number density profiles at the liquid–vapor interface decreases for the

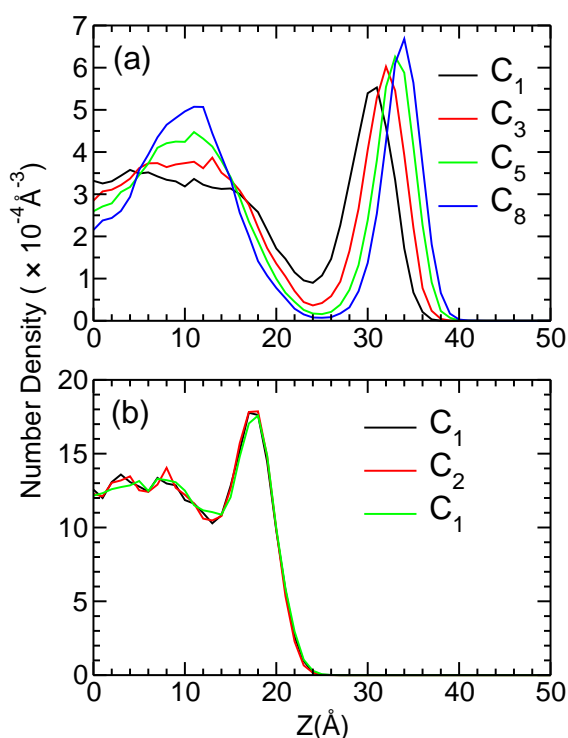


Figure 6.11: Atom number density profiles of different carbon atoms of the (a) hexadecyl spacer of $[\text{C}_{16}(\text{MIm})_2]$ cations and (b) propyl spacers of $[\text{C}_3(\text{MIm})_2]$ cations, along the interface normal (z-axis) in their respective solution–vapor interfaces.

carbon atoms towards the imidazolium ring. This observation suggests the preferential adsorption of the spacer carbon atoms at the liquid–vapor interface with the central atoms of the spacer at the interface. It can also be said from these observations, that both the ends of the hexadecyl spacer are immersed in the aqueous phase while the central spacer carbon atom is located towards the vapor phase. The most probable location of the center and the ends of the spacer chain differ by 3 \AA along the interface normal. The atom number density profiles for the second, fourth, sixth and seventh carbon atoms of the hexadecyl spacer are present within the range of density profiles of the first and eighth carbon atoms and follow the same trends as discussed (Figure E.10, Appendix E). The atom number density profiles of different carbon atoms in the spacer in $[\text{C}_{10}(\text{MIm})_2][2\text{Br}]$ and $[\text{C}_8(\text{MIm})_2][2\text{Br}]$ solutions are qualitatively similar (Figure E.11 and Figure E.12, Appendix E). The carbon atoms on the pentyl spacer exhibit similar density profiles along interface normal (Figure E.13, Appendix E).

We have found that the separation between the two peaks, corresponding to the carbon atom

linked to the imidazolium nitrogen and the central spacer carbon atom, decreases as the spacer chain lengths decrease from hexadecyl to pentyl. This suggests that with decrease in the spacer chain length, the tendency of the central spacer carbon atom to protrude into the vapor phase decreases. From figure 6.11(b), we can observe that all three carbon atoms of the propyl spacer have similar density profiles in the aqueous solution of $[C_3(\text{MIm})_2][2\text{Br}]$ cations. This suggests that they are located at the plane near the interface.

Figure 6.12(a) shows the atom number density profiles of central spacer carbon atom along the interface normal (z-axis) for the $[C_{16}(\text{MIm})_2]$, $[C_{10}(\text{MIm})_2]$, $[C_8(\text{MIm})_2]$, $[C_5(\text{MIm})_2]$ and $[C_3(\text{MIm})_2]$ cations in their aqueous solutions. The central spacer carbon atoms have been chosen to be eighth, fifth, fourth, third and second carbon atom from either of the imidazolium ends for the hexadecyl, decyl, octyl, pentyl and propyl spacers, respectively. The density profiles

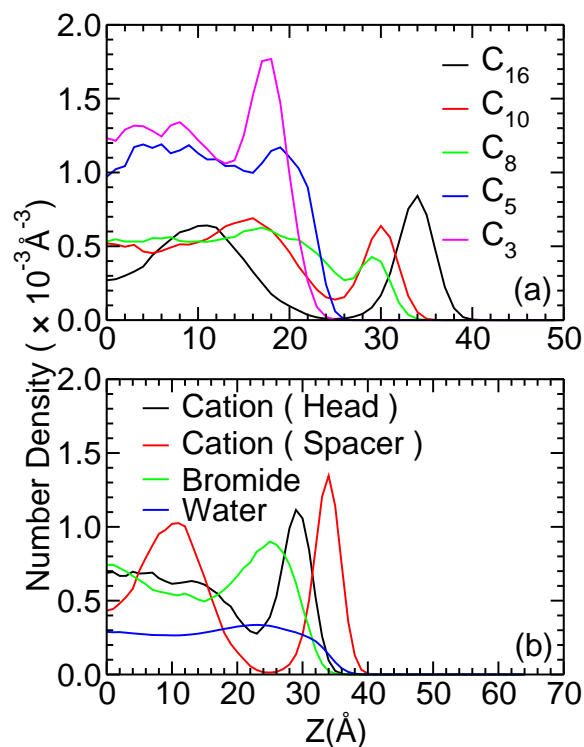


Figure 6.12: Atom number density profiles of (a) central carbon atom of hexadecyl, decyl, octyl, pentyl and propyl spacers in their corresponding aqueous solutions and (b) head groups, central spacer carbon of $[C_{16}(\text{MIm})_2]$ cations, anions and water along the interface normal (z-axis) in aqueous solution.

show peaks at the interface. The number density of the central carbon atom at the first minimum

is almost zero for the hexadecyl spacer, and the density at the first minima increases with the decrease in the spacer chain length. We observe a well defined peak in case of hexadecyl spacer indicating the presence of an interfacial layer where preferential adsorption of the central spacer carbon atom occurs. The formation of interfacial layer in case of hexadecyl spacer is evident from the snapshot (Figure E.14, Appendix E). The cations in the bulk region of this interfacial system form aggregates. The peak heights decrease with decrease in the spacer chain length up to the octyl chain. This reflects the lack of preferential adsorption of the hydrocarbon spacer at the liquid–vapor interface due to the decrease in the hydrophobic interaction between the spacer chain and water molecules. In case of decyl spacer, the cations at the interface are oriented such that their spacer chains are exposed to vapor phase. However, the interfacial layer is not clearly defined in this case (Figure E.15, Appendix E). We see that there is no well defined interfacial layer for the pentyl spacer compared to the propyl spacer. This suggests preferential adsorption of the propyl spacer compared to the pentyl spacer at the liquid–vapor interface. This is due to efficient packing of the propyl group than the pentyl at the liquid–vapor interface. This observation is also supported by the greater surface concentration of the central carbon atom of the propyl spacer (0.0117 \AA^{-2}) than that of the pentyl spacer (0.0089 \AA^{-2}).

Figure 6.12(b) shows the atom number density profiles of different moieties in the aqueous solution containing the $[\text{C}_{16}(\text{MIm})_2]$ cations along the surface normal. The head group represents the geometric center of the imidazolium ring, and the spacer represents the central carbon atom of the hexadecyl chain as defined earlier. The number density of water molecules is scaled to make it comparable with the bulk number density of the cations. From the figure, it is evident that the hexadecyl spacer is protruding into the vapor phase while the imidazolium rings are present in the aqueous phase. The peak in the number density profile of the anions is closer to the peak in the density profile of the head groups suggesting a strong association of the anions with the head groups through coulombic interactions. The water number density profile shows less enhancement at the liquid–vapor interface than the cations and anions.

The interfacial region in each of the system is defined as the region along z -axis enclosing the

first peak (towards the interface) of the central spacer carbon atom density profile. For the following discussions, a cation, anion or a water molecule is said to be at interface if the z-coordinate of any of its constituent atoms fall in the interfacial region.

6.3.10 Organisation of Cations at the Interface

Cations present at the liquid–vapor interface are less solvated and will experience a different molecular environment due to the presence of lesser number of water molecules at the interface than those in the bulk. So one can expect some sort of orientational ordering of the cations present in the interfacial layer, due to the van der Waals attraction between the hydrocarbon spacers.

Figure 6.13(a) shows the probability distribution of the angle between two spacers (defined as the angle between the vectors connecting the two nitrogen atoms separated by the spacer) for cations present in the liquid–vapor interfacial layer. In $[C_{16}(MIm)_2]$ cations present at the inter-

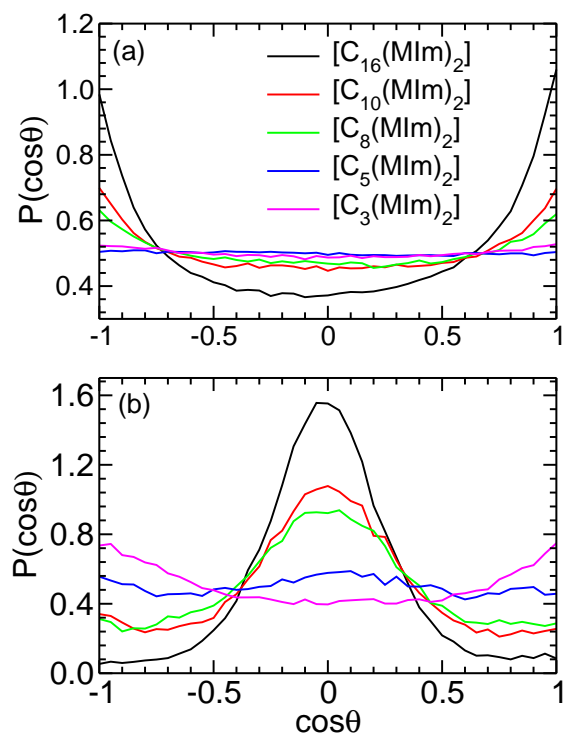


Figure 6.13: Distribution of angle between (a) the spacer vectors (connecting the two nitrogen atoms of the imidazolium rings separated by the spacer) of cations present in the interface (b) the spacer vector and the interface normal (z-axis).

face, the spacers are more likely to be oriented either parallel or antiparallel to each other. This probability decreases with the decrease in the spacer chain length and become almost random for

the pentyl and propyl spacers. This suggests that the organised assembly of the spacers of the cations present at the interface reduces and disappears as the spacer chain length is decreased. This is due to the decrease in the van der Waals interaction among the hydrocarbon spacers with reduction in their chain length. Figure 6.13(b) shows the angle distribution between the spacer vector and the interface normal (z-axis) for the cations present at the liquid–vapor interface in their aqueous solutions. The hexadecyl spacers show a high probability to be oriented perpendicular to the interface normal, i.e., remain parallel to the surface. The preference for the spacers to be oriented perpendicular to the interface normal decreases with the decrease in the spacer length and the orientation becomes almost random for the pentyl and propyl spacers. This observation confirms the decrease in the ordering of the cations at the liquid–vapor interface with decrease in the spacer length.

The distribution of angles between the NN vector (vector connecting the two nitrogen atoms of the imidazolium ring) and the interface normal for the cations present at the interface in various systems is shown in figure 6.14(a). We see that the NN vectors of $[C_{16}(MIm)_2]$ cations are more likely to be oriented along the interface normal in their aqueous solution. This orientation can be attributed to the upward pull exerted by the hexadecyl spacer on the imidazolium rings toward the vapor phase. With decrease in the spacer length, there will be a reduction in this upward pull by the spacer and the probability of the NN vectors to be oriented along the interface normal will decrease as evidenced from the figure.

Figure 6.14(b) represents the angle distribution between the vectors connecting the central spacer atom to the nitrogen atoms on either imidazolium rings at the interface, that characterizes the folding of the spacer chain. The distribution characterizing the folding is different for the cations present at the interface compared to those present at the bulk, in case of cations with octyl or longer spacers. In case of propyl and pentyl spacers, the cations at the interface and in the bulk region exhibit similar folding. The deviation is significant in case of hexadecyl spacer and negligible in case of pentyl and propyl spacers (Figure E.16 and Figure E.17, Appendix E). The angle distribution for the hexadecyl spacer folding shows a broad peak with most probable angle of

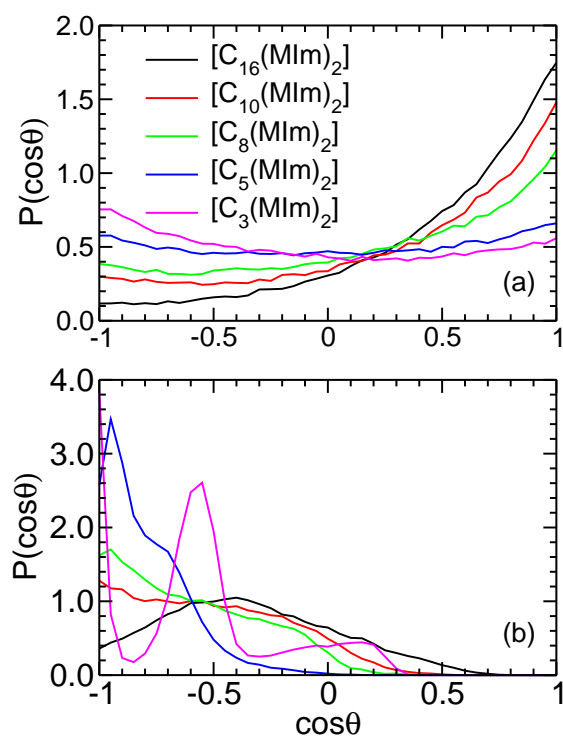


Figure 6.14: Distribution of angle between (a) the vectors connecting the two nitrogen atoms of the imidazolium rings and the interface normal (z-axis) (b) the two vectors joining the central spacer carbon atom with the nitrogen atoms of the imidazolium rings separated by the spacer.

folding being 115° . The folding arises due to the affinity of the spacer towards the vapor phase and the head groups toward the aqueous phase. For the $[C_{10}(\text{MIm})_2]$ and $[C_8(\text{MIm})_2]$ cations present at the interface, the probability of the spacers to remain unfolded is less compared to cations in the bulk region.

6.3.11 Surface Tension.

The surface tension γ of the solution–vapor interface was calculated from the diagonal components of pressure tensor P_{ii} using the formula [60]

$$\gamma = -b_z(P_{xx} + P_{yy} - 2P_{zz})/4 \quad (6.1)$$

where b_z is the length of the super-cell along the interface normal (z-axis). The factor 2 has been introduced in the denominator to account for the presence of two equivalent interfaces. The surface tension for the simulated systems are found to be 72, 68, 52, 54 and 39 mNm^{-1} respectively for the systems containing propyl, pentyl, octyl, decyl and hexadecyl spacer. Gradual decrease in

the surface tension is observed with the increase in spacer length from propyl to octyl. The surface tension values of $[C_8(\text{MIm})_2]$ and $[C_{10}(\text{MIm})_2]$ solutions are almost same while it decreases sharply for $[C_{16}(\text{MIm})_2]$ solution.

6.4. Conclusions Atomistic MD simulations have been carried out on a series of aqueous solutions of imidazolium based dicationic ionic liquids $[C_n(\text{MIm})_2][2\text{Br}]$ (where n varies from 3 to 16) from a uniform configuration of the ion units. The structure of the solution is found to depend on the number of carbon atoms in the alkyl spacer. The solution with propyl spacer ($[C_3(\text{MIm})_2][2\text{Br}]$) is homogeneous whereas spatial heterogeneity is observed with the increase in the length of the spacer chain. The $[C_{16}(\text{MIm})_2]$ cations in their solution are found to form aggregates with the central carbon of the hexadecyl spacers buried in the hydrophobic core and the imidazolium rings forming the hydrophilic surface. RDFs reveal that the organisation of the anions and water around the cationic head groups varies with the spacer length as well as concentration. The intramolecular imidazolium ring orientation and folding of the alkyl spacers are found to be influenced by the $\pi - \pi$ stacking interaction between the two imidazolium rings of the cation.

In the solution–vapor interface, the organization of the alkyl spacers increases with increase in the spacer length from pentyl to hexadecyl. In case of the solution with hexadecyl spacer, the central spacer carbon is more likely to be protruding into the vapor phase and the carbon atoms of the spacer that are near the imidazolium rings stay in the aqueous phase. In case of propyl spacer, all the three spacer carbon atoms are present in the aqueous phase. The tendency of the spacers to be oriented parallel to each other and perpendicular to the interface normal (z -axis) decreases with decrease in the spacer length implying the decrease in the organization of cations present at the interface with decrease in the spacer chain length.

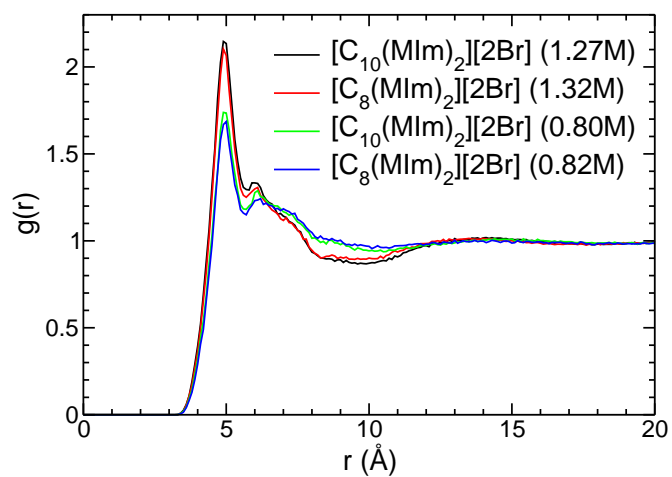


Figure E.1: RDFs of anions around the geometric center of the imidazolium rings in aqueous solutions

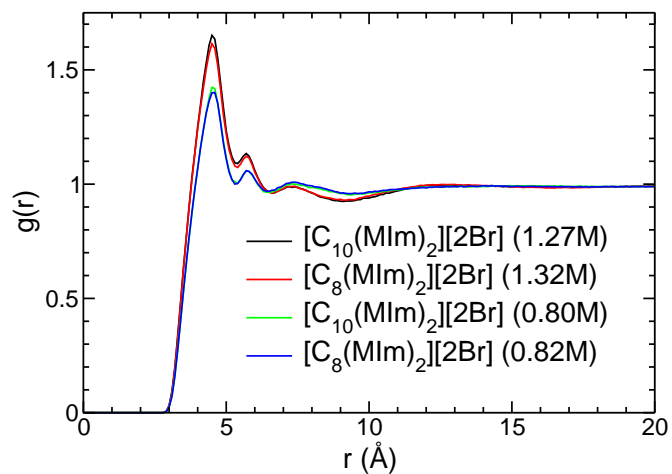


Figure E.2: RDFs of water molecules around the geometric center of the imidazolium rings in aqueous solutions

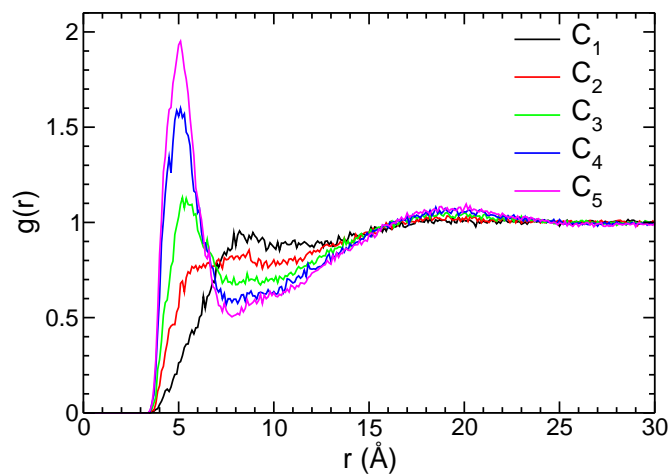


Figure E.3: RDFs of different carbon atoms of the decyl spacer around themselves in aqueous solution of $[C_{10}(MIm)_2][2Br]$.

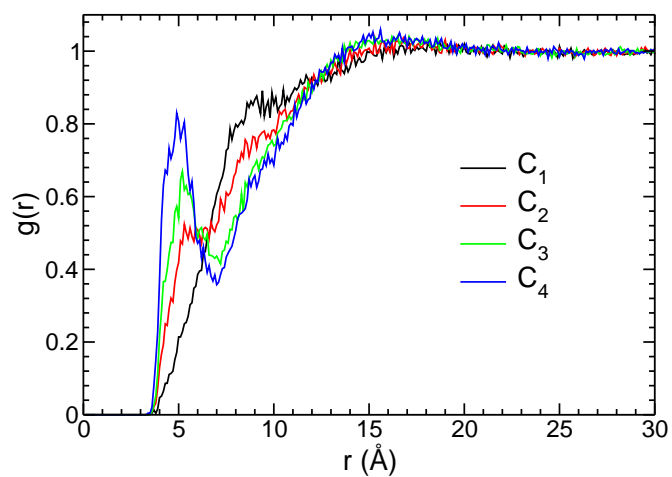


Figure E.4: RDFs of different carbon atoms of the octyl spacer around themselves in aqueous solution of $[\text{C}_8(\text{MIm})_2][2\text{Br}]$.

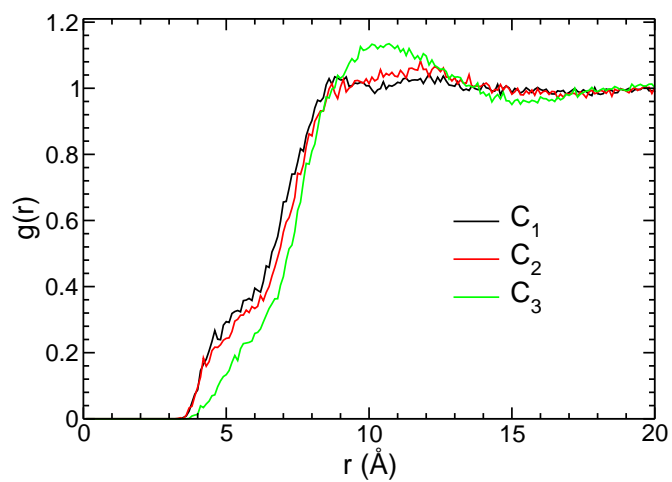


Figure E.5: RDFs of different carbon atoms of the pentyl spacer around themselves in aqueous solution of $[\text{C}_5(\text{MIm})_2][2\text{Br}]$.

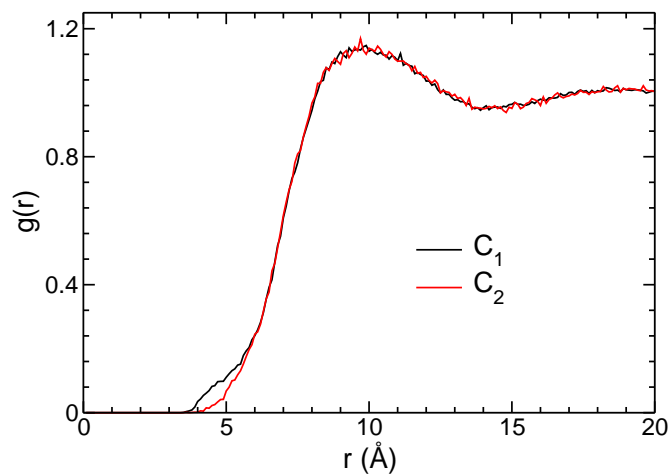


Figure E.6: RDFs of different carbon atoms of the propyl spacer around themselves in aqueous solution of $[C_3(\text{MIm})_2][2\text{Br}]$.

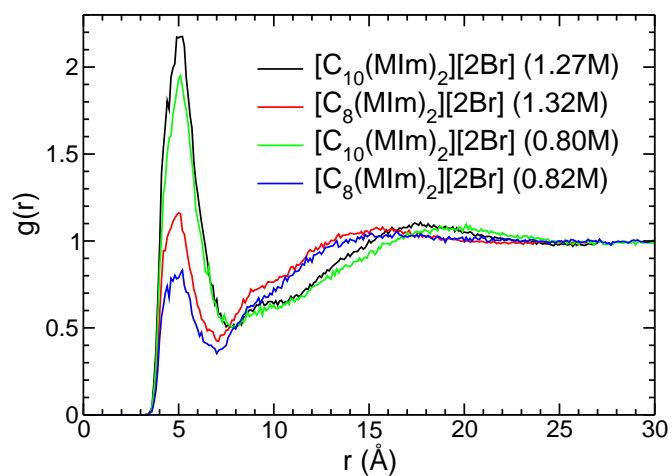


Figure E.7: RDFs of central carbon atom of the spacer chain around themselves in aqueous solutions of $[C_{10}(\text{MIm})_2][2\text{Br}]$ and $[C_8(\text{MIm})_2][2\text{Br}]$.

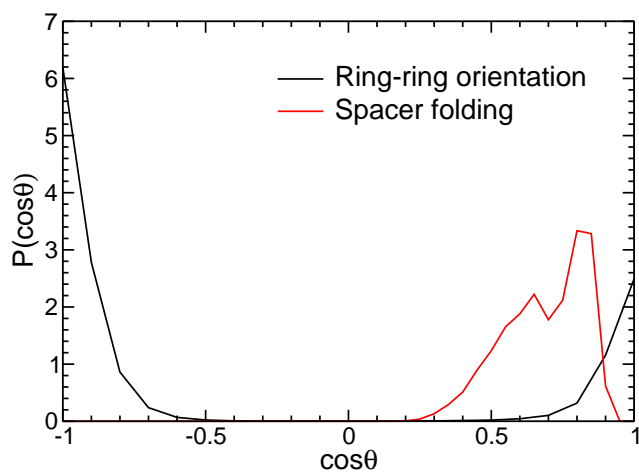


Figure E.8: Distribution of angles between the normal vectors of two imidazolium rings, and two vectors joining the central carbon atom of the spacer with the imidazolium nitrogen atoms connected to the spacer in $[C_{16}(MIm)_2][2Br]$ in gas phase.

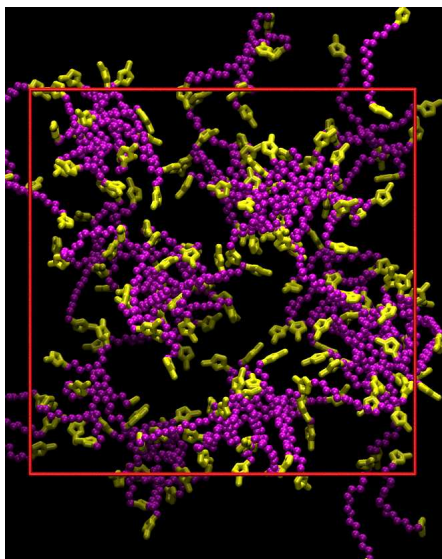


Figure E.9: Snapshot of the aqueous solution of $[C_{16}(MIm)_2][2Br]$ after 50 ns simulations. Head groups are shown in yellow and the tail groups are shown in magenta. Anions, water and hydrogen atoms on the cation are not shown for the ease of visualization.

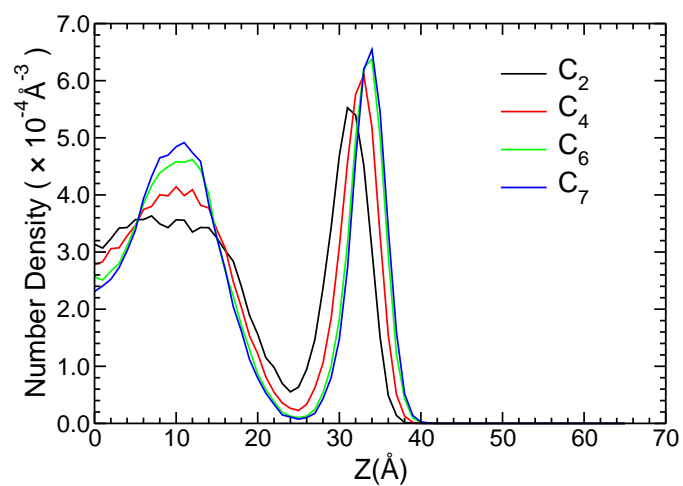


Figure E.10: Atom number density profiles of different carbon atoms of the hexadecyl spacer along the interface normal (z -axis) in the liquid–vapor interface of $[\text{C}_{16}(\text{MIm})_2][2\text{Br}]$ solution.

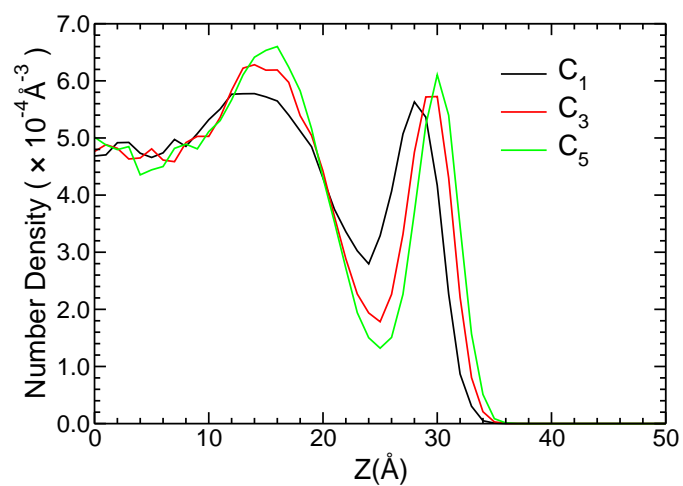


Figure E.11: Atom number density profiles of different carbon atoms of the decyl spacer along the interface normal (z -axis) in the liquid–vapor interface of $[\text{C}_{10}(\text{MIm})_2][2\text{Br}]$ solution.

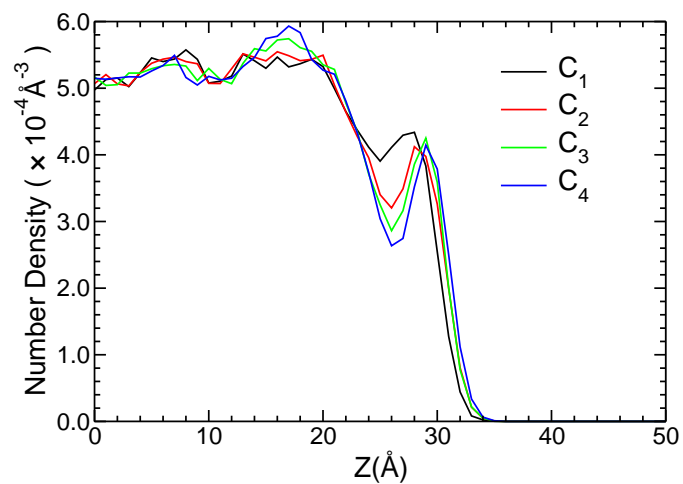


Figure E.12: Atom number density profiles of different carbon atoms of the octyl spacer along the interface normal (z -axis) in the liquid-vapor interface of $[C_8(\text{MIm})_2][2\text{Br}]$ solution.

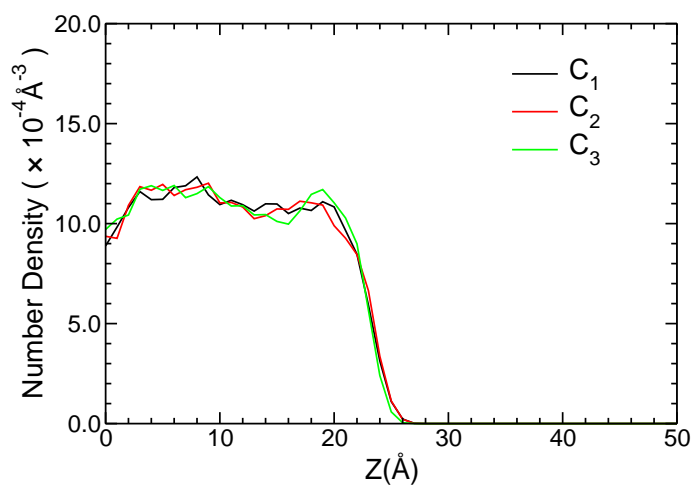


Figure E.13: Atom number density profiles of different carbon atoms of the pentyl spacer along the interface normal (z -axis) for the $[C_5(\text{MIm})_2]$ cations in aqueous solution.

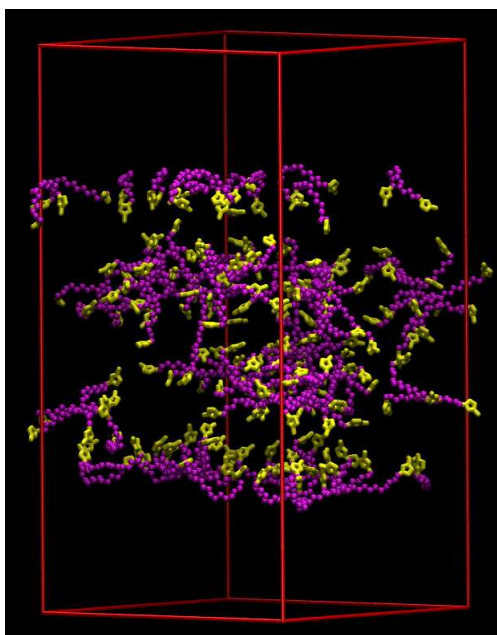


Figure E.14: Snapshot of the liquid–vapor interface of the aqueous solution of $[\text{C}_{16}(\text{MIm})_2][2\text{Br}]$ after 25 ns simulations. Head groups are shown in yellow and the tail groups are shown in magenta. Anions, water and hydrogen atoms on the cation are not shown for the ease of visualization.

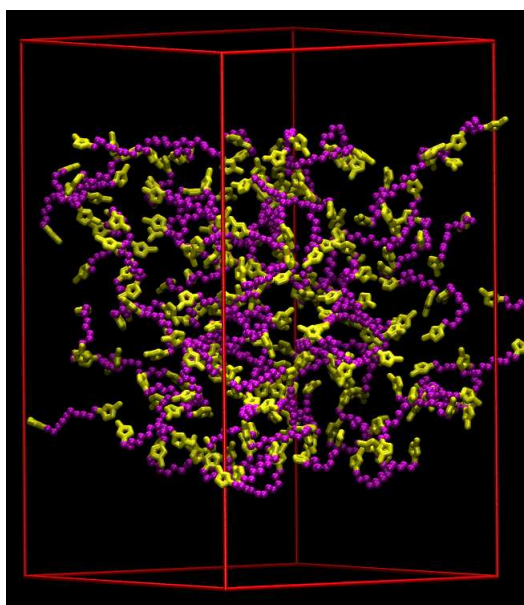


Figure E.15: Snapshot of the liquid–vapor interface of aqueous solution of $[\text{C}_{10}(\text{MIm})_2][2\text{Br}]$ after 25 ns simulations. Head groups are shown in yellow and the tail groups are shown in magenta. Anions, water and hydrogen atoms on the cation are not shown for the ease of visualization.

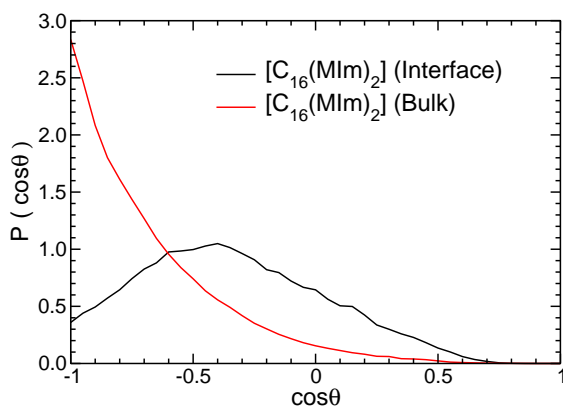


Figure E.16: Distribution of angles between the two vectors joining the central carbon atom of the spacer with the imidazolium nitrogen atoms connected to the spacer in the aqueous solution of $[C_{16}(MIm)_2][2Br]$.

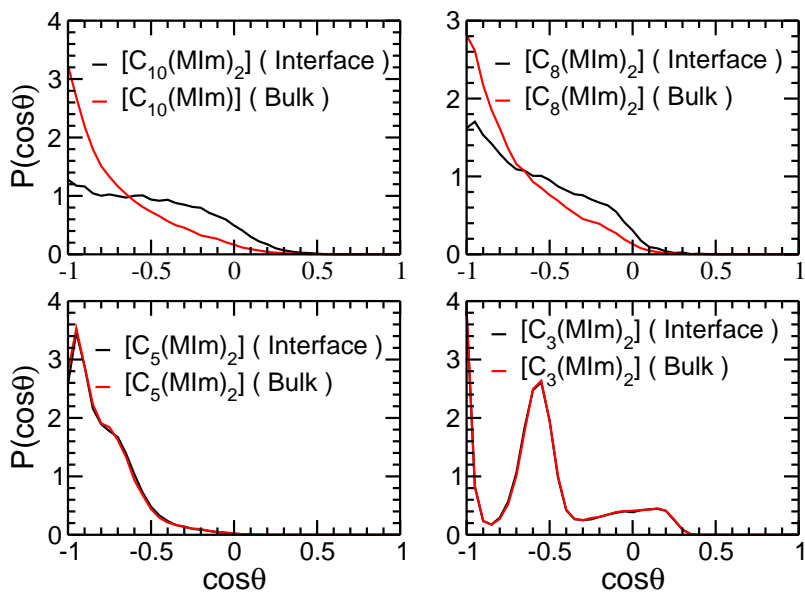


Figure E.17: Distribution of angles between the two vectors joining the central carbon atom of the spacer with the imidazolium nitrogen atoms connected to the spacer in the aqueous solution of DILs.

Bibliography

- [1] Menger, F. M. and Littau, C. A. *J. Am. Chem. Soc.* **1991**, *113*, 1451-1452.
- [2] Menger, F. M. and Keiper, J. S. *Angew. Chem. Int. Ed.* **2000**, *39*, 1906-1920.
- [3] Tsubone, K. ; Arakawa, Y. and Rosen, M. J. *J. Colloid Interface Sci.* **2003**, *262*, 516-524.
- [4] Baltazar, Q. Q. ; Chandawalla, J. ; Sawyer, K. and Anderson, J. L. *Colloids Surf. A* **2007**, *302*, 150-156.
- [5] Han, Y. and Wang, Y. *Phys. Chem. Chem. Phys.* **2011**, *13*, 1939-1956.
- [6] Zhang, Q. ; Gao, Z. ; Xu, F. ; Tai, S. ; Liu, X. ; Mo, S. and Niu, F. *Langmuir* **2012**, *28*, 11979-11987.
- [7] Cui, X. ; Yang, X. ; Chen, H. ; Liu, A. ; Mao, S. ; Liu, M. ; Yuan, H. ; Luo, P. and Du, Y. *J. Phys. Chem. B* **2008**, *112*, 2874- 2879.
- [8] Amiri, R. ; Bordbar, A. and Laurents, D. V. *J. Phys. Chem. B* **2014**, *118*, 10633-10642.
- [9] Gospodarczyk, W. ; Szutkowski, K and Kozak, M. *J. Phys. Chem. B* **2014**, *118*, 8652-8661.
- [10] Dong, J. ; Cai, J. ; Guo, X. and Xiao, J. *Soft Matter* **2013**, *9*, 11383-11391.
- [11] Muñoz-Úbeda, M. ; Misra, S. K. ; Barrán-Berdón, A. L. ; Aicart-Ramos, C. ; Sierra, M. B. ; Biswas, J. ; Kondaiah, P. ; Junquera, E. ; Bhattacharya, S. and Aicart, E. *J. Am. Chem. Soc.* **2011**, *133*, 18014-18017.
- [12] Bajaj, A. ; Kondaiah, P. and Bhattacharya, S. *Bioconjugate Chem.* **2007**, *18*, 1537-1546.

- [13] Kirby, A. J. ; Camilleri, P. ; Engberts, J. B. F. N. ; Feiters, M. C. ; Nolte, R. J. M. ; Söderman, O. ; Bergsma, M. ; Bell, P. C. ; Fielden, M. L. ; Rodríguez, C. L. G. ; Guédat, P. ; Kremer, A. ; McGregor, C. ; Perrin, C. ; Ronsin, G. and van Eijk, M. C. P. *Angew. Chem. Int. Ed.* **2003**, *42*, 1448-1457.
- [14] Bombelli, C. ; Giansanti, L. ; Luciani, P. and Mancini, G. *Curr. Med. Chem.* **2009**, *16*, 171-183.
- [15] Li, W. ; Shi, J. ; Zhang, C. ; Li, M. ; Gan, L. ; Xu, H. and Yang, X. *J. Mater. Chem. B* **2014**, *2*, 4901-4910.
- [16] Badr, E. E. ; Kandeel, E. M. and El-Sadek, B. M. *J. Oleo. Sci.* **2010**, *59*, 647-652.
- [17] He, S. ; Wang, B. ; Chen, H. ; Tang, C. and Feng, Y. *ACS Appl. Mater. Interfaces* **2012**, *4*, 2116-2123.
- [18] Tavano, L. ; Infante, M. R. ; Abo Riya, M. ; Pinazo, A. ; Vinardell, M. P. ; Mitjans, M. ; Manresa, M. A. and Perez, L. *Soft Matter* **2013**, *9*, 306-319.
- [19] jain, T. ; Tehrani-Bagha, A. R. ; Shekhar, H. ; Crawford, R. ; Johnson, E. ; Nørgaard, K. ; Holmberg, K. ; Erhart, P. and Moth-Poulsen, K. *J. Mater. Chem. C* **2014**, *2*, 994-1003.
- [20] Barclay, T. G. ; Constantopoulos, K. and Matisons, J. *Chem. Rev.* **2014**, *114*, 10217-10291.
- [21] Jacquemin, J. ; Husson, P. ; Pádua, A. A. H. and Majer, P. *Green Chem.* **2006**, *8*, 172-180.
- [22] Triolo, A. ; Mandanici, A. ; Russina, O. ; Rodriguez-Mora, V. ; Cutroni, M. ; Hardacre, C. ; Nieuwenhuyzen, M. ; Bleif, H. ; Keller, L. and Ramos, M. A. *J. Phys. Chem. B* **2006**, *110*, 21357-21364.
- [23] Huddleston, J. G. ; Visser, A. E. ; Reichert, W. M. ; Willauer, H. D. ; Broker, G. A. and Rogers, R. D. *Green Chem.* **2001**, *3*, 156-164.
- [24] Rocha, M. A. A. ; Coutinho, J. A. P. and Santos, M. N. B. F. *J. Phys. Chem. B* **2012**, *116*, 10922-10927.

- [25] Tong, J. ; Liu, Q. ; Xu, W. ; Fang, D. and Yang, J. *J. Phys. Chem. B* **2008**, *112*, 4381-4386.
- [26] Anderson, J. L. ; Ding, R. ; Ellern, A. and Armstrong, D. W. *J. Am. Chem. Soc.* **2005**, *127*, 593-604.
- [27] Ao, M. ; Xu, G. ; Pang, J. and Zhao, T. *Langmuir* **2009**, *25*, 9721-9727.
- [28] Casal-Dujat, L. ; Rodrigues, M. ; Yagüe, A. ; Calpena, A. C. ; Amabilino, D. B. ; González-Linares, J. ; Borràs, M. and Pérez-García, L. *Langmuir* **2011**, *28*, 2368-2381.
- [29] Misra, S. K. ; Naz, S. ; Kondaiah, P. and Bhattacharya, S. *Biomaterials* **2014**, *35*, 1334-1346.
- [30] Huang, Q. ; Chen, H. ; Zhou, L. ; Huang, J. ; Wu, J. and Yu, X. *Chem. Biol. Drug. Des.* **2008**, *71*, 224-229.
- [31] Datta, S. ; Biswas, J. and Bhattacharya, S. *J. Colloid Interface Sci.* **2014**, *430*, 85-92.
- [32] Ao, M. ; Huang, P. ; Xu, G. ; Yang, X. and Wang, Y. *Colloid Polym. Sci.* **2009**, *287*, 395-402.
- [33] Bhadani, A. and Singh, S. *Langmuir* **2011**, *27*, 14033-14044.
- [34] Kamboj, R. ; Singh, S. ; Bhadani, A. ; Kataria, H. and Kaur, G. *Langmuir* **2012**, *28*, 11969-11978.
- [35] M. Yang, K. Stappert and A. Mudring, *J. Mater. Chem. C* **2014**, *2*, 458-473.
- [36] Bodo, E. and Caminiti, R. *J. Phys. Chem. A* **2010**, *114*, 12506-12512.
- [37] Bodo, E. ; Chiricotto, M. and Caminiti, R. *J. Phys. Chem. B* **2011**, *115*, 14341-14347.
- [38] Li, S. ; Feng, G. ; Bañuelos, J. L. ; Rother, G. ; Fulvio, P. F. and Dai, S. *J. Phys. Chem. C* **2013**, *117*, 18251-18257.
- [39] Ishida, T. and Shirota, H. *J. Phys. Chem. B* **2013**, *117*, 1136-1150.
- [40] Yeganegi, S. ; Soltanabadi, A. and Farmanzadeh, D. *J. Phys. Chem. B* **2012**, *116*, 11517-11526.

- [41] Bhargava, B. L. and Klein, M. L. *J. Chem. Theory. Comput.* **2010**, *6*, 873-879.
- [42] Bhargava, B. L. and Klein, M. L. *J. Phys. Chem. B* **2011**, *115*, 10439-10446.
- [43] Plimpton, S. *J. Comput. Phys.* **1995**, *117*, 1-19 (<http://lammmps.sandia.gov>).
- [44] Lopes, J. N. C. and Pádua, A. A. H. *J. Phys. Chem. B* **2006**, *110*, 19586-19592.
- [45] Berendsen, H. J. C. ; Postma, J. P. M. ; van Gunsteren, W. F. and Hermans, J. in *Intermolecular Forces*, ed. B. Pullman, Reidel: Dordrecht, The Netherlands, **1981**, p 331.
- [46] Allen, M. P. and Tildesley, D. J. *Computer Simulation of Liquids*; Clarendon Press: Oxford, U.K., **1987**.
- [47] Ryckaert, J. P. ; Ciccotti, J. and Berendsen, H. J. C. *J. Comput. Phys.* **1977**, *23*, 327-341.
- [48] Humphrey, W. ; Dalke, A. and Schulten, K. *J. Mol. Graphics* **1996**, *14*, 33-38.
- [49] Bini, R. ; Bortolini, O. ; Chiappe, C. ; Pieraccini, D. and Siciliano, T. *J. Phys. Chem. B* **2007**, *111*, 598-604.
- [50] Bhargava, B. L. and Klein, M. L. *Soft Matter* **2009**, *5*, 3475-3480.
- [51] Palchowdhury, S. and Bhargava, B. L. *J. Phys. Chem. B* **2014**, *118*, 6241-6249.
- [52] Desiraju, G. R. and Steiner, T. *The Weak Hydrogen Bond, In Structural Chemistry and Biology*; Oxford University Press: New York, **2001**.
- [53] Gierszal, K. P. ; Davis, J. G. ; Hands, M. D. ; Wilcox, D. S. ; Slipchenko, L. V. and Ben-Amotz, D. *J. Phys. Chem. Lett.* **2011**, *2*, 2930-2933.
- [54] Slipchenko, L. V. and Gordon, M. S. *J. Phys. Chem. A* **2009**, *113*, 2092-2102.
- [55] Vanyúr, R. ; Biczók, L. and Miskolczy, Z. *Colloids Surf., A* **2007**, *299*, 256-261.
- [56] Yan, T. ; Burnham, C. J. ; Pópolo, M. G. D. and Voth, G. A. *J. Phys. Chem. B* **2004**, *108*, 11877-11881.

- [57] Bango, A. ; D'Amico, F. and Saielli, G. *J. Mol. Liq.* **2007**, *131-132*,17-23.
- [58] Bhargava, B. L. and Balasubramanian, S. *J. Am. Chem. Soc.* **2006**, *128*, 10073-10078.
- [59] Bhargava, B. L. and Klein, M. L. *J. Phys. Chem. A* **2009**, *113*, 1898-1904.
- [60] Rao, M. and Berne, B. J. *Mol. Phys.*, **1979**, *37*, 455-461.

Chapter 7

Glycine Molecules in Ionic Liquid based Reverse Micelles: Investigation of Structure and Dynamics using Molecular Dynamics Simulations

Abstract:

Amino acids, the building blocks of proteins, are probed in reverse micellar encapsulation processes of biological molecules. To achieve a theoretical picture of the effect of confinement of amino acids on the structure and dynamics of reverse micellar aqueous core, a water/[C₁C₁₀Im][Br] reverse micelles containing variable number of glycine molecules (0 to 8), dispersed in pure nonane has been studied using atomistic molecular dynamics simulations. The size of the central water pool was found to become stable with increase in the number of glycine molecules. Glycine molecules associate together through H-bonding interaction within the aqueous core of the reverse micelles. The radial density profile of glycine molecules from the center of mass of the reverse micellar aqueous core shows the preferential presence of glycine molecules near the center. Confinement in nano-space region stabilizes the H-bonds formed between glycine molecules compared to bulk aqueous solution. Increase in the number of glycine molecules within the reverse micellar aqueous core increases the survival time of H-bonds among glycine molecules as well as among water molecules. Translational and reorientational motion of glycine and water molecules are found to be directly related to the survival probability of intermolecular glycine–glycine and water–water H-bonds suggesting the correlation between the mobility of molecules with the rearrangement of the H-bonding network.

7.1. Introduction. Reverse micelles have potential applications in the field of downstream processes and enzyme recovery due to their ability to encapsulate and probe biological molecules [1, 2, 3]. Investigations to understand the mechanism of reverse micellar extraction of proteins have been done previously. For this purpose, amino acids, the building blocks of proteins, are probed in the reverse micellar extraction processes [4, 5, 6, 7]. Phase-transfer method has been employed to determine the partition coefficients of amino acids between water and the reverse micellar interface [8]. From investigations of the effect of pH, ionic strength and concentrations of amino acids and surfactants used, exchange of counter ions with the amino acids in the water pool was proposed to be the mechanism of reverse micellar extraction of amino acids [9]. COSMO-RS modelling [10] and fluorescence spectroscopy [11] have been used to elucidate the nature of amino acids responsible for their localization within the reverse micellar water pool. Mass spectrometry study had revealed the driving forces for amino acid encapsulation in gas-phase reverse micelles [12] as well as the effect of charge state on the micellar structure and encapsulation [13]. Ionic liquids, being useful replacements for the organic solvents have been used as the dispersion phase for the formation of reverse micelles [14, 15]. The role of entrapped ionic liquids in reverse micelles as nanoreactors for bimolecular nucleophilic substitution [16] had been investigated. Few reports are there on the recovery of amino acids by imidazolium based ionic liquids of varying chain length and counter anions as alternative solvents from aqueous media [17]. The role and utility of ionic liquids as potential surfactants for the formation of reverse micellar aggregates is yet to be explored.

Even though many experimental [22, 23, 24, 25] and computational studies [26, 27, 28, 29, 30] have been reported on the structure and water dynamics in reverse micellar confinement, to the best of our knowledge, no computational studies are focused on the effect of confinement on the dynamics of amino acids encapsulated in a reverse micelle consisting of imidazolium based ionic liquids. Glycine, being the simplest one in the amino acid family, is chosen as the representative probe for our study. In the present study, we have carried out atomistic molecular dynamics simulations of reverse micelles consist of imidazolium based ionic liquids and encapsulating variable

number of glycine molecules in zwitterionic forms with the aim of exploring the effect of increase in the number of amino acids on the structure of the aqueous core of the reverse micelles as well as dynamics of species confined in the aqueous core.

7.2. Methodology and Simulation Details. All-atom molecular dynamics (MD) simulations have been performed on reverse micellar systems containing varying number of glycine molecules.

The simulations were started from an uniform configuration of surfactant (1-(*n*-decyl)-3-methylimidazolium bromide, [C₁C₁₀Im][Br]) and nonane molecules as dispersion phase. All the systems contain 200 water molecules, 36 [C₁C₁₀Im][Br] ion pair units and 1200 nonane molecules but differ in the number of glycine molecules (ranging from 0 to 8) taken. The size of a reverse micelle is characterized by its water loading (W_0), which is the ratio of water molecules to surfactant molecules

$$W_0 = \frac{[H_2O]}{[surfactant]} \quad (7.1)$$

W_0 is ≈ 5.0 , for the systems that we have studied making them small sized reverse micelles. Binary glycine–water bulk solution is also studied for making comparison with the reverse micellar systems. Details of the parameters characterizing the systems have been presented in Table 7.1. The

Table 7.1: Details of the simulated systems.

no. of glycine	no. of waters	no. of [C ₁ C ₁₀ Im][Br]	no. of nonanes	no. of atoms	run length(ns)	box length(Å)
0	200	36	1200	36984	35	74.219
1	200	36	1200	36994	35	74.116
2	200	36	1200	37004	35	74.692
4	200	36	1200	37024	35	74.493
8	200	36	1200	37064	35	74.414
125	2246	–	–	7988	27	42.632

simulations have been performed using the LAMMPS [31] MD package. The simple point charge model (SPC/E) has been used to model water molecules [32] as it gives the best bulk structure and dynamics [33] for water molecules. The all-atom force field parameters for [C₁C₁₀Im][Br] and glycine molecules are adapted from the work of Lopes et. al [34, 35] and Jorgensen et. al [36], respectively. For nonane, the OPLS-AA force field parameters developed by Siu et. al [37] have

been used. Even though the model used in this study is known to underestimate the dynamics of ions, it is suitable for a comparative investigation among the systems studied.

Isothermal-isobaric ensemble simulations (constant NPT) at 1 atmosphere pressure using the N ose-Hoover barostat with a pressure damping parameter of 500 fs were carried out on each solution for 2 ns to get the equilibrated density. The canonical ensemble simulations (constant NVT) were then performed from the last configuration of NPT simulation. All simulations at constant NVT conditions were performed at 330 K using the temperature controller N ose-Hoover thermostat with a temperature damping parameter of 1000 fs. The temperatures of the simulations have been kept higher than the room temperature to accelerate the dynamics of ions and molecules through the high viscous oil (nonane) phase. The equations of motion were integrated using the verlet algorithm with a time step of 0.5 fs. Three dimensional periodic boundary conditions were used to simulate the bulk behavior. The atom coordinates were stored at an interval of 5 ps. Visualization software The structural properties are calculated from the last 5 ns of trajectory whereas last 10 ns of trajectory is used to calculate the dynamical properties. In the figures, reverse micelle without any glycine molecules are termed as “Model RM” and reverse micelles containing amino acids are denoted by the number of glycine molecules in them. The binary glycine–water bulk solution is termed as “Binary”. A schematic of the molecular structures of [C₁C₁₀Im] cation, glycine, nonane and water are presented in Figure 7.1.

7.3. Results and Discussion

7.3.1 Formation of Reverse Micelles

The simulations were started from an uniform configuration of ions and molecules. The snapshots of the different stages in the formation of reverse micelle in the system containing 8 glycine molecules are shown in figure 7.2. In the figure, the oil phase (nonane) and hydrogen atoms of [C₁C₁₀Im] cations are not shown for the ease of visualization. The water molecules, the glycine molecules and the bromide ions are shown in pink, blue, and black respectively and the imidazolium rings and alkyl carbon atoms of [C₁C₁₀Im] cations are shown in red and green respectively. We observe that the water molecules and [C₁C₁₀Im] cations that are spread out in the nonane phase

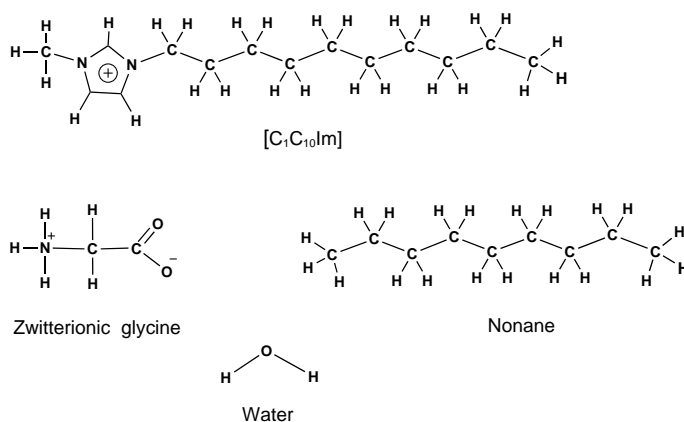


Figure 7.1: Schematic representation of the [C₁C₁₀Im] cation, glycine, nonane and water molecule.

come together to form small irregular shaped clusters within the first 0.25 ns of simulation (Figure 7.2(b)). The glycine molecules and bromide anions are distributed within these clusters. Then these small clusters coalesce to form bigger liquid droplets (Figure 7.2(c) and (d)) within 2.25 ns of simulation. Then the two intermediate-sized liquid droplets fuse together by the formation of a bridge of water molecules between them as depicted in Figure 7.2(e). Aggregate elongated along the direction of water bridge then reorganizes to form spherical reverse micelle encapsulating the amino acids (Figure 7.2(f)). This is a representative of all other systems with different number of glycine molecules, where encapsulation of glycine occur at constant water loading (i. e., at constant W_0) without replacing any water molecule from within the reverse micellar aqueous pool. It will be interesting to know the effect of increasing the size of the system. Further work needs to be done to establish the phase behavior of the system and the stability of the reverse micelle.

7.3.2 Structure of the Reverse Micelles.

The structures of the reverse micelles containing varying number of glycine molecules are shown in Figure 7.3. The color scheme to identify different moieties are same as discussed in the preceding section. Additionally, bromide ions are not shown for clarity. The reverse micelles are spherical in shape. The imidazolium head groups of [C₁C₁₀Im] cations are immersed in the water pool and are distributed throughout the aqueous phase. The aqueous phase does not solvate any

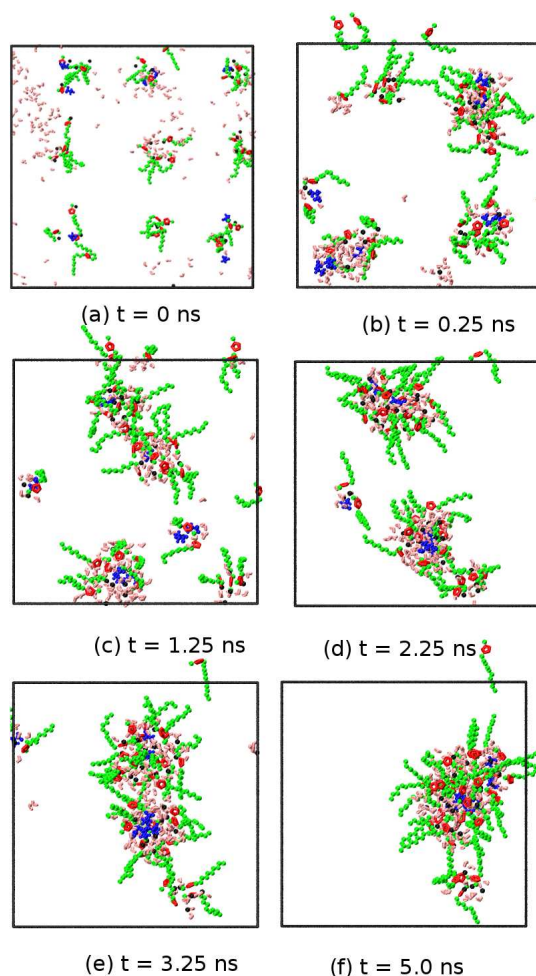


Figure 7.2: The snapshots of different stages of aggregation of various species to form the reverse micelle in the system containing 8 glycine molecules. The water molecules, the glycine molecules and the bromide ions are shown in pink, blue and black respectively and the imidazolium rings and alkyl carbon atoms of $[C_1C_{10}Im]$ cations are shown in red and green respectively. The oil phase (nonane) and hydrogen atoms of $[C_1C_{10}Im]$ cations are not shown for the ease of visualization.

decyl chain carbon atoms beyond the second carbon atom from the imidazolium end. The alkyl chains of $[C_1C_{10}Im]$ cations protrude into the nonane phase (not shown). The bromide ions are also distributed across the aqueous core (not shown). In systems containing more than one amino acids, the glycine molecules associate together through the formation of H-bonds as depicted in Figure 7.4. The three-dimensional spatial distribution functions (SDFs) of amino hydrogen atoms (in yellow) and carboxylate oxygen atoms (in green) around the α -C atom of glycine molecule also confirm the H-bonding interaction between the amino hydrogen atoms and carboxylate oxygen atoms belonging to two distinct glycine molecules as shown in Figure 7.5. We see that the

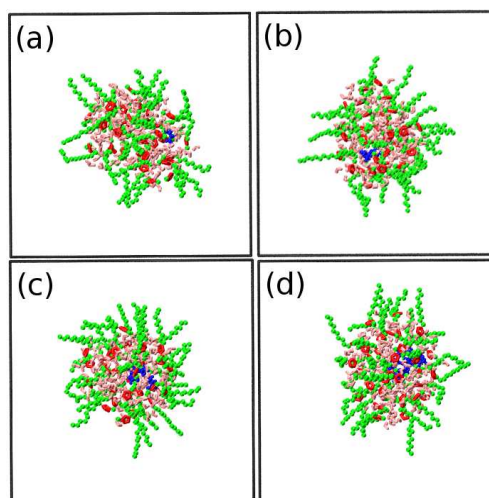


Figure 7.3: Structures of the reverse micelles containing (a) 1 (b) 2 (c) 4 and (d) 8 glycine molecules. The water molecules are shown in pink, the glycine molecules are shown in blue, the imidazolium rings and alkyl chain carbon atoms of $[C_1C_{10}Im]$ cations are shown in red and green respectively. The oil phase (nonane), hydrogen atoms of $[C_1C_{10}Im]$ cations and bromide anions are not shown for the ease of visualization.

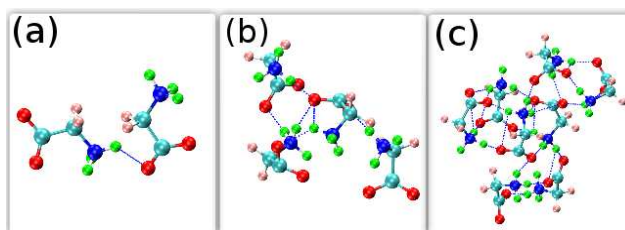


Figure 7.4: Snapshot of glycine molecules within the reverse micellar aqueous core containing (a) 2 (b) 4 and (c) 8 glycine molecules. The oxygen, carbon and nitrogen atoms are shown in red, cyan and blue respectively and the hydrogen atoms attached to the α -C atom, and the amino hydrogen atoms are shown in pink and green respectively.

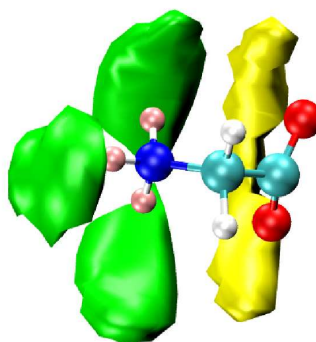


Figure 7.5: Spatial density of amino hydrogens (in yellow) and carboxylate oxygens (in green) around the α -C atom of glycine molecule.

amino hydrogen atoms are preferentially located near the carboxylate oxygen atoms whereas the carboxylate oxygens tend to accumulate near the amino hydrogen atoms. The isosurface density values in Figure 7.5 correspond to 0.052 and 0.135 for carboxylate oxygens and amino hydrogens respectively for the reverse micelle containing 8 amino acids.

Radius of gyration, R_g , provides an estimate of the size of a micelle. We have calculated R_g for the aqueous core of the reverse micelles by using the following formula,

$$R_g = \sqrt{\frac{\sum_i m_i r_i^2}{\sum_i m_i}} \quad (7.2)$$

where m_i is the mass of the i -th atom in the aqueous core situated at radial distance r_i from the center of mass of the reverse micelle. Here i includes atoms of water molecules, glycine molecules, bromide anions, imidazolium rings and tail atoms up to the second carbon atom from the imidazolium ring of $[C_1C_{10}Im]$ cations. Figure 7.6 presents the probability distribution of R_g of aqueous pool of the reverse micelles containing varying number of glycine molecules. The most probable

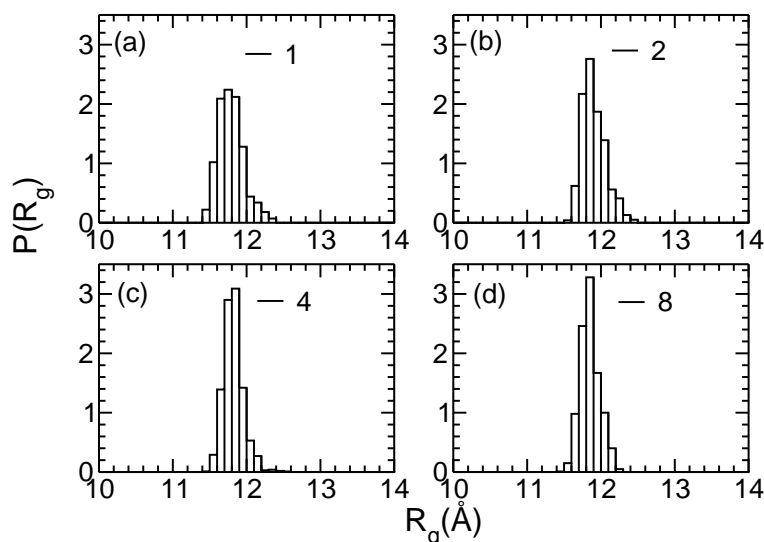


Figure 7.6: Probability distribution of R_g of aqueous core of the reverse micellar systems containing (a) 1 (b) 2 (c) 4 and (d) 8 glycine molecules.

value of R_g is 11.9Å in all the systems studied. It can be observed that the probability distribution of R_g for the reverse micellar aqueous core becomes narrower and the peak height increases at the most probable value of R_g , as the number of glycine molecules increases. This suggests that the aqueous core becomes stable with less fluctuation in shape as the number of glycine molecules in

the core increases. The reduced fluctuation can be attributed to the formation of H-bonding network between water and glycine molecules, which holds the aqueous pool tightly. The probability distribution of R_g value of the model reverse micellar water pool resembles that of the reverse micelle containing single glycine molecule (Figure F.1(a), Appendix F). We have also computed the probability distribution of R_g for the entire reverse micellar aggregates containing varying number of glycine molecules (Figure F.2, Appendix F). Although the most probable value of R_g for the reverse micellar aggregate is $\sim 14.0\text{\AA}$ irrespective of the systems studied, the trend in fluctuation in the corresponding distributions follows the same pattern as of the distribution of R_g for the aqueous pool. We can say that the overall shape of the entire aggregate is influenced by the shape of the reverse micellar aqueous pool. The most probable values of eccentricities, ϵ for the aqueous core of the reverse micelles studied are < 0.15 , implying a slight deviation from the spherical shape. Figure 7.7 presents the snapshot of the reverse micellar aqueous core containing 8 glycine molecules. Based on the assumption of uniform mass distribution of a spherical aggregate, the

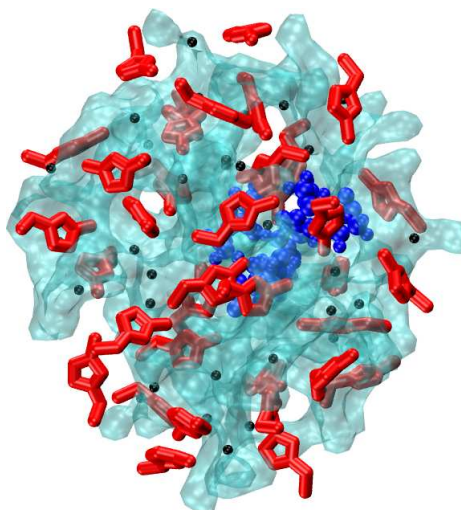


Figure 7.7: Snapshot of the reverse micellar aqueous core containing 8 glycine molecules. The water phase is shown as a continuous medium (in cyan), the glycine molecules are shown in blue, the imidazolium rings along with the first two carbon atoms attached to the ring of $[\text{C}_1\text{C}_{10}\text{Im}]$ cations are shown in red and the bromide anions are shown in black.

radius (R_c) of the reverse micellar aqueous core is computed by a simple relation: $R_g^2 = (3/5)R_c^2$.

The most probable value of R_c in all the systems is found to be 15.3\AA .

The orientational order parameter q has been computed to study the local structural order in

water in the reverse micellar systems containing amino acids. The orientational order parameter is given by [41, 42]

$$q = \left\langle 1 - \frac{3}{8} \sum_{j=1}^3 \sum_{k=j+1}^4 \left(\cos \psi_{jk} + \frac{1}{3} \right)^2 \right\rangle \quad (7.3)$$

where ψ_{jk} is the angle formed by the vectors joining the oxygen atom of a given water molecule and those of its four nearest neighbors j and k . The $\langle \dots \rangle$ means that q is averaged over all the water molecules. The values of q is in the range $-3 \leq q \leq 1$. In a perfect tetrahedral, $q=1$ whereas for a random molecular arrangement, as in an ideal gas, the mean value of q vanishes. Thus, q is a measure of the degree of tetrahedrality in the arrangement of four nearest neighbors around a central one.

Figure 7.8 shows the histograms of the order parameter q around those water molecules that are present in the first solvation shell of the α -C atom of the glycine molecule. In constructing

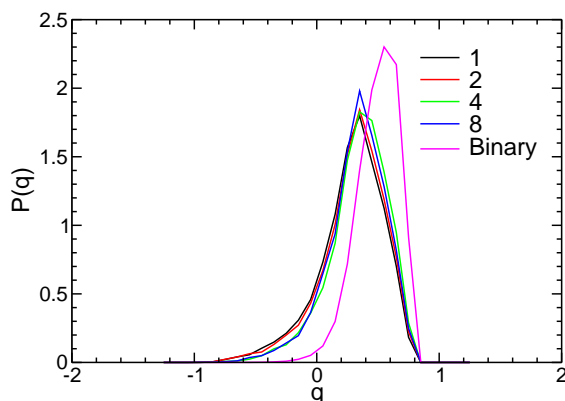


Figure 7.8: Probability distribution of the tetrahedral order parameter around those water molecules which are present in the first solvation shell of the α carbon atom of the glycine molecule.

the neighbor list of four nearest water molecules around the water molecules present in the first solvation shell of the glycine molecule, those within a spherical shell of 3.0 \AA from the edge of the corresponding first solvation shell have also been considered. The most probable value of q in binary glycine–water bulk solution is ~ 0.55 whereas the value decreases to ~ 0.35 within the reverse micellar aqueous core. The decrease in the value of q from the bulk to the reverse micellar aqueous pool can be attributed to two phenomena. One is that the water molecules in the reverse micellar aqueous pool participate in the formation of H-bonds with other ions, e.g. bromide

anions and imidazolium cations which may displace other water molecules from the tetrahedral arrangement. Second, the availability of tetrahedrally arranged nearest neighbor water molecules are limited for the peripheral water molecules in the aqueous core of the reverse micelles.

7.3.3 Density Profiles

The distribution of different moieties in a reverse micelle can be described by the radial density profile, ρ_α from the center of mass of the reverse micelle. We have calculated radial density profiles by using the equation

$$\rho_\alpha = \frac{1}{4\pi r^2} \sum_i \langle \delta(|r_i^\alpha - r_{CM}| - r) \rangle \quad (7.4)$$

where r_i^α represents the distance of the i -th species from the center of mass, r_{CM} of the reverse micelle. To overcome the problem of less statistics within short distance (e. g. 1.0 Å) from the center of mass of the reverse micelle, we have particularly taken the first spherical shell with 5.0 Å of radius and then onward, the thickness of the spherical shells are kept to be 1.0 Å. Figure 7.9(a) presents the radial density distribution of α -C atoms of glycine molecules for the reverse micelles having varying number of amino acids. We observe that the glycine molecules are likely to be present at the center of the aqueous core. Glycine molecules, being hydrophilic, will try to hide themselves from the oil (nonane) phase and interact with the water core. It was seen that the glycine molecules prefer to stay together by the formation of inter glycine H-bonds (Figure 7.4). The enhancement in α -C density near the center of mass of the reverse micelle with increase in the number of glycine molecules is also evident in Figure 7.3. This increment in α -C density at the center of the aqueous core is balanced by the shifting of the local density of other species towards the surfactant–nonane interface, as is evident from the radial density profiles of water oxygen atoms in Figure 7.9(b) for the corresponding systems. Density profiles of geometric center of imidazolium rings and bromide ions are shown elsewhere (Figure F.3, Appendix F).

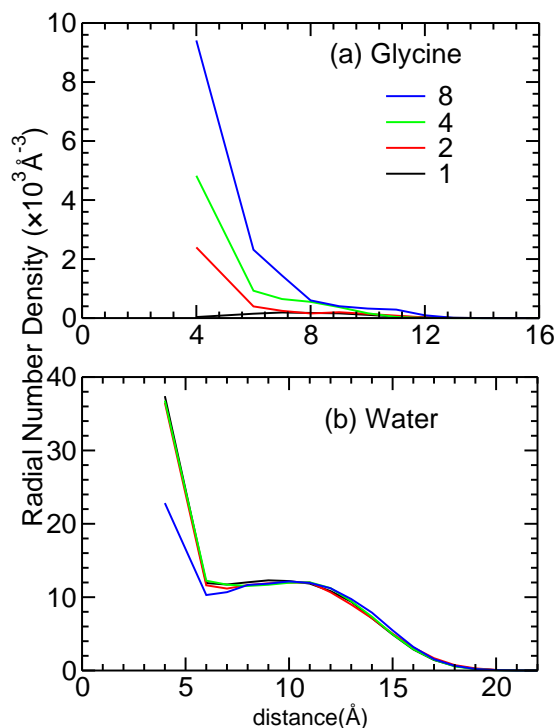


Figure 7.9: Radial density profiles of (a) α -C atoms of glycine molecules and (b) water oxygen atoms for the reverse micelles containing varying number of glycine molecules.

7.3.4 Hydrogen Bond Dynamics.

The fluctuations in hydrogen-bond populations with time are characterized by the time correlation function (TCF) [43]

$$C_{HB}(t) = \frac{1}{N} \sum_{ij=1}^N \langle h_{ij}(t) \cdot h_{ij}(0) \rangle \quad (7.5)$$

where $h_{ij}(t)$, an instantaneous hydrogen-bond operator takes the value 1 if molecules i and j are H-bonded at time t and 0 otherwise, assuming the intermittent approximation [44, 45]. The function $C_{HB}(t)$ gives the probability that the molecules i and j are H-bonded at time t , given that they were H-bonded at time 0. Our definition of hydrogen bond adapts the geometric criteria [46] according to which hydrogen atom and the acceptor are separated by a distance less than 3.0\AA and the angle made by the donor, H atom and the acceptor falls within the range $90\text{-}180^\circ$ to form a H-bond.

Even though there are different kinds of H-bonds present in aqueous pool of the studied reverse micelles, we are focusing on H-bonds formed among the glycine molecules and among the water molecules. In a glycine molecule, the more electronegative carboxylate oxygen acts as the H-

bond acceptor and the amino nitrogen acts as the H-bond donor [48]. For H-bonds formed among the water molecules, the water oxygen acts both as the donor as well as the acceptor. The mean lifetimes (τ_{HB}) have been evaluated from the time integral of $C_{HB}(t)$ [45]

$$\tau_{HB} = \int_0^{\infty} C_{HB}(t) dt \quad (7.6)$$

The mean lifetimes for H-bonds among glycine and among water molecules are summarized in Table 7.2.

Table 7.2: Mean lifetimes (τ_{HB}) for H-bonds between species of the same kinds in different systems studied.

System	$\tau_{HB}(\text{ps})$	
	GLY–GLY	W–W
Binary	517.54	6.47
Model RM	–	21.66
1	–	22.62
2	1178.44	22.37
4	1557.10	23.06
8	1737.40	24.63

Figure 7.10(a) shows the time evolution of $C_{HB}(t)$ for H-bonds formed among the glycine molecules (GLY–GLY) in different systems studied. The survival TCF for H-bonds among the glycine molecules decays more quickly in binary glycine-water bulk solution compared to reverse micellar water pool. The mean lifetimes (τ_{HB}) for GLY–GLY H-bonds in different reverse micellar water pools are ~ 2 – 3 times longer than in glycine–water bulk solution (Table 7.2). This suggests that confinement in small region of space stabilizes the H-bonds compared to bulk solution. We also observe a decrease in rate of decay of $C_{HB}(t)$ with increase in number of glycine molecules in reverse micellar water pool, which is also reflected in the increase in corresponding τ_{HB} s (Table 7.2). More number of glycine molecules in the confined water pool introduces greater steric crowding which will force the glycine molecules to stay together leading to the increase in the mean lifetime of GLY–GLY H-bonds.

Figure 7.10(b) shows the survival TCFs ($C_{HB}(t)$) for H-bonds among the water molecules (W–W) in different reverse micellar systems studied. From the inset in Figure 7.10(b), we see that

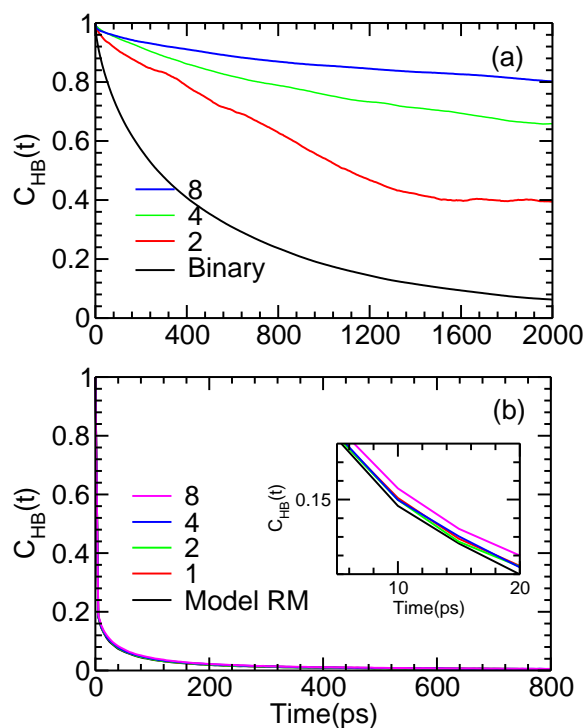


Figure 7.10: Survival autocorrelation function, $C_{HB}(t)$ for H-bonds between (a) glycine molecules and (b) water molecules in different systems studied.

$C_{HB}(t)$ decays more quickly in the reverse micellar water pool with no glycine molecules than with glycine molecules. The mean lifetimes of H-bonds (τ_{HB}) formed between water molecules is slightly higher for the reverse micellar systems containing glycine molecules than the model reverse micellar system (Table 7.2). Although the $C_{HB}(t)$ s decay almost at the same rate for reverse micellar systems having 1, 2 and 4 glycine molecules, system with 8 glycine molecules shows noticeable slow down in the decay of $C_{HB}(t)$. From Table 7.2, we observe that τ_{HB} for the reverse micellar systems differ negligibly in systems with 1 and 2 glycine molecules and it increases with increase in number of glycine molecules in the remaining systems. τ_{HB} for W–W H-bonds in the binary glycine–water bulk solution was calculated to be only 6.47 ps which suggests that the glycine molecules in the reverse micellar water pool stabilizes the W–W H-bonds.

7.3.5 Translational Mobility

In order to obtain the actual picture of translational mobility of a species within the reverse micellar aqueous pool, we have studied the mean squared displacement (MSD) calculated in the center of

mass frame of the reverse micelle [27]. Figure 7.11(a) shows the MSD of glycine molecules in different systems studied. In 2000 ps window, we observe that the rate of increase in MSD for

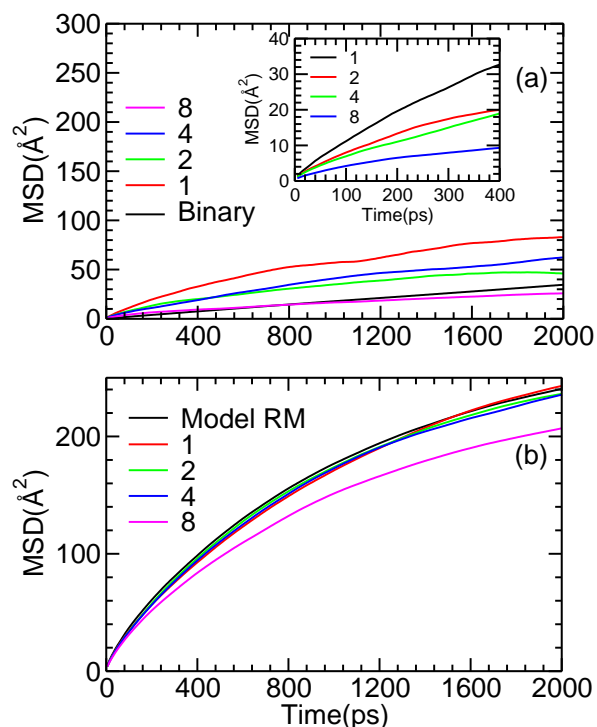


Figure 7.11: Mean squared displacement (MSD) of (a) glycine and (b) water in the center of mass frame of the reverse micelle in different systems studied.

glycine molecules in the center of mass frame of the reverse micelle decreases with increase in the number of glycine molecules. Reverse micelle having single glycine molecule has the highest rate of increase in glycine MSD whereas the rate is minimum for the reverse micelle having 8 glycine molecules. Glycine molecules in the reverse micellar water pool tend to cluster together through the formation of H-bonding network. In the reverse micelle with 8 glycine molecules, all the amino acids club together leading to increase in apparent mass of glycine molecules. As a result, glycine molecules in this system show slowest rate of increase in MSD. Reverse micelles with 2 and 4 amino acids show intermediate rate of increase in glycine MSD. In a smaller time window of 400 ps (inset in Figure 7.11(a)), one can see that the rate of increase in glycine MSD follows the same trend as that of mean lifetimes (τ_{HB}) of GLY-GLY H-bonds across the different reverse micelles studied (Table 7.2), i.e., more the value of τ_{HB} , slower will be the diffusion. In a longer time window of 10 ns, it is observed that the MSD of glycine molecules increases with

time in binary glycine–water bulk solution (Figure F.4, Appendix F). Figure 7.11(b) shows the MSD of water molecules in different systems studied. We see that water molecules in the model reverse micelle show highest rate of increase in MSD whereas the rates are slightly lower in reverse micellar water pool with 1, 2 and 4 glycine molecules. Reverse micelle having 8 amino acids show slowest rate of diffusion of water molecules which is in accordance with the highest τ_{HB} for W–W H-bonds (Table 7.2).

7.3.6 Re-orientation Dynamics

Orientalional time correlation functions (TCFs), $C_l(t)$ determine orientational relaxation of a species. Usually, $C_l(t)$ is formulated in terms of reorientation of a unit vector \hat{e}_i belonging to the i -th species as

$$C_l(t) = \frac{1}{N} \sum_{i=1}^N \langle \hat{e}_i(t) \cdot \hat{e}_i(0) \rangle \quad (7.7)$$

We have calculated the $C_l(t)$ in the laboratory frame instead of the center of mass frame of the reverse micelle, as the rotational motion of the reverse micelle as a whole has a small contribution to the orientational relaxation [27]. The computed TCFs were fitted by single stretched exponential decay function [47]

$$C_l(t) = \exp(-(t/\tau_{rot})^\beta) \quad (7.8)$$

where τ_{rot} is the reorientation time or relaxation time associated with the exponential function and β is the stretched exponent.

In the present study, the rotation of a glycine molecule is investigated using the reorientation of three vectors, two located on the plane of the molecule (the vector joining the amino nitrogen atom and the carboxylate carbon atom (NG–CX) and the vector joining the α -carbon atom and the middle point (M) of the NG–CX vector (CL–M)) and one normal to the plane of the molecule (the normal vector to the plane constituted by NG, CL and CX atoms (M–P)). A schematic of the aforementioned vectors are presented in figure 7.12. Figure 7.13(a) presents the time evolution of $C_l(t)$ of different vectors in a glycine molecule for the reverse micelle containing 8 glycine molecules up to 500 ps. We see that the rate of decay of TCF for the reorientation of NG–CX

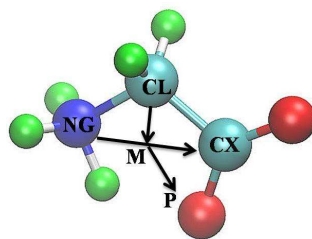


Figure 7.12: Different vectors of interest for orientational relaxation in a glycine molecule.

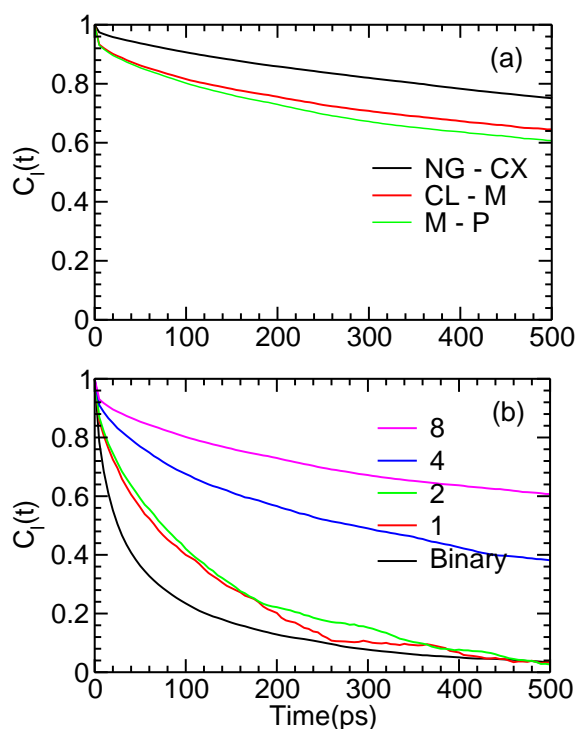


Figure 7.13: Variation of $C_l(t)$ for (a) vectors characterizing the glycine molecule in reverse micelle with 8 glycine molecules and (b) M–P vector of glycine molecules across the systems studied.

vector is the slowest implying that both in-plane and out of plane rotation of NG–CX is not favored due to largest moment of inertia along this direction. The rate of decay of $C_l(t)$ for the reorientation of CL–M and M–P vectors are very close to each other with slightly faster decay observed for the rotation of M–P vector. This suggests that the orientational relaxation of CL–M vector is largely coupled with the reorientation of M–P vector with small contribution from the orientational relaxation of NG–CX vector. τ_{rot} s are calculated to be 3448 ps, 2902 ps and 1960 ps for reorientation of NG–CX, CL–M and M–P vectors respectively. The time evolution of $C_l(t)$ s of different molecular vectors in glycine molecule shows similar trend in rest of the systems studied.

(Figure F.5, Figure F.6, Figure F.7, Figure F.8, Appendix F).

As the rotation of the M–P vector is the fastest among the specified molecular vectors in a glycine molecule irrespective of the systems studied, the reorientation of the M–P vector has major contribution towards rotational relaxation of glycine. Figure 7.13(b) shows rotational relaxation ($C_l(t)$) of M–P vector in glycine molecule across the systems studied, up to 500 ps of elapsed time. Table 7.3 lists the corresponding fitted parameters. It was observed that the rate of decay of

Table 7.3: Parameters of the stretched exponential fit to the reorientation time correlation function.

System	τ_{rot} (ps)	β
Binary	51.34	0.54
1	105.60	0.75
2	117.54	0.75
4	536.16	0.56
8	1960.0	0.50

$C_l(t)$ s for glycine molecules decreases in the reverse micellar water pool compared to the binary glycine–water bulk solution, which is a direct consequence of confinement. For reverse micelles with varying number of amino acids, a gradual increase in reorientational time, τ_{rot} , is observed with increase in the number of glycine molecules. Orientational motion requires a rearrangement in H-bond network. So, the increase in the reorientational time is a consequence of the stability of inter glycine H-bonds, i.e., more the mean lifetime of H-bonds formed among glycine molecules (Figure 7.10 and Table 7.2), more strongly the glycine molecules are held together and slower will be the decay in rotational TCFs of the M–P vectors. Single glycine molecule in the reverse micellar water pool which can not form a inter glycine H-bond, shows fastest decay of $C_l(t)$.

Figure 7.14 presents the rotational relaxation ($C_l(t)$) of a unit vector along the direction of the dipole moment of a water molecule in the reverse micelles studied. Table 7.4 lists the corresponding fitted parameters up to 4000 ps of elapsed time. The τ_{rot} for water molecules in the aqueous pool of model reverse micellar aggregate is calculated to be ~ 32.0 ps which is in excellent agreement with the experimentally determined rotational relaxation time of water molecules encapsulated in AOT/isooctane reverse micelles with $W_0 = 5.0$ [49]. We see that the rate of decay of

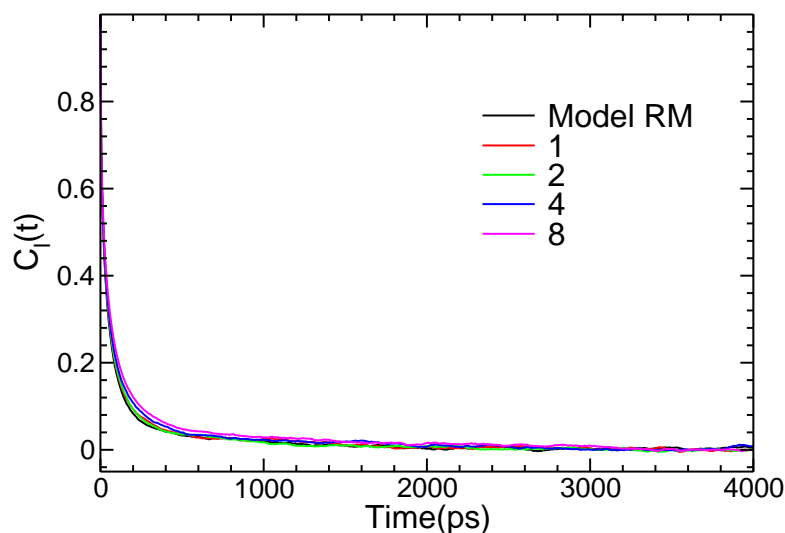


Figure 7.14: Variation of $C_l(t)$ for the unit vector along the dipole moment of a water molecule across the reverse micellar systems studied.

Table 7.4: Parameters of the stretched exponential fit to the reorientation time correlation function.

System	$\tau_{rot}(\text{ps})$	β
Model RM	31.94	0.46
1	33.71	0.45
2	34.64	0.46
4	35.48	0.43
8	38.98	0.41

$C_l(t)$ for the dipole orientational relaxation of water molecules in the reverse micellar water pool decreases with increase in the number of amino acids. The trend is similar to that of the decay of $C_{HB}(t)$ (Figure 7.10(b) and Table 7.2), which suggests that the dynamics of hydrogen bonds play an important role in the orientational relaxation of molecules in the reverse micellar water pool.

7.4. Conclusions

Atomistic molecular dynamics simulations have been carried out on water/[C₁C₁₀Im][Br] reverse micelles encapsulating varying number of zwitterionic glycine molecules (0 to 8) in pure nonane at $W_0 \approx 5.0$. Spherical reverse micelles were formed from uniform initial distribution of surfactant and nonane molecules. Within the reverse micelles, glycine molecules associate to form inter-glycine H-bonds. Spatial distribution function shows preferential accumulation of amino hydrogen atoms near the carboxylate oxygens of glycine molecules and vice versa due to the formation of H-bonds between them. The probability distribution of radius of gyration

(R_g) of the reverse micellar aqueous core becomes narrower and the intensity of the peak increases as the number of glycine molecules increases. We have found that the distribution of radius of gyration (R_g) of the aqueous core of the reverse micelle has a direct consequence on the overall size of the reverse micelle. The shape of the aqueous core was spherical in all the systems studied. The most probable value of tetrahedral order parameter decreases from ~ 0.55 for binary glycine–water bulk solution to ~ 0.35 within the reverse micellar aqueous core. Glycine molecules within the reverse micelle are preferentially located near the center of the water pool.

The survival time correlation functions ($C_{HB}(t)$) of H-bonds between glycine molecules indicates that nano-confinement stabilizes the H-bonds compared to the bulk solution. The mean lifetime of H-bonds between glycine molecules in reverse micellar aqueous pool increases with increase in the number of glycine molecules. The increase in the number of glycine molecules also stabilizes water–water H-bonds within the reverse micelles. In a smaller time window of 400 ps, rate of increase in MSD of glycine molecules in the center of mass frame of the reverse micelle shows similar trend as that of mean lifetimes of glycine–glycine H-bonds. The rotation of the vector normal to the plane constructed by the nitrogen atom, α -C atom and carboxyl carbon atom of a glycine molecule provides major contribution to the reorientation of the glycine molecule. The reorientational TCF ($C_l(t)$) of this vector shows slower decay in reverse micellar water pool than in the bulk solution. The reorientational relaxation time for a glycine molecule increases with increase in the number of glycine molecules in the reverse micellar aqueous core as a result of formation of stable glycine–glycine H-bonds. Farther experimental and computational studies are required to explore the structure and dynamics of biomolecules encapsulated in the aqueous core of reverse micelles consisting of ionic liquid based surfactants.

Chapter F

Appendix F

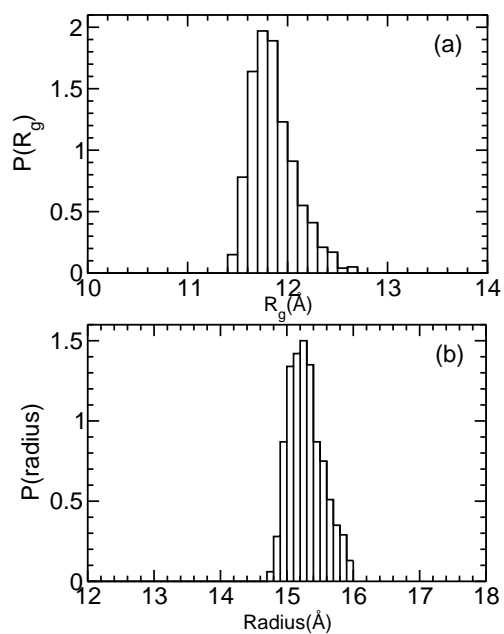


Figure F.1: Probability distribution of (a) R_g and (b) radius of aqueous core of the model reverse micelle.

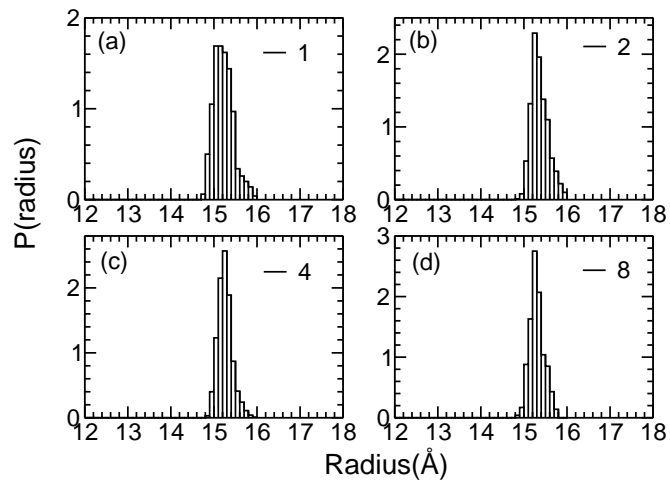


Figure F.2: Probability distribution of radius of aqueous core of the reverse micellar systems containing (a) 1 (b) 2 (c) 4 and (d) 8 glycine molecules respectively.

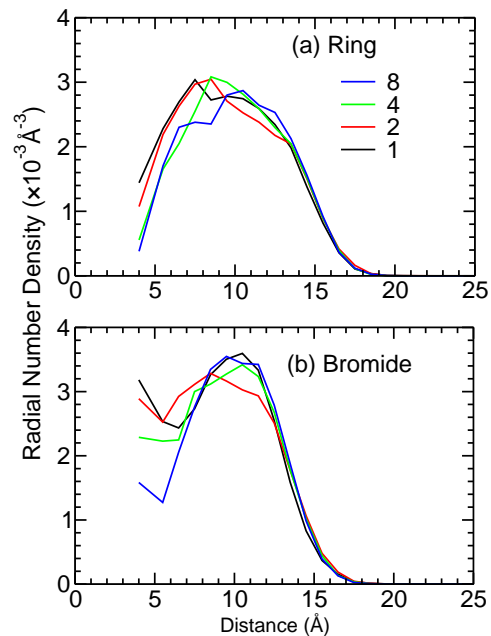


Figure F.3: Radial density profiles of (a) geometric center of imidazolium ring and (b) bromide anions for the reverse micelles containing varying number of glycine molecules.

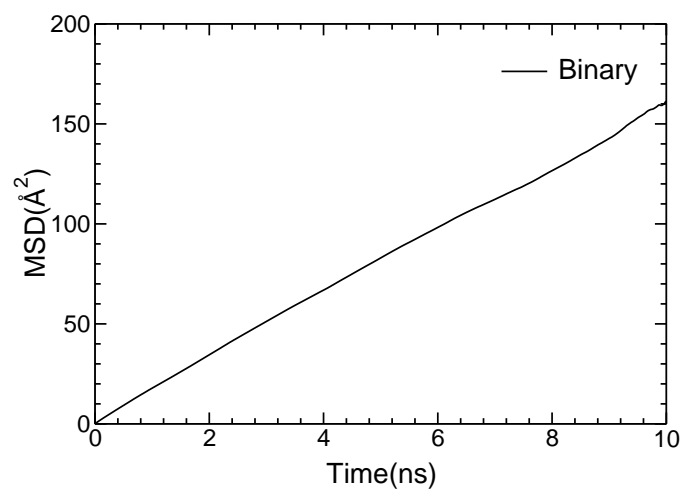


Figure F.4: Mean squared displacement (MSD) of glycine molecules in binary glycine–water bulk solution.

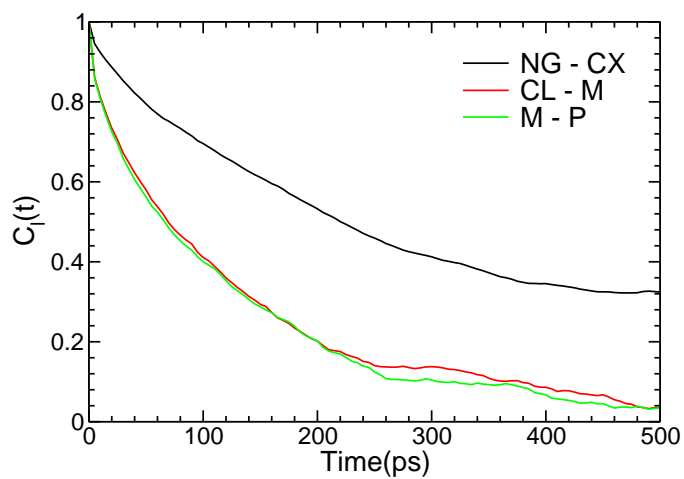


Figure F.5: Variation of reorientational time correlation function ($C_l(t)$) for different molecular vectors of glycine molecule in reverse micelle with single glycine molecule.

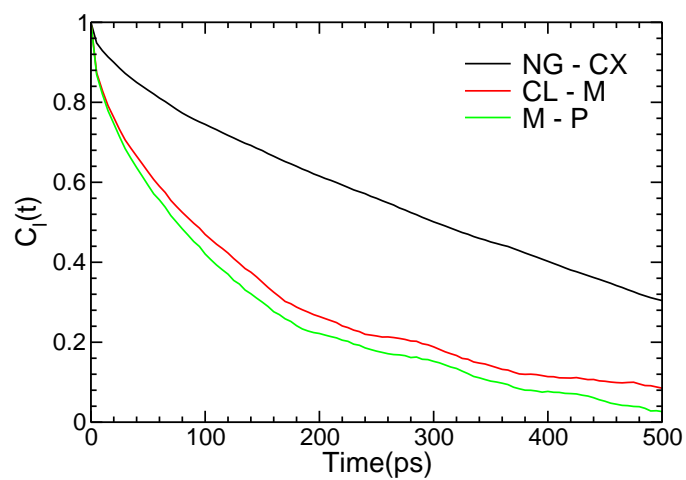


Figure F.6: Variation of reorientational time correlation function ($C_l(t)$) for different molecular vectors of glycine molecule in reverse micelle with two glycine molecules.

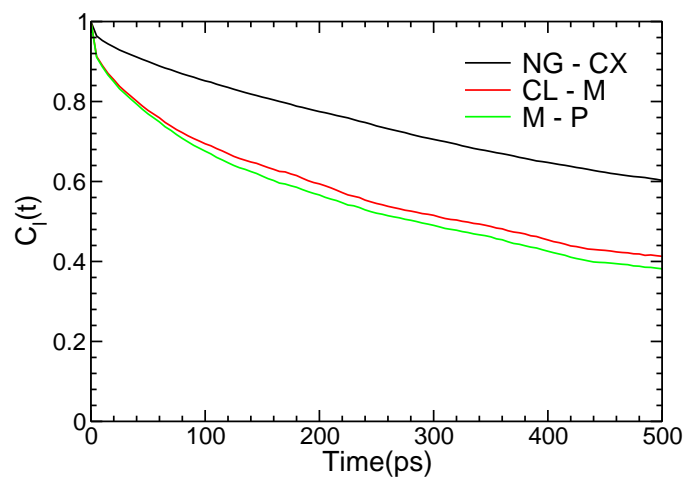


Figure F.7: Variation of reorientational time correlation function ($C_l(t)$) for different molecular vectors of glycine molecule in reverse micelle with four glycine molecules.

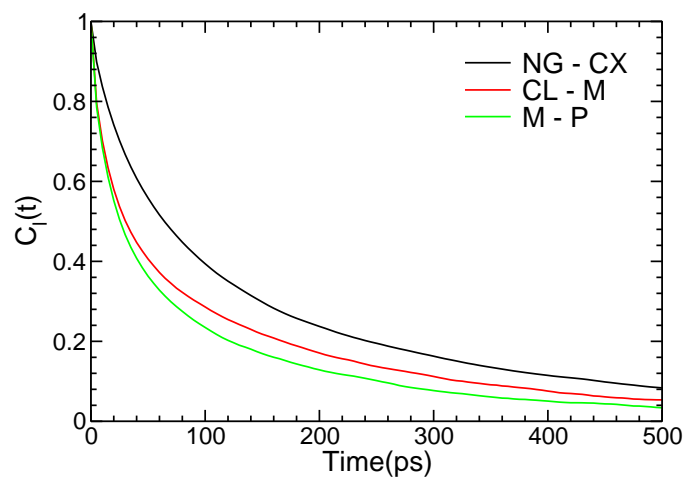


Figure F.8: Variation of reorientational time correlation function ($C_l(t)$) for different molecular vectors of glycine molecule in binary glycine–water bulk solution.

Bibliography

- [1] Abel, S.; Waks, M.; Urbach, W.; Marchi, M. *J. Am. Chem. Soc.* **2006**, *128*, 382-383.
- [2] Mukherjee, S.; Chowdhury, P.; Gai, F. *J. Phys. Chem. B.* **2006**, *110*, 11615-11619.
- [3] Mukherjee, S.; Chowdhury, P.; Gai, F. *J. Phys. Chem. B.* **2009**, *113*, 531-535.
- [4] Leodidis, E. B.; Hatton, T. A. *J. Phys. Chem.* **1990**, *94*, 6411-6420.
- [5] Furusaki, S.; Kishi, K. *J. Chem. Eng. Jpn.* **1990**, *23*, 91-93.
- [6] Hano, T.; Ohtake, T.; Matsumoto, M.; Kitayama, D.; Hori, F.; Nakashio, F. *J. Chem. Eng. Jpn.* **1991**, *24*, 20-24.
- [7] Sharma, L.; Saroj.; Singh, N. *J. Surfact. Deterg.* **2015**, *18*, 33-39.
- [8] Leodidis, E. B.; Hatton, T. A. *J. Phys. Chem.* **1990**, *94*, 6400-6411.
- [9] Wang, W.; Weber, M. E.; Vera, J. H. *Ind. Eng. Chem. Res.* **1995**, *34*, 599-606.
- [10] Storm, S.; Aschenbrenner, D.; Smirnova, I. *Sep. Purif. Technol.* **2014**, *123*, 23-34.
- [11] Adachi M.; Harada, M.; Shioi, A.; Sato. *J. Phys. Chem.* **1991**, *95*, 7925-7931.
- [12] Fang, Y.; Bennett, A.; Liu, J. *Phys. Chem. Chem. Phys.* **2011**, *13*, 1466-1478.
- [13] Fang, Y.; Liu, F.; Liu, J. *J. Am. Soc. Mass. Spectrom.* **2012**.
- [14] Liu, J.; Cheng, S.; Zhang, J.; Feng, X.; Fu, X.; Han, B. *Angew. Chem. Int. Ed.* **2007**, *46*, 3313-3315.

- [15] Moniruzzaman, M. ; Kamiya, N.; Nakashima, K.; Goto, M. *Chem. Phys. Chem* **2008**, *9*, 689-692.
- [16] Blach, D.; Pességo, M.; Silber, J.; Correa, N. M.; García-Río, L.; Falcone, R. D. *Langmuir* **2014**, *30*, 12130-12137.
- [17] Wang, J.; Pei, Y.; Zhao, Y.; Hu, Z. *Green Chem.* **2005** *7*, 196-202.
- [18] Tian, J.; Garcia, A. E. *Biophys. J.* **2009**, *96*, 57-59.
- [19] Tian, J.; Garcia, A. E. *J. Chem. Phys.* **2011**, *134*, 225101-225111.
- [20] Martinez, A. V.; Desensi, S. C.; Dominguez, L.; Rivera, E.; Straub, J. E. *J. Chem. Phys.* **2011**, *135*, 055107-055109.
- [21] Martinez, A. V.; Malolepsza, E.; Dominguez, L.; Lu, Q.; Straub, J. E. *J. Phys. Chem. B* **2015**, *119*, 9084-9090.
- [22] Fayer, M. D.; Levinger, N. E. *Annu. Rev. Anal. Chem.* **2010**, *3*, 89-107.
- [23] Levinger, N. E. *Science* **2002**, *298*, 1722-1723.
- [24] Riter, R. E.; Undiks, E. P.; Levinger, N. E. *J. Am. Chem. Soc.* **1998**, *120*, 6062-6067.
- [25] Pieniazek, P. A.; Lin, Y.; Chowdhury, J.; Ladanyi, B.; Skinner, J. L. *J. Phys. Chem. B* **2009**, *113*, 15017-15028.
- [26] Faeder, J.; Ladanyi, B. M. *J. Phys. Chem. B* **2000**, *104*, 1033-1046.
- [27] Chowdhury, J.; Ladanyi, B. M. *J. Phys. Chem. A* **2009**, *115*, 6306-6316.
- [28] Biswas, R.; Chakraborti, T.; Bagchi, B.; Ayappa, K. G. *J. Chem. Phys.* **2012**, *137*, 14515-14524.
- [29] Chandran, A.; Prakash, K.; Senapati, S. *J. Am. Chem. Soc.* **2010**, *132*, 12511-12516.
- [30] Agazzi, F. M.; Correa, N. M.; Rodriguez, J. *Langmuir* **2014**, *30*, 9643-9653.

- [31] Plimpton, S. *J. Comput. Phys.* **1995**, *117*, 1-19.
- [32] Berendsen, H. J. C.; Postma, J. P. M.; van Gunsteren, W. F.; Hermans, J. In *Intermolecular Forces*; Pullman, B., Ed.; Reidel: Dordrecht, The Netherlands, 1981; p 331.
- [33] P Mark, P.; L Nilsson, L. *J. Phys. Chem. A* **2001**, *105*, 9954-9960.
- [34] Lopes, J. N. C.; Deschamps, J.; Pádua, A. A. H. *J. Phys. Chem. B* **2004**, *108*, 2038-2047; **108**, 11250.
- [35] Lopes, J. N. C.; Pádua, A. A. H. *J. Phys. Chem. B* **2006**, *110*, 19586-19592.
- [36] Jorgensen, W. L.; Maxwell, D. S.; Tirado-Rives, J. *J. Am. Chem. Soc.* **1996**, *118*, 11225-11236.
- [37] Siu, S. W. I.; Pluhackova, K.; Böckmann, R. A. *J. Chem. Theory Comput.* **2011**, *8*, 1459-1470.
- [38] Allen, M. P.; Tildesley, D. J. *Computer Simulation of Liquids*; Clarendon Press: Oxford, U.K., 1987.
- [39] Ryckaert, J. P.; Ciccotti, J.; Berendsen, H. J. C. *J. Comput. Phys.* **1977**, *23*, 327-341.
- [40] Humphrey, W.; Dalke, A.; Schulten, K. *J. Mol. Graphics* **1996**, *14*, 33-38.
- [41] Chau, P. L.; Hardwick, A. *J. Mol. Phys.* **1998**, *93*, 511-518.
- [42] Errington, J. R.; Debendetti, P. G. *Nature* **2001**, *409*, 318-321.
- [43] Luzar, A.; Chandler, D. *Nature* **1996**, *379*, 55-57.
- [44] E. Lloyd, *Handbook of Applicable Mathematics. Volume II: Probability*, Wiley, New York, 1st edn, 1980.
- [45] Eloa, M. D.; Ladanyi, B. M. *J. Chem. Phys.* **2006**, *125*, 184506-184519.
- [46] Desiraju, G. R.; Steiner, T. *The Weak Hydrogen Bond, In Structural Chemistry and Biology*; Oxford University Press: New York, 2001.

- [47] Berberan-Santos, M. N.; Bodunov, E. N.; Valeur B. *Chem. Phys.* **2005**, *315*, 171-182.
- [48] A. Panuszko, A.; M. Śmiechowski, M.; J. Stangret, J. *J. Chem. Phys.* **2011**, *134*, 115104-115104-9.
- [49] Piletic, I. R.; Moilanen, D. E.; Spry, D. B.; Levinger, L. E.; Fayer, M. D. *J. Phys. Chem. A* **2006**, *110*, 4985-4999.

Chapter 8

Ionic Liquids at Nonane – Water Interfaces: Molecular Dynamics Studies

Abstract:

Structure of ternary systems with water, nonane and an ionic liquid, with the ionic liquid placed between water and nonane have been studied using atomistic molecular dynamics simulations. Three different ionic liquids with 1-*n*-butyl-3-methylimidazolium cation and bromide, tetrafluoroborate and trifluoromethanesulfonate anions have been studied. The ionic liquids disperse into aqueous phase quickly and are solubilized in water within 15 ns to form two equivalent nonane - aqueous ionic liquid interfaces. Interfacial region is enriched with ionic liquids due to the amphiphilicity of the cations. The presence of ionic liquids at the interface reduces the interfacial tension between the nonane and water, thus facilitating the mixing of aqueous and nonane phases. The reduction in the interfacial tension is found to be inversely related to the solubility of the corresponding ionic liquid in water. The butyl chains of the cations and the trifluoromethanesulfonate anions present in the interfacial region are found to be preferentially oriented parallel to the interface normal.

8.1. Introduction Room-temperature ionic liquids (RTILs), with wide liquid range, low vapor pressure, and many potential applications in synthesis, catalysis and electrochemistry have received significant attention of researchers [1, 2, 3, 4, 5]. Imidazolium-based ionic liquids (ILs) are extensively studied using experimental [5, 6, 7] and computational methods [8, 9, 10, 11, 12, 13, 14]. Structure of the vapor-liquid interface of ILs has also been investigated [15, 16, 17, 18]. Imidazolium cations with long alkyl chain substituent form well defined aggregates in their aqueous solution [19], whereas cations with intermediate length alkyl chain (butyl to hexyl) behave as amphiphilic molecules and form oligomers at high concentration [20].

Amphiphilic ILs, with polar head groups and non-polar hydrocarbon tails, have affinity for both water and oil phases. In a ternary system composed of oil, water and amphiphilic ILs, the amphiphiles are preferentially adsorbed at the oil-water interface, thus reducing the interfacial tension between aqueous and the oil phase [21, 22, 23]. This leads to enhanced solubilization of the oil into the aqueous phase, and such formulations are widely used in chemical flooding induced enhanced oil recovery (EOR) of the remaining oil from reservoirs [24, 25, 26] and solubilization of sparingly soluble drugs [27]. In two phase homogeneous catalysis, where the phase containing reactants and products is immiscible with the phase containing catalyst, amphiphilic ILs increase the solubility of the reactants in catalyst phase to give practical reaction rates [28].

In an attempt to gain insights into the atomic level details, we have investigated the structure of ternary systems composed of water, 1-*n*-butyl-3-methylimidazolium ($[C_4C_1Im]$) cation based IL and nonane. We have used nonane to model the oil phase. To study the effect of anion on the structure of the interface we have carried out MD simulations on three different systems by varying the counter anion (Br^- , BF_4^- and $CF_3SO_3^-$) associated with the cation.

8.2. Methodology and Simulation Details Three different ternary systems consisting of water, $[C_4C_1Im]$ cation based IL and nonane, have been studied employing atomistic MD simulations, using the LAMMPS [40] package. Each of the three systems composed of a different anion (bromide (Br^-), tetrafluoroborate (BF_4^-) and trifluoromethanesulfonate ($CF_3SO_3^-$)). Force field parameters for the nonane were taken from the model developed

by Jorgensen [41] *et. al.* and Siu [42] *et. al.* The force field parameters for the ionic liquids have been adapted from the the works of Padua [43, 44] and co-workers. For water molecules, simple point charge (SPC) model [45] has been used.

The ternary systems were constructed as follows: Nonane, water and IL were equilibrated separately in canonical ensemble at a temperature of 333 K and a density that is 5% higher than the experimental density at that temperature. The orthogonal boxes with dimensions, 40 Å along each axes were used to equilibrate water and nonane, while equilibration of IL was carried out in a box of dimension 40 Å along x- and y-axis and 20 Å along z-axis. These three equilibrated simulation boxes were fused along z-axis to build the ternary systems. During this process, the molecules that were very close to each other were removed. Few molecules of each of the species were removed randomly to ensure that the final density of each of the phases in the simulation box was equal to the experimental density at the simulated temperature. Simulations of water-nonane biphasic system was also carried out at 333 K. All the simulated systems contained 206 nonane molecules.

Details of the systems that were studied are presented in table 8.1. In the table, ternary systems are represented by the anions they are composed of.

Table 8.1: Details of the Simulated Systems

system	no. of ion pairs	no. of water	no. of atoms	run length(ns)	box length(Å)
nonane-water	0	2106	12292	20	40.0, 40.0, 80.0
Br ⁻	111	2106	15178	30	40.0, 40.0, 100.0
BF ₄ ⁻	103	2105	15379	30	40.0, 40.0, 100.0
CF ₃ SO ₃ ⁻	93	2105	15358	30	40.0, 40.0, 100.0

All simulations were performed in canonical ensemble (constant *NVT*) at 333 K. The simulations were carried out at higher temperature as the ILs used in our studies are very viscous at room temperature. Stretching and bending interactions in the water molecule were constrained using the SHAKE algorithm [47]. The equations of motion were integrated using the verlet algorithm with a time step of 0.5 fs. Three-dimensional periodic boundary conditions were used, giving an infinite

stack of thin films of nonane, IL and water along z-direction. The positions of the atoms were stored at an interval of 5 ps and were used for analyses. The pressure tensor was stored every time step during the last 1 ns simulation and was used to calculate the interfacial tension. The results reported have been averaged over the last 10 ns of the trajectory unless mentioned otherwise.

8.3. Results and Discussions Schematic of $[C_4C_1Im]$ cation and nonane, describing the atom types and their connectivity is shown in figure 8.1 to aid the discussion. In the following discussion, head group refers to the geometric center of the imidazolium

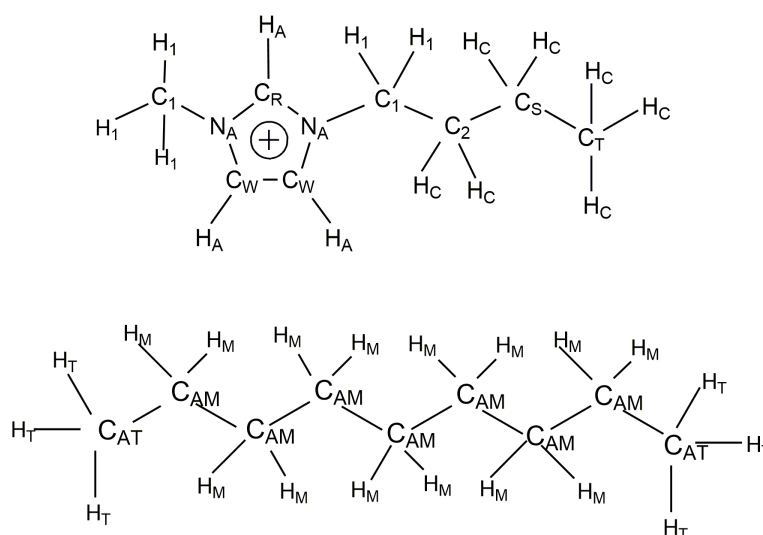


Figure 8.1: Schematic representation of the $[C_4C_1Im]$ cation and nonane showing the atom types used in the discussion.

ring and the tail group refers to the terminal methyl group of the butyl chain attached to the imidazolium ring.

Ionic liquids quickly diffused into aqueous phase within few nanoseconds and formed an equilibrated biphasic system of nonane and aqueous IL solution within 15 ns. Snapshots of the initial configuration, after 1 ns, and after 30 ns of simulation for the ternary system with $[C_4C_1Im][Br]$ are shown in figure 8.2. The resultant configuration resembled Winsor Type I solution [29].

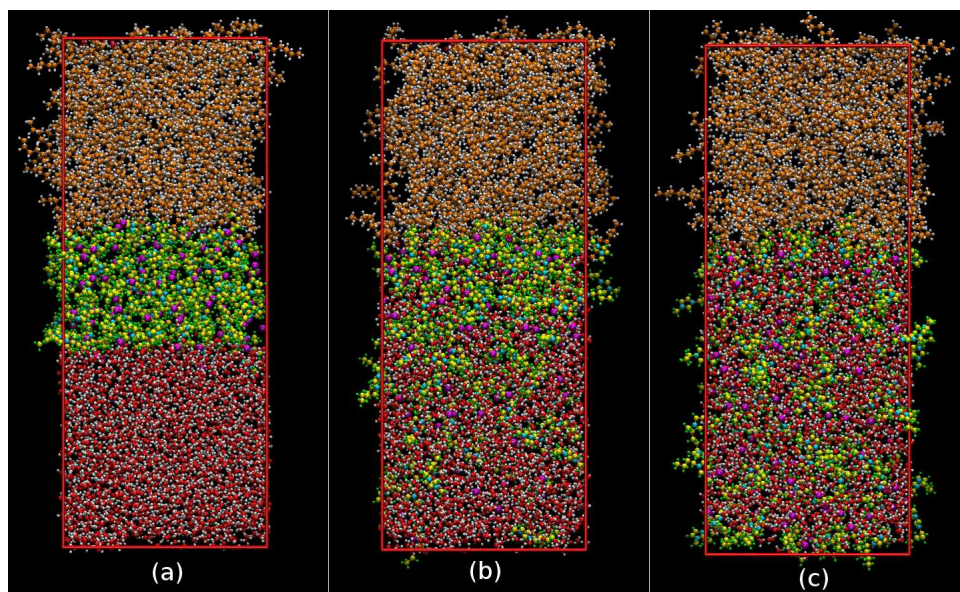


Figure 8.2: Snapshots of the ternary system with bromide anion. (a) initial configuration (b) after 1 ns simulation (c) after 30 ns simulation. Carbon atoms of nonane are shown in orange and the oxygen atoms of water are shown in red. Anions are represented as magenta beads.

8.3.1 Number Density

Number density profile of atoms or groups along the interface normal provides information about the structure of the interface [49, 50]. The number density profiles of the nonane (C_{AT}), water, cation (head and tail groups), and anion (bromide), along z -axis, for the ternary system with nonane, $[C_4C_1Im][Br]$ and water are shown in figure 8.3a. The total atom number density profile is also shown in the same figure. As the number of water and nonane molecules in the system is more compared to cations and anions, the corresponding number density profiles and total atom number density profile are scaled accordingly, for the ease of comparison.

In the figure 8.3a, the presence of peaks in the cation (head and tail) number density profiles indicate the preferential adsorption of cations at the interface. The peak in the anion number density profile close to that of the head group, at the interface indicates their strong association with the head groups. The hydrophobic tails of cations penetrates deeper into the oil phase compared to the hydrophilic head group, which is expected. The number density profiles of nonane and water show less enhancement in the density at the interface. The number density profiles of different moieties

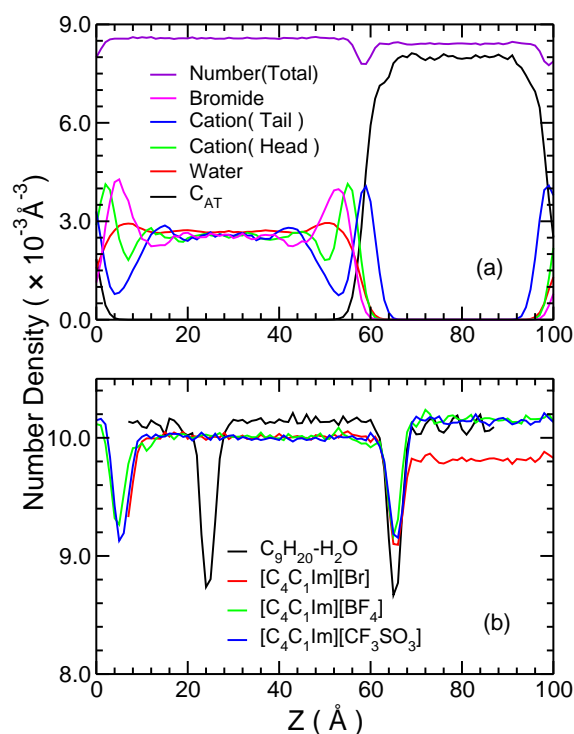


Figure 8.3: (a) Number density profiles of different moieties along interface normal (z-axis) in nonane-[C₄C₁Im][Br]-water system. (b) Atom number density profiles of nonane-water binary system and ternary systems along z-axis.

along interface normal in ternary systems with BF₄⁻ and CF₃SO₃⁻ anions are qualitatively similar (Figure G.1 and Figure G.2, Appendix G). Enhancement of the density of water at the interface is highest for the ternary system with Br⁻ anion and least for the system with CF₃SO₃⁻ anion. The density profiles calculated from our studies are similar to those reported from a computational study of water-IL-heptane systems [39]. The density enhancement of water at the interface in case of most water soluble IL is also observed in their studies. Bromide ions interact with the cations at the interface and these anions being highly soluble in water, draw water molecules to the interfacial region. While CF₃SO₃⁻ anions present at the interface, being less soluble in water, does not draw water molecules to the interface, thus reducing the number of cation-water hydrogen bonds in the interfacial region, that will be discussed later in this section.

The total atom number density in the figure 8.3a shows a depletion at the interface. Such a depletion is also observed in earlier studies of a ternary system [51]. The repulsive interaction between the oil and the water phases is responsible for the depletion of the total atom number

density at the oil-water interface.

The atom number density profiles of the binary nonane-water system and the ternary systems are shown in figure 8.3b. It is evident from the figure that the depletion in the total number density at the interface is more in the absence of ionic liquid. Decrease in the depletion of atom number density in the presence of IL indicates the decrease in repulsive interactions between the oil and the water phase. Due to their amphiphilic nature (i.e., the preference of the head groups to interact with the water and the tails to interact with the oil), $[C_4C_1Im]$ cations decreases repulsion between water and oil phases and enhances the miscibility of these two phases.

The number density profiles of anions in the ternary systems are shown in figure 8.4a. It can

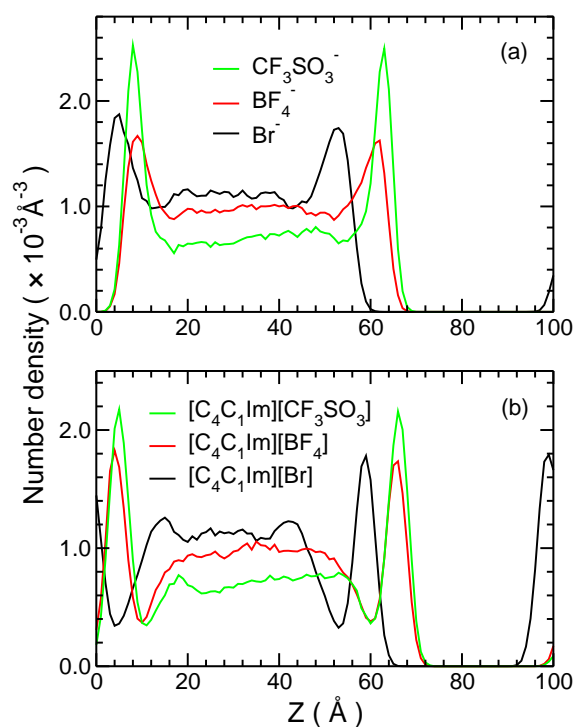


Figure 8.4: (a) Anion number density profiles along z-axis, in ternary systems. (b) Tail number density profiles in ternary systems along the interface normal.

be observed that all the three anions show peak in the interface region. The amplitude of the peak is higher in case of $CF_3SO_3^-$ anion, compared to bromide and tetrafluoroborate anions, indicating their preference to be present at the solution-oil interface. The higher amplitude peak arises due to the nature of the $CF_3SO_3^-$ anion, which shows orientational ordering along the interface normal,

that will be discussed later in this section.

Preferential accumulation of the butyl tails of cations at the interface is evident from their density profiles shown in figure 8.4b. The adsorption is higher in the case of ternary system with CF_3SO_3^- anions. Similar trend is observed in the head group density profile also (data not shown). From the density profiles, it is evident that anions play an important role in determining the interfacial structure of the aqueous IL solution-nonane system. The fact that the number density of head and tail groups of cations also varies with variation of anion suggests that the cation-anion interactions also contribute to interface structure variations. Hence, anions of the ILs can also be varied to design ternary systems with desired interfacial properties.

To characterize the structure of the interfacial region, we define interface as the region where the solution phase and the nonane phase coexist. So, the interface is the region along z-axis, between the points, where the number density of the tail group of cations (C_T) and the nonane (C_{AT}) falls to zero. The ternary systems studied have two equivalent interfaces, as evidenced by the peaks with similar amplitudes in the density profiles. A nonane molecule is considered to be at the interface if the z-coordinate of either of its terminal carbon atoms falls within this region. A $[\text{C}_4\text{C}_1\text{Im}]$ cation is considered to be at the interface if the z-coordinate of any of its atoms is within this region. Water and anions, with the z-coordinate of the oxygen atom and the z-coordinate of the central atom of the anion (Br, B or S), respectively, falling within the above mentioned region are considered to be at the interface.

8.3.2 Hydrogen Bonding

Hydrogen bonding plays an important role in determining the structure of aqueous IL solutions [20] and hence is also important in ternary systems consisting of nonane, IL and water. We have adapted the geometric criteria [52] to define a H-bond, that is, for a strong H-bond, the distance between the H-atom and the acceptor should be less than 2.2 \AA and the angle made by the donor, H-atom and the acceptor should fall within the range of $130\text{-}180^\circ$. For a weak H-bond, the corresponding distance range and angular range should be $2.0\text{-}3.0 \text{ \AA}$ and $90\text{-}180^\circ$ respectively.

Imidazolium cation based ILs are known to exhibit cation - anion, cation - water and anion -

water H-bonds in their aqueous solutions [53]. Formation of H-bonds was also observed in the ternary systems.

The radial distribution functions (RDFs) of the H-bond acceptor atom on the anion around ring hydrogen atoms show the first peak at 3.1 Å, 2.7 Å, and 2.7 Å, respectively for ternary systems with Br⁻, BF₄⁻ and CF₃SO₃⁻ anions (Figure G.3(a), Appendix G). The position of the first peak of the RDFs suggests the formation of H-bond between the cation and the anion. The amplitude of the first peak is higher for the system with CF₃SO₃⁻ anion compared to that with BF₄⁻ anion. These observations are consistent with the number of head-anion H-bonds per cation observed in the ternary systems. The RDFs of oxygen atom of water around the ring hydrogen atoms show the first peak at 2.8 Å in all the ternary systems (Figure G.3(b), Appendix G), suggesting the formation of H-bonds. The amplitudes of the first peaks are consistent with the average number of cation-water H-bonds observed per cation in these systems.

Average number of head-group - anion and head-group - water H-bonds observed in the bulk region and in the interfacial region of different ternary systems studied are tabulated in table 8.2.

Table 8.2: Average number of H-bonds formed per cation

system	head-anion (bulk)	head-anion (interface)	head-water (bulk)	head-water (interface)
[C ₄ C ₁ Im][Br]	0.127	0.148	3.843	3.562
[C ₄ C ₁ Im][BF ₄]	2.014	1.143	3.435	1.369
[C ₄ C ₁ Im][CF ₃ SO ₃]	3.006	1.257	3.545	0.495

From the table 8.2, we see that number of H-bonds formed per cation between the ring hydrogen atoms and the anions, in bulk phase and in the interfacial region, increases for the ternary systems in the following order: Br⁻ < BF₄⁻ < CF₃SO₃⁻. The trend is opposite of the solubility of the corresponding IL in water [54, 55]. Greater aqueous solubility of IL leads to less number of H-bonding interactions between cation and anion in the solution, which is expected. Less than 1% of the observed H-bonds were strong.

It is also observed that there is a decrease in the average number of H-bonds per cation, between the head group and the water molecules in the interfacial region compared to bulk. This

decrease is significant for the ternary system with the CF_3SO_3^- anion (86%) and marginal for the Br^- system (7%). The large decrease in case of CF_3SO_3^- ternary system can be attributed to the presence of more anions at the interface (Figure 8.4(a)) thus decreasing the number of water molecules at the interface compared to other systems (Figure G.4, Appendix G). These anions also form H-bonds with the cations, thus reducing the cation-water H-bonds. The difference, between the average number of cation-water H-bonds per cation in bulk and in interfacial region, is highest for the least soluble IL in water (among the ILs studied) and is least for the most soluble IL in water (among the ILs studied). This difference follows the opposite trend of solubility [54, 55] of the corresponding ILs in water. The ILs (present at the interface) that are less soluble in water have more interaction with the nonane phase, thus reducing the number of cation-water H-bonds.

Greater aqueous solubility of the IL results in more number of water molecules in the interfacial region, which ensures more H-bonding interaction between the imidazolium ring and water molecules. Hence the difference between the cation-water H-bonds in the bulk and interface region will not be significant as observed for the ternary system with $[\text{C}_4\text{C}_1\text{Im}][\text{Br}]$ amphiphile. The number of cation-anion hydrogen bonds in the bulk and at interface suggests that the Br^- anion has similar environment in bulk and interface regions, whereas the environment differs for less water soluble anions. The anions in the ternary system also influences the cation-water interaction at the interface to a great extent which is evident from the number of cation-water H-bonds at the interface compared to bulk region.

8.3.3 Radial Distribution Functions (RDFs)

RDF provides information about the organization of atoms or groups around other atoms or groups. As we are dealing with inhomogeneous systems, we have computed the RDFs using only those molecules that are present in the interfacial region. The RDF of nonane (C_{AT}) around different types of carbon atoms in the butyl chain of $[\text{C}_4\text{C}_1\text{Im}]$ cation in the ternary system with bromide anion is shown in figure 8.5a. From the figure, it is seen that the first maximum for $C_T - C_{AT}$ pair is at 4.2 Å. The amplitude of the first maximum is highest for the RDF corresponding to $C_T - C_{AT}$ pair, and is least for $C_1 - C_{AT}$ pair. This indicates that the spatial correlation between the

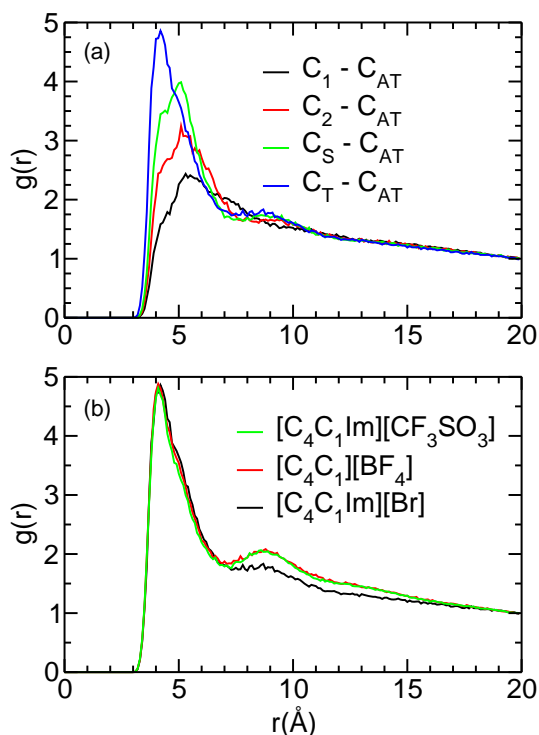


Figure 8.5: RDFs of (a) nonane (C_{AT}) around different carbon atoms of $[C_4C_1Im]$ cation in the ternary system with bromide anion. (b) nonane (C_{AT}) around tail group (C_T) in ternary systems.

nonane and the butyl chain of cation decreases as we move towards the imidazolium ring (head group) of the cation.

Figure 8.5b shows the RDFs of nonane (C_{AT}) around the C_T atoms for the ternary systems. It can be seen from the figure, that the first maxima are observed at 4.2 Å in all the ternary systems. The RDFs of nonane (C_{AT}) - anion pair are shown in figure 8.6a. The amplitude of first maximum is highest for the ternary system with $CF_3SO_3^-$ anion and least for the system with Br^- anion. It is evident from the figure 8.6a, that the spatial correlation of nonane and ILs follows the opposite trend of the solubility of ILs in water [54, 55]. In other words, the spatial correlation of nonane and anions is highest for the IL that is least soluble in water and lowest for the IL that is most soluble (among the ILs studied).

The RDFs for the water - nonane (C_{AT}) pair in the binary nonane-water system and ternary systems are shown in figure 8.6b. All four RDFs exhibit first maxima at 3.9 Å and first minima at 5.3 Å. One can see that the amplitude of first maximum is highest in case of the nonane-water bi-

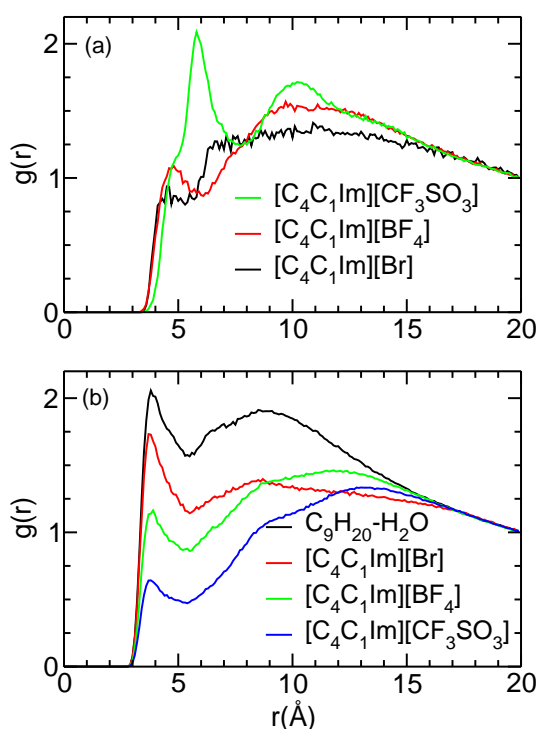


Figure 8.6: RDFs of (a) nonane (C_{AT}) around the central atoms of anions in ternary systems. (b) nonane (C_{AT}) around water in the binary and ternary systems.

nary system and decreases in the following order : bromide > tetrafluoroborate > trifluoromethanesulfonate. Nonane being hydrophobic, water-nonane interactions will be repulsive in nature. In the absence of ILs, water molecules at the interface will be in contact with the nonane molecules. With addition of IL, the cations and anions are adsorbed onto the interface, thus reducing the number of unfavorable interactions between water and nonane. Adsorption of IL molecules at the water-heptane interface has also been reported earlier [39]. The IL molecules at the interface facilitates the presence of both water and nonane in the interfacial region without directly interacting with each other. This can be observed in the reduction of the amplitude of first maximum of water-nonane (C_{AT}) RDF in ternary systems with ILs. The reduction in the amplitude of RDF can be related to the reduction of unfavorable interactions between nonane and water. This reduction follows the opposite trend as the solubility the ILs in water, that is, ILs that are less water soluble will cause greater reduction in the unfavorable interactions between water and nonane.

8.3.4 Spatial Distribution

Spatial distribution provides three dimensional probability density of atoms or a group around an atom or a group of interest. Figure 8.7 shows the spatial distribution of anions, water and nonane (C_{AT}) around the cations that are present at the interface, in the ternary system containing the IL, $[C_4C_1Im][Br]$. From the figure, one can see that the anion density is highest near the ring hydrogen

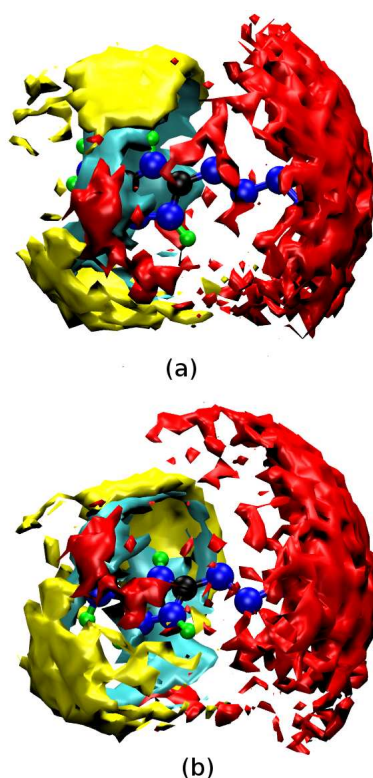


Figure 8.7: (a) Spatial density of anions (in yellow), water (in cyan) and nonane (C_{AT}) (in red) around the cations that are in the interfacial region, in the ternary system with bromide anion. Hydrogen atoms on the butyl chain are not shown for the ease of visualization. (b) Another view of the same figure.

atoms, especially near the unique hydrogen atom (H-atom attached to the carbon atom between the two nitrogen atoms). While in the bulk region, the anion density is higher near all ring H-atoms, in the interfacial region, anion density is lower near the H-atom that is closer to the butyl chain. The reason for this reduction in the density is due to the orientational preference shown by the cations in the interfacial region which will be discussed later. Water molecules show higher density above and below the plane of the ring as well as near two of the ring hydrogen atoms. However, the

density of water molecules is very less in the region directly above the unique hydrogen atom, as the density of bromide ions is high in that region. The density isosurface shown for water and anions are ten times greater than that for nonane molecules. It can be seen that the nonane (C_{AT}) density is highest around the butyl chain of the cation and is negligible in other regions which clearly shows that the nonane molecules interact with the butyl chain of the cations.

8.3.5 Orientation of Ions and Molecules

Distribution of the angle between the vector connecting the nitrogen atoms of the imidazolium ring (NN vector) and the interface normal, for the cations that are present in the interfacial region of the ternary systems are shown in figure 8.8a. It is evident from the figure that for the cations that

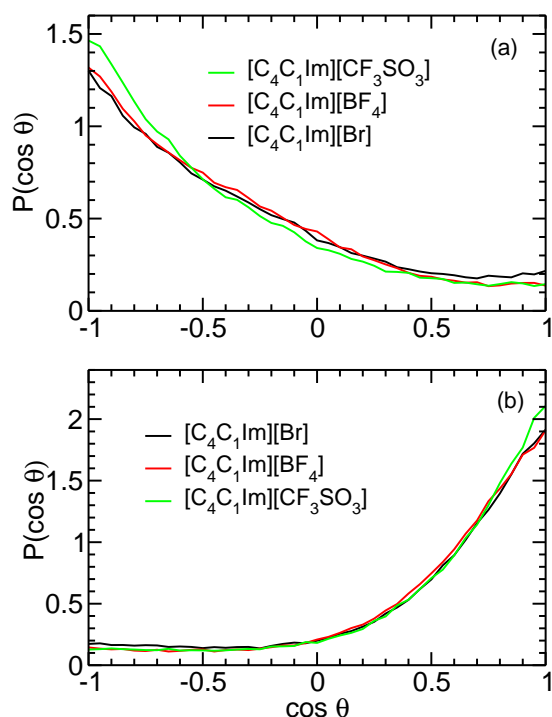


Figure 8.8: Distribution of angle between (a) the vector connecting the nitrogen atoms of the imidazolium ring (NN vector) and the interface normal (z-axis), for the cations that are present in the interfacial region. (b) the butyl chain of cations present at the interface and the interface normal.

are in the interface region, the NN vector of the ring is more likely to be parallel to the interface normal. Figure 8.8b shows the distribution of angle between the butyl chains of cations at the interface and the interface normal. From the figure, one can see that the butyl chains are more

likely to be oriented parallel to the interface normal. Angle distributions of NN vector and the butyl chain of the cations at the interface suggests that the cations at the interface are oriented in such a way that the butyl tail is perpendicular to the interface, pointing towards the nonane phase, whereas the imidazolium ring is pointing towards the aqueous phase of the ternary system. Such an orientation of the butyl chains at the interface, facilitates the interaction of cations with both the nonane phase (van der Waals interaction between alkyl chains) and the aqueous phase (head-water interaction). The orientational preference is slightly higher in case of ternary system with CF_3SO_3^- anion. Orientation of cation derived from our studies agrees with the previous MD studies [39].

Figure 8.9a shows the distribution of angle between the butyl chains (vector connecting N_A and C_T) of the cation, in the interfacial region and bulk that are within 8 \AA of each other. From

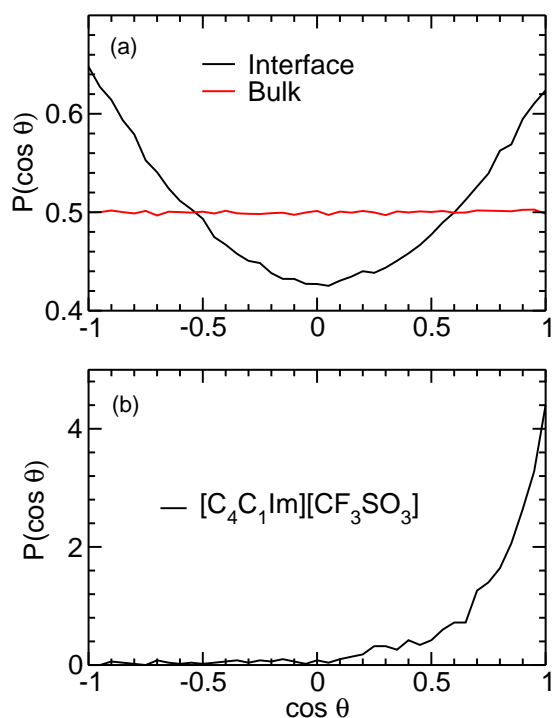


Figure 8.9: Distribution of angle between (a) the butyl chains in the interfacial region and in the bulk that are within 8 \AA of each other. (b) carbon-sulfur bond vector and the interface normal, for the anions that are present in the interfacial region.

the figure, we observe that the distribution is uniform for the cations present in the bulk region, whereas for cations that are present at the interface, the butyl chains are more likely to be oriented either parallel or antiparallel to each other. This suggests that the alkyl chains are organised in the

interfacial region. The organization is also evident from their orientational preference along the interface normal.

The orientation of the carbon-sulfur bond vector of the CF_3SO_3^- anion along the interface normal, for the anions present at the interface in the ternary system, is shown in figure 8.9b. The bond vector is more likely to be aligned parallel to the z-axis. This suggests strong affinity of the CF_3SO_3^- anions for the interface due to favorable interaction between the trifluoromethyl region of the anion with the oil phase. This is also the reason for the appearance of the high amplitude peak in the interfacial region, in the number density profile of that group.

Snapshot of the interfacial region in the ternary system containing $[\text{C}_4\text{C}_1\text{Im}][\text{CF}_3\text{SO}_3]$ IL is shown in figure 8.10. From the figure, we can see that the butyl chains of the cations that are

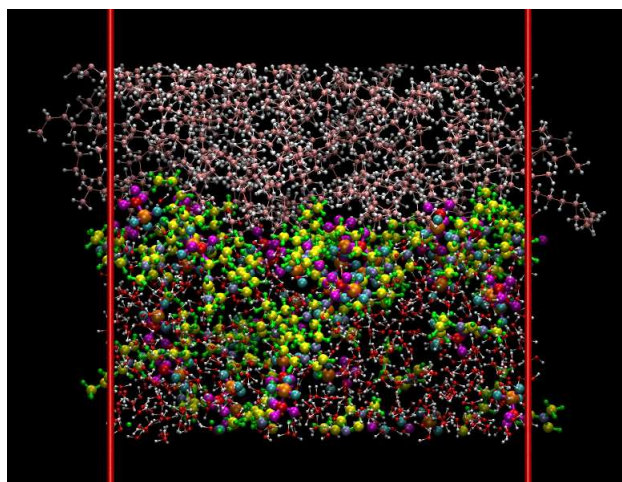


Figure 8.10: Snapshot of the interfacial region in the ternary system with CF_3SO_3^- anion. Only the atoms that are present in the interfacial region are shown. Carbon atoms of nonane are shown in pink color and oxygen atoms of water are shown in red color. Fluorine, sulfur and oxygen atoms of anions are shown in magenta, orange and cyan, respectively.

present at the interface are more likely to be aligned parallel to the interface normal. The adsorption of cations and anions on to the interface and the orientational preference of anions are also evident from the figure.

8.3.6 Interfacial Tension and Interface Composition

The interfacial tension γ between the aqueous phase and nonane was calculated from the diagonal components of pressure tensor P_{ii} using the formula [56]

$$\gamma = -b_z(P_{xx} + P_{yy} - 2P_{zz})/4$$

where b_z is the length of the simulation box along the interface normal (z-axis). The factor 2 has been introduced in the denominator to account for the presence of two equivalent interfaces.

The interfacial tension is related to the composition of the interface. The accumulation of amphiphiles in the interfacial region reduces the interfacial tension. Therefore the adsorption of the ILs at the interface leading to better mixing of aqueous and the oil phase will lead to lower interfacial tension. The interfacial tension for the nonane - water binary system was calculated to be 56.2 mNm^{-1} . This value is slightly higher than the experimentally reported value [57] of 48.8 mNm^{-1} at 60°C . In ternary systems, we observe a decrease in the interfacial tension between the aqueous and the nonane phase. The interfacial tension of ternary systems decrease in the following order: $\text{Br}^- > \text{BF}_4^- > \text{CF}_3\text{SO}_3^-$ (33.44 mNm^{-1} , 32.04 mNm^{-1} and 23.5 mNm^{-1} respectively). The adsorption of ions at the interface was highest for the ternary system with CF_3SO_3^- anion, which is also evident from the reduction in the interfacial tension. Experimental studies [58] have shown that the interfacial tension between ILs and alkanes decreases with the increase in the length of the alkyl chain substituent on the imidazolium cation, when the anion is common among the ILs. It is also observed that the interfacial tension between IL and octane/decane is smaller for $[\text{C}_4\text{C}_1\text{Im}][\text{NTf}_2]$ compared to $[\text{C}_4\text{C}_1\text{Im}][\text{CF}_3\text{SO}_3]$. These observations suggests that the interfacial tension between ILs and alkanes decreases with the decrease in the water solubility of ILs. As the aqueous IL solution and oil interface is populated with IL molecules one can speculate that, in general the amphiphilic ILs with low water solubility (higher amphiphilicity) reduces the interfacial tension to a greater extent. The number of nonane molecules in the interfacial region of ternary systems is higher compared to that of water - nonane binary system. The addition of amphiphilic ILs facilitates the mixing of aqueous and nonane phases. Increasing the substituent chain length of ILs will increase the amphiphilicity and causes the reduction in the interfacial tension

between the aqueous and oil phases.

8.4. Conclusions All-atom MD simulations of three ternary systems composed of nonane, ionic liquid and water have been carried out in canonical ensemble at 333 K. The systems differed from each other in terms of anions (Br^- , BF_4^- and CF_3SO_3^-) associated with the $[\text{C}_4\text{C}_1\text{Im}]$ cation. The simulated systems are found to be biphasic. The ionic liquid quickly disperses into aqueous phase to form a homogeneous solution which remain in equilibrium with the nonane phase. The amount of nonane solubilized in the aqueous phase increases with the decrease in the interfacial tension between the oil and the aqueous phase. The density profiles along the interface normal of different moieties in the ternary systems show that the amphiphilic cations are adsorbed at the interface. The alkyl tails of the cations at the interface are protruding into the oil phase due to the favorable hydrocarbon tail-tail interaction between the cation and the nonane.

Imidazolium rings were found to form H-bonds with both anions and water. The extent of H-bonds formed depends on the the solubility of the ionic liquids in water. The spatial distributions show an enhanced density of anions and water near the ring hydrogen atoms which also support the formation of H-bonds. Nonanes are found to be located near the butyl chain of the cations at the interface.

The most probable orientation of cations at the interface is such that the butyl chains are oriented parallel to interface normal, protruding into the nonane phase. The NN vector of the imidazolium ring is also oriented parallel to the interface normal but with the head group directed towards the aqueous phase. This orientation minimizes the unfavorable interaction of butyl chain with water while maximizing the favorable interactions between the butyl chain of cation and nonane as well as head group and water. Butyl tails in the interfacial region are more likely to be parallel or antiparallel to each other, thus showing an ordered orientation.

The structure of the interface depends upon the extent of H-bonds formed by the imidazolium rings with the anions and water molecules, the extent of solvation of ions in water and interactions of ions with the oil hydrocarbon chains. Solubility of ILs in water governs the structure and

composition of the interface. Ternary system containing the IL, $[\text{C}_4\text{C}_1\text{Im}][\text{CF}_3\text{SO}_3]$ (with least water solubility among the ILs studied) facilitates the mixing of oil and water phases to a greater extent by reducing the interfacial tension.

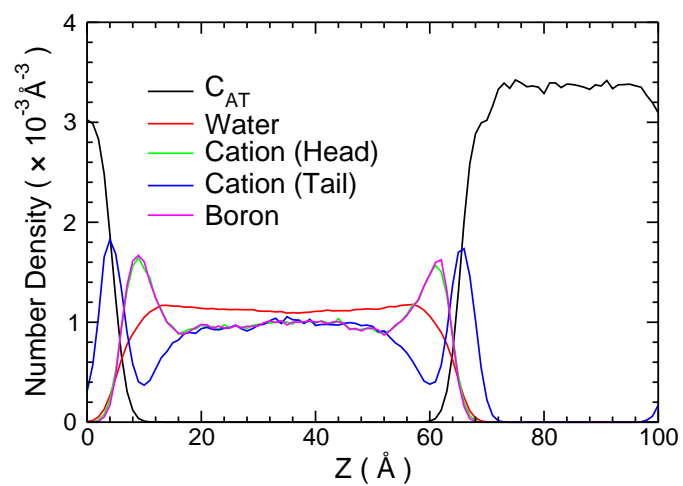


Figure G.1: Number density profiles of different moieties along interface normal (z-axis) in nonane-[C₄C₁Im][BF₄]-water system. Water and nonane densities have been scaled according to their ratio with respect to the cation numbers for ease of comparison.

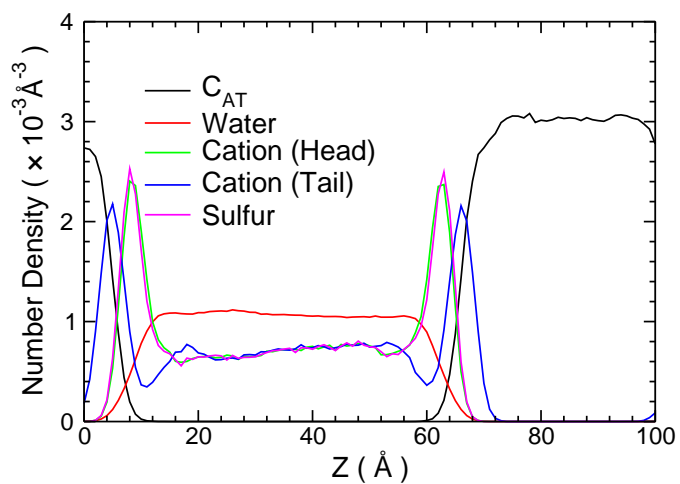


Figure G.2: Number density profiles of different moieties along interface normal (z-axis) in nonane-[C₄C₁Im][CF₃SO₃]-water system. Water and nonane densities have been scaled according to their ratio with respect to the cation numbers for ease of comparison.

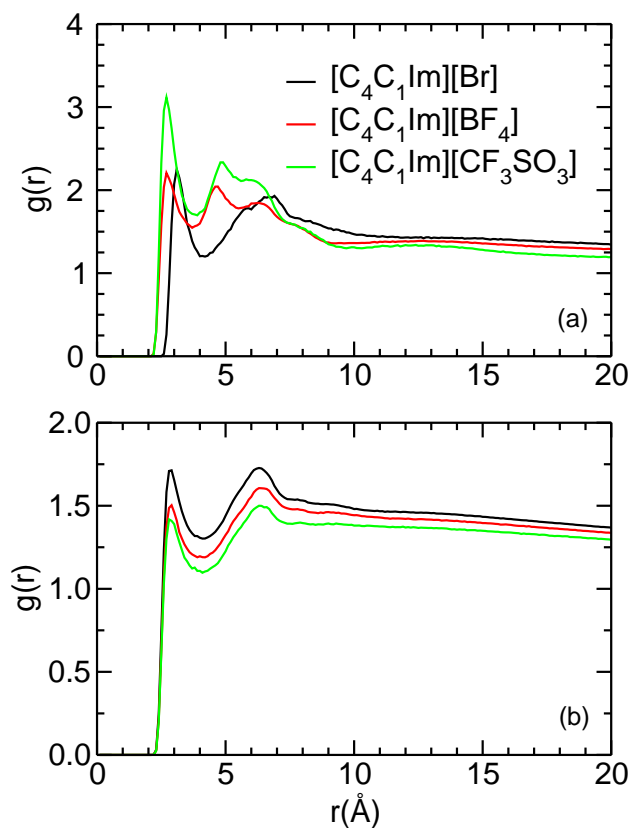


Figure G.3: Radial distribution functions of (a) hydrogen bond acceptor on anions around the ring hydrogen atoms (b) hydrogen bond acceptor on water (oxygen atom) around the ring hydrogen atoms.

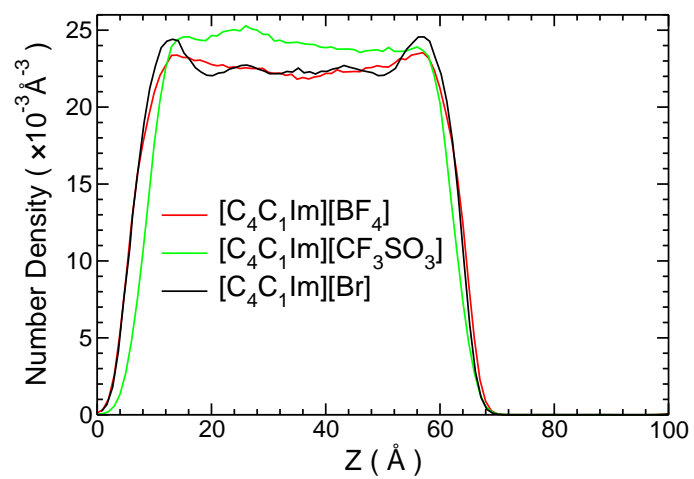


Figure G.4: Water number density profiles along interface normal (z-axis) in different ternary systems.

Bibliography

- [1] Jacquemin, J.; Husson, P.; Pádua, A. A. H.; Majer, P. *Green Chem.* **2006**, *8*, 172-180.
- [2] Triolo, A.; Mandanici, A.; Russina, O.; Rodriguez-Mora, V.; Cutroni, M.; Hardacre, C.; Nieuwenhuyzen, M.; Bleif, H.; Keller, L.; Ramos, M. A. *J. Phys. Chem. B* **2006**, *110*, 21357-21364.
- [3] Huddleston, J. G.; Visser, A. E.; Reichert, W. M.; Willauer, H. D.; Broker, G. A.; Rogers, R. D. *Green Chem.* **2001**, *3*, 156-164.
- [4] Rocha, M. A. A.; Coutinho, J. A. P.; Santos, M. N. B. F. *J. Phys. Chem. B* **2012**, *116*, 10922-10927.
- [5] Tong, J.; Liu, Q.; Xu, W.; Fang, D.; Yang, J. *J. Phys. Chem. B* **2008**, *112*, 4381-4386.
- [6] Anouti, M.; Sizaret, P. Y.; Ghimbeu, C.; Galiano, H.; Lemordant, D. *Colloids Surf., A* **2012**, *395*, 190-198.
- [7] Triolo, A.; Russina, O.; Bleif, H.; Di Cola, E. *J. Phys. Chem. B* **2007**, *111*, 4641-4644.
- [8] Bhargava, B. L.; Balasubramanian, S. *J. Am. Chem. Soc.* **2006**, *128*, 10073-10078.
- [9] Hunt, P. A. *J. Phys. Chem. B* **2007**, *111*, 4844-4853.
- [10] Annapureddy, H. V. R.; Hu, Z.; Xia, J.; Margulis, C. J. *J. Phys. Chem. B* **2008**, *112*, 1770-1776.
- [11] Shi, W.; Maginn, E. J. *J. Phys. Chem. B* **2006**, *112*, 2045-2055.

- [12] Raju, S. R.; Balasubramanian, S. *J. Phys. Chem. B* **2009**, *113*, 4799-4806.
- [13] Skarmoutsos, I.; Dellis, D.; Matthews, R. P.; Welton, T.; Hunt, P. A. *J. Phys. Chem. B* **2012**, *116*, 4921-4933.
- [14] Hettige, J. J.; Kashyap, H. K.; Annapureddy, H. V. R.; Margulis, C. J. *J. Phys. Chem. Lett.* **2013**, *4*, 105-110.
- [15] Lynden-Bell, R. M. *Mol. Phys.* **2003**, *101*, 2625-2633.
- [16] Solutskin, E.; Ocko, B. M.; Taman, L.; Kuzmenko, I.; Gog, T.; Deutsch, M. *J. Am. Chem. Soc.* **2005**, *127*, 7796-7804.
- [17] Yan, T.; Li, S.; Jiang, W.; Gao, X.; Xiang, B.; Voth, G. A. *J. Phys. Chem. B* **2006**, *110*, 1800-1806.
- [18] Jiang, W.; Wang, Y.; Yan, T.; Voth, G. A. *J. Phys. Chem. C* **2008**, *112*, 1132-1139.
- [19] Bhargava, B. L.; Yasaka, Y.; Klein, M. L. *Soft Matter* **2011**, *47*, 6228-6241.
- [20] Bhargava, B. L.; Klein, M. L. *Soft Matter* **1009**, *5*, 3475-3480.
- [21] Salager, J. L.; Manchego, L.; Márquez, L.; Bullón, J.; Forgiarini, A. *J. Surfactants Deterg.* **2014**, *17*, 199-213.
- [22] Lago, S.; Rodríguez, H.; Khoshkbarchi, M. K.; Soto, A.; Arce, A. *RSC Adv.* **2012**, *2*, 9392-9397.
- [23] Hezave, A. Z.; Dorostkar, S.; Ayatollahi, S.; Nabipour, M.; *J. Mol. Liq.* **2013**, *187*, 83-89.
- [24] Rosen, M. J.; Wang, H.; Shen, P.; Zhu, Y. *Langmuir* **2005**, *21*, 3749-3756.
- [25] Prochaska, K.; Staszak, K. *J. Colloid Interface Sci.* **2005**, *285*, 1-8.
- [26] Sabhapondit, A.; Borthakur, A.; Haque, I. *Energy Fuels* **2003**, *17*, 683-688.
- [27] Dobler, D.; Schmidts, T.; Klingenhöfer, I.; Runkel, F. *Int. J. Pharma.* **2013**, *441*, 620-627.

- [28] Olivier-Bourbigou, H.; Magna, L.; Morvan, D. *Appl. Catal., A* **2010**, *373*, 1-56.
- [29] Winsor, P.A. *Trans. Faraday Soc.* **1948**, *44*, 376-398.
- [30] Sottmann, T.; Strey, R. *J. Chem. Phys.* **1997**, *106*, 8606-8615.
- [31] Tichelkamp, T.; Vu, Y.; Nourani, M.; Øye, G. *Energy Fuels* **2014**, *28*, 2408-2414.
- [32] Scheu, R.; Chen, Y.; Aguiar, H. B. D.; Rankin, B. M. ; Ben-Amotz, D; Roke, S. *J. Am. Chem. Soc.* **2014**, *136*, 2040-2047.
- [33] Lago, S.; Francisco, M.; Arce, A.; Soto, A. *Energy Fuels* **2013**, *27*, 5806-5810.
- [34] Lago, S.; Rodríguez-Cabo, B.; Arce, A.; Soto, A. *J. Chem. Thermodyn.* **2014**, *75*, 63-68.
- [35] Chai, J.; Xu, L.; Liu, W.; Zhu, M. *J. Chem. Eng. Data* **2012**, *57*, 2394-2400.
- [36] Williams, P.; Lupinsky, A.; Painter, P. *Energy Fuels* **2010**, *24*, 2172-2173.
- [37] Painter, P.; Williams, P.; Mannebach, E. *Energy Fuels* **2010**, *24*, 1094-1098.
- [38] Hezave, A. Z.; Dorostkar, S.; Ayatollahi, S.; Nabipour, M.; Hemmateenejad, B. *Fluid Phase Equil.* **2013**, *360*, 139-145.
- [39] Zolghadr, A. R.; Ghatee, M. H.; Zolghadr, A. *J. Phys. Chem. C* **2014**, *118*, 19889-19903.
- [40] Plimpton, S. *J. Comput. Phys.* **1995**, *117*, 1-19; web: <http://lammps.sandia.gov>.
- [41] Jorgensen, W. L.; Maxwell, D. S.; Tirado-Rives, J. *J. Am. Chem. Soc.* **1996**, *118*, 11225-11236.
- [42] Siu, S. W. I.; Pluhackova, K.; Böckmann, R. A. *J. Chem. Theory Comput.* **2012**, *8*, 1459-1470.
- [43] Lopes, J. N. C.; Deschamps, J.; Pádua, A. A. H. *J. Phys. Chem. B* **2004**, *108*, 2038-2047; **108**, 11250.
- [44] Lopes, J. N. C.; Pádua, A. A. H. *J. Phys. Chem. B* **2006**, *110*, 19586-19592.

- [45] Berendsen, H. J. C.; Postma, J. P. M.; van Gunsteren, W. F.; Hermans, J. In *Intermolecular Forces*; Pullman, B., Ed.; Reidel: Dordrecht, The Netherlands, 1981; p 331.
- [46] Allen, M. P.; Tildesley, D. J. *Computer Simulation of Liquids*; Clarendon Press: Oxford, U.K., 1987.
- [47] Ryckaert, J. P.; Ciccotti, J.; Berendsen, H. J. C. *N J. Comput. Phys.* **1977**, *23*, 327-341.
- [48] Humphrey, W.; Dalke, A.; Schulten, K. *VMD J. Mol. Graphics* **1996**, *14*, 33-38.
- [49] Bhargava, B. L.; Klein, M. L. *Mol. Phys.* **2009**, *107*, 393-401.
- [50] Bhargava, B. L.; Klein, M. L. *J. Phys. Chem. A* **2009**, *113*, 1898-1904.
- [51] Smit, B.; Hilbers, P. A. J.; Esselink, K.; Rupert, L. A. M.; Van Os, N. M.; Schlijper, A. G. *J. Phys. Chem.* **1991**, *95*, 6361-6368.
- [52] Desiraju, G. R.; Steiner, T. *The Weak Hydrogen Bond, In Structural Chemistry and Biology*; Oxford University Press: New York, 2001
- [53] Palchowdhury, S.; Bhargava, B. L. *J. Phys. Chem. B.* **2014**, *118*, 6241-6249.
- [54] Freire, M. G.; Neves, C. M. S. S.; Carvalho, P. J.; Gardas, R. L.; Fernandes, A. M.; Marrucho, I. M.; Santos, L. M. N. B. F.; Coutinho, J. A. P. *J. Phys. Chem. B* **2007**, *111*, 13082-13089.
- [55] Bini, R.; Bortolini, O.; Chiappe, C.; Pieraccini, D.; Siciliano, T. *J. Phys. Chem. B* **2007**, *111*, 598-604.
- [56] Rao, M.; Berne, B. J. *Mol. Phys.* **1979**, *37*, 455-461
- [57] Zeppieri, S.; Rodríguez, J.; de Ramos, A. L. L. *J. Chem. Eng. Data* **2001**, *46*, 1086-1088.
- [58] Gardas, R. L.; Ge, R.; Manan N. A.; Rooney, D. W.; Hardacre, C. *Fluid Phase Equil.* **2010**, *294*, 139-147.

Chapter 9

Insights into the Structure and Dynamics at the Hexadecane Droplet–water Interface in the Presence of 1-alkanols as Emulsifiers: Molecular Dynamics Studies

Abstract:

The structure and dynamics at the surface of nanoscopic hexadecane droplets immersed in aqueous phase with and without emulsifiers (1-alkanols of varying chain length; pentanol, heptanol, decanol and dodecanol) have been studied using atomistic molecular dynamics simulations. The nature of layering of alcohol molecules on the oil droplet is governed by the hydrophobicity of alkanols. Longer chain alkanols are more likely to penetrate into the oil droplet. The probability of tangential orientation of hexadecane molecules at the interface decreases with decreasing hydrophobic environment around the droplet. The interfacial hexadecane molecules show greater probability to obtain a puckered conformation in binary oil–water system than in ternary oil–water–alkanol systems. Decrease in hydrophobic interaction between hexadecane and water molecules due to the efficient screening of oil surface by longer chain alkanols in ternary oil–water–alkanol systems leads to greater survival probability of water molecules in the oil–water interfacial layer and enhancement in life time of H-bonds formed between alcohol and water molecules.

9.1. Introduction Oil-in-water droplet systems or emulsions are supramolecular assemblies which act as artificial life models representing the hydrophobic domains in contact with aqueous regions (with oil corresponding to the lipid membranes of the cell) [1]. Active emulsions exhibiting self-propelled motion mimic collective phenomenon in biological populations [2]. So, understanding the effect of emulsifier on an oil compartment floated in aqueous media has long been an interest among the researchers [3]. Although several experimental [4, 5, 6, 7, 8] and computational studies [9, 10, 11, 12, 13] have been reported on planar oil-water interfaces, the reports on the influence of surfactants on nanoscopic curved oil-water interfaces are rare [14, 15, 16, 17, 18].

Aliphatic alkanols, particularly 1-alkanols have wide applications as anesthetics [19] and penetration enhancer in transdermal drug delivery [20]. Recently, they have been used as a component in self-evolvable droplet system in a chemrobotic platform [21]. SFS and SHG studies have been performed to gain molecular level insights into the structural aspects of the transition from a hydrophobic to an aqueous phase on hexadecane droplet by employing different chain length alkanols as emulsifiers [18]. The aforementioned study primarily focuses on interfacial alkyl chain conformation of the oil and various alcohol molecules and the orientational alignment of water molecules in a qualitative manner. Although computer simulation studies on planar interface of *n*-alkane-methanol-water system have been performed [22], to the best of our knowledge, there are no reports of computational studies exploring the structural transition from a hydrophobic to an aqueous environment around an oil droplet. So, we have carried out atomistic molecular dynamics simulations on a binary system consisting of hexadecane droplet immersed in water as well as on a series of ternary systems consisting of a hexadecane droplet immersed in aqueous solutions of alkanols of varying chain length to get insights into structural transition from hydrophobic to aqueous region around the droplet and the organization of the hexadecane, water and alkanols near the oil-water spherical interface.

9.2. Methodology and Simulation Details We have carried out all-atom molecular dynamics simulations on a binary system consisting of a hexadecane droplet immersed in water as well as on a series of ternary systems consisting of hexadecane droplets immersed in pre-equilibrated aqueous solutions of alkanols of varying chain length. The four different hexadecane–water–alkanol ternary systems were constructed with pentanol, heptanol, decanol and dodecanol. The hexadecane droplet was constructed in two steps. In the first step, an isothermal-isobaric simulation (constant NPT) was carried out on a system containing 1000 uniformly distributed hexadecane molecules at 1 atmosphere pressure for 2 ns to achieve the equilibrated density at 300 K. In the second step, hexadecane molecules whose center of mass falls beyond a distance cutoff of 20.0 Å from the center of mass of the equilibrated central simulation cell were removed to get a spherical hexadecane droplet of radius 20.0 Å. The hexadecane droplet was immersed in a water box with randomly oriented water molecules to form the binary hexadecane–water system. To construct the hexadecane–water–alkanol ternary system, the hexadecane droplet was immersed into a pre equilibrated water–alkanol binary mixture, equilibrated for 1 ns under isothermal-isobaric condition (constant NPT) at 1 atmosphere pressure and 300 K temperature. While constructing a binary system (e. g. hexadecane–water or water–alkanol), the water molecules that were within 3.0 Å of any of the atoms of hexadecane or alcohol were discarded to remove bad overlap of atom coordinates. The same protocol was applied for water and alcohol molecules while constructing a ternary hexadecane–water–alkanol system. Details of the simulated systems have been presented in Table 9.1. The binary hexadecane–water system is mentioned as “Binary” and the ternary systems are named after the alcohol in the system, e. g., “Pentanol” for the ternary system containing pentanol. The binary hexadecane–water and ternary hexadecane–water–alkanol systems were subjected to a equilibration run under isothermal–isobaric condition (constant NPT) at 1 atmosphere pressure and 300 K temperature for 2 ns followed by a production run of 30 ns under canonical ensemble condition (constant NVT), started from the last configuration of NPT simulation at the same temperature. The pressure and temperature were controlled by Nosé-Hoover barostat and thermostat with a pressure damping parameter of 500 fs and a tem-

Table 9.1: Details of the simulated systems.

system	no. of hexadecane	no. of water	no. of alkanols	no. of atoms	run length(ns)	box length(Å)
Binary	65	12000	100	39250	30.0	73.191
Pentanol	65	12000	100	41050	30.0	74.331
Heptanol	65	12000	100	41650	30.0	74.656
Decanol	65	12000	100	42550	30.0	75.311
Dodecanol	65	12000	100	43150	30.0	75.636

perature damping parameter of 1000 fs respectively. The simulations were performed using the LAMMPS [23] MD package. The simple point charge model (SPC/E) was used to model water molecules [24]. The OPLS-AA force field parameters for hexadecane and alcohol molecules are adapted from the work of Siu et. al [25] and Jorgensen et. al [26]. The stretching of C–H bonds of hexadecane and alkanols, O–H bonds of water molecules and the bending of H–C–H angles of alkane and alkanols as well as of H–O–H angle for water molecules were constrained using the SHAKE [28] algorithm. The equations of motion were integrated using the verlet algorithm with a time step of 1.0 fs. Three dimensional periodic boundary conditions were used to simulate the bulk behavior. The atomic coordinates were stored at an interval of 10 ps. The reported properties are calculated from the last 10 ns of trajectory. A schematic of the molecular structures of hexadecane, water and different 1-alkanols mentioning different atom types are presented in Figure 9.1.

9.3. Results and Discussion

9.3.1 Density Profiles

It has been known for long time that alcohol molecules act as emulsifiers by forming a layer on an oil droplet. The pattern of layering as well as the ability to penetrate the oil droplet by the alkanol depends on its hydrophobicity and can be determined from the distribution of its segments across the oil droplet. Radial density profile, ρ_α of different moieties from the center of mass of the hexadecane droplet gives an idea about the spatial arrangement of different chemical species

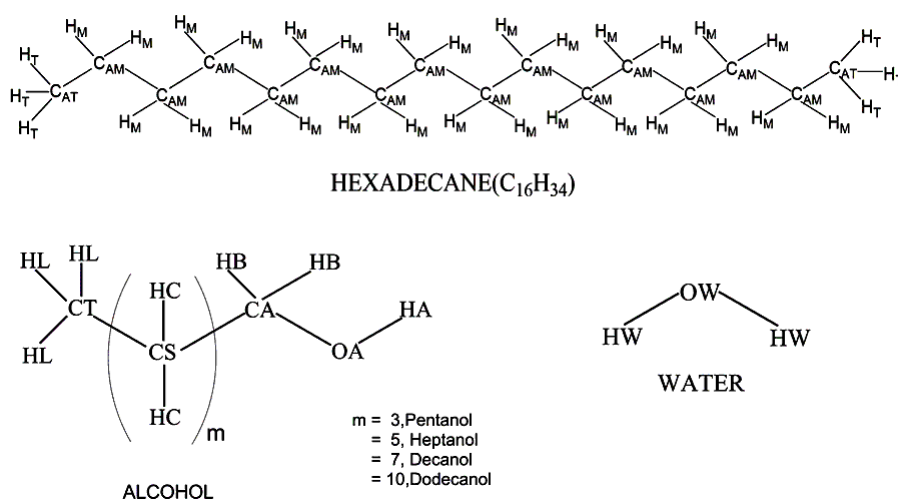


Figure 9.1: Schematic representation of the hexadecane, alkanols and water molecule showing the atom types used in the discussion.

across the oil droplet. ρ_α is calculated by using the equation

$$\rho_\alpha = \frac{1}{4\pi r^2} \sum_i \langle \delta(|r_i^\alpha - r_{CM}| - r) \rangle \quad (9.1)$$

where r_i^α represents the distance of the i -th species from the center of mass, r_{CM} of the hexadecane droplet. It is obvious that within short distance (e.g. 1.0 Å) from the center of mass of the oil droplet, presence of fewer number of chemical species leads to poor statistics. To overcome this problem, the first spherical shell is constructed with 5.0 Å of radius and then onward, the thickness of the spherical shells are kept to be 1.0 Å. Figure 9.2(a) compares the radial density distribution of different moieties from the center of mass of the oil droplet in binary hexadecane–water and ternary hexadecane–dodecanol–water systems. As there are more number of water molecules compared to that of hexadecane and alcohol molecules, the water number density is scaled accordingly. Even though the region of intersection of the density profiles of the terminal carbon atom (C_{AT}) of the hexadecane and oxygen atom (OW) of water is ~ 7.0 Å thick in both the binary and ternary systems presented, the number of water and hexadecane molecules present in the interfacial region is more in the binary system than in the ternary systems. This observation suggests that the penetration of water molecules into the oil phase is diminished in the presence of dodecanol in the ternary system due to the screening of the oil droplet by the dodecanol molecules, with water molecules preferring interaction with the hydroxyl group of the dodecanol molecules through H-bonding.

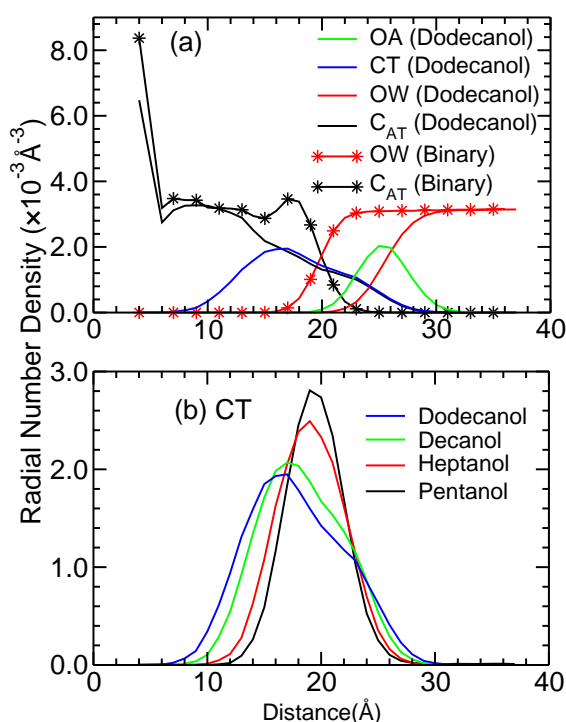


Figure 9.2: Radial number density profiles of (a) different chemical species in binary hexadecane–water and ternary hexadecane–dodecanol–water systems and (b) terminal carbon atoms (CT) of different alkanols in their respective ternary systems with hexadecane and water.

The area of the interfacial region (described above) is found to decrease with the chain length of alcohols (Figure H.1, Appendix H). We see that the density profile of water oxygen (OW) atom lies within the density profile of hydroxyl oxygen atom (OA) of dodecanol molecule towards the oil phase. The density profile of terminal carbon atom (CT) of dodecanol molecule merges with the density profile of terminal carbon atom (C_{AT}) of hexadecane molecule near the interfacial region. This comparative pattern in density profile of different chemical species is also observed in rest of the systems with different chain length alcohols. Enhancement in the number density of terminal carbon atom (C_{AT}) of hexadecane molecule is observed at the interface in binary hexadecane–water system only but not in ternary systems with alkanols. It was also observed that the density of the hexadecane molecules decreases rapidly in binary system whereas with increase in the length of the chain of alcohols, the slope of this density profile near the interface decreases.

Figure 9.2(b) represents the radial density distribution of terminal carbon atom (CT) of different alcohols from the center of mass of the hexadecane droplet in their respective ternary systems

studied. The maxima in the density profile for the terminal carbon atom (CT) appear at around ~ 19.0 Å from the center of mass of the droplet for pentanol and heptanol whereas it appears at around ~ 17.0 Å for decanol and dodecanol. The peak intensity in the corresponding density profiles decreases with increase in chain length of the alcohol molecules. Also, we see that the profiles show significant deviation from a gaussian type distribution as we move towards dodecanol. Longer chain alcohols, being more lipophilic, interacts strongly with the oil phase leading to greater penetration into the oil droplet. As a result, longer chain alcohols are likely to be found in a wider range across the oil droplet leading to broadening of the density distribution compared to the shorter chain alcohols. We have also seen that the water molecules are shifted away from the center of mass of the hexadecane droplet with increase in the chain length of the alcohol molecules. This is due to the fact that the longer chain alkanols form bigger aggregate leading to the shift of water molecules away from the center of mass of the oil droplet.

The interfacial region is defined as the region where the oil phase and the water phase coexist. We have taken the interfacial region along the radial vector from the center of mass of the oil droplet between the spherical surfaces, where the radial number density of the terminal carbon atom of hexadecane molecule (C_{AT}) and the water oxygen atom (OW) falls to zero. A hexadecane molecule is considered to be at the interface if the distance of either of its terminal carbon atoms (C_{AT}) from the center of mass of the oil droplet falls within this region. If the distance of a water oxygen atom (OW) from the center of mass of the oil droplet falls within this region, the water molecule is said to be present in the interfacial layer. For an alcohol molecule, it is the terminal carbon atom (CT) of the alkoxy chain whose distance from the center of mass of the oil droplet determines whether it is in interfacial layer.

9.3.2 Interface Organization

The orientational profiles of hexadecane, alkanol and water molecules with respect to the radial vector joining the center of mass of the hexadecane droplet and the specified atom of the corresponding molecule (e.g. the eighth carbon atom of a hexadecane chain, the terminal carbon atom (CT) of an alcohol molecule and oxygen (OW) atom of a water molecule) are obtained by calculat-

ing the bivariate distribution of probability between the Legendre polynomial of first kind (defined as $P_1(\cos \theta) = \cos \theta$) and the distance from the center of mass of the hexadecane droplet. The angle θ is computed between the aforementioned radial vector and the molecular vector (represented by the principal axis of hexadecane chain, the principal axis of alkoxy chain and the dipole moment vector of water molecule). We have also computed the probability distribution of the Legendre polynomial of second kind (defined as $P_2(\cos \theta) = (\frac{1}{2})(3 \cos \theta^2 - 1)$) between the aforementioned angles and the distance from the center of mass of the oil droplet.

Figure 9.3 presents the bivariate distribution of the orientational probability $P_1(\cos \theta)$ for the hexadecane chains and the distance from the center of mass of the oil droplet in all the systems studied. We observe that the hexadecane molecules are randomly oriented near the center of mass

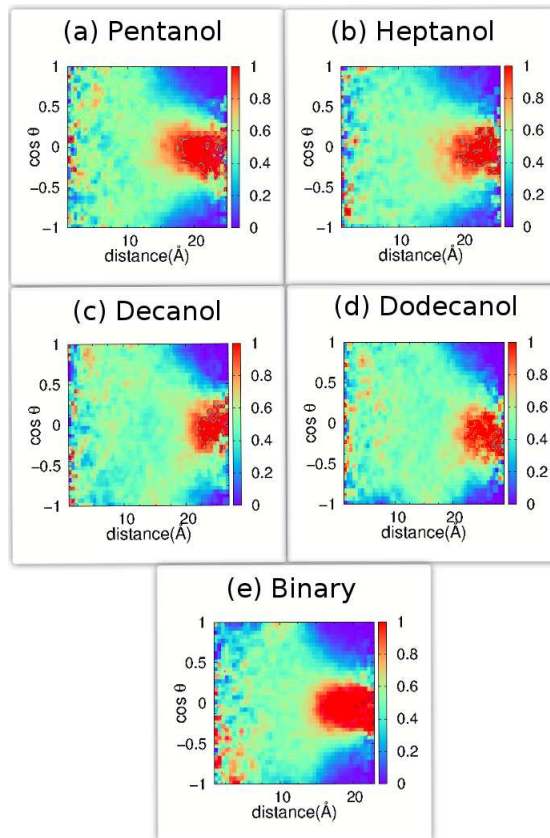


Figure 9.3: Bivariate distribution of the probability $P_1(\cos \theta)$ and the distance from the center of mass of the oil droplet in ternary systems containing (a) pentanol (b) heptanol (c) decanol (d) dodecanol and in (e) binary hexadecane–water system. θ is the angle between the radial vector and the principal axis of the hexadecane chain.

of the corresponding oil droplet irrespective of the systems studied. As we move away from the

center of mass of the oil droplet, the hexadecane molecules begin to show orientational preference to be aligned perpendicular to the radial vector. In the oil–water interfacial layer, the hexadecane molecules are most likely to be oriented tangential with respect to the droplet surface which is in good agreement with the experimental finding on SDS-stabilized nanoscopic oil droplets in water, where the oil molecules are preferentially orienting parallel to the plane [16]. The probability of being oriented perpendicular to the radial vector in the oil–water interfacial layer is maximum in case of the binary hexadecane–water system and decreases with increase in the chain length of the alcohol molecules in ternary hexadecane–alkanol–water systems. The $\langle P_2(\cos \theta) \rangle$ profile for the hexadecane chains along the radial vector from the center of mass of the oil droplet also confirms this observation (Figure H.2, Appendix H). Snapshots of hexadecane molecules near the water rich phase (in magenta) and within the oil core (in yellow) shown in Figure 9.4 also proves their tangential alignment at the droplet surface in all the systems. We can say that the layering of

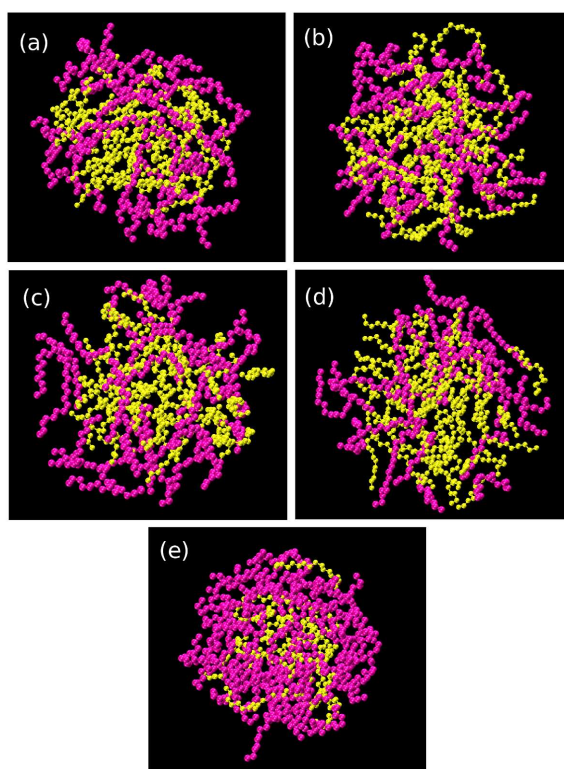


Figure 9.4: Hexadecane molecules in oil droplets of ternary systems containing (a) pentanol (b) heptanol (c) decanol and (d) dodecanol and in (e) binary hexadecane–water system. The hexadecane molecules near the water rich side and oil rich core are shown in magenta and yellow respectively. Hydrogen atoms are not shown for clarity.

longer chain alcohols at the surface of the hexadecane droplet relaxes the orientational preference of alkane molecules in the oil–water interfacial layer.

The bivariate distribution of orientational probability $P_1(\cos \theta)$ and distance from the center of mass of the oil droplet for alkanol molecules in different hexadecane–alkanol–water ternary systems are shown in figure 9.5. Unlike hexadecane molecules, alkanol alkoxy chains with their

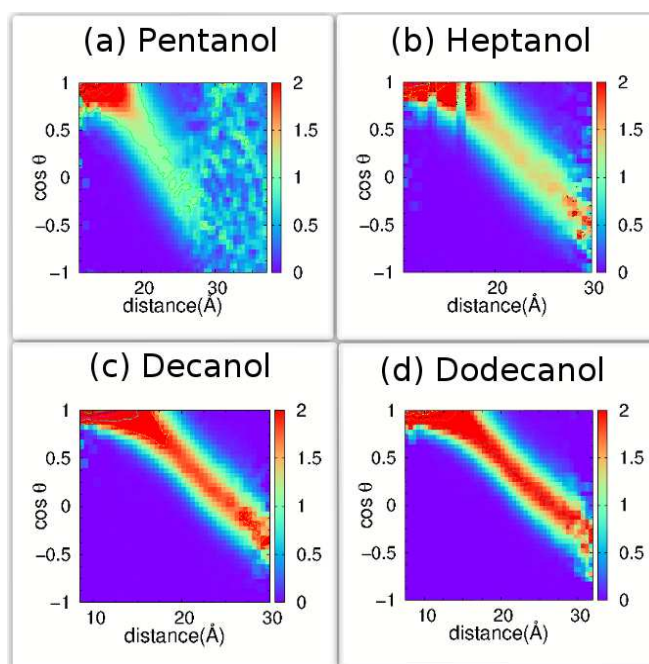


Figure 9.5: Bivariate distribution of the probability $P_1(\cos \theta)$ and the distance from the center of mass of the oil droplet in ternary systems containing (a) pentanol (b) heptanol (c) decanol (d) dodecanol. θ is the angle between the radial vector and the principal axis of the alkoxy chain.

terminal carbon atoms penetrating into the hexadecane droplet tend to orient themselves radially outward. We observe that alkanols with hydrocarbon chain length greater than seven show very high probability of their alkoxy chains orienting perpendicular to the radial vector as we move away from the center of mass of the oil droplet towards the aqueous phase. We see that the probability of the alkoxy chains of the alkanol molecules to be oriented tangential at the droplet surface increases with increase in carbon number in the alkyl chain of the alcohol molecule. The $\langle P_2(\cos \theta) \rangle$ for the alkoxy chains along the distance from the center of mass of the hexadecane droplet also confirms this observation (Figure H.3, Appendix H). Figure 9.6 depicts the alcohol molecules with their terminal carbon atoms (CT) present near water rich region (in magenta) and

near oil rich region (in yellow) for the ternary systems studied. We see that alkanol molecules with

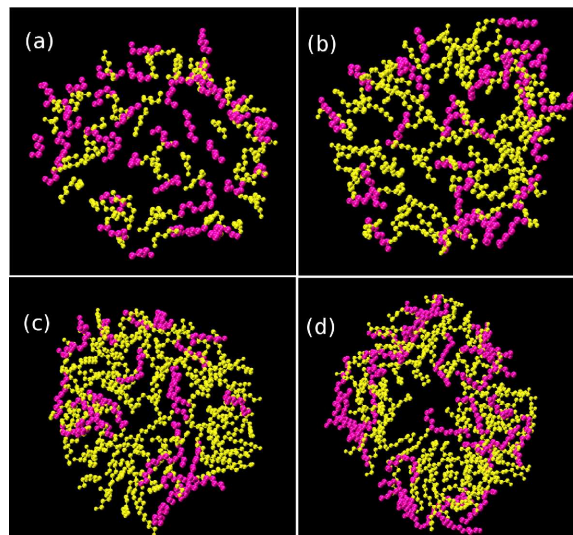


Figure 9.6: Alcohol molecules present near water rich region (magenta) and near oil rich region (yellow) of the ternary systems containing (a) pentanol (b) heptanol (c) decanol and (d) dodecanol. The oil and water phases are not shown for the ease of visualization

longer hydrocarbon chain show greater probability to lie tangential to the surface of the oil droplet near the water rich phase.

Figure 9.7 depicts the bivariate distribution of the orientational probability $P_1(\cos \theta)$ of dipole moment vectors of water molecules along the radial vector originating from the center of mass of the oil droplet in different systems studied. The water molecules near the hexadecane droplet surface in binary hexadecane–water system show the highest probability to orient their dipole moment vectors perpendicular to the radial vector joining the center of mass of the droplet and the oxygen atom of water molecule. Layering of alcohol molecules on the oil droplet in ternary hexadecane–alkanol–water system reduces the probability of the dipole moment vectors of water molecules to be oriented tangential to the the droplet surface which is in good agreement with the experimental result [18]. We have found that in ternary systems with shorter chain alcohols (e.g. pentanol and heptanol), decrease in this probability is more compared to longer chain hydrophobic alcohols (e. g. decanol and dodecanol). The $\langle P_2(\cos \theta) \rangle$ for the dipole moment vectors along the radial vector from the center of mass of the hexadecane droplet also confirms our observation (Figure H.4, Appendix H). Snapshot of water molecules near the droplet surface shown in Figure 9.8

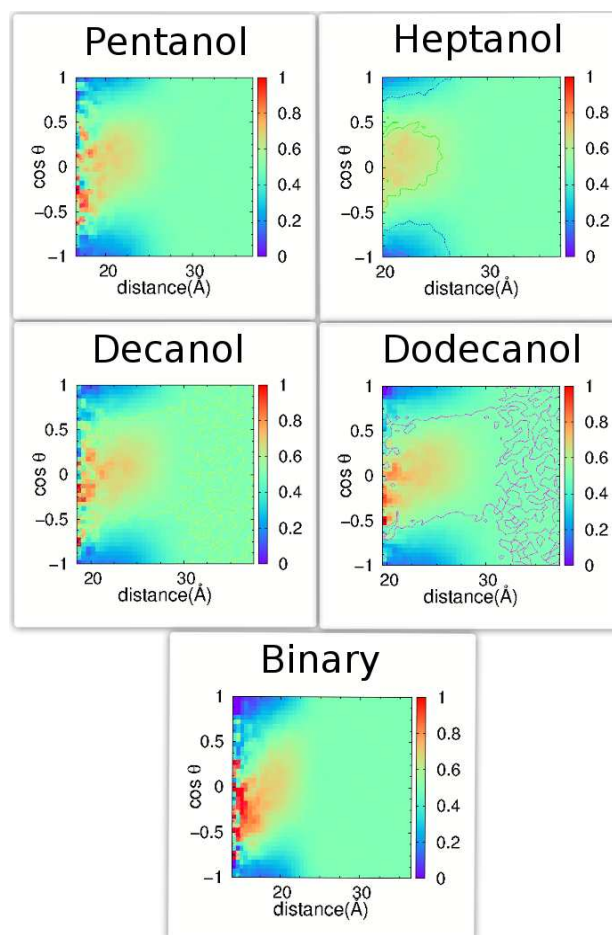


Figure 9.7: Bivariate distribution of the probability $P_1(\cos \theta)$ and the distance from the center of mass of the oil droplet in ternary systems containing (a) pentanol (b) heptanol (c) decanol (d) dodecanol and in (e) binary hexadecane–water system. θ is the angle between the radial vector and the dipole moment vector of the water molecule

depicts the tendency of the planes of water molecules to lie tangential to the droplet surface. In this figure, the hexadecane molecules are shown in blue, the alcohol molecules are shown in green, the oxygen atoms of water molecules are shown in red and hydrogen atoms of water molecules are shown in white. We observe that water molecules at the droplet surface orient in such a way that their dipole moment vectors are tangential to the droplet surface. Though it can be asserted that the hydrophobicity of the droplet surface imposes selectivity on the orientation of the adjacent water molecules, further experimental and computational studies are required to explore the underlying reasons for this orientational selectivity.

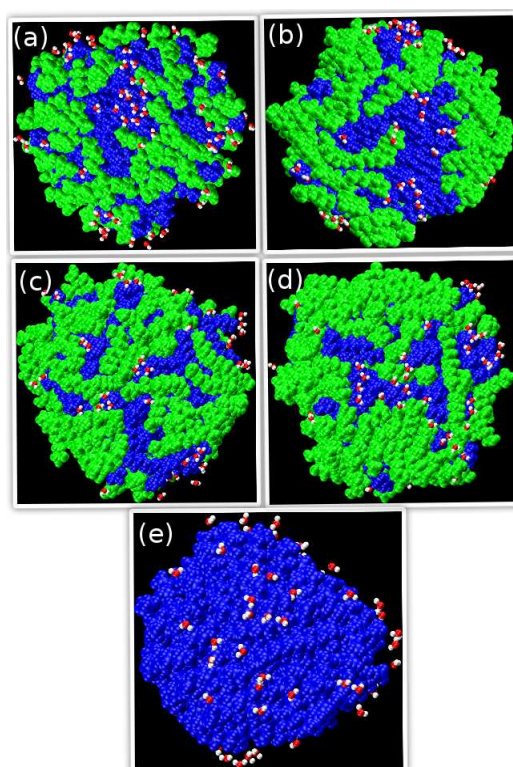


Figure 9.8: Water molecules near the droplet surface in ternary systems containing (a) pentanol (b) heptanol (c) decanol and (d) dodecanol and in (e) binary hexadecane–water system. The hexadecane molecules are shown in blue, the alcohol molecules are shown in green, the oxygen and hydrogen atoms of the water molecules are shown in red and white respectively.

9.3.3 Conformational Analysis of Hydrocarbon Chains.

Gauche population for each dihedral along the hydrocarbon chain gives an idea about its departure from fully stretched all-trans conformation in a heterogeneous aqueous environment. Figure 9.9(a) presents the percentage of gauche population for each C-C-C-C dihedral along the hexadecane chain from either of the termini (C_{AT}) for the molecules present in the oil–water interfacial layer in different systems studied. The percentage of gauche population is averaged over the equivalent dihedrals from both termini of the hexadecane molecule. We see that the probability of finding gauche conformation in any of the C-C-C-C dihedral in hexadecane molecule is ~ 1.5 times more in binary hexadecane–water system than in ternary hexadecane–alkanol–water systems. In the ternary systems containing shorter chain alcohols (e.g. pentanol and heptanol), C-C-C-C dihedrals along the hexadecane chains show slightly higher probability to be in gauche conformation than the ternary systems containing longer chain alcohols (e.g. decanol and dodecanol). We have

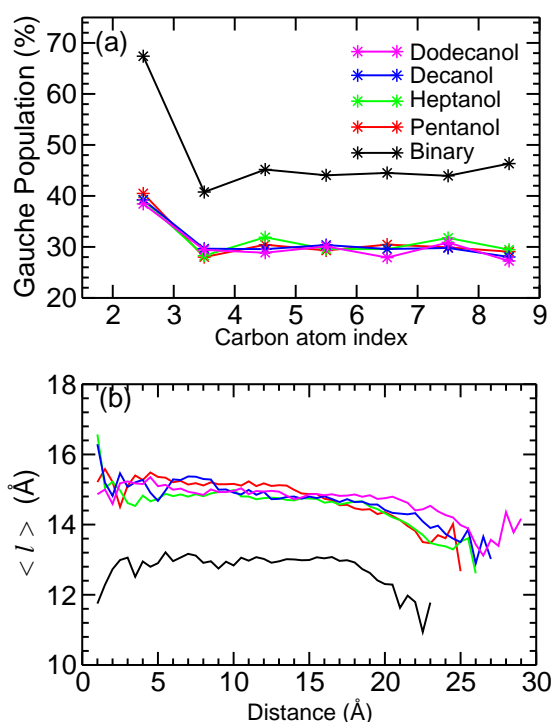


Figure 9.9: (a) Gauche population of C-C-C-C dihedrals of the hexadecane molecules (averaged over both termini (C_{AT})) present in the interfacial layer. Dihedral around the bond connecting 2nd and 3rd carbon atoms of the hexadecane chain from the terminal are plotted between 2 and 3 in the graph. (b) the average end to end distance of the hexadecane molecules present at a given distance from the center of mass of the oil droplet in binary hexadecane–water and ternary hexadecane–alkanol–water systems.

also calculated the average end to end distance of hexadecane molecules (measured as the distance between two terminal carbon atoms of hexadecane (C_{AT})) as a function of the distance of the molecule (8th carbon atom from the either of the termini) from the center of mass of oil droplet which is shown in Figure 9.9(b) in all the systems studied. We observe that the end to end distance in hexadecane molecules decreases gradually as we move farther from the center of mass of the oil droplet towards the aqueous phase in all the systems. Also, the end to end distance in the alkane molecules increases from the binary hexadecane–water system to ternary hexadecane–alkanol–water systems with longer chain alcohols near the oil–water interfacial layer. Combining the trends observed in the gauche population among the C-C-C-C dihedrals along the hexadecane chain and $\langle l \rangle$, we can say that layering of more hydrophobic longer chain alcohol molecules on the hexadecane droplet results in less gauche defects in the alkane molecules. This observation is also consistent with the area under the intersection region of the number density profiles

of the terminal carbon atoms (C_{AT}) of hexadecane molecules and oxygen atoms (OW) of water molecules (Figure H.1, Appendix H). Greater the volume of the oil–water interfacial layer, greater will be the unfavorable hydrophobic interaction between oil and water leading to folded structure of hexadecane molecules.

In alcohol molecules of ternary hexadecane–alkanol–water systems, we have found that the percentage of gauche conformations for any of the C-C-C-C dihedrals of alkanols along the hydrocarbon chain from the alkyl terminal end is slightly higher in the water rich phase compared to the oil rich phase (Figure H.5, Appendix H). It was also observed that the decrease in the length of the alkoxy chain ($\langle l \rangle$) as we move away from the center of mass of the oil droplet towards the aqueous phase is more in longer chain hydrophobic alcohols (e. g. decanol and dodecanol) than shorter chain alcohols (e. g. pentanol and heptanol) (Figure H.6, Appendix H). Based on these observations, we can say that longer chain alkanols are more probable to have a folded structure in aqueous environment.

9.3.4 Survival Probability and Hydrogen Bond Dynamics

We have computed the probability, $L(t)$, of a water molecule to be found in the oil–water interfacial layer at time t_0 and $t_0 + t$ to get an idea about the mean residence time of that molecule in the specified region [30, 31, 32]. $L(t)$ corresponds to the intermittent survival probability [33] and is calculated by the equation,

$$L(t) = \frac{1}{N} \sum_i \langle l_i(t) \cdot l_i(0) \rangle$$

where $l_i(t)$, the instantaneous survival probability operator takes the value 1 if the $i - th$ molecule is present in the interfacial layer at time t and 0 otherwise.

$L(t)$ for water molecules to be found in the oil–water interfacial layer of the binary hexadecane–water and different ternary hexadecane–water–alkanol systems are shown in Figure 9.10. We observe a rapid decay in the time correlation functions (TCFs) to ~65% within a short period of (~10 ps) elapsed time in all systems. After that, the rate of decay of TCF is highest for the binary hexadecane–water system and decreases as we move to the ternary hexadecane–water–alkanol

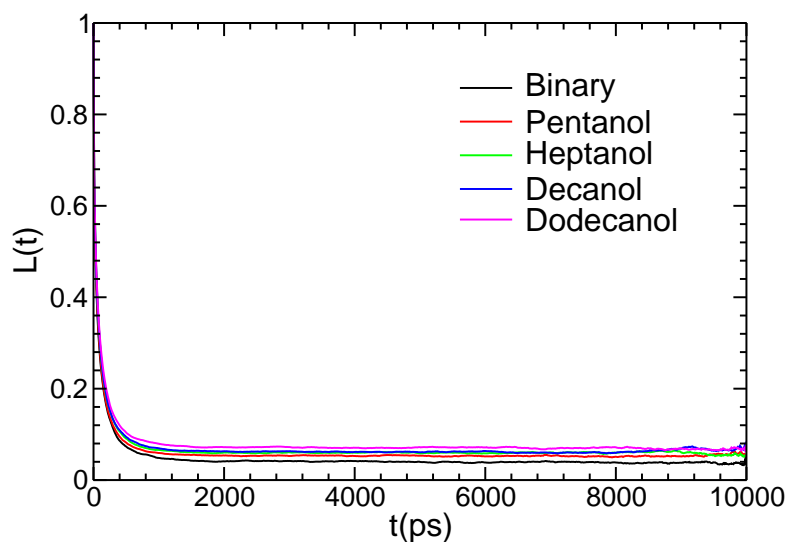


Figure 9.10: Survival probability of water molecules in the oil–water interfacial layer of binary hexadecane–water and different ternary hexadecane–water–alkanol systems.

systems with longer chain alcohols. The decay of the TCFs is correlated to the average number of hexadecane molecules present in the oil–water interfacial layer which are calculated to be 51, 42, 37, 36 and 33 for the binary hexadecane–water and ternary hexadecane–water–alkanol systems consisting of pentanol, heptanol, decanol and dodecanol molecules respectively. A hexadecane molecule is said to be present in the oil–water interfacial layer if any of its heavier atom is found in the specified region. The extent of hexadecane molecules exposed to the aqueous phase increases with decrease in hydrocarbon chain length of alcohol molecules in hexadecane–water–alkanol ternary systems, which is also evident from the figure 9.8. Greater the number of hexadecane molecules in the interfacial layer, greater will be the unfavorable hydrophobic interactions experienced by the water molecules that will prevent the water molecules from remaining in the interfacial layer for a longer time. Longer chain alkanols screen the oil phase more efficiently from the water phase. As a result, the probability of the water molecules to stay in the oil–water interfacial layer increases in the ternary systems with longer chain alcohol molecules.

The survival probability of water molecules in the oil–water interfacial layer has direct impact on the fluctuations in hydrogen-bond populations between alcohol and water molecules with time. The fluctuations in hydrogen-bond populations with time are characterized by the time correlation

function (TCF) [34]

$$C_{HB}(t) = \frac{1}{N} \sum_{i,j=1}^N \langle h_{ij}(t) \cdot h_{ij}(0) \rangle$$

where $h_{ij}(t)$, an instantaneous hydrogen-bond operator takes the value 1 if molecules i and j are H-bonded at time t and 0 otherwise, assuming the intermittent approximation [33, 35]. The function $C_{HB}(t)$ gives the probability that the molecules i and j are H-bonded at time t , given that they were H-bonded at time 0. We have adapted the geometric criteria [36] to define a hydrogen bond. In a strong H bond, the H atom and the acceptor are separated by a distance less than 2.2 Å, and the angle made by the donor, H atom, and the acceptor is within the range 130-180°. The corresponding distance and angular ranges are 2.0–3.0 Å and 90-180°, respectively to form a weak H-bond. The more electronegative alkoxy and water oxygen atoms can act both as H-bond donors and H-bond acceptors in the H-bond interaction between alcohol and water molecules. Figure 9.11 presents the time evolution of $C_{HB}(t)$ for H-bond formed between alcohol and water molecules in different hexadecane–water–alkanol ternary systems studied. We have found that the rate of

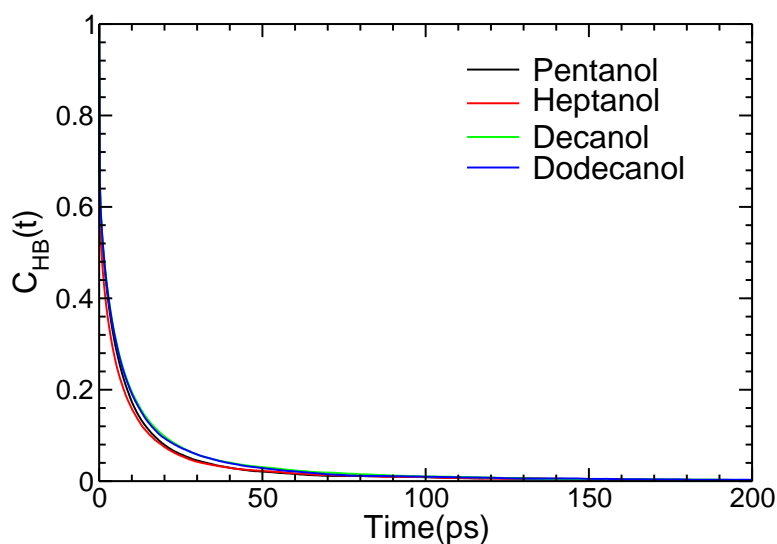


Figure 9.11: Survival autocorrelation function, $C_{HB}(t)$ for H-bonds between alcohol and water molecules in different ternary hexadecane–water–alkanol systems.

decay of $C_{HB}(t)$ is almost identical in the systems containing pentanol and heptanol and also in the systems containing decanol and dodecanol. The TCFs for more hydrophobic alcohols (decanol and dodecanol) decay slowly compared to less hydrophobic alcohols (pentanol and heptanol) which

contradicts the generally expected trend of increase in H-bond lifetime between water and alcohol molecules with decrease in alkoxy chain length. This observation can be explained based on the survival probability of water molecules in the oil–water interfacial layer. We have seen in Figure 9.10 that the average lifetime of water molecules in the oil–water interfacial layer increase as we move from shorter chain alkanols to longer chain alkanols. More the average life time of water molecules in the oil–water interfacial layer, greater is the probability of formation of H-bonds between water and alcohol molecules that are long lived leading to longer H-bond lifetime.

9.4. Conclusions All-atom molecular dynamics simulations have been performed on a series of systems consisting of nanoscopic hexadecane droplets immersed in aqueous phase with and without 1-alkanols of varying chain length (pentanol, heptanol, decanol and dodecanol) as emulsifiers. Dependence of the pattern of layering of alcohol molecules on the hexadecane droplet on the hydrophobicity of the alcohols employed has been observed, with the longer chain alkanols more likely to penetrate into the oil droplet compared to their shorter chain homologues. With increase in the alkyl chain length, alkanols exhibit a greater probability to orient their alkoxy chains tangential to the droplet surface. On the other hand, with the decrease in hydrophobic environment around the oil droplet, the hexadecane chains show greater probability to be oriented perpendicular to the radial vector. Water molecules are found to lose their orientational alignment on the droplet surface in presence of alkanols compared to neat oil–water binary system.

The interfacial hexadecane molecules in binary oil–water system show greater gauche defect probability about any of their dihedrals than those in ternary oil–water–alcohol systems. The interfacial hexadecane molecules are more distorted from all-trans conformation in the binary system compared to the ternary systems. The survival probability of water molecules in the oil–water interfacial layer is correlated with the number of hexadecane molecules exposed to the layer. In the systems with longer chain alkanols, the hexadecane molecules are screened from the water phase more effectively leading to decrease in unfavorable hydrophobic interaction between oil and water phase resulting in the greater probability of observing a water molecule in the oil–water

interfacial layer. The survival probability of water molecules in the oil–water interfacial layer determines the lifetime of H-bonds formed between alcohol and water molecules.

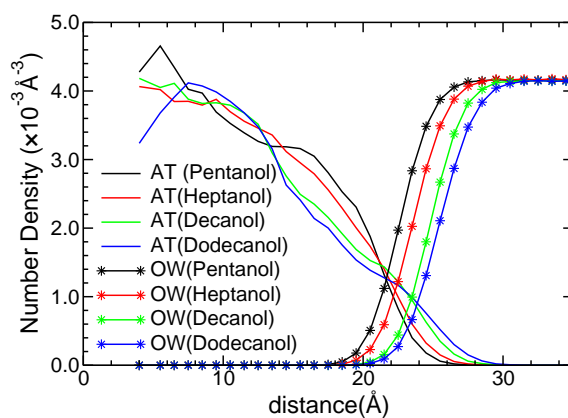


Figure H.1: Radial number density profiles of terminal carbon atoms of the hexadecane molecules (C_{AT}) and the oxygen atoms of the water molecules (OW) in the ternary systems containing different alkanols.

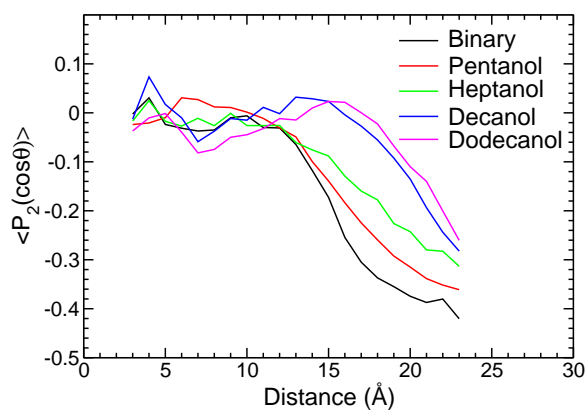


Figure H.2: Distribution of $\langle P_2(\cos \theta) \rangle$ with distance from the center of the mass of the oil droplet in binary and ternary systems studied. θ is the angle between the radial vector and the principal axis of the hexadecane molecule.

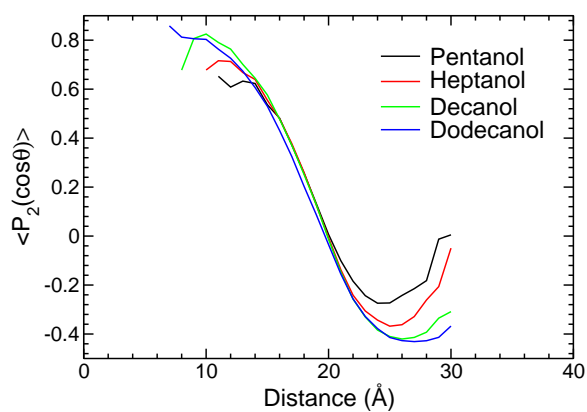


Figure H.3: Distribution of $\langle P_2(\cos \theta) \rangle$ with distance from the center of the mass of the oil droplet in binary and ternary systems studied. θ is the angle between the radial vector and the principal axis of the alkoxy chain.

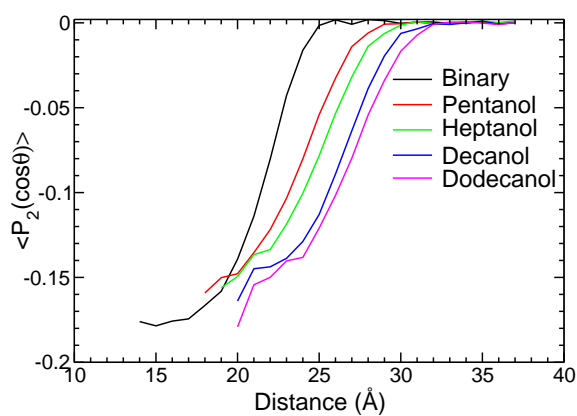


Figure H.4: Distribution of $\langle P_2(\cos \theta) \rangle$ with distance from the center of the mass of the oil droplet in binary and ternary systems studied. θ is the angle between the radial vector and the dipole moment vector of the water molecule.

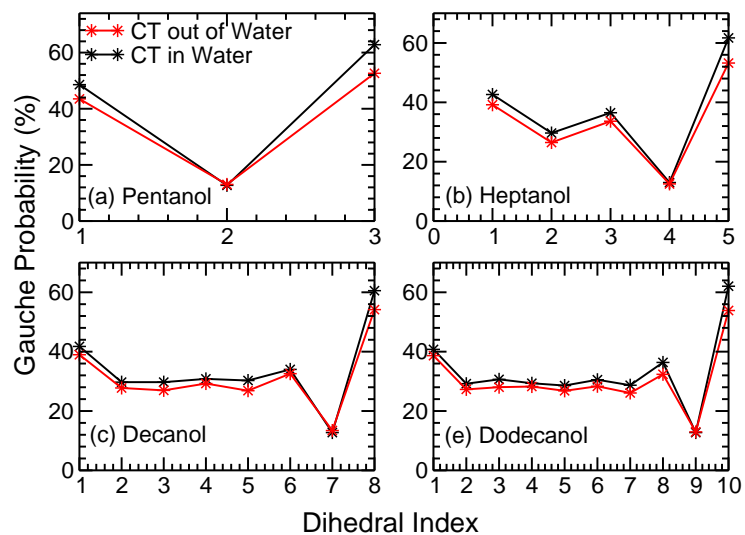


Figure H.5: Percentage of gauche population of each C-C-C-C dihedral along the alkoxy chain from the terminal (CT) of various alkanol molecules present in the interfacial layer for the ternary hexadecane–water–alkanol systems.

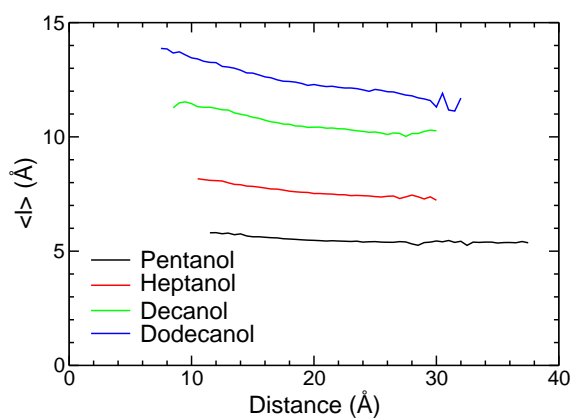


Figure H.6: Probability distribution of the length of the alkoxy chains as a function of distance from the center of mass of the oil droplet in ternary hexadecane–alkanol–water systems containing pentanol, heptanol, decanol and dodecanol molecules.

Bibliography

- [1] Tu, Y.; Peng, F.; Adawy, A.; Men, Y.; Abdelmohsen, L. K. E. A.; Wilson, D. A. *Chem. Rev.* **2016**, *116*, 2023-2078.
- [2] Hanczyc, M. *Life* **2014**, *4*, 1038-1049.
- [3] Harkins, W. D.; Davies E. C. H.; Clark, G. L. *J. Am. Chem. Soc.* **1917**, *39*, 541-596.
- [4] Beaman, D. K.; Robertson, E. J.; Richmond, G. L. *J. Phys. Chem. C* **2011**, *115*, 12508-12516.
- [5] Wu, W.; Fang, H.; Yang, F.; Chen, S.; Zhu, X.; Yuan, Q.; Gan, W. *J. Phys. Chem. C* **2016**, *120*, 6515-6523.
- [6] Pradilla, D.; Simon, S.; Sjöblom, J.; Samaniuk, J.; Skrzypiec, M.; Vernant, J. *Langmuir* **2016**, *32*, 2900-2911.
- [7] Pichot, R.; Watson, R. L.; Norton, I. N. *Int. J. Mol. Sci.* **2013**, *14*, 11767-11794.
- [8] Levin, Y.; Santos, A. P. D. *J. Phys.: Condens. Matter* **2014**, *26*, 203101-2013111.
- [9] Bresme, F.; Chacón, E.; Tarazona, P.; Tay, K. *Phys. Rev. Lett.* **2008**, *101*, 056102-1-4.
- [10] Vácha, R.; Roke, S. *J. Phys. Chem. B* **2012**, *116*, 11936-11942.
- [11] Palchowdhury, S.; Bhargava, B. L. *J. Phys. Chem. B* **2014**, *118*, 13930-13939.
- [12] Vazdar, M.; Pluhařová, E.; Mason, P. E.; Vácha, R.; Jungwirth, P. *J. Phys. Chem. Lett.* **2012**, *3*, 2087-2091.

- [13] Valley, N. A.; Robertson, E. J.; Richmond, G. L. *Langmuir* **2014**, *30*, 14226-14233.
- [14] Aguiar, H. B. D.; Beer, A. G. F. D.; Strader, M. L.; Roke, S. *J. Am. Chem. Soc.* **2010**, *132*, 2122-2123.
- [15] Vácha, R.; Rick, S. W.; Jungwirth, P.; Beer, A. G. F. D.; Aguiar, H. B.; Samson, J.; Roke, S. *J. Am. Chem. Soc.* **2011**, *133*, 10204-10210.
- [16] Aguiar, H. B. D.; Strader, M. L.; Beer, A. G. F. D.; *J. Phys. Chem. B* **2011**, *115*, 2970-2978.
- [17] Sang, Y.; Yang, F.; Chen, S.; Xu, H.; Zhang, S.; Yuan, Q.; Gan, W. *J. Chem. Phys.* **2015**, *142*, 22704-1-6.
- [18] Chen, Y.; Jena, K. C.; Roke, S. *J. Phys. Chem. C* **2015**, *119*, 17725-17734.
- [19] Urban, B. W.; Bleckwenn, M.; Barann, M. *Pharmacol. Ther.* **2006**, *111*, 729-770.
- [20] Williams, A. C. Barry, B. W. *Adv. Drug Deliv. Rev.* **2004**, *56*, 603-618.
- [21] Gutierrez, J. M. P.; Hinkley, T.; Taylor, J. W.; Yanev, K.; Cronin, L. *Nat. Commun.* **2014**, *5*, 1-8.
- [22] Rivera, J.; McCabe, C.; Cummings, P. T. *Phys. Rev. E* **2003**, *67*, 011603-1-10.
- [23] Plimpton, S. *J. Comput. Phys.* **1995**, *117*, 1-19.
- [24] Berendsen, H. J. C.; Postma, J. P. M.; van Gunsteren, W. F.; Hermans, J. In *Intermolecular Forces*; Pullman, B., Ed.; Reidel: Dordrecht, The Netherlands, 1981; p 331.
- [25] Siu, S. W. I.; Pluhackova, K.; Böckmann, R. A. *J. Chem. Theory Comput.* **2011**, *8*, 1459-1470.
- [26] Jorgensen, W. L.; Maxwell, D. S.; Tirado-Rives, J. *J. Am. Chem. Soc.* **1996**, *118*, 11225-11236.
- [27] Allen, M. P.; Tildesley, D. J. *Computer Simulation of Liquids*; Clarendon Press: Oxford, U.K., 1987.

- [28] Ryckaert, J. P.; Ciccotti, J.; Berendsen, H. J. C. *Numerical J. Comput. Phys.* **1977**, *23*, 327-341.
- [29] Humphrey, W.; Dalke, A.; Schulten, K. *J. Mol. Graphics* **1996**, *14*, 33-38.
- [30] Lisal, M.; Posel, Z.; Izák, P. *Phys. Chem. Chem. Phys.* **2012**, *14*, 5164-5177.
- [31] Lisal, M. *J. Chem. Phys.* **2013**, *139*, 214701.
- [32] Palchowdhury, S.; Bhargava, B. L. *J. Phys. Chem. C* **2016**, *120*, 5430-5441.
- [33] Lloyd, E. *Handbook of Applicable Mathematics. Volume II: Probability*, Wiley, New York, 1st edn, 1980
- [34] Luzar, A.; Chandler, D. Hydrogen-Bond Kinetics in Liquid Water. *Nature* **1996**, *379*, 55-57.
- [35] Eloa, M. D.; Ladanyi, B. M. *J. Chem. Phys.* **2006**, *125*, 184506-184519.
- [36] Desiraju, G. R.; Steiner, T. *The Weak Hydrogen Bond, In Structural Chemistry and Biology*; Oxford University Press: New York, 2001.

Summary

- For equimolar binary mixture of imidazolium based ionic liquids, the spatial correlation between ions, the liquid-vapor interface population and the pattern of interface organisation is governed by the hydrophobicity of the ions.
- Composition variation in binary mixture of imidazolium based ionic liquids sets trends in surface population, surface roughness and dynamics in the liquid-vapor interfacial layer.
- Increase in shorter alkyl chain length of double tailed imidazolium based ionic liquids controls the intermolecular organisation, size and structures of the aggregates formed in aqueous solutions.
- Introduction of hydroxyl group at the terminal carbon atom of varying alkyl chain in [HOC_nC₁₀Im] cations leads to formation of aggregates having size and shape different than their non-hydroxyl analogues in aqueous solutions.
- Spacer chain length of [C_n(MIm)₂] cations in their aqueous solutions regulates the intracationic structure, bulk solution structure and dynamics as well as solution-vapor interface organisation.
- Enhanced intake of amino acids into the ionic liquid based reverse micelles stabilizes the shape of the reverse micelles, intermolecular H-bonds and slows down mobility of molecules.
- Hydrophobic ionic liquids facilitates removal of water from the vicinity of the oil phase at the planar interface of water-IL-nonane ternary systems.

- The orientational ordering and conformation of alkane and alkanol molecules at the curved oil-water interface is governed by the hydrophobicity of alkanols.